



Furnari, Giandomenico (2017) *Rapid microwave-assisted synthesis and characterization of transition metal carbides and nitrides*. PhD thesis.

<http://theses.gla.ac.uk/8612/>

Copyright and moral rights for this work are retained by the author

A copy can be downloaded for personal non-commercial research or study, without prior permission or charge

This work cannot be reproduced or quoted extensively from without first obtaining permission in writing from the author

The content must not be changed in any way or sold commercially in any format or medium without the formal permission of the author

When referring to this work, full bibliographic details including the author, title, awarding institution and date of the thesis must be given

Enlighten:Theses  
<http://theses.gla.ac.uk/>  
theses@gla.ac.uk

# **Rapid Microwave-assisted Synthesis and Characterization of Transition Metal Carbides and Nitrides**

by

Giandomenico Furnari, BSci (*Hons*)

Submitted in fulfilment of the requirements  
for the degree of Doctor of Philosophy



University of Glasgow | School of  
Chemistry

School of Chemistry  
College of Science and Engineering  
University of Glasgow

May 2017

## Abstract

The aim of this thesis is to describe the rapid microwave synthesis of a number of transition metal carbides and nitrides as well as their structural characterization and develop reproducible procedures that can cut processing times and, hence, reduce the energy consumption. Specifically, 4 binary systems are investigated: V–C, Zr–C, Hf–C and Zr–N. Carbide syntheses were conducted using either elemental or oxide precursors under argon, whereas the nitride system was investigated from zirconium powder under either nitrogen or ammonia gas.

Microwave syntheses were conducted using both multi-mode cavity (MMC) and single-mode cavity (SMC) microwave reactors at a power of 800 W and 1 kW, respectively, with an operating microwave frequency of 2.45 GHz. Vanadium carbide production from both oxide and elemental precursors was achieved in 6 minutes for MMC experiments and 2 minutes for SMC experiments. Zirconium carbide was obtained from zirconium powder and graphite in 20 minutes in a MMC reactor and 6 minutes in a SMC reactor. Unfortunately, the carbothermal reduction of  $ZrO_2$  to  $ZrC$  was not successful as the starting materials did not react with each other and no product formation was observed. Similar results were obtained for the carburization of  $HfO_2$ . However, hafnium carbide was synthesized combining graphite with hafnium metal in 20 minutes in a MMC reactor and 6 minutes in a SMC reactor but the formation of additional oxide phases (i.e.  $HfO_2$ ) was also observed. Finally, zirconium nitride production was investigated in a MMC reactor and prepared in 20 minutes from zirconium metal under either  $N_2$  or  $NH_3$  gas. Generally, oxygen inclusion was observed in all experiments either in the form of oxycarbide or additional oxide phase(s).

Once a reproducible experimental technique was established, products were characterized by several analytical techniques. Powder X-ray diffraction (PXRD) was used to identify product phases, study the phase evolution of the microwave processes and refine the MW-synthesized structures by Rietveld method. Powder neutron diffraction (PND) was used on the V-C and Zr-C samples to evaluate product purity and the C and O occupancies of the final products. Scanning electron microscopy coupled with energy dispersive X-ray spectroscopy (SEM-EDX) provided information about product morphology, particle size and purity. EDX supported the evidence for oxygen inclusion across samples. Supporting information in favour of this was additionally offered by Raman spectroscopy. X-ray

photoelectron spectroscopy (XPS) was used to analyze the surface of products together with the chemical state of the elements present in it.

## Acknowledgements

Firstly, I would like to thank the University of Glasgow for funding and my supervisor Prof. Duncan H. Gregory for his guidance and assistance throughout the course of my PhD as well as his patience in correcting this thesis. It was a pleasure to have worked with him. I would also like to thank other academic staff members/collaborators, particularly, Dr. Justin Hargreaves for his useful help and suggestions about my work, Mr. Jim Gallagher for his support with SEM-EDX, Dr. Ron Smith for his assistance in PND data collection and Dr. Sina Saremi-Yarahmadi for the XPS measurements and his friendship.

To the past and present members of the Gregory Group and my friends in and outside the department from all over the world – you are too many to be mentioned all together, but just to name a few: Davide, Simon, Hallam, Holly, Nicholas, the two Irenes, Marc, Dr. Christos, Elina, Mustafa, Francesca, Amaia, Luis (the numero uno) and so on... I'm glad I've met you guys and hope to see you all somewhere around the world at some point. Thanks for all the good and bad moments shared together in this endless but useful experience.

And here goes the Italian bit! Un grande ringraziamento va a tutti i miei altrettanto numerosi amici e parenti in Italia per la loro calorosa accoglienza durante le mie vacanze a Palermo e dintorni, per le nottate passate fuori, per i bagni a mare, le “*arrostute*”, le risate.

E ultimo ma non per importanza, un ringraziamento speciale va a mia madre, mio padre e mio fratello che mi hanno sempre supportato nel corso di questo dottorato sino alla fine. Questa tesi è per voi.

# Table of Contents

<b>Abstract</b>	<b>i</b>
<b>Acknowledgements</b>	<b>iii</b>
<b>Table of Contents</b>	<b>iv</b>
<b>List of Figures</b>	<b>vii</b>
<b>List of Tables</b>	<b>xvi</b>
<b>Definitions</b>	<b>xix</b>
<b>1 Introduction</b>	<b>1</b>
1.1 Microwave History and Theory	1
1.2 Microwave Heating Mechanisms	4
1.2.1 Dipolar Polarization	5
1.2.2 Conduction	6
1.3 Interaction of MWs with Matter	6
1.4 Microwave vs. Conventional Heating	10
1.4.1 Properties of MW Heating	11
1.4.2 Volumetric Heating	11
1.4.3 Conventional Heating	12
1.5 Conventional Routes to Transition Metal Carbides and Nitrides	13
1.6 Solid-state Microwave Synthesis	16
1.7 Transition Metal Carbides and Nitrides	20
1.7.1 Structure, Synthesis and Applications of TMCs and TMNs	21
1.8 Chapter Summary and Scope of This Work	25
1.9 References	26
<b>2 Experimental Theory and Methods</b>	<b>34</b>
2.1 Microwave Reactors	34
2.1.1 Multi-mode Cavity (MMC) Microwave Reactors	35
2.1.2 Single-mode Cavity (SMC) Microwave Reactors	37

2.2	Synthesis and Processing	39
2.2.1	Sample Preparation	39
2.2.2	Synthesis Using a MMC Reactor	41
2.2.3	Synthesis Using a SMC Reactor	43
2.3	Characterization Techniques	44
2.3.1	Powder X-ray Diffraction	45
2.3.2	Powder Neutron Diffraction	51
2.3.3	Rietveld Refinement	53
2.3.4	Scanning Electron Microscopy coupled with Energy-dispersive X-ray	56
2.3.5	Raman Spectroscopy	58
2.3.6	X-ray Photoelectron Spectroscopy	60
2.4	Chapter Summary	61
2.5	References	62

### **3 Microwave Synthesis and Structural Characterization of Carbides in the V-C System – The V<sub>8</sub>C<sub>7</sub> Superstructure** **65**

3.1	Introduction to Vanadium Carbide	65
3.2	Microwave Synthesis Studies in the V–C system	67
3.2.1	Introduction	67
3.2.2	Experimental	69
3.2.3	Results and Discussion	70
3.3	Microwave Synthesis Studies in the V <sub>2</sub> O <sub>5</sub> –C system	92
3.3.1	Introduction	92
3.3.2	Experimental	92
3.3.3	Results and Discussion	94
3.4	Chapter Summary	106
3.5	References	107

### **4 Microwave Synthesis and Structural Characterization of Carbides in the Zr-C and Hf-C Systems** **111**

4.1	Introduction to Zirconium and Hafnium Carbide	111
4.2	Microwave Synthesis Studies in Zr–C system	114
4.2.1	Introduction	114
4.2.2	Experimental	115
4.2.3	Results and Discussion	117
4.3	Microwave Synthesis Studies in the ZrO <sub>2</sub> –C system	139

4.3.1	Introduction	139
4.3.2	Experimental	140
4.3.3	Results and Discussion	141
4.4	Microwave Synthesis Studies in Hf–C system	143
4.4.1	Introduction	143
4.4.2	Experimental	144
4.4.3	Results and Discussion	145
4.5	Chapter Summary	148
4.6	References	149
<b>5</b>	<b>Preliminary Studies on the Microwave Synthesis and Structural Characterization of Nitrides in the Zr-N System</b>	<b>153</b>
5.1	Introduction to Zirconium Nitride	153
5.2	Microwave Synthesis Studies in Zr-N system	155
5.2.1	Introduction	155
5.2.2	Experimental	155
5.2.3	Results and Discussion	156
5.3	Chapter Summary	170
5.4	References	171
<b>6</b>	<b>Conclusions and Future Work</b>	<b>173</b>
<b>7</b>	<b>Appendix</b>	<b>177</b>

## List of Figures

Figure 1-1 Schematic representation of an electromagnetic wave. The electric field, E, is in a vertical plane and the magnetic field, H, in a horizontal plane. <sup>1</sup> .....	1
Figure 1-2 The electromagnetic spectrum, showing the frequency and wavelength associated with each type of electromagnetic wave. <sup>5</sup> .....	2
Figure 1-3 The resonant-cavity magnetron and its components. <sup>11</sup> .....	3
Figure 1-4 Schematic illustration of the dipole moment in a water molecule. Its negative pole ( <i>red</i> ) is at the oxygen atom (the more electronegative one) whereas its positive pole ( <i>blue</i> ) is at the hydrogen atoms (the less electronegative ones). <sup>29</sup> .....	5
Figure 1-5 Side view of the layered and planar structure of graphite. <sup>31</sup> .....	6
Figure 1-6 The interaction of transparent ( <i>top</i> ), reflective ( <i>middle</i> ) and absorbing ( <i>bottom</i> ) materials with microwave energy. ....	7
Figure 1-7 Schematic showing the main differences between conventional ( <i>left</i> ) and microwave heating ( <i>right</i> ). In conventional heating, heat is driven into the substance through thermal conduction, resulting in the surface being warmer than the interior. In microwave heating, microwaves interact directly with the material being heated and volumetric heating occurs, giving an inverse temperature gradient. ....	11
Figure 1-8 Common crystal structures in TMCs and TMNs. The blue balls represent transition metal atoms and the brown balls represent carbon/nitrogen atoms. ....	22
Figure 2-1 Schematic diagram of a typical microwave oven showing key internal components. <sup>6</sup> .....	35
Figure 2-2 Visualization of the horizontal mode structure in a domestic microwave oven using infrared thermal imaging. <sup>8</sup> .....	36
Figure 2-3 CEM Mars 6 multi-mode cavity MW reactor. <sup>13</sup> .....	37
Figure 2-4 Nodes and antinodes standing wave pattern. ....	37
Figure 2-5 Schematic illustration of the single-mode cavity MW reactor used. ....	38
Figure 2-6 Schematic illustration of the reaction set-up under flowing gas using a capped and sealed quartz tube in an MMC microwave reactor for the synthesis of TMCs.....	41
Figure 2-7 Photograph ( <i>left</i> ) and diagram ( <i>right</i> ) of the reaction set-up under flowing gas using a capped and sealed quartz tube in an MMC microwave reactor for the synthesis of TMCs. ....	42

Figure 2-8 Schematic illustration of the reaction set-up under flowing gas using a capped and sealed quartz tube in an MMC microwave reactor for the synthesis of zirconium nitride. ....	42
Figure 2-9 Photograph ( <i>left</i> ) and diagram ( <i>right</i> ) of the reaction set-up under flowing gas using a capped and sealed quartz tube in an MMC microwave reactor for the synthesis of zirconium nitride. ....	43
Figure 2-10 Schematic illustration of the reaction set-up under flowing gas using a capped and sealed quartz tube in an SMC microwave reactor. ....	43
Figure 2-11 Photographs of the reaction set-up under flowing gas using a capped and sealed quartz tube in an SMC microwave reactor. ....	44
Figure 2-12 General representation of a simple unit cell showing cell lengths and angles. <sup>18</sup> .....	45
Figure 2-13 Diagram showing the lattice centering types in three-dimensional space: primitive ( <i>left</i> ), base-centered ( <i>middle-left</i> ), body-centered ( <i>middle-right</i> ), and face-centered ( <i>right</i> ). ....	47
Figure 2-14 Schematic showing diffraction of X-rays on parallel crystallographic planes within a crystal. A and B are two incident X-ray beams, A' and B' are the corresponding diffracted X-ray beams. The distance between crystallographic planes is $d_{hkl}$ and $\theta$ is the angle between the plane and the incident beam. ....	48
Figure 2-15 Diffracted X-ray cones from a powder (polycrystalline) sample. <sup>23</sup> .....	49
Figure 2-16 Schematic illustration of a PXRD flat plate sample holder. ....	50
Figure 2-17 Setup of the diffractometer in a Bragg-Brentano geometry. ....	50
Figure 2-18 Schematic of the POLARIS diffractometer at ISIS. The numbers indicate the different detector banks. <sup>31</sup> .....	53
Figure 2-19 Schematic representation of a SEM microscope. ....	57
Figure 2-20 Typical optical configuration in a Raman spectrometer. <sup>40</sup> .....	58
Figure 2-21 Rayleigh, Stokes and Anti-Stokes scattering in Raman spectroscopy. ....	59
Figure 2-22 Diagram showing the photoelectric effect. An incident X-ray photon excites the atom and a photoelectron is subsequently emitted. ....	60
Figure 2-23 Basic components of a monochromatic XPS system. <sup>45</sup> .....	61
Figure 3-1 Phase diagram of the V-C system. <sup>1</sup> .....	66
Figure 3-2 Structures of VC ( <i>a</i> ), $V_8C_7$ ( <i>b</i> ), $V_6C_5$ ( <i>c</i> ) and $V_2C$ ( <i>d</i> ). V atoms ( <i>blue</i> ), C atoms ( <i>grey</i> ). ....	67
Figure 3-3 PXRD pattern taken ex-situ from vanadium metal plus graphite (8:7) heated in a MMC reactor for 6 minutes at a power of 800 W. All reflections can be attributed to $V_8C_7$ except the one marked with *, which belongs to the (002) reflection from graphite.	

The reflections marked with • are superstructure lines characteristic of the $V_8C_7$ phase. .....	71
Figure 3-4 The structure of $V_8C_7$ as proposed by de Novion <i>et al.</i> (1977). <sup>6</sup> .....	72
Figure 3-5 Observed ( <i>plusses</i> ), calculated ( <i>solid green line</i> ), and difference ( <i>solid purple line</i> ) profile plot for the Rietveld refinement against PXR data for the vanadium carbide superstructure $V_8C_7$ . Tick marks denote $V_8C_7$ diffraction peaks. The (002) graphite reflection at $2\theta = 26.5^\circ$ was excluded from the refinement.....	73
Figure 3-6 <i>Ex-situ</i> patterns for V + C pellets irradiated in an MMC reactor at a power of 800 W from $t = 0$ (reagents – <i>bottom</i> ) to reaction completion ( <i>top</i> ).....	75
Figure 3-7 <i>Ex-situ</i> patterns for V + C pellets irradiated in an SMC reactor at a power of 1 kW from $t = 0$ (reagents – <i>bottom</i> ) to reaction completion ( <i>top</i> ).....	76
Figure 3-8 SEM micrographs for the $V_8C_7$ synthesized from vanadium metal and carbon in 6 minutes in an MMC microwave reactor at a power of 800 W.....	78
Figure 3-9 SEM micrographs for the $V_8C_7$ synthesized from vanadium metal and carbon in 2 minutes in a single-mode cavity (SMC) microwave reactor at a power of 1 kW.....	78
Figure 3-10 EDX spectrum for the $V_8C_7$ synthesized from vanadium metal and carbon in 6 minutes in an MMC microwave reactor, showing that only vanadium and carbon were present. ....	79
Figure 3-11 EDX spectrum for the $V_8C_7$ synthesized from vanadium metal and carbon in 6 minutes in an MMC microwave reactor, showing that oxygen was present as well as vanadium and carbon. ....	79
Figure 3-12 Experimental Raman spectrum for the MW-synthesized $V_8C_7$ from vanadium metal and carbon in 6 minutes in an MMC microwave reactor.....	80
Figure 3-13 Raman spectrum for commercial $V_2O_5$ .....	81
Figure 3-14 Structure of vanadium pentoxide. ....	83
Figure 3-15 Wide survey X-ray photoelectron spectrum for the MW-synthesized $V_8C_7$ samples prepared from vanadium metal and carbon in 6 minutes in a MMC microwave reactor. ....	84
Figure 3-16 Fitted V2p X-ray photoelectron spectrum for the MW-synthesized $V_8C_7$ samples prepared from vanadium metal and carbon in 6 minutes in a multi-mode MW reactor. ....	85
Figure 3-17 Fitted C1s X-ray photoelectron spectrum for the MW-synthesized $V_8C_7$ samples prepared from vanadium metal and carbon in 6 minutes in a multi-mode MW reactor. ....	86

Figure 3-18 Fitted O1s X-ray photoelectron spectrum for the MW-synthesized $V_8C_7$ samples prepared from vanadium metal and carbon in 6 minutes in a multi-mode MW reactor. ....	86
Figure 3-19 C1s X-ray photoelectron spectrum for the MW-synthesized $V_8C_7$ prepared from vanadium metal and carbon in 6 minutes in a multi-mode MW reactor after three Ar ion etchings. ....	87
Figure 3-20 V2p and O1s X-ray photoelectron spectrum for the MW-synthesized $V_8C_7$ samples prepared from vanadium metal and carbon in 6 minutes in a multi-mode MW reactor after three Ar ion etchings. ....	88
Figure 3-21 OCD plot from POLARIS bank 4 generated by Rietveld refinement against vanadium carbide PND data using the cubic $P4_332$ $V_8C_7$ structure model taken from the ICSD database. Data collected at room temperature for approx. 2 hours. The red tick marks indicate reflections from graphite and the black tick marks indicate reflections from $V_8C_7$ . ....	90
Figure 3-22 PXRD pattern taken ex-situ from vanadium(V) oxide plus graphite (4:27) heated for 6 minutes in an MMC microwave reactor at a power of 800 W. All reflections can be attributed to $V_8C_7$ except the one marked with *, which belongs to the (002) reflection from graphite. The reflections marked with • are superstructure lines characteristic of the $V_8C_7$ phase. ....	94
Figure 3-23 Observed ( <i>plusses</i> ), calculated ( <i>solid green line</i> ), and difference ( <i>solid purple line</i> ) profile plot for the Rietveld refinement against PXRD data for the vanadium carbide superstructure $V_8C_7$ . Tick marks denote $V_8C_7$ diffraction peaks. The (002) graphite reflection at $2\theta = 26.5^\circ$ was excluded from the refinement. ....	96
Figure 3-24 <i>Ex-situ</i> patterns for $V_2O_5 + C$ pellets heated for 6 minutes in an MMC reactor at a power of 800 W from reagents ( <i>bottom</i> ) to reaction completion ( <i>top</i> ). ....	98
Figure 3-25 <i>Ex-situ</i> patterns for $V_2O_5 + C$ pellets heated for 2 minutes in a SMC reactor at a power of 1kW from reagents ( <i>bottom</i> ) to reaction completion ( <i>top</i> ). ....	99
Figure 3-26 SEM micrographs for the MW-synthesized $V_8C_7$ from vanadium(V) oxide and carbon in a MMC reactor at a power of 800 W. ....	100
Figure 3-27 SEM micrographs for the MW-synthesized $V_8C_7$ from vanadium(V) oxide and carbon in a single-mode cavity (SMC) microwave reactor at a power of 1 kW. ....	101
Figure 3-28 Experimental Raman spectrum for the MW-synthesized $V_8C_7$ from vanadium(V) oxide and carbon in an MMC at a power of 800 W. ....	102
Figure 3-29 Wide survey X-ray photoelectron spectrum for the MW-synthesized $V_8C_7$ sample prepared from $V_2O_5 + C$ powders in an MMC reactor at a power of 800 W. ....	104

Figure 3-30 Fitted V2p X-ray photoelectron spectrum for the MW-synthesized V <sub>8</sub> C <sub>7</sub> sample prepared from V <sub>2</sub> O <sub>5</sub> + C powders in an MMC reactor at a power of 800 W. ....	105
Figure 3-31 Fitted C1s X-ray photoelectron spectrum for the MW-synthesized V <sub>8</sub> C <sub>7</sub> samples prepared from V <sub>2</sub> O <sub>5</sub> + C powders in an MMC reactor at a power of 800 W. ....	105
Figure 3-32 Fitted O1s X-ray photoelectron spectrum for the MW-synthesized V <sub>8</sub> C <sub>7</sub> samples prepared from V <sub>2</sub> O <sub>5</sub> + C powders in an MMC reactor at a power of 800 W. ....	106
Figure 4-1 Phase diagram of the Zr-C system. <sup>1</sup> .....	112
Figure 4-2 Phase diagram of the Hf-C system. <sup>2</sup> .....	113
Figure 4-3 Crystal structure of ZrC and HfC. Zr/Hf atoms (blue), C atom (grey). ....	113
Figure 4-4 PXRD pattern taken <i>ex-situ</i> from zirconium metal plus graphite (1:1) heated in an MMC reactor for 20 minutes at a power of 800 W under Ar. All reflections can be attributed to ZrC except the one marked with *, which belongs to the (002) reflection from graphite.....	118
Figure 4-5 Observed ( <i>plusses</i> ), calculated ( <i>solid green line</i> ), and difference ( <i>solid purple line</i> ) profile plot for the Rietveld refinement against PXRD data for the zirconium carbide ZrC. Tick marks denote ZrC diffraction peaks. The (002) graphite reflection at 2θ = 26.5° was excluded from the refinement. ....	119
Figure 4-6 <i>Ex-situ</i> patterns for Zr + C pellets heated in an 800 W domestic MW oven from reagents ( <i>bottom</i> ) to reaction completion ( <i>top</i> ).....	121
Figure 4-7 <i>Ex-situ</i> patterns for Zr + C pellets heated in a single-mode cavity MW reactor at a power of 1 kW from reagents ( <i>bottom</i> ) to reaction completion ( <i>top</i> ). ....	122
Figure 4-8 SEM micrographs at (a) low and (b) higher magnification for the MW-synthesized ZrC from zirconium metal and carbon in 20 minutes in an MMC reactor at a power of 800 W.....	123
Figure 4-9 SEM micrographs at (a) low and (b) higher magnification for the MW-synthesized ZrC from zirconium metal and carbon in 6 minutes in a SMC microwave reactor at a power of 1 kW.....	124
Figure 4-10 EDX spectrum for the MW-synthesized ZrC from zirconium metal and carbon in 20 minutes in an MMC microwave reactor, showing that only zirconium and carbon were present. ....	125
Figure 4-11 EDX spectrum for the MW-synthesized ZrC from zirconium metal and carbon in 20 minutes in an MMC microwave reactor, showing that oxygen was present as well as zirconium and carbon. ....	125
Figure 4-12 EDX spectrum for the MW-synthesized ZrC from zirconium metal and carbon in 20 minutes in an MMC microwave reactor, showing that hafnium impurities were present as well as zirconium and carbon.....	125

Figure 4-13 Experimental Raman spectrum for the MW-synthesized ZrC from zirconium metal and carbon in 20 minutes in an MMC microwave reactor.....	126
Figure 4-14 Experimental Raman spectrum for commercial <i>m</i> -ZrO <sub>2</sub> . ....	127
Figure 4-15 Crystal structures for <i>m</i> -ZrO <sub>2</sub> ( <i>a</i> ), <i>t</i> -ZrO <sub>2</sub> ( <i>b</i> ) and <i>c</i> -ZrO <sub>2</sub> ( <i>c</i> ). Zr atoms ( <i>blue</i> ), O atoms ( <i>red</i> ). ....	128
Figure 4-16 Wide survey X-ray photoelectron spectrum for the MW-synthesized ZrC samples prepared from zirconium metal and carbon in 20 minutes in a multi-mode MW reactor. ....	130
Figure 4-17 Fitted Zr3d X-ray photoelectron spectrum for the MW-synthesized ZrC samples prepared from zirconium metal and carbon in 20 minutes in a multi-mode MW reactor. ....	131
Figure 4-18 Fitted C1s X-ray photoelectron spectrum for the MW-synthesized ZrC samples prepared from zirconium metal and carbon in 20 minutes in a multi-mode MW reactor. ....	132
Figure 4-19 Fitted O1s X-ray photoelectron spectrum for the MW-synthesized ZrC samples prepared from zirconium metal and carbon in 20 minutes in a multi-mode MW reactor. ....	132
Figure 4-20 Zr3d X-ray photoelectron spectrum for the MW-synthesized ZrC samples prepared from zirconium metal and carbon in 20 minutes in a multi-mode MW reactor before and after Ar ion etching. ....	133
Figure 4-21 C1s X-ray photoelectron spectrum for the MW-synthesized ZrC samples prepared from zirconium metal and carbon in 20 minutes in a multi-mode MW reactor before and after Ar ion etching. ....	134
Figure 4-22 O1s X-ray photoelectron spectrum for the MW-synthesized ZrC samples prepared from zirconium metal and carbon in 20 minutes in a multi-mode MW reactor before and after Ar ion etching. ....	134
Figure 4-23 OCD plot from POLARIS bank 5 generated by Rietveld refinement against PND data using the cubic <i>Fm-3m</i> ZrC structure model taken from the ICSD database. Data were collected at room temperature for approx. 2 h. The red tick marks indicated reflections from graphite and the black tick marks indicate reflections from ZrC. ....	136
Figure 4-24 OCD plot from POLARIS bank 5 generated by Rietveld refinement against PND data using the cubic <i>Fm-3m</i> ZrC <sub>x</sub> O <sub>y</sub> structure model derived from the ZrC structure model taken from the ICSD database. Data collected at room temperature for approx. 2 h. The red tick marks indicated reflections from graphite and the black tick marks indicate reflections from ZrC. ....	137

Figure 4-25 <i>Ex-situ</i> PXRD patterns for the ZrO <sub>2</sub> + C pellets heated in a domestic MW oven at a power of 800 W from reagents (bottom) to products (top).	141
Figure 4-26 PXRD pattern taken <i>ex-situ</i> from hafnium metal plus graphite (1:1) heated in a DMO for 20 minutes at a power of 800 W under Ar. The reflection marked * can be attributed to the (002) reflection from graphite whereas the low intensity reflections marked • belong to the hafnium dioxide phase.	145
Figure 4-27 <i>Ex-situ</i> patterns for Hf + C pellets heated in an MMC reactor at a power of 800 W for 0 seconds ( <i>bottom</i> ) to 20 minutes ( <i>top</i> ).	147
Figure 5-1 Phase diagram of the Zr-N system. <sup>1</sup>	154
Figure 5-2 Crystal structure of ZrN. Zr atoms (red), N atoms (blue).	154
Figure 5-3 PXRD pattern taken <i>ex-situ</i> from zirconium metal under nitrogen gas heated in a DMO for 20 minutes at a power of 800 W. Reflections marked with the <i>hkl</i> indices belong to the zirconium nitride phase, the ones marked with “ * ” to zirconium metal, “ ° ” to <i>m</i> -ZrO <sub>2</sub> and “ • ” to an unknown cubic phase. The unmarked extra reflections could not be characterized.	157
Figure 5-4 PXRD pattern taken <i>ex-situ</i> from zirconium metal under ammonia gas heated in an MMC reactor for 20 minutes at a power of 800 W. Reflections marked with the <i>hkl</i> indices belong to the zirconium nitride phase, the ones marked with “ * ” to zirconium oxide and the extra reflections marked with “ • ” can be attributed to an uncharacterized cubic phase.	159
Figure 5-5 Observed ( <i>plusses</i> ), calculated ( <i>solid green line</i> ), and difference ( <i>solid purple line</i> ) profile plot for the Rietveld refinement against PXRD data for the zirconium nitride ZrN synthesized under nitrogen gas. Tick marks denote ZrN ( <i>bottom</i> ), Zr, <i>m</i> -ZrO <sub>2</sub> and <i>c</i> -ZrO <sub>2</sub> ( <i>top</i> ) diffraction peaks.	160
Figure 5-6 Observed ( <i>plusses</i> ), calculated ( <i>solid green line</i> ), and difference ( <i>solid purple line</i> ) profile plot for the Rietveld refinement against PXRD data for the zirconium nitride ZrN synthesized under ammonia gas. Tick marks denote ZrN ( <i>bottom</i> ), <i>m</i> -ZrO <sub>2</sub> and <i>c</i> -ZrO <sub>2</sub> ( <i>top</i> ) diffraction peaks.	162
Figure 5-7 <i>Ex-situ</i> PXRD patterns for Zr powder heated under nitrogen gas in a multi-mode cavity MW reactor at a power of 800 W from reagents ( <i>bottom</i> ) to reaction completion ( <i>top</i> ).	164
Figure 5-8 <i>Ex-situ</i> patterns for Zr powder heated under ammonia gas in a multimode cavity MW reactor at a power of 800 W from reagents ( <i>bottom</i> ) to reaction completion ( <i>top</i> ).	165
Figure 5-9 SEM micrographs for the ZrN synthesized from zirconium metal under nitrogen gas in 20 minutes in a MMC microwave reactor at a power of 800 W.	166

Figure 5-10 SEM micrographs for the ZrN synthesized from zirconium metal under ammonia gas in 20 minutes in a MMC microwave reactor at a power of 800 W. ....	167
Figure 5-11 EDX spectrum for the ZrN sample synthesized from zirconium metal under nitrogen gas in 20 minutes in a MMC microwave reactor, showing that zirconium, nitrogen, oxygen and hafnium were present. ....	167
Figure 5-12 EDX spectrum for the ZrN samples synthesized from zirconium metal under nitrogen gas in 20 minutes in a MMC microwave reactor, showing that zirconium, nitrogen, oxygen and carbon were present. ....	168
Figure 5-13 Experimental Raman spectrum for the MW-synthesized ZrN from zirconium metal under nitrogen and gas in 20 minutes in a MMC microwave reactor at a power of 800 W. ....	168
Figure 7-1 PXRD pattern taken ex-situ from vanadium metal plus graphite (8:7) heated in a SMC reactor for 2 minutes at a power of 1 kW. All reflections can be attributed to $V_8C_7$ except the one marked with *, which belongs to the (002) reflection from graphite.	177
Figure 7-2 Magnified image of the superstructure lines found in the PXRD pattern taken ex-situ from vanadium metal plus graphite (8:7) heated in a MMC reactor for 6 minutes at a power of 800 W. ....	178
Figure 7-3 Magnified image of the $V_8C_7$ PXRD pattern after a 2-minute reaction illustrating the unsymmetrical nature of the reflections at $75.7^\circ$ and $79.6^\circ$ $2\theta$ angles. ....	180
Figure 7-4 PXRD pattern taken ex-situ from vanadium metal plus graphite (8:7) heated in a MMC reactor for 0 seconds at a power of 800 W. ....	181
Figure 7-5 PXRD pattern taken ex-situ from vanadium metal plus graphite (8:7) heated in a MMC reactor for 30 seconds at a power of 800 W. ....	182
Figure 7-6 PXRD pattern taken ex-situ from vanadium metal plus graphite (8:7) heated in a MMC reactor for 2 min at a power of 800 W. ....	183
Figure 7-7 Observed ( <i>plusses</i> ), calculated ( <i>solid green line</i> ), and difference ( <i>solid purple line</i> ) profile plot for the Rietveld refinement against PXRD data for the vanadium carbide superstructure $V_8C_7$ , synthesized from vanadium metal and carbon in 6 minutes in a MMC reactor at power of 800 W. Tick marks denote $V_8C_7$ diffraction peaks. The (002) graphite reflection at $2\theta = 26.5^\circ$ was excluded from the refinement. ....	184
Figure 7-8 PXRD pattern taken ex-situ from vanadium(V) oxide plus graphite (4:27) heated for 6 minutes in a SMC microwave reactor for 2 minutes at a power of 1 kW. All reflections can be attributed to $V_8C_7$ except the one marked with *, which belongs to the (002) reflection from graphite. ....	187

Figure 7-9 PXRD pattern taken ex-situ from vanadium(V) oxide plus graphite (4:27) heated for 0 seconds in an MMC microwave reactor at a power of 800 W.....	188
Figure 7-10 PXRD pattern taken ex-situ from vanadium(V) oxide plus graphite (4:27) heated for 30 seconds in an MMC microwave reactor at a power of 800 W.....	189
Figure 7-11 PXRD pattern taken ex-situ from vanadium(V) oxide plus graphite (4:27) heated for 1 minute in an MMC microwave reactor at a power of 800 W. ....	190
Figure 7-12 PXRD pattern taken ex-situ from vanadium(V) oxide plus graphite (4:27) heated for 2 minutes in an MMC microwave reactor at a power of 800 W.....	191
Figure 7-13 PXRD pattern taken <i>ex-situ</i> from zirconium metal plus graphite (1:1) heated in a SMC reactor for 6 minutes at a power of 1 kW under Ar. All reflections can be attributed to ZrC except the one marked with *, which belongs to the (002) reflection from graphite.....	192
Figure 7-14 Magnified image of the ZrC PXRD pattern after a 10-minute reaction illustrating the unsymmetrical nature of the reflections at $66^\circ$ and $69.5^\circ$ $2\theta$ angles.....	193
Figure 7-15 PXRD pattern taken ex-situ from zirconium metal plus graphite (1:1) heated in a MMC reactor for 0 seconds at a power of 800 W. Impurities were present in the Zr starting material bought from Alfa Aesar. ....	194
Figure 7-16 PXRD pattern taken ex-situ from zirconium metal plus graphite (1:1) heated in a MMC reactor for 5 minutes at a power of 800 W.....	195
Figure 7-17 PXRD pattern taken ex-situ from zirconium metal plus graphite (1:1) heated in a MMC reactor for 10 minutes at a power of 800 W.....	196
Figure 7-18 Observed (plusses), calculated (solid green line), and difference (solid purple line) profile plot for the Rietveld refinement against PXRD data for the MW-synthesized ZrC from zirconium metal and graphite. Tick marks denote ZrC diffraction peaks .....	197

## List of Tables

Table 1-1 Main differences between microwave and conventional heating.....	13
Table 1-2 Most common synthetic procedure employed for the production of transition metal carbides and nitrides. <sup>50</sup> .....	14
Table 1-3 Stoichiometry of the most stable Group 4-10 transition metal carbides and nitrides. <sup>97,98</sup> .....	20
Table 1-4 Physical and mechanical properties of Group 4-6 transition metals and their carbide and nitride compounds. <sup>112</sup> Highlighted are the materials investigated in this research project. ....	24
Table 2-1 Manufacturer, purity and nominal particle size of the starting materials used. ..	40
Table 2-2 List of all the attempted reactions for the synthesis of transition metal carbides and nitrides.....	40
Table 2-3 The seven crystal systems and corresponding Bravais lattices. <sup>20</sup> .....	46
Table 3-1 Crystallographic data from Rietveld refinement against PXRD data for V <sub>8</sub> C <sub>7</sub> prepared from vanadium metal and carbon in 6 minutes in an MMC reactor at a power of 800 W. ....	73
Table 3-2 Atomic parameters from Rietveld Refinement against PXRD data for V <sub>8</sub> C <sub>7</sub> prepared from vanadium metal and carbon in 6 minutes in an MMC reactor at a power of 800 W. ....	74
Table 3-3 Comparison of the Raman shifts of the MW-synthesized V <sub>8</sub> C <sub>7</sub> and commercial V <sub>2</sub> O <sub>5</sub> and their assigned symmetry modes.....	82
Table 3-4 Crystallographic data from Rietveld refinement against PND data for V <sub>8</sub> C <sub>7</sub> synthesized from vanadium metal and graphite heated in a MMC for 6 minutes at a power of 800 W. ....	90
Table 3-5 Atomic parameters from Rietveld refinement against PND data for V <sub>8</sub> C <sub>7</sub> synthesized from vanadium metal and graphite heated in a MMC for 6 minutes at a power of 800 W. ....	91
Table 3-6 Crystallographic data from Rietveld refinement against PXRD data for V <sub>8</sub> C <sub>7</sub> prepared from vanadium(V) oxide and carbon in 6 minutes in an MMC reactor at a power of 800 W. ....	96
Table 3-7 Atomic parameters from Rietveld Refinement against PXRD data for V <sub>8</sub> C <sub>7</sub> prepared from vanadium(V) oxide and carbon in 6 minutes in an MMC reactor at a power of 800 W. ....	97

Table 3-8 Raman shifts of the MW-synthesized $V_8C_7$ from vanadium(V) oxide and carbon in an MMC at a power of 800 W and commercial $V_2O_5$ and their assigned symmetry modes. ....	103
Table 4-1 Chemical composition of zircon sand. <sup>15</sup> .....	115
Table 4-2 Crystallographic data from Rietveld refinement against PXRD data for ZrC. .	120
Table 4-3 Atomic parameters from Rietveld Refinement against PXRD data for ZrC. ....	120
Table 4-4 Raman shifts of the MW-synthesized ZrC compared to those of <i>m</i> -ZrO <sub>2</sub> and <i>t</i> -ZrO <sub>2</sub> with their respective assignments. “ <i>m</i> ” stands for monoclinic, “ <i>t</i> ” for tetragonal. ....	129
Table 4-5 Crystallographic data for Rietveld refinement against PND data for ZrC <sub>0.98</sub> using the cubic <i>Fm-3m</i> ZrC structure model taken from the ICSD database. <sup>16</sup> .....	136
Table 4-6 Atomic parameters from Rietveld refinement against PND data for ZrC <sub>0.98</sub> using the cubic using the cubic <i>Fm-3m</i> ZrC structure model taken from the ICSD database. <sup>16</sup> .....	137
Table 4-7 Crystallographic data for Rietveld refinement against PND data for ZrC <sub>0.97</sub> O <sub>0.03</sub> using the cubic <i>Fm-3m</i> ZrC <sub>x</sub> O <sub>y</sub> structure model derived from the ZrC structure model taken from the ICSD database. <sup>16</sup> .....	138
Table 4-8 Atomic parameters for Rietveld refinement against PND data for ZrC <sub>0.97</sub> O <sub>0.03</sub> using the cubic <i>Fm-3m</i> ZrC <sub>x</sub> O <sub>y</sub> structure model derived from the ZrC structure model taken from the ICSD database. ....	138
Table 4-9 Stoichiometry and respective lattice parameter for the different zirconium oxycarbide specimens synthesized by Gendre <i>et al.</i> <sup>35</sup> .....	139
Table 4-10 Bond energies for SiO <sub>2</sub> and ZrO <sub>2</sub> . <sup>36</sup> .....	142
Table 5-1 Crystallographic data for the uncharacterized cubic phase (obtained as a by-product during the microwave reaction) and <i>c</i> -ZrO <sub>2</sub> taken from literature. *Range of values for the lattice parameter of the <i>c</i> -ZrO <sub>2</sub> phase reported in literature.....	158
Table 5-2 Crystallographic data from Rietveld refinement against PXRD data for ZrN synthesized from zirconium metal under nitrogen gas. ....	161
Table 5-3 Atomic parameters from Rietveld Refinement against PXRD data for ZrN synthesized under nitrogen gas. ....	161
Table 5-4 Crystallographic data from Rietveld refinement against PXRD data for ZrN synthesized from zirconium metal under ammonia gas.....	162
Table 5-5 Atomic parameters from Rietveld Refinement against PXRD data for ZrN synthesized under ammonia gas. The fractional coordinates were not refined, as they are fixed by the structure.....	163

Table 5-6 Raman shifts of the MW-synthesized ZrN compared to those from <i>m</i> -ZrO <sub>2</sub> and <i>t</i> -ZrO <sub>2</sub> and their assignments. The bands in the experimental spectrum closely resemble a combination of these seen for the 2 phases of ZrO <sub>2</sub> .....	169
Table 7-1 Selected atomic lengths (Å) and angles (°) from Rietveld refinement against PXRD data for V <sub>8</sub> C <sub>7</sub> . .....	179
Table 7-2 Crystallographic data from Rietveld refinement against PXRD data for V <sub>8</sub> C <sub>7</sub> prepared from vanadium metal and carbon in 6 minutes in an MMC reactor at a power of 800 W. ....	184
Table 7-3 Atomic parameters from Rietveld refinement against PND data for V <sub>8</sub> C <sub>7</sub> synthesized from vanadium metal and graphite heated in a MMC for 6 minutes at a power of 800 W. ....	185
Table 7-4 Selected atomic lengths (Å) and angles (°) from Rietveld refinement against PND data for V <sub>8</sub> C <sub>7</sub> synthesized from vanadium metal and graphite heated in a MMC for 6 minutes at a power of 800 W. ....	186
Table 7-5 Crystallographic data from Rietveld refinement against PXRD data for ZrC prepared from zirconium metal and carbon in 20 minutes in an MMC reactor at a power of 800 W. ....	197
Table 7-6 Atomic parameters from Rietveld refinement against PND data for ZrC synthesized from zirconium metal and graphite heated in a MMC for 20 minutes at a power of 800 W. ....	198

## Definitions

<b>Abbreviations</b>	<b>Definitions</b>
CELREF	Unit cell refinement software package
EDX	Energy Dispersive X-ray Spectroscopy
GSAS-EXPGUI	General Structural Analysis System – EXP Graphical User Interface
ICSD	Inorganic Crystal Structure Database
ISIS	ISIS Neutron and Muon Source
MMC	Multi-mode Cavity
MW	Microwave
OCD	Observed, calculated and difference
PND	Powder Neutron Diffraction
PXRD	Powder X-ray Diffraction
RF	Radio Frequency
SEM	Scanning Electron Microscopy
SMC	Single-mode Cavity
TE	Transverse Electric
TMC	Transition Metal Carbide
TMN	Transition Metal Nitride
TOF	Time of Flight
XPS	X-ray Photoelectron Spectroscopy

<b>Physical Constants</b>		
<b>Symbol</b>	<b>Definition</b>	<b>Value</b>
$h$	Planck's constant	$6.63 \times 10^{-34} \text{ J s}$
$m_n$	Mass of a neutron	$1.67 \times 10^{-27} \text{ kg}$
$\epsilon_0$	Permittivity of free space	$8.85418782 \times 10^{-12} \text{ kg}^{-1} \text{ s}^4 \text{ A}^2$
$\alpha$	Stefan-Boltzmann constant	$5.670373 \times 10^{-8} \text{ W m}^{-2} \text{ K}^{-4}$
$c$	Speed of light	$299\,792\,458 \text{ m s}^{-1}$

# 1 Introduction

## 1.1 Microwave History and Theory

A microwave (MW) is a form of non-ionizing electromagnetic radiation and, as such, consists of synchronized oscillations of electric and magnetic fields, perpendicular to each other, that self-propagate at the speed of light through vacuum [Figure 1-1]. Microwaves can then be characterized by the frequency of oscillation ( $f$  – number of oscillations per unit time) and its wavelength ( $\lambda$  – distance between crests).

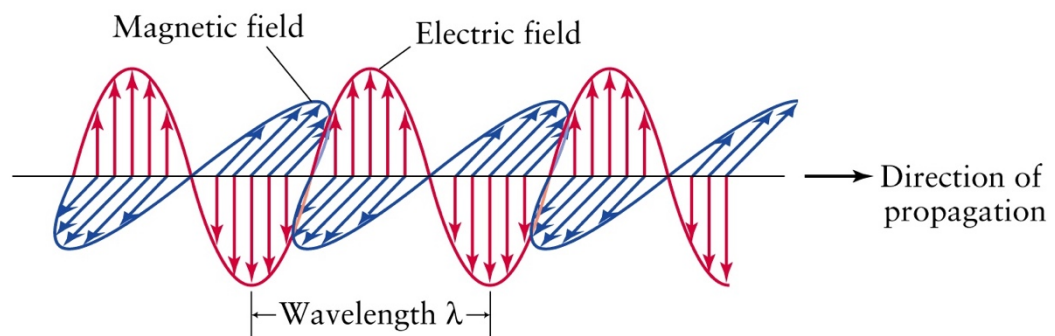


**Figure 1-1** Schematic representation of an electromagnetic wave. The electric field, E, is in a vertical plane and the magnetic field, H, in a horizontal plane.<sup>1</sup>

Microwaves have a frequency range that goes from 0.3 – 300 GHz and wavelengths from 1 m – 1 mm (photon energy 1.24  $\mu\text{eV}$  – 1.24 meV, respectively)<sup>2</sup> which situate them between infrared and radio waves in the electromagnetic spectrum, shown in Figure 1-2.

Several specific microwave frequencies have been allocated for industrial, medical and scientific applications,<sup>3,4</sup> with the intent to minimize interference with communication devices, but the most widespread frequency used for both cooking and chemistry is 2.45 GHz. At this frequency, the wavelength is  $\sim 12.2$  cm and the energy of a single microwave photon  $\sim 1$  meV, which is very low with respect to the typical energy required to ionize water molecules (12-13 eV)<sup>2</sup> and contribute only to molecular rotation and vibration. For industrial heating applications, a microwave frequency of 900 MHz is also used. The reason lies in the fact that at this frequency MWs have a greater wavelength ( $\sim 33.3$  cm) with respect to those at 2.45GHz which is more suitable for the heating of bigger loads.

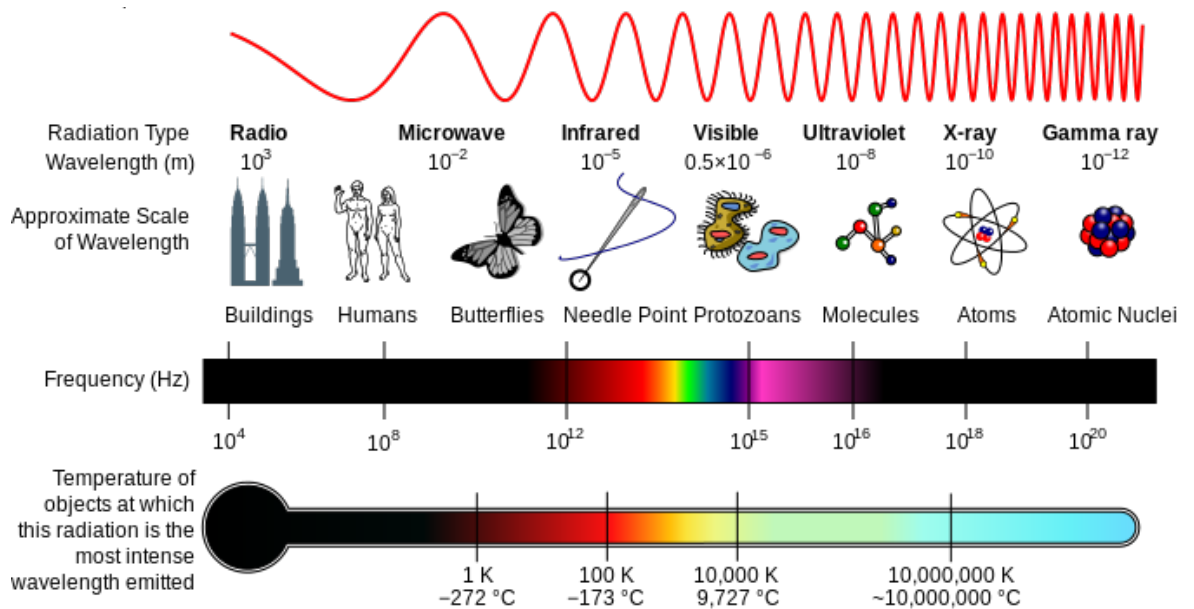


**Figure 1-2** The electromagnetic spectrum, showing the frequency and wavelength associated with each type of electromagnetic wave.<sup>5</sup>

The topic of microwave technology is based on historical events dating back to the 19<sup>th</sup> century. The existence of radio waves was predicted by James Clerk Maxwell in 1864 from his equations and it was not until many years later that their existence was conclusively demonstrated for the first time by Heinrich Hertz in 1888 by building a primitive spark-gap radio transmitter.<sup>6</sup> In 1920, the American physicist and electrical engineer Albert Hull invented the cavity magnetron,<sup>7,8</sup> a high-powered vacuum tube that could generate microwaves. Although the first prototypes were not efficient enough to gain commercial success, the first real world applications of microwaves in communications arrived with the development of radar technology.<sup>9</sup> During World War II, in 1940, the design of the magnetron was drastically improved by John Randall and Henry Boot, who built on Hull's concept to develop what is known as the modern cavity magnetron<sup>10</sup> [Figure 1-3].

This revolutionary device is a diode-type electron tube, consisting of a solid metal rod which acts as a cathode, a ring-shaped iron anode surrounding the cathode, two magnets and an antenna. These components are all incorporated within a container that has been evacuated to allow free movement of electrons. Upon application of a very high voltage (~4000 V) to the diode, electrons are emitted from the hot cathode (also called '*filament*' or '*heater*'). In the absence of a magnetic field, the emitted electrons would be expected to follow a straight line trajectory towards the anode. However, as two magnets are mounted above and below the tube structure, the generated magnetic field (parallel to the cathode axis) forces the electrons to travel in a circular motion towards the anode. The latter contains a series of cavities arranged in circles that resonate at a certain frequency when the electron

cloud blows across each cavity opening, thereby emitting electromagnetic radiation. The as-generated microwaves are then collected by the antenna and channeled into the waveguide, a hollow metal pipe that confines the wave so as to propagate in one direction with minimal energy loss.

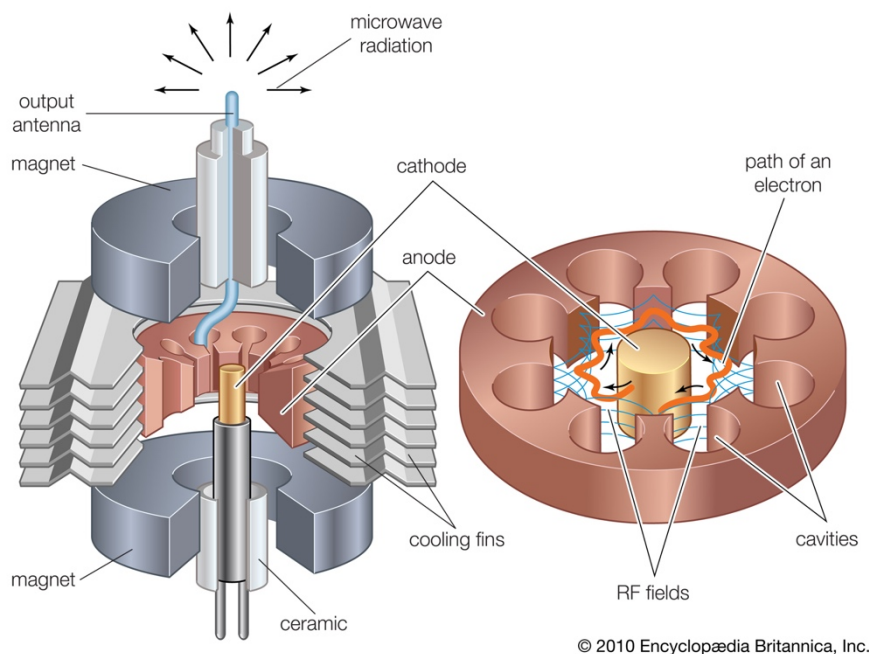


**Figure 1-3** The resonant-cavity magnetron and its components.<sup>11</sup>

1946 was the year that saw the marketing of the first microwave oven, named “*Radarange*” and invented by Percy Lebaron Spencer of the Raytheon Company. He realized that microwave energy could potentially cook food when a candy bar melted in his pocket while experimenting with radar.<sup>12</sup> However, *Radarange* was too large and expensive (US\$5,000 – the equivalent of \$54,000 in 2017) for general home applications and consumed 3 kW of power, about three times as much today’s microwave ovens. Since then, the microwave oven market kept rising with the development of more affordable, energy-efficient and smaller microwave ovens. Amana Corporation, a division of Raytheon, released the first counter-top microwave oven in 1967 which rapidly became popular for home use around the world.

The first use of microwave heating in chemical research was proposed in 1971 by Liu *et al.* who studied the decomposition of oxygen-containing organic compounds such as alcohols, ketones and ethers.<sup>13</sup> Since then, chemical laboratories started to be equipped with inexpensive domestic microwave ovens (DMOs) and the number of publications in the area grew exponentially. The first successful chemical reactions using DMOs were reported in

1986 by Gedye *et al.*<sup>14</sup> The authors investigated four different types of organic reactions and prepared seven different organic compounds, observing a substantial boost (up to 1000-fold) in the reaction rates with respect to the equivalent reactions using conventional heating. These initial papers set the foundations for MW-induced chemical processing and led to the development of novel synthetic methods especially in organic and solution-phase chemistry.<sup>15–18</sup>

On the other hand, the advancement of microwave methods in solid-state chemistry has faced more challenges than solution-phase chemistry and has progressed at a much slower pace. This has mainly been due to the unavailability of commercial laboratory microwave reactors for solid-state chemistry as well as the limited understanding of the interaction between MWs and solid materials.<sup>19</sup> However, it was not until the early 1990s that scientists showed a growing interest in the microwave processing of ceramics and the number of published papers in the area drastically increased.<sup>20–27</sup> To date, MWs have been employed extensively for the synthesis and processing of a variety of materials such as oxides, carbides, nitrides, etc. (see Section 1.6). Nevertheless, the use of MWs in materials processing still faces several challenges, including the high cost of laboratory MW apparatus and the lack of heating for poor MW-absorbing materials.<sup>28</sup>

## 1.2 Microwave Heating Mechanisms

As will be described further in Section 1.4.1, MWs interact directly with molecules, causing a fast rise in temperature within seconds/minutes. The two main mechanisms through which microwaves couple with matter are dipolar polarization and conduction – which are described in Section 1.2.1 and 1.2.2, respectively. The theory behind the interaction of MWs with matter is discussed in more details in Section 1.3.

Generally, only the electric component of the microwave field is responsible of the heating effects in materials. The electric field can interact with temporary/permanent electric dipoles and/or charged particles, inducing one (or both) of the MW heating mechanisms, described below. The magnetic component of the MW field may also interact with materials, in case the substance contains magnetic dipoles, but this only occurs rarely.

## 1.2.1 Dipolar Polarization<sup>12,19</sup>

Dipolar polarization ( $P_d$ ) applies to substances with temporary or permanent electric dipoles. In electromagnetism, a dipole is a separation of positive and negative charges within a system and can be characterized by its dipole moment – a measure of the separation of the positive and negative charges. A substance having molecules with a non-uniform distribution of positive and negative charges possesses such dipole moments. Such molecules are said to be polar. An example of a polar substance is water ( $H_2O$ ) [Figure 1-4] in which the electron cloud is displaced towards the more electronegative oxygen atom.

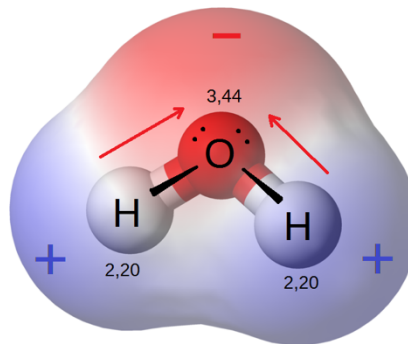


**Figure 1-4** Schematic illustration of the dipole moment in a water molecule. Its negative pole (*red*) is at the oxygen atom (the more electronegative one) whereas its positive pole (*blue*) is at the hydrogen atoms (the less electronegative ones).<sup>29</sup>

When a polar molecule is subjected to a microwave field, it aligns itself with the rapidly changing electric field of the MWs and collides with surrounding molecules. This results in the conversion of MW energy into thermal energy and heat is then dissipated by molecular frictions and collisions. Generally, this mechanism is the dominant effect in liquid-phase substances, such as water.

The larger the dipole moment, the greater the tendency of the solvent to respond to an applied field by reorientation of the electric dipoles. A polar molecule behaves as a dielectric which is defined as an electrical insulator that can be polarized by an applied electric field. When a dielectric is subjected to an internal electric field,  $E$ , the polarization is proportional to this field and is given by equation (1-1):

$$P_d = \epsilon_0(\epsilon_r - 1)E = \epsilon_0\chi_e E \quad (1-1)$$

where  $\epsilon_0$  is the permittivity of free space,  $\epsilon_r$  is the relative permittivity and  $\chi_e$  is the electric susceptibility of the material.<sup>30</sup>

## 1.2.2 Conduction<sup>12,19</sup>

The conduction mechanism occurs in electrically conducting materials and, generally, in all the substances that contain free ions or charged particles such as electrons. When such a material is irradiated with microwaves, the electric component of the MW field induces indeed electronic/ionic motion throughout the material. This results in an increased collision rate between the moving particles, converting their kinetic energy into thermal energy. Generally, this mechanism is the dominant effect in solid materials (such as graphite).

Graphite is one of the allotropes of carbon and has a layered and planar structure, shown in Figure 1-5.

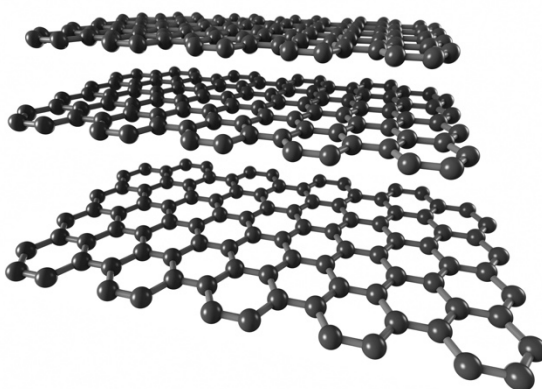


**Figure 1-5** Side view of the layered and planar structure of graphite.<sup>31</sup>

$\pi$ -electrons are free to move in between the layers, making the material electrically conductive. Graphite is known to be a strong microwave absorber as the  $\pi$ -electrons will start following the electric field component when irradiated with MWs, reaching very high temperatures ( $> 1000^{\circ}\text{C}$ ) within minute timescales.<sup>32</sup> In the experiments described in this thesis, graphite powder was used as both a starting material and a susceptor (a substance that couples very well with microwaves – see Section 1.3).

## 1.3 Interaction of MWs with Matter

Microwaves obey the law of optics and, as such, can be absorbed, reflected and/or transmitted, depending on the type of materials they interact with. Materials can therefore be classified as transparent (little or no interaction with MW fields, e.g. quartz), reflective (most of MW energy is reflected, e.g. metals) or absorbing (most of MW energy is absorbed, e.g. graphite),<sup>21,22</sup> as shown in Figure 1-6.

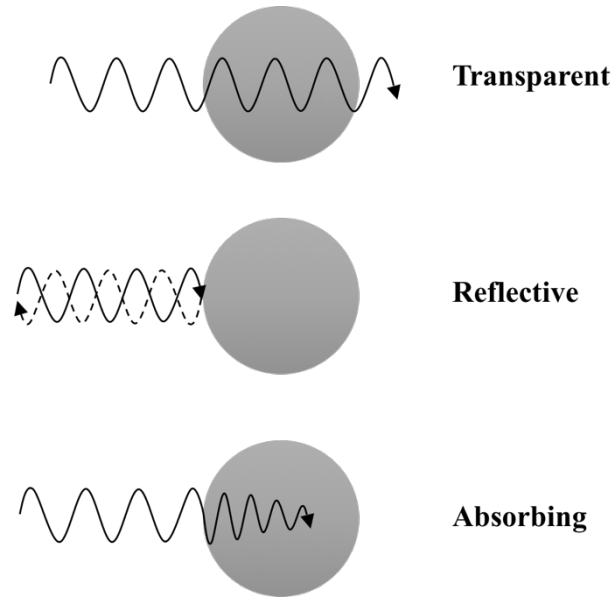


**Figure 1-6** The interaction of transparent (*top*), reflective (*middle*) and absorbing (*bottom*) materials with microwave energy.

The absorption of microwave energy by a material is called dielectric heating and depends upon the complex permittivity,  $\varepsilon^*$ , of the material given by:<sup>23,30</sup>

$$\varepsilon^* = \varepsilon' - i\varepsilon'' = \varepsilon_0(\varepsilon_r - i\varepsilon_{eff}) \quad (1-2)$$

where  $\varepsilon'$  (the real component) is the dielectric constant,  $\varepsilon''$  (the imaginary component) is dielectric loss factor,  $\varepsilon_0$  is the permittivity of free space,  $\varepsilon_r$  is the relative dielectric constant and  $\varepsilon_{eff}$  is the relative dielectric loss factor.

The dielectric constant is a measure of the ability of a substance to store electrical energy in an electric field, whereas the dielectric loss factor is the loss of energy that goes into heating a dielectric material in a changing electric field. In other words, the dielectric loss factor is the amount of input microwave energy that is actually dissipated as heat and relates directly to the electrical conductivity of a material,  $\sigma$ :<sup>33</sup>

$$\varepsilon'' = \frac{\sigma}{\varepsilon_0\omega} \quad (1-3)$$

where  $\varepsilon_0$  is the permittivity of free space and  $\omega$  is the frequency of the microwave radiation.

Epsilon prime,  $\epsilon'$ , and epsilon double-prime,  $\epsilon''$ , are important and useful terms for microwave engineers as their ratio gives the so-called loss tangent (also referred to as the dissipation factor),  $\tan\delta$ , which represents the ability of a substance to convert microwave energy into thermal energy at a given frequency and temperature:<sup>4,19</sup>

$$\tan \delta = \frac{\epsilon''}{\epsilon'} \quad (1-4)$$

The greater the loss tangent, the more efficiently microwave power is converted into thermal energy. Microwave transparent (low-loss) materials usually have a low dissipation factor ( $\tan\delta < 0.1$ ), whereas microwave absorbers (high-loss) materials have a high loss tangent ( $\tan\delta > 0.1$ ).

The dielectric properties of a material are highly dependent on the temperature, and it has been shown how the loss factor increases as the temperature of the material rises at a given frequency.<sup>34,35</sup> In other words, microwave transparent solids – that usually do not couple with microwaves at room temperature – can become capable of absorbing MW energy more efficiently when the temperature is increased. To achieve such an effect, the use of a high-loss material called susceptor is usually needed. A susceptor is a substance used for its ability to absorb microwave energy and convert it to heat (such as graphite, SiC, etc.). MWs are absorbed by the susceptor and heat is transferred to the low-loss material via a conventional heating process which, in turn, will start absorbing MW energy as the temperature increases. Potentially, almost all materials can undergo “*hybrid*” heating with the above method.

The rate of change of temperature of a given material during a dielectric heating process is given by the following:<sup>36</sup>

$$\frac{dT}{dt} = \frac{K\epsilon''fE^2}{\rho C_p} \quad (1-5)$$

where  $dT/dt$  is the rate of change of temperature of the material,  $K$  is a constant,  $E$  is the field strength,  $\rho$  is the density of the material and  $C_p$  is the specific heat capacity.

Similar to Equation (1-5), Equation (1-6) describes the energy loss due to radiation of infrared waves from the surface of the material.<sup>36</sup>

$$\frac{dT}{dt} = -\frac{e\alpha A_s}{\rho C_p V_s} T^4 \quad (1-6)$$

where  $e$  is the sample emissivity ratio,  $\alpha$  is the Stefan-Boltzmann constant,  $A_s$  and  $V_s$  are the surface area and the volume of the sample, respectively.

The microwave power effectively absorbed by a sample per unit volume,  $P$  (in  $\text{W}/\text{m}^3$ ), can be determined from Equations (1-7), (1-8) and (1-9) by making use of the dielectric properties of materials:<sup>22</sup>

$$P = \sigma |E|^2 \quad (1-7)$$

$$= 2\pi f \varepsilon_0 \varepsilon'' |E|^2 \quad (1-8)$$

$$= 2\pi f \varepsilon_0 \varepsilon' \tan \delta |E|^2 \quad (1-9)$$

where  $\sigma$  is the total effective conductivity (in  $\text{S}/\text{m}$ ),  $E$  is the magnitude of the internal electric field (in  $\text{V}/\text{m}$ ) and  $f$  is the frequency of the microwave radiation (in  $\text{Hz}$ ). The equations described above assume that the power is uniform throughout the volume and that thermal equilibrium has been reached, which is not always the case. Also, the electric field inside the load depends on the dielectric properties of the material itself and its geometry and, hence, the determination of the distribution of the electric field is a complex task.<sup>37,38</sup> However, these equations represent an acceptable approximation for calculating the power absorbed by the sample.

The microwave power absorbed by the sample is then converted into thermal energy, causing an increase in temperature,  $\Delta T$ , from  $T_i$  to  $T_f$ , in a time interval,  $\Delta t$ . Equations (1-11) and (1-12) are particularly useful to calculate the final temperature reached by the sample,  $T_f$ , and the time interval in which the latter is approached,  $\Delta t$ .<sup>39</sup>

$$P = \frac{KC_p m \Delta T}{\Delta t} \quad (1-10)$$

$$T_f = T_i + \frac{P \Delta t}{KC_p m} \quad (1-11)$$

$$\Delta t = \frac{KC_p m \Delta T}{P} \quad (1-12)$$

where  $K$  is the conversion factor for thermochemical calories to  $\text{W}$  ( $= 4.184$ ) and  $m$  is the mass of the sample (in  $\text{g}$ ).

When microwaves interact with an absorbing material, the amplitude of the MW field and the power density will decrease exponentially from the surface to the core region [Figure 1-6]. The penetration depth for a substance,  $D_p$ , is defined as the depth at which the field

amplitudes has decreased to  $1/e$  ( $= 0.36788$ ), 37% of its initial value at the surface, and is given by the following equation:<sup>37</sup>

$$D_p \cong \frac{\lambda_0 \sqrt{\epsilon'}}{2\pi\epsilon''} \quad \text{only when } \epsilon'' \ll \epsilon' \quad (1-13)$$

where  $\lambda_0$  is the wavelength of the microwave radiation (in m). The penetration depth is zero in perfectly reflective materials and infinite in perfectly transparent materials.

In conducting materials – which are microwave reflective (e.g. metals) – the skin depth,  $\delta$ , is usually used to describe the propagation of microwaves within the material and is defined as the depth at which the magnitude of the electric field falls to  $1/e$  of the value at the surface.<sup>23</sup>

$$\delta = \frac{1}{\sqrt{\pi f \mu \sigma}} \quad (1-14)$$

where  $f$  is the frequency of the microwave radiation,  $\mu$  is the magnetic permittivity of the sample and  $\sigma$  is the electrical conductivity. Metals usually show a very low skin depth which means that microwaves do not penetrate the core region of the material. As a consequence, most of the microwave radiation will be indeed reflected in bulky metals but will be absorbed in fine metal powders, causing very rapid heating of the latter.

## 1.4 Microwave vs. Conventional Heating

As a consequence of the MW heating mechanisms and the dielectric properties of materials, microwave heating shows some features that make this process considerably different from conventional heating. These characteristics are: direct heating, volumetric heating, instantaneous heating and selective heating. The sections below will describe in detail the most common properties of microwave heating and the advantages as well as disadvantages that this process has over conventional heating.

### 1.4.1 Properties of MW Heating

MWs reach the substance being heated at the speed of light and subsequently couple directly with it. Heat is then generated within the substance itself through “*direct heating*” with minimal loss of energy. On the other hand, conventional heating behaves in a completely different way. Heat is transferred to the surface of the substance through conduction, convection or radiation and then into the substance itself by thermal conduction. Figure 1-7 provides a schematic illustration on how heat is transferred in both heating processes.

The direct heating properties seen in microwave heating are often associated with a very fast conversion of electromagnetic energy into thermal energy. Heat can therefore be generated almost instantaneously (“*instantaneous heating*”) from the onset of microwave irradiation and very rapid reaction times are often observed.<sup>40</sup> Also, different types of materials within the same sample will interact with MWs to a different extent (dependent on the interaction mechanisms discussed in the previous sections) and this allows specific substances to be heated selectively (“*selective heating*”).<sup>40–42</sup>

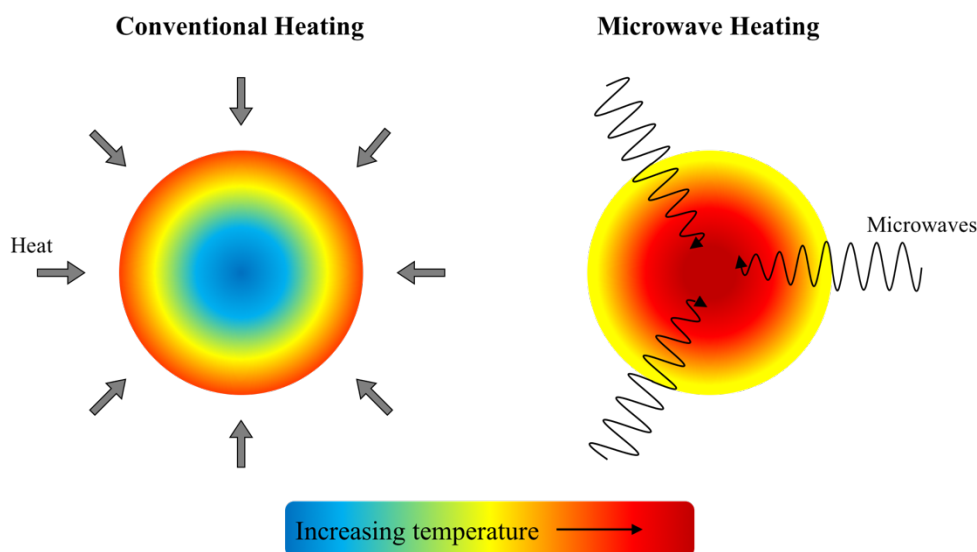


**Figure 1-7** Schematic showing the main differences between conventional (*left*) and microwave heating (*right*). In conventional heating, heat is driven into the substance through thermal conduction, resulting in the surface being warmer than the interior. In microwave heating, microwaves interact directly with the material being heated and volumetric heating occurs, giving an inverse temperature gradient.

### 1.4.2 Volumetric Heating<sup>19</sup>

As microwaves can penetrate materials and convert to thermal energy by coupling with them at a molecular level, heat can be generated “*volumetrically*” – throughout the volume

of the material [Figure 1-7]. Diffusion of heat does not occur from the surface to the core of the material (as in conventional heating), so all the infinitesimal elements of volume within a given sample are heated simultaneously. In this way, the rate of heating does not depend principally on the thermal conductivity and diffusivity of the sample but, instead, on the dielectric properties of the material itself and it is possible to achieve a more uniform and energy-efficient heating with respect to conventional heating.

Unfortunately, not all materials show the dielectric or conduction properties which are favourable for microwave heating. In this case, a combination of microwave and conventional heating, called *hybrid heating*, is often necessary.

### 1.4.3 Conventional Heating

As discussed above, conventional and microwave heating are two very different processes through which a substance can be heated. Conventional heating often results in a relatively slow and inefficient method of transferring energy into a system.<sup>43-45</sup> In a conventionally heated substance, the interior of the material is cooler than the surface [Figure 1-7]. The rate at which heat flows through a material depends upon its thermal conductivity,  $k$ , which is the ability of the material to conduct or transmit heat and is given by the following equation:

$$k = \frac{QL}{A\Delta T} \quad (1-15)$$

where  $k$  is the thermal conductivity (in W/m·K),  $Q$  is the amount of heat transfer through the material (in J/s or W),  $A$  is the cross-sectional area of the body (in m<sup>2</sup>),  $L$  is the length of the body (in m) and  $\Delta T$  is the difference in temperature (in K). The rate of transfer of heat of a material from the hot side to the cold side is then given by the thermal diffusivity,  $\alpha$  [equation (1-16)]:

$$\alpha = \frac{k}{\rho C_p} \quad (1-16)$$

where  $\alpha$  is the thermal diffusivity (m<sup>2</sup>/s),  $k$  is the thermal conductivity (in W/m·K),  $\rho$  is the density (in kg/m<sup>3</sup>) and  $C_p$  is the specific heat capacity (in J/kg·K).

In conclusion, the thermal conductivity and diffusivity of a material, together with the surface area and total volume of the sample, represents an important limitation in the diffusion of heat within the material itself. In light of Equations (1-15) and (1-16), it can be said that the greater the thermal conductivity and diffusivity, the faster heat will flow through a given material.

Table 1-1 illustrates the main differences, including advantages and disadvantages, of both microwave and conventional heating processes.

**Table 1-1** Main differences between microwave and conventional heating.

<b>Microwave Heating</b>	<b>Conventional Heating</b>
Energetic coupling	Conduction/convection
Volumetric	Superficial
Selective	Non selective
Dependent on the dielectric properties of the material	Dependant on the thermal conductivity of the material

## **1.5 Conventional Routes to Transition Metal Carbides and Nitrides**

Several conventional synthetic routes for the production of polycrystalline transition metal carbides and nitrides have been reported in the literature.<sup>46-48</sup> The manufacturing process of these compounds usually requires elevated temperatures for extended periods of time (typically 1500-2300 K for several hours). The main methods of producing carbides and nitrides can be divided into five types: synthesis from the elements, carbothermal reduction of the oxide powders, deposition from the gaseous phase, electrolysis of molten salts and chemical precipitation.

The first three types [Table 1-2] are the most industrially relevant due to their ability of mass producing large scale (up to tons) of products and will be discussed below. However, these methods mostly yield low surface area compounds.

The direct reaction of the elemental powders represents the most common synthetic process and involves the reaction of the metal powder with either carbon (for carbides) or either nitrogen gas (for nitrides) at temperatures below the melting point of the metal

(normally between 1500 and 2300 K).<sup>48</sup> Carbide formation is usually performed under either vacuum or a reducing gas atmosphere (such as hydrogen, H<sub>2</sub>). An example of direct reaction of the elemental powders is the synthesis of vanadium carbide performed by Storms *et al.* (1962).<sup>49</sup> The authors used vanadium metal and graphite as starting materials, mixed them in appropriate stoichiometric ratios and heated the compact at temperatures above 1000 °C.

**Table 1-2** Most common synthetic procedure employed for the production of transition metal carbides and nitrides.<sup>50</sup>

<b>1. Direct reaction of elemental powders</b>	
Carbides	$M + C \rightarrow MC$
Nitrides	$M + \frac{1}{2}N_2 \rightarrow MN$
<b>2. Carbothermal reduction of metal oxides</b>	
Carbides	$MO + 2C \rightarrow MC + CO$
Nitrides	$MO + C + \frac{1}{2}N_2 \rightarrow MN + CO$
<b>3. Deposition from the gaseous phase</b>	
Carbides	$MX + C_xH_y \rightarrow MC + HX + \dots$
Nitrides	$MX + N_2/H_2 \rightarrow MN + HX + \dots$

Due to the high cost of some metal powders, the carbothermal reduction of the corresponding metal oxide provides an economically advantageous alternative to the direct reaction of the elements. The carbide/nitride phase can be synthesized by mixing the metal oxide powder with carbon and heating at temperatures typically between 1500 and 2300 K in a hydrocarbon (for carbides) or nitrogen-containing gas atmosphere (for nitrides).<sup>50</sup> The term “carbothermal reduction” that the reaction proceeds by either reduction of the metal oxide to the corresponding metal, followed by diffusion of carbon into the latter or reduction of the oxide to one or more suboxides, followed by formation of an oxycarbide phase. However, the main downside of the aforementioned synthetic route is that it yields impurity phases (such as uncombined carbon) which almost always necessitate extra purification steps by arc melting or high vacuum annealing.<sup>47</sup> An example of this synthetic method is given by the carbothermal reduction of vanadium pentoxide by Meunier *et al.* (1997) which was performed by a two-stage temperature-programmed reaction process.<sup>51</sup> The temperature was rapidly raised to 430 K in the first stage and maintained for 2 h, whereas it was increased to 1250-1320 K in the second stage and maintained for 4 h.

Deposition from a gaseous phase works similarly to the methods discussed previously and involves the direct reaction of a metal compound (usually hydride or halide) with either a carbon- or nitrogen-containing gas, respectively.<sup>52</sup> Methane is usually used as a carbon-containing gas, whereas nitrogen as well as ammonia can be used as a nitrogen-containing gas. However, ammonia is favoured over nitrogen gas as it is a stronger nitriding agent.<sup>50</sup>

In recent years, other alternative synthetic methods have been developed aiming at increasing the purity and reducing the production cost of carbide and nitride materials. Examples of these methods are: mechanical alloying,<sup>46</sup> chemical vapour deposition (CVD),<sup>48</sup> RF plasma torch,<sup>52</sup> liquid-phase method,<sup>50</sup> self-propagating high-temperature synthesis (SHS),<sup>52</sup> and sol-gel processing.<sup>52</sup>

Mechanical alloying is a solid-state powder processing technique that can be used to produce nanostructured alloy phases by ball milling the precursor materials to a fine powder. This synthetic route is time consuming but relatively inexpensive. However, contamination issues are often encountered which could be avoided by employing grinding media made of the same material as the powder being ground. Tungsten carbide, WC, has been successfully synthesized by ball-milling tungsten metal and carbon at room temperature for up to 310 h.<sup>53,54</sup>

Chemical vapour deposition (CVD) is often used to produce solid materials precipitated from the gas phase. Although this method yields high quality materials with very few impurities, it cannot produce large scales of bulk carbides/nitrides. Examples of materials synthesized through this technique are SiC and TiN, produced using a volatile silane derivative, hydrogen and nitrogen for the former and TiCl<sub>4</sub> and ammonia for the latter.<sup>55,56</sup>

SiC has also been synthesized by RF plasma technique from silica and various types of carbon source, such as graphite carbon black.<sup>57</sup> Similarly to CVD, this technique produces nanoparticles by vapour phase reactions.

Self-propagating high-temperature synthesis (SHS) is a synthetic method known for the production of both inorganic and organic compounds. Initially, the reagents are mixed and mechanically activated through ball milling. An exothermic reaction is then initiated which will spread as a combustion wave throughout the reactants. Several carbides from group IV, V, VI have been synthesized by using this process.<sup>52</sup>

The sol-gel technique is used to produce a solid material from liquid reactive precursor materials. For carbide production, the procedure starts from a metal alkoxide solution (sol) which goes through a gelling process to form a system containing both a liquid and a solid phase (gel). The latter is then subjected to a drying process and a thermal treatment in order to obtain the final product. The synthesis of SiC through sol-gel technique has been

previously investigated from tetraethoxysilane (TEOS) and methyltriethoxysilane (MTES) in the presence of phenolic resin, ethylcellulose, polyacrylonitrile (PAN) and starch.<sup>58</sup>

The manufacturing processes described above are all reliable options for carbide and nitride production. However, they still present significant challenges that need to be overcome in order to make them commercially and laboratory applicable. Indeed, some of them are not suitable for mass production while some others require very high temperatures and long reaction times to obtain the target material.

## 1.6 Solid-state Microwave Synthesis

This section focuses on the microwave synthesis of solid materials that have been reported in the literature during late the 20<sup>th</sup>/early 21<sup>st</sup> century, with particular emphasis on the microwave processing of carbide and nitride materials.

As discussed previously, the advancement of microwave synthesis in solid-state chemistry has proceeded at a much slower pace with respect to solution-phase chemistry. This is also due to the lack of coupling between microwaves and MW-transparent materials. Indeed, such materials show little or no interaction, transmitting most of the MW energy and undergoing no reaction [Section 1.3].

If the synthesis of a given material does not include the use of MW-absorbing reactant, a susceptor is usually employed as a heat source. This substance exhibits a high coupling efficiency at MW frequencies and promotes the rapid heating of the reagents. The latter couple with MWs more efficiently at higher temperature and may lead to the production of the target material in shorter reaction times with respect to conventional heating methods.<sup>19</sup>

A number of broad families of materials have been synthesized in the recent years using MW irradiation and reported in the literature<sup>19</sup> with the most important ones being oxides, carbides and nitrides.

Oxides represent the most synthesized materials using MW energy because of the often less complex experimental conditions required and the vast variety of applications of many of the materials. These include materials such as  $\text{Na}_x\text{Co}_{1-x}\text{Mn}_y\text{O}_2$ ,<sup>59</sup>  $\text{YBa}_2\text{Cu}_3\text{O}_{7-x}$ <sup>60</sup> and  $\text{La}_{1-x}\text{Sr}_x\text{CoO}_3$ .<sup>61</sup>

Iwasaki et al. (2000) synthesized  $\text{Na}_x\text{Co}_{1-x}\text{Mn}_y\text{O}_2$  as a thermoelectric conversion material from  $\text{Na}_x\text{CoO}_2$  and  $\text{Na}_x\text{MnO}_2$  in a multi-mode 28 GHz microwave heating system.<sup>59</sup> The authors employed a microwave frequency of 28 GHz as it can achieve a uniform dielectric

field distribution and a more effective heating of inorganic materials.<sup>62</sup> The starting materials were mixed and pressed into pellets which were subsequently heated in air, controlling the microwave power to maintain the sample temperature at 900 °C for 2 h. The same solid solution was previously prepared by the authors using a conventional electric furnace for 6 h at a temperature of 900 °C which indicates that microwave processing reduced the reaction time by one third. Moreover, Iwasaki *et al.* observed an accelerated grain growth in a specific direction in the MW-synthesized samples which, according to the authors, might be due to the fact that  $\text{Na}_x\text{Co}_{1-x}\text{Mn}_y\text{O}_2$  couples with microwave energy selectively. Unfortunately, the reason why this occurred remain unclear.

$\text{YBa}_2\text{Cu}_3\text{O}_{7-x}$  was synthesized as a superconducting material using microwave irradiation by Agostino *et al.* (2004).<sup>60</sup> The material was obtained by mixing the oxide precursors ( $\text{Y}_2\text{O}_3$ , BaO and CuO), pelletizing the powdered mixture and heating the compact in a domestic microwave oven at a power of 600 W for 3.5 h. The reaction was performed under an oxygen flow. In this study, the authors showed how the reaction time for the synthesis of yttrium barium copper oxide can be reduced by using microwave processing (3.5 h compared to 1-2 days if conventional heating is used).

Although most of the oxides reported in the literature have been prepared from the respective binary oxides using a multimode cavity reactor, a number of oxide materials has also been prepared by employing a single-mode cavity. Grossin *et al.* reported the synthesis of  $\text{La}_{0.8}\text{Sr}_{0.2}\text{MnO}_3$  from lanthanum hydroxide,  $\text{La}(\text{OH})_3$ , strontium carbonate,  $\text{SrCO}_3$ , and manganese oxide,  $\text{MnO}_2$ , using an indirect microwave heating process. The starting materials were mixed in appropriate stoichiometric ratios and uniaxially cold pressed into compacts. The pellet was positioned in the center of a single-mode cavity, inside a SiC tube that acts as a susceptor, and heated for 10 min at several microwave input powers: 700, 750, 800, 900, 950 and 1000 W. This showed the effect on temperature and reaction rate as a function of microwave input power. In particular, the temperature rises as the power increases. This is due to the fact that the power effectively absorbed by the sample is proportional to the electric field strength squared (see Section 1.3). Moreover, the authors showed that single-phase products were only obtained at powers higher than 800 W as impurities were observed at powers below that value.

Carbide and nitride materials have also been the subject of microwave studies in recent years because of their excellent properties and industrially important applications, which will be discussed further in Section 1.7. The conventional manufacturing process of such materials is unfortunately time- and energy-intensive as it requires the heating of the starting materials at high temperatures for prolonged reaction times.<sup>47</sup> Microwave synthesis therefore

represents a very interesting option for the production of these substances as it can potentially reduce reaction times and improve the energy efficiency of the whole manufacturing process. A major convenience of using this method over conventional heating is that carbon can be used as both a starting material and susceptor. It efficiently absorbs MW energy which is rapidly converted into thermal energy, providing additional thermal heating to the reaction.

The current research on the synthesis of carbides using microwave irradiation is generally focused on the more industrially relevant materials, including tungsten,<sup>63–73</sup> silicon<sup>74–80</sup> and titanium carbide.<sup>79,81–83</sup> However, many other compounds have been prepared.<sup>84–87</sup> Carbide materials are usually produced by pelletizing mixtures of metal/metal oxide and carbon (either graphite or activated charcoal) in an appropriate stoichiometric ratio and heating them up with the use of a susceptor material in a MW cavity (either multi- or single-mode).

The microwave-assisted synthesis of tungsten carbide was investigated by Vallance *et al.* (2007).<sup>63</sup> The material was prepared by direct reaction of the elemental powders (W + C) in air using either a domestic microwave oven (800 W) or a variable-power single-mode MW reactor (1-3 kW). Tungsten metal and graphite were mixed together with a stoichiometric ratio of 1:1 and uniaxially cold-pressed into compacts. Each pellet was placed into a quartz tube and embedded in graphite powder used as a susceptor, without which the reaction would not take place. The authors reported reaction times of 20 min in a DMO at a power of 800 W and 40 s in an SMC reactor at a power of 3 kW. These represent unprecedented values for the synthesis of such material, if compared to the conventionally synthesized WC which requires up to 10 h to be prepared.

Carassiti *et al.* (2011) studied the microwave-assisted synthesis of SiC, one of the most important industrial material in the world today.<sup>74</sup> The ceramic was prepared from either silicon or silica combined with graphite powder. The experimental set-up used by the authors is similar to that used by Vallance *et al.* for the synthesis of WC. The use of a graphite susceptor was crucial as well. The reaction times reported by the authors are once again reduced when compared to those obtained using conventional heating (up to 12 h). Single-phase SiC was prepared in 5 min in a MMC reactor at a power of 800 W, which could be further reduced to 20 s in a SMC reactor at a power 3 kW.

Another important material prepared by microwave irradiation is aluminium carbide, Al<sub>4</sub>C<sub>3</sub>. The microwave-assisted synthesis of this material faced more challenges with respect to those for WC and SiC described above. Al<sub>4</sub>C<sub>3</sub> is not as stable as TMCs at high temperatures. It can indeed undergo oxidation at temperatures above 1400 °C.<sup>84</sup> The use of an inert/sealed environment is therefore essential. Kennedy *et al.* (2015) successfully

synthesized  $\text{Al}_4\text{C}_3$  from aluminium metal and graphite in 30 min in a MMC reactor at a power of 800 W.<sup>84</sup> The pellet containing the starting materials was inserted in a quartz tube and embedded in graphite powder which was used as a susceptor. The reaction tube was evacuated in order to prevent unwanted oxide phases to form (such as  $\text{Al}_2\text{O}_3$  and  $\text{Al}_2\text{OC}$ ). Up to 12 h are required to synthesize  $\text{Al}_4\text{C}_3$  conventionally, whereas a much reduced reaction time (30 min) was reported by the authors using microwave irradiation.

A number of publications can also be found in the literature concerning the microwave synthesis of binary and ternary nitrides, most of which report the employment of multimode cavities.<sup>88-95</sup> These materials are usually synthesized by either direct nitridation of the corresponding metals or reduction of their oxides and subsequent nitridation.

Brooks *et al.* (2004) reported the synthesis of three different nitride phases (GaN, TiN and VN) using a microwave-induced plasma reactor based on a domestic microwave oven at a power of 900 W.<sup>94</sup> The precursors used for the preparation of such materials were  $\text{Ga}_2\text{O}_3$ ,  $\text{TiO}_2$  and  $\text{V}_2\text{O}_5$ , respectively. The powdered metal oxides (2 g) were placed in an alumina boat inside a U tube which was subsequently evacuated to  $10^{-2}$  mbar. Ammonia was used as a nitriding agent at a flow rate  $113 \text{ cm}^3 \text{ min}^{-1}$  to give a pressure of 20 mbar. Finally, the plasma was ignited and the reaction occurred. The total duration of each experiment was 2.5 h for GaN, 3.5 h for TiN and 6 h for VN which is much lower than the 8-12 h required in the commercial process.<sup>94</sup>

Examples of nitrides synthesized in a single-mode microwave reactor can be found in the literature as well. Hsieh *et al.* (2007) investigated the synthesis of AlN which was performed under nitrogen gas.<sup>96</sup> The material usually requires approximately 8 h to be prepared conventionally but the authors synthesized the same phase in 30 min using a single-mode MW cavity.

In summary, the same trends in processing are usually observed in the synthesis of oxide, carbide and nitride materials using microwave irradiation. The microwave processing of such materials is often accompanied by reduced reaction times with respect to the corresponding method using conventional heating. Moreover, it is known that the observed reaction time decreases as the microwave input power increases and the employment of a single-mode cavity can further decrease reaction time over a multimode equivalent.

## 1.7 Transition Metal Carbides and Nitrides

The majority of transition metal carbides (TMCs) and transition metal nitrides (TMNs) are interstitial alloys formed by the incorporation of carbon or nitrogen into the lattices of transition metals and are classified as nonoxidic ceramics. They combine the physical properties of ceramics (high melting points, hardness, resistance to corrosion, etc.) with the electric and magnetic properties of metals. Because of these outstanding features, these compounds find a myriad of applications in several technological areas as well as at extreme conditions of pressure and temperature.

The most commonly useful TMCs and TMNs are those formed from the elements of group 4-6 but generally most transition metals form carbides and nitrides. Table 1-3 summarizes the Group 4-10 metals and their most stable carbides and nitrides.

**Table 1-3** Stoichiometry of the most stable Group 4-10 transition metal carbides and nitrides.<sup>97,98</sup>

Group 4	Group 5	Group 6	Group 7	Group 8	Group 9	Group 10
Ti	V	Cr	Mn	Fe	Co	Ni
Zr	Nb	Mo	Tc	Ru	Rh	Pd
Hf	Ta	W	Re	Os	Ir	Pt

MC/MN	MC <sub>1-x</sub> / MN <sub>1-x</sub>	M <sub>3</sub> C <sub>2</sub> / M <sub>3</sub> N <sub>2</sub>	M <sub>2</sub> C/M <sub>2</sub> N	M <sub>3</sub> C/M <sub>3</sub> N	M <sub>3</sub> N	No stable carbide/ nitride
-------	--	--	-----------------------------------	-----------------------------------	------------------	----------------------------------

Early transition metals tend to form simple structures, such as in TiC that crystallizes in a face-centered cubic structure.<sup>99</sup> Conversely, late transition metal carbides and nitrides are characterized by more complex structures with formula M<sub>3</sub>C<sub>2</sub>/M<sub>3</sub>N<sub>2</sub> (as in the orthorhombic Cr<sub>3</sub>C<sub>2</sub> – space group *Pnma*)<sup>100</sup> or M<sub>3</sub>C/M<sub>3</sub>N (as in the orthorhombic Fe<sub>3</sub>C – space group *Pnma*).<sup>101</sup> The factors that influence the structure of TMCs and TMNs will be further discussed in the next section.

### 1.7.1 Structure, Synthesis and Applications of TMCs and TMNs

The structure of transition metal carbides and nitrides can be thought of as metallic lattices in which the non-metal atoms (C and N) are incorporated at interstitial positions. The non-metal atoms sit in a position between the metallic atoms, called interstices. The metal lattice may subsequently undergo an expansion due to the incorporation of the non-metal atoms, which weakens the energy of the metal-metal bonds.

The bonding in TMCs and TMNs derives from the interaction of the  $2s$  and  $2p$  orbitals of carbon or nitrogen with the  $d$  orbitals of the transition metal atoms. It is predominantly metallic or covalent with a small percentage of ionic bonding (due to the difference in electronegativity between the transition metal and the non-metal atoms).<sup>46</sup> The percentage of ionic bonding is higher in nitrides due to the higher value of the first ionization energy of nitrogen than that of carbon.

The crystal structure of TMCs and TMNs is affected by electronic (the total number of valence electrons) and geometric (Hägg's rules) factors.<sup>99,102</sup> Hägg, a Norwegian scientist, formulated a set of empirical rules, stating that the crystal structure is determined by the radius ratio,  $r$ , which is given by the following equation:<sup>103,104</sup>

$$r = \frac{r_X}{r_M} \quad (1-17)$$

where  $r_X$  and  $r_M$  are the radii of the non-metal ( $X = \text{C, N, B or H}$ ) and metal atoms, respectively. When  $r < 0.59$  (for early transition metal carbides/nitrides), the structures tend to be simple and resemble those of the pure metal, such as face-centered cubic (*fcc*), body-centered cubic (*bcc*), hexagonal closed packed (*hcp*) and simple hexagonal (*hex*) [Figure 1-8]. Usually, in this case, octahedral interstitial sites are occupied by the non-metal atom and the formulas  $\text{MX}$  and  $\text{M}_2\text{X}$  are more common. For  $r > 0.59$ , the carbide/nitride compounds tend to form more complex structures (to prevent the expansion of the lattice) and the available interstitial sites are trigonal prisms. The stoichiometry changes to  $\text{M}_3\text{X}$  and  $\text{M}_4\text{X}$ .

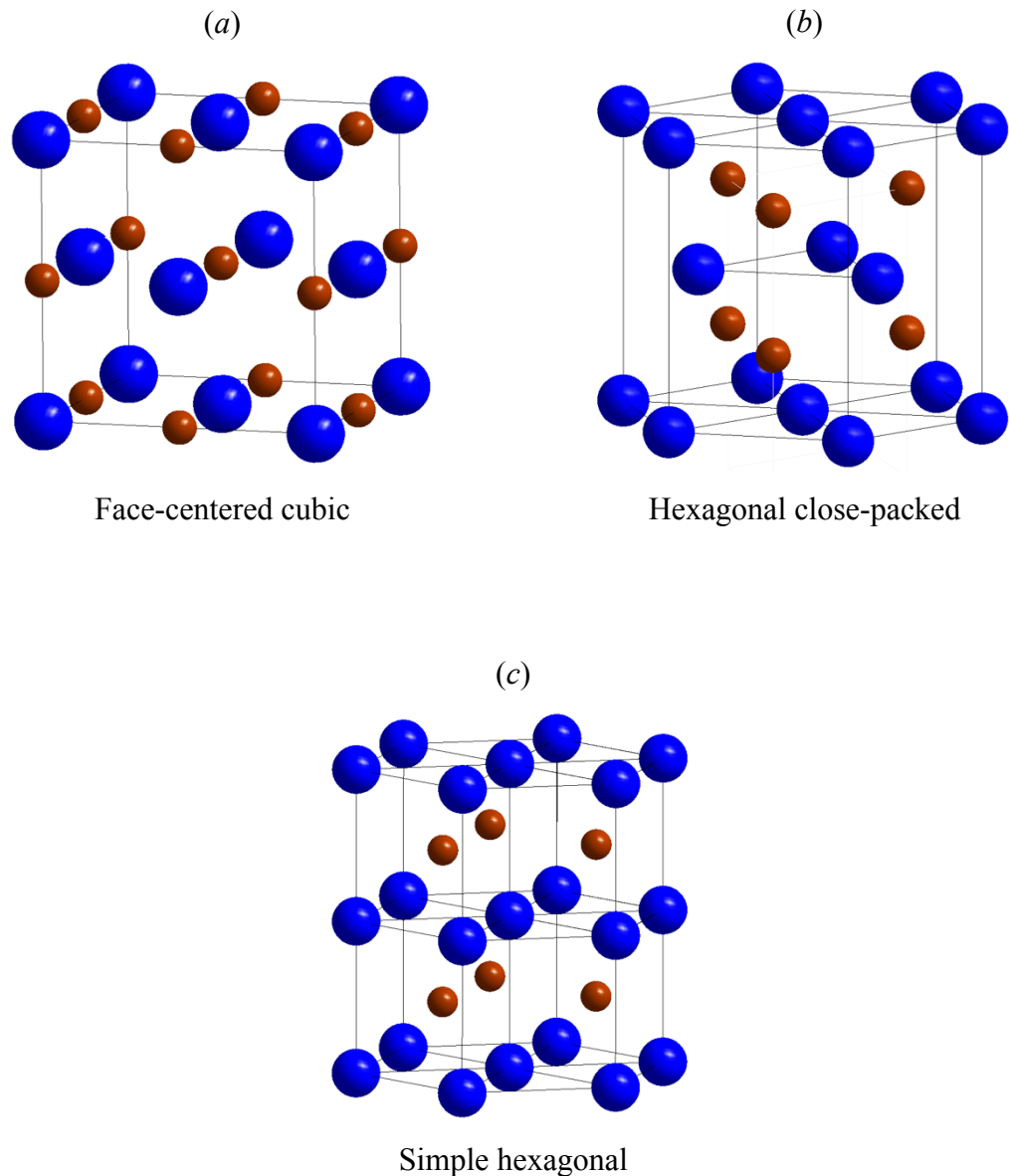


**Figure 1-8** Common crystal structures in TMCs and TMNs. The blue balls represent transition metal atoms and the brown balls represent carbon/nitrogen atoms.

Compounds of mixed C, N and O compositions are also common in the literature. Those with carbon and oxygen at the interstitial sites are called oxycarbides (such as tungsten and zirconium oxycarbides,  $WC_xO_y$  and  $ZrC_xO_y$ ),<sup>105–107</sup> those with nitrogen and oxygen are called oxynitrides (such as  $TiN_xO_y$ ,  $ZrN_xO_y$  and  $HfN_xO_y$ )<sup>108–110</sup> and those with carbon and nitrogen are called carbonitrides (such as  $TiC_{1-x}N_x$ ).<sup>111</sup> Oxycarbide compounds are very common, indeed many carbides that are normally “pure” contain a certain amount of oxygen co-dissolved in them.<sup>102</sup>

As mentioned previously, TMCs and TMNs are characterized by several exceptional physical, mechanical and chemical properties and, as a consequence of this, have attracted

wide interest over the past years. Table 1-4 lists the most common physical and mechanical properties of Group 4-6 transition metals and their compounds.<sup>112</sup> Early TMC and TMN materials have relatively high melting points (compared to that of the corresponding metal), which contribute to their stability at high temperature. They are therefore referred to as “refractory carbides or nitrides”, finding applications as rocket nozzles and jet engine parts. Typical melting point values for such materials go from ~2000 to 4000 K. In addition, they are characterized by a remarkably high hardness (1200-3000 kg/mm<sup>2</sup>), which is retained to very high temperatures and makes them among the hardest materials known. Because of these qualities, they have widespread use in industry as cutting tools and wear-resistant parts. The refractory carbides and nitrides show high Young’s moduli (300-700 GPa) – a measure of the ability of a material to withstand changes in length when under lengthwise tension or compression. Moreover, transition metal carbides and nitrides are also characterized by high chemical resistance and are attacked, at room temperature, only by concentrated acid or base in the presence of oxidizing agents. Due to the metallic nature of the lattice, these compounds show interesting electrical properties. They usually have a higher resistivity than the parent transition metal (in the order of  $10^1 - 10^2 \mu\Omega \text{ cm}$ ) in spite of which are still classified as metallic conductors.<sup>50</sup> In addition, many transition metal compounds (such as ZrN, NbC and TaC) are superconductors at temperatures marginally above absolute.<sup>113-115</sup> Superconductivity was discovered by H. Kamerlingh Onnes in 1911 and constitutes an interesting property, according to which a material exhibits zero resistivity below the threshold of a certain critical temperature.<sup>116,117</sup>

In conclusion, transition metal carbides and nitrides represent an important class of materials that find several real-world applications. Different synthetic methods exist to manufacture these compounds with different yields, purity, particle size and morphology. The choice of one route over alternatives depends largely on the aimed application for a given carbide.

**Table 1-4** Physical and mechanical properties of Group 4-6 transition metals and their carbide and nitride compounds.<sup>112</sup> Highlighted are the materials investigated in this research project.

<b>Compound</b>	<b>Melting Point (K)</b>	<b>Micro-hardness (kg/mm<sup>2</sup>)</b>	<b>Young's Modulus (GPa)</b>
<b>Group 4</b>			
Ti	1940	–	110
TiC	3370	3000	451
TiN	3220	2000	612
Zr	2120	–	95
ZrC	3670	2700	348
ZrN	3250	1500	460
Hf	2490	–	138
HfC	4170	2600	352
HfN	3660	1600	380
<b>Group 5</b>			
V	2170	–	130
VC	2970	2900	422
VN	2450	1500	–
Nb	2740	80	101
NbC	3870	2000	338
NbN	2470	1400	–
Ta	3250	110	186
TaC	3983	2500	53-78
TaN	3360	1050	–
<b>Group 6</b>			
Cr	2130	–	248
Cr <sub>3</sub> C <sub>2</sub>	2070	1400	373
CrN	1770	1100	–
Mo	2890	210	325
Mo <sub>2</sub> C	2770	1500	533
W	3670	400	345
WC	3070	2200	696

## 1.8 Chapter Summary and Scope of This Work

This chapter defines microwaves from their prediction by James Clerk Maxwell in 1888 to their discovery by Heinrich Hertz in 1920 and how they can be efficiently produced thanks to the invention of the modern cavity magnetron in 1940. The dielectric properties of materials were discussed together with the mechanisms through which MWs interact with matter, such as dipolar polarization and conduction, and how these are exploited in MW heating. The features of MW heating present several advantages and disadvantages over conventional methods and as TMCs and TMNs are materials that can be synthesized efficiently by MWs, their structure, synthesis and properties were discussed.

The scope of this work is to study the microwave synthesis and structural characterization of some important transition metal carbides and nitrides. This thesis primarily focuses on four binary systems, V–C, Zr–C, Hf–C and Zr–N, with a main emphasis on carbides. As discussed in the previous sections, these materials find several applications in powder metallurgy and technology, as superhard and corrosion-resistant materials and materials for nuclear-energy production. Vanadium carbide is vastly used as a wear-resistant part in cutting tool bits as well as an additive to tungsten carbide to inhibit its grain growth and thus improve the property of the cermet.<sup>118</sup> Zirconium carbide is also used in tool bits for cutting tools and in ceramic knives. Moreover, due to its low neutron absorption cross-section and excellent resistance against fission product corrosion, ZrC can be used as a potential refractory coating in nuclear reactors, replacing the currently used silicon carbide.<sup>119</sup> Zirconium nitride is a hard ceramic used as a coating material in industrial parts (such as drill bits and burs) and aerospace components. It is usually deposited by physical vapour deposition.<sup>120</sup> ZrN is also used in laboratory crucibles, refractories and cermets. Hafnium carbide is one of most refractory binary compounds known (with a melting point of 4170 K – see Table 1-4). Despite that, it finds limited applications due to the high cost of production.

Previous studies have shown that MW heating is a viable method of synthesizing such materials over minutes or seconds timescales, thus reducing their cost of production.<sup>63,74,86,87,121</sup> When compared to corresponding furnace reactions, MW heating processes generally show faster reaction times<sup>86</sup> and lower reaction temperatures.<sup>122</sup> In this thesis, MW irradiation was used with the aim of reducing the reaction time (and, hence, the cost of production) for the synthesis of the carbide materials described above. Moreover, the oxygen inclusion within the structure of carbides and nitrides is a common feature observed for such materials but not much information can be found in the literature. This research project provides a small contribution in this regard.

Carbide synthesis was investigated via both direct reaction of the elemental powders and carbothermal reduction of the metal oxides in either a multimode or a single-mode cavity MW reactor, whereas the nitride production was investigated by nitridation of zirconium powder using a multimode cavity MW reactor. Throughout the programme of research, it was first necessary to establish a reproducible experimental procedure. The phase evolution in each system was subsequently probed as a function of time using Powder X-ray Diffraction to establish an optimum synthesis procedure and to understand reaction pathways in more detail. The final products were further characterized using several techniques such as Scanning Electron Microscopy coupled with Energy-dispersive X-ray Spectroscopy, Raman Spectroscopy, X-ray Photoelectron Spectroscopy and Powder Neutron Diffraction.

## 1.9 References

1. Retrieved from: <http://www.physast.uga.edu/~jss/1010/ch5/emwave.jpg>.
2. Hitchcock, T. R. *Radio-frequency and Microwave Radiation*. (American Industrial Hygiene Assn., 2004).
3. Katz, J. D. Microwave Sintering of Ceramics. *Annu. Rev. Mater. Sci.* **22**, 153–170 (1992).
4. Thostenson, E. T. & Chou, T. W. Microwave processing: fundamentals and applications. *Compos. Part A Appl. Sci. Manuf.* **30**, 1055–1071 (1999).
5. Retrieved from: [https://en.wikipedia.org/wiki/Electromagnetic\\_spectrum](https://en.wikipedia.org/wiki/Electromagnetic_spectrum).
6. Appelyard, R. Pioneers of Electrical Communication - Heinrich Rudolf Hertz. *Electr. Commun.* **6**, 63–77 (1927).
7. Hull, A. W. The effect of a uniform magnetic field on the motion of electrons between coaxial cylinders. *Phys. Rev.* **18**, 31–57 (1921).
8. Hull, A. W. The magnetron. *J. Am. Inst. Electr. Eng.* **40**, 715–723 (1921).
9. Barton, K. A Half Century of Radar. *IEEE Trans. Microw. Theory Tech.* **32**, 1161–1170 (1984).
10. Boot, H. A. H. & Randall, J. T. Historical notes on the cavity magnetron. *IEEE Trans. Electron Devices* **23**, 51–70 (1976).
11. Retrieved from: [http://www.emforensics.com/pictures/huge\\_96\\_481052magnetron.jpg](http://www.emforensics.com/pictures/huge_96_481052magnetron.jpg).
12. Brittany, H. Microwave Synthesis: Chemistry at the speed of light. 1–296 (2002).

13. Liu, S. W. & Wightman, J. P. Decomposition of simple alcohols, ethers and ketones in a microwave discharge. *J. Appl. Chem. Biotechnol.* **21**, 168–172 (1971).
14. Gedye, R. *et al.* The use of microwave ovens for rapid organic synthesis. *Tetrahedron Lett.* **27**, 279–282 (1986).
15. Bykov, Y., Rybakov, K. & Semenov, V. E. High-temperature microwave processing of materials. *J. Phys. D. Appl. Phys.* **34**, R55–R75 (2001).
16. Lidström, P., Tierney, J., Wathey, B. & Westman, J. Microwave assisted organic synthesis—a review. *Tetrahedron* **57**, 9225–9283 (2001).
17. Rao, K. J. & Ramesh, P. D. Use of microwaves for the synthesis and processing of materials. *Bull. Mater. Sci.* **18**, 447–465 (1995).
18. Whittaker, A. G. & Mingos, D. M. P. The Application of Microwave Heating to Chemical Syntheses. *J. Microw. Power Electromagn. Energy* **29**, 195–219 (1994).
19. Kitchen, H. J. *et al.* Modern microwave methods in solid-state inorganic materials chemistry: From fundamentals to manufacturing. *Chem. Rev.* **114**, 1170–1206 (2014).
20. Agrawal, D. Microwave sintering of ceramics, composites, metals and transparent materials. *Journal of materials Education* **19**, 49–57 (1997).
21. Agrawal, D. K. Microwave processing of ceramics. *Curr. Opin. Solid State Mater. Sci.* **3**, 480–485 (1998).
22. Clark, D. E., Folz, D. C. & West, J. K. Processing materials with microwave energy. *Mater. Sci. Eng. A* **287**, 153–158 (2000).
23. Katz, J. D. Microwave Sintering of Ceramics. *Annu. Rev. Mater. Sci.* **22**, 153–170 (1992).
24. Menéndez, J. A. *et al.* Microwave heating processes involving carbon materials. *Fuel Process. Technol.* **91**, 1–8 (2010).
25. Rao, K. J., Vaidhyanathan, B., Ganguli, M. & Ramakrishnan, P. a. Synthesis of Inorganic Solids Using Microwaves. *Chem. Mater.* **11**, 882–895 (1999).
26. Ravi, B. G., Ramesh, P. D., Gupta, N. & Rao, K. J. Microwave assisted preparation and sintering of Al<sub>2</sub>O<sub>3</sub>, ZrO<sub>2</sub> and their composites from metalorganics. *J. Mater. Chem.* **7**, 2043–2048 (1997).
27. Whittaker, A. G. & Mingos, D. M. P. Synthetic reactions using metal powders under microwave irradiation. *J. Chem. Soc. Dalt. Trans.* 3967–3970 (2002).
28. Regier, M. & Schubert, H. Microwave processing of materials. *Therm. Technol. food Process.* **55**, 178–207 (2001).
29. Retrieved from: [https://en.wikipedia.org/wiki/Chemical\\_polarity](https://en.wikipedia.org/wiki/Chemical_polarity).
30. Metaxas, A. C. & Meredith, R. J. Industrial Microwave Heating. *Peter Peregrinus, London* (1983).

31. Retrieved from: <http://nisenet.org/catalog/scientific-image-graphite-models>.
32. McGill, B. S. L. & Walkiewicz, W. Microwave Heating of Chemical and Minerals. *Dep. Inter. Bur. Mines* **95**, 1–28 (1995).
33. Meredith, R. J. *Engineers' handbook of industrial microwave heating*. (IET, 1998).
34. Kriegsmann, G. A. Thermal runaway in microwave heated ceramics: A one-dimensional model. *J. Appl. Phys.* **71**, 1960–1966 (1992).
35. Kenkre, V. M., Skala, L., Weiser, M. W. & Katz, J. D. Theory of microwave interactions in ceramic materials: the phenomenon of thermal runaway. *J. Mater. Sci.* **26**, 2483–2489 (1991).
36. Michael, D., Mingos, P. & Baghurst, D. R. Highlight fast solid state chemistry; Reaction under the influence of MW. *Chem. Soc. Rev* **20**, 1–12 (1991).
37. Venkatesh, M. S. & Raghavan, G. S. V. An overview of microwave processing and dielectric properties of agri-food materials. *Biosyst. Eng.* **88**, 1–18 (2004).
38. Buffler, C. R. *Microwave cooking and processing*. (Van Nostrand Reinhold, 1993).
39. Kingston, H. M. & Jassie, L. B. *Introduction to Microwave Sample Preparation: Theory and Practice*. (American Chemical Society, 1988).
40. Sutton, W. H. Microwave processing of ceramic materials. *Am. Ceram. Soc. Bull.* **68**, 376–386 (1989).
41. Zhang, X., Hayward, D. O. & Mingos, D. M. P. Effects of Microwave Dielectric Heating on Heterogeneous Catalysis. *Catal. Letters* **88**, 33–38 (2003).
42. Bykov, Y. V, Rybakov, K. I. & Semenov, V. E. High-temperature microwave processing of materials. *J. Phys. D. Appl. Phys.* **34**, R55–R75 (2001).
43. Deng, S. G. & Lin, Y. S. Microwave heating synthesis of supported sorbents. *Chem. Eng. Sci.* **52**, 1563–1575 (1997).
44. Li, J., Zhu, L. & Cai, W. Characteristics of organobentonite prepared by microwave as a sorbent to organic contaminants in water. *Colloids Surfaces A Physicochem. Eng. Asp.* **281**, 177–183 (2006).
45. Zhang, X. & Liu, Z. Recent advances in microwave initiated synthesis of nanocarbon materials. *Nanoscale* **4**, 707–14 (2012).
46. Toth, L. E. *Transition Metal Carbides and Nitrides*. (Elsevier, 2014).
47. Nickl, J. J. The refractory carbides. Von E. K. Storms. Aus der Reihe refractory materials. Vol. 2, herausgeg. von J. L. Margrave. Academic Press, New York-London 1967. *Angew. Chemie* **81**, 436–442 (1969).
48. Kosolapova, T. Y. *Carbides: properties, production, and applications*. (Springer Science & Business Media, 1971).
49. Storms, E. K. & McNeal, R. J. The Vanadium-Vanadium Carbide System. *J. Phys.*

- Chem.* **66**, 1401–1408 (1962).
50. Oyama, S. T. in *The Chemistry of Transition Metal Carbides and Nitrides SE - 1* (ed. Oyama, S. T.) 1–27 (Springer Netherlands, 1996).
  51. Meunier, F. *et al.* Synthesis and Characterization of High Specific Surface Area Vanadium Carbide; Application to Catalytic Oxidation. *J. Catal.* **44**, 33–44 (1997).
  52. Pierson, H. O. *Handbook of Refractory Carbides & Nitrides: Properties, Characteristics, Processing and Apps.* (William Andrew, 1996).
  53. El-Eskandarany, M. S., Mahday, A. A., Ahmed, H. A. & Amer, A. H. Synthesis and characterizations of ball-milled nanocrystalline WC and nanocomposite WC–Co powders and subsequent consolidations. *J. Alloys Compd.* **312**, 315–325 (2000).
  54. Wang, G. M., Campbell, S. J., Calka, A. & Kakzmarek, W. A. Synthesis and structural evolution of tungsten carbide prepared by ball milling. *J. Mater. Sci.* **32**, 1461–1467 (1997).
  55. Brüttsch, R. Chemical vapour deposition of silicon carbide and its applications. *Thin Solid Films* **126**, 313–318 (1985).
  56. Hegde, R. I., Fiordalice, R. W., Travis, E. O. & Tobin, P. J. Thin film properties of low-pressure chemical vapor deposition TiN barrier for ultra-large-scale integration applications. *J. Vac. Sci. Technol. B Microelectron. Nanom. Struct. Process. Meas. Phenom.* **11**, 1287–1296 (1993).
  57. Karoly, Z. *et al.* Synthesis of SiC powder by RF plasma technique. *Powder Technol.* **214**, 300–305 (2011).
  58. Raman, V., Bahl, O. P. & Dhawan, U. Synthesis of silicon carbide through the sol-gel process from different precursors. *J. Mater. Sci.* **30**, 2686–2693 (1995).
  59. Iwasaki, M., Takizawa, H., Uheda, K. & Endo, T. Microwave synthesis and the electrical properties of  $\text{Na}_x\text{Co}_{1-y}\text{MnyO}_2$ . *J. Mater. Sci. Lett.* **19**, 2033–2035 (2000).
  60. Agostino, A., Benzi, P., Castiglioni, M., Rizzi, N. & Volpe, P.  $\text{YBa}_2\text{Cu}_3\text{O}_7$  synthesis using microwave heating. *Supercond. Sci. Technol.* **17**, 685–688 (2004).
  61. Liu, Y. F., Liu, X. Q. & Meng, G. Y. A novel route of synthesizing  $\text{La}_{1-x}\text{Sr}_x\text{CoO}_3$  by microwave irradiation. *Mater. Lett.* **48**, 176–183 (2001).
  62. Saji, T. Mechanism of Microwave Sintering, and Millimeter Wave Sintering. *New Ceram.* **8**, 21–30 (1995).
  63. Vallance, S. R., Kingman, S. & Gregory, D. H. Ultrarapid materials processing: Synthesis of tungsten carbide on subminute timescales. *Adv. Mater.* **19**, 138–142 (2007).
  64. Vallance, S. R. *et al.* Probing the microwave interaction mechanisms and reaction pathways in the energy-efficient, ultra-rapid synthesis of tungsten carbide. *Green*

- Chem.* **14**, 2184–2192 (2012).
65. Ahlgren, M. Methods of making cemented carbide. **1**, 4–7 (2004).
  66. Essaki, K., Rees, E. J. & Burstein, G. T. Influence of precursor preparation on the synthesis of WC under microwave irradiation. *Mater. Lett.* **63**, 2185–2187 (2009).
  67. Rees, E. J., Essaki, K., Brady, C. D. A. & Burstein, G. T. Hydrogen electrocatalysts from microwave-synthesised nanoparticulate carbides. *J. Power Sources* **188**, 75–81 (2009).
  68. Shen, P. K., Yin, S., Li, Z. & Chen, C. Preparation and performance of nanosized tungsten carbides for electrocatalysis. *Electrochim. Acta* **55**, 7969–7974 (2010).
  69. Breval, E. *et al.* Comparison between microwave and conventional sintering of WC/Co composites. *Mater. Sci. Eng. A* **391**, 285–295 (2005).
  70. Cheng, J. P. Microwave processing of WC-Co composites and ferroic titanates. *Mater. Res. Innov.* **1**, 44–52 (1997).
  71. Sunil, B. R., Sivaprahasam, D. & Subasri, R. Microwave sintering of nanocrystalline WC-12Co: Challenges and perspectives. *Int. J. Refract. Met. Hard Mater.* **28**, 180–186 (2010).
  72. Hu, F., Cui, G., Wei, Z. & Shen, P. K. Improved kinetics of ethanol oxidation on Pd catalysts supported on tungsten carbides/carbon nanotubes. *Electrochem. commun.* **10**, 1303–1306 (2008).
  73. Lu, J. L., Li, Z. H., Jiang, S. P., Shen, P. K. & Li, L. Nanostructured tungsten carbide/carbon composites synthesized by a microwave heating method as supports of platinum catalysts for methanol oxidation. *J. Power Sources* **202**, 56–62 (2012).
  74. Carassiti, L. *et al.* Ultra-rapid, sustainable and selective synthesis of silicon carbide powders and nanomaterials via microwave heating. *Energy Environ. Sci.* **4**, 1503–1510 (2011).
  75. Satapathy, L. N., Ramesh, P. D., Agrawal, D. & Roy, R. Microwave synthesis of phase-pure, fine silicon carbide powder. *Mater. Res. Bull.* **40**, 1871–1882 (2005).
  76. Ebadzadeh, T. & Marzban-Rad, E. Microwave hybrid synthesis of silicon carbide nanopowders. *Mater. Charact.* **60**, 69–72 (2009).
  77. Panneerselvam, M., Agrawal, A. & Rao, K. J. Microwave sintering of MoSi<sub>2</sub>-SiC composites. *Mater. Sci. Eng. A* **356**, 267–273 (2003).
  78. Das, B. P., Panneerselvam, M. & Rao, K. J. A novel microwave route for the preparation of ZrC-SiC composites. *J. Solid State Chem.* **173**, 196–202 (2003).
  79. Wei, G. *et al.* Large-scale synthesis of wide band gap semiconductor nanostructures by microwave method. *J. Phys. Chem. C* **113**, 19432–19438 (2009).
  80. Deksnys, T. P., Menezes, R. R., Fagury-Neto, E. & Kiminami, R. H. G. A.

- Synthesizing Al<sub>2</sub>O<sub>3</sub>/SiC in a microwave oven: A study of process parameters. *Ceram. Int.* **33**, 67–71 (2007).
81. Hassine, N. A., Binner, J. G. P. & Cross, T. E. Synthesis of refractory metal carbide powders via microwave carbothermal reduction. *Int. J. Refract. Met. Hard Mater.* **13**, 353–358 (1995).
  82. West, C. P., Harrison, I., Cussen, E. J. & Gregory, D. H. Facile synthesis of bimetallic carbonitrides, V<sub>1-x</sub>Ti<sub>x</sub>(C,N), by microwave carbothermal reduction-ammonolysis/carburisation (MW-CRAC) methods. *J. Eur. Ceram. Soc.* **29**, 2355–2361 (2009).
  83. Kitiwan, M. & Atong, D. Synthesis and Characterization of Microwave and Conventional Combustion Synthesized Alumina-Titanium Carbide Powders. **49**, 85–90 (2006).
  84. Kennedy, J. L., Drysdale, T. D. & Gregory, D. H. Rapid, energy-efficient synthesis of the layered carbide, Al<sub>4</sub>C<sub>3</sub>. *Green Chem.* **17**, 285–290 (2015).
  85. Pillai, R. C., Sabolsky, E. M., Rowan, S. L., Celik, I. B. & Morrow, S. Solid-State Synthesis of Calcium Carbide by Using 2.45 GHz Microwave Reactor. *Ind. Eng. Chem. Res.* **54**, 11001–11010 (2015).
  86. Vallance, S. R., Kingman, S. & Gregory, D. H. Ultra-rapid processing of refractory carbides; 20 s synthesis of molybdenum carbide, Mo<sub>2</sub>C. *Chem. Commun. (Camb).* 742–744 (2007).
  87. Vallance, S. R. *et al.* Ultrarapid microwave synthesis of superconducting refractory carbides. *Adv. Mater.* **21**, 4502–4504 (2009).
  88. Hong, Y. C., Shin, D. H. & Uhm, H. S. Production of vanadium nitride nanopowders from gas-phase VOCl<sub>3</sub> by making use of microwave plasma torch. *Mater. Chem. Phys.* **101**, 35–40 (2007).
  89. Jain, A. & Brezinsky, K. Microwave-assisted combustion synthesis of tantalum nitride in a fluidized bed. *J. Am. Ceram. Soc.* **86**, 222–226 (2003).
  90. Bang, C. U., Hong, Y. C. & Uhm, H. S. Synthesis and characterization of nano-sized nitride particles by using an atmospheric microwave plasma technique. *Surf. Coatings Technol.* **201**, 5007–5011 (2007).
  91. Craciun, S., Craciun, E. & Sava, B. Silicon Nitride Ceramics Obatined By Microwave Field Sintering Method. *Rev. Rom. Mater.* **35**, 97–109 (2005).
  92. Huang, J.-W., Li, J. & Peng, H. Microwave synthesis of manganese nitride. *Powder Metall.* **50**, 137–141 (2007).
  93. Ozawa, T., Dohi, M., Matsuura, T. & Hayakawa, Y. Synthesis of GaN bulk crystals and melt growth of GaN layers under nitrogen plasma. *J. Cryst. Growth* **310**, 1785–

- 1789 (2008).
94. Brooks, D. J. & Douthwaite, R. E. Microwave-induced plasma reactor based on a domestic microwave oven for bulk solid state chemistry. *Rev. Sci. Instrum.* **75**, 5277–5279 (2004).
  95. Vaidhyanathan, B., Agrawal, D. K. & Roy, R. Novel synthesis of nitride powders of microwave-assisted combustion. *J. Mater. Res.* **15**, 974–981 (2000).
  96. Hsieh, C. Y., Lin, C. N., Chung, S. L., Cheng, J. & Agrawal, D. K. Microwave sintering of AlN powder synthesized by a SHS method. *J. Eur. Ceram. Soc.* **27**, 343–350 (2007).
  97. Liu, Y., Kelly, T. G., Chen, J. G. & Mustain, W. E. Metal Carbides as Alternative Electrocatalyst Supports. *ACS Catal.* **3**, 1184–1194 (2013).
  98. Zhong, Y. *et al.* Transition Metal Carbides and Nitrides in Energy Storage and Conversion. *Adv. Sci.* **3**, 1–28 (2016).
  99. Adams, D. M. *Inorganic solids: an introduction to concepts in solid-state structural chemistry.* (John Wiley & Sons, 1974).
  100. Rundqvist, S. & Runnsjo, G. Crystal Structure Refinement of Cr<sub>3</sub>C<sub>2</sub>. *Acta Chem. Scand.* **23**, 1191–1199 (1969).
  101. Lipson, H. & Petch, N. J. The crystal structure of cementite, Fe<sub>3</sub>C. *Iron Steel Inst.* **142**, (1940).
  102. Oyama, S. T. Preparation and catalytic properties of transition metal carbides and nitrides. *Catal. Today* **15**, 179–200 (1992).
  103. Hagg, G. Regularities in the crystal structure with hydrides, borides, carbides and nitrides of the transition elements. *Z. Phys. Chem* **12**, 33–56 (1931).
  104. Blank, H. Hägg's rule and fast solute diffusion in cubic transition-metal phases. *Philos. Mag. Part B* **73**, 833–844 (1996).
  105. Gao, Z. & Qin, D.-Y. Catalyt properties of tungsten oxycarbide and carbide in hydrocarbon conversion. *Chinese J. Chem.* **8**, 207–214 (1990).
  106. Gendre, M., Maître, A. & Trolliard, G. Synthesis of zirconium oxycarbide (ZrC<sub>x</sub>O<sub>y</sub>) powders: Influence of stoichiometry on densification kinetics during spark plasma sintering and on mechanical properties. *J. Eur. Ceram. Soc.* **31**, 2377–2385 (2011).
  107. Pantano, C. G. *et al.* Silicon Oxycarbide Glasses. *J. Sol-Gel Sci. Technol.* **14**, 7–25 (1999).
  108. Gusev, E. P. *et al.* The composition of ultrathin silicon oxynitrides thermally grown in nitric oxide. *J. Appl. Phys.* **82**, 896–898 (1997).
  109. Marchand, R., Laurent, Y., Guyader, J., L'Haridon, P. & Verdier, P. Nitrides and oxynitrides: Preparation, crystal chemistry and properties. *J. Eur. Ceram. Soc.* **8**, 197–

- 213 (1991).
110. Venkataraj, S. *et al.* Towards understanding the superior properties of transition metal oxynitrides prepared by reactive DC magnetron sputtering. *Thin Solid Films* **502**, 228–234 (2006).
  111. Wang, Y., Jiang, T., Zhang, L. & An, L. Electron transport in polymer-derived amorphous silicon oxycarbonitride ceramics. *J. Am. Ceram. Soc.* **92**, 1603–1606 (2009).
  112. Santhanam, A. T. *Application of transition metal carbides and nitrides in industrial tools BT - The Chemistry of Transition Metal Carbides and Nitrides*. (Springer Netherlands, 1996).
  113. Hardy, G. F. & Hulm, J. K. The Superconductivity of Some Transition Metal Compounds. *Phys. Rev.* **93**, 1004–1016 (1954).
  114. Soediono, B. Superconducting critical temperature of nonstoichiometric transition metal carbides and nitride. *J. Chem. Inf. Model.* **53**, 160 (1989).
  115. Willens, R., Buehler, E. & Matthias, B. Superconductivity of the transition-metal carbides. *Phys. Rev.* **159**, 327 (1967).
  116. Onnes, H. K. in *Through Measurement to Knowledge* 261–263 (Springer, 1991).
  117. Onnes, H. K. in *Through Measurement to Knowledge* 267–272 (Springer, 1991).
  118. Lee, H. R., Kim, D. J., Hwang, N. M. & Kim, D.-Y. Role of Vanadium Carbide Additive during Sintering of WC–Co: Mechanism of Grain Growth Inhibition. *J. Am. Ceram. Soc.* **86**, 152–154 (2003).
  119. Katoh, Y., Vasudevamurthy, G., Nozawa, T. & Snead, L. L. Properties of Zirconium Carbide for Nuclear Fuel Applications. *J. Nucl. Mater.* **441**, 718–742 (2013).
  120. Wiiala, U. K., Penttinen, I. M., Korhonen, A. S., Aromaa, J. & Ristolainen, E. Improved corrosion resistance of physical vapour deposition coated TiN and ZrN. *Surf. Coatings Technol.* **41**, 191–204 (1990).
  121. Kennedy, J. L., Drysdale, T. D. & Gregory, D. H. Rapid, energy-efficient synthesis of the layered carbide, Al<sub>4</sub>C<sub>3</sub>. *Green Chem.* **17**, 285–290 (2015).
  122. Chen, C., Guo, J., Fu, G. C., Yang, L. H. & Chen, H. Rapid preparation of MgB<sub>2</sub> superconductor using hybrid microwave synthesis. *Supercond. Sci. Technol.* **17**, L55–L57 (2004).

## 2 Experimental Theory and Methods

### 2.1 Microwave Reactors

Ever since microwave heating gained popularity for the synthesis of materials, the requirements for microwave cavities to act as reactors has led to the development of MW instrumentation encompassing both so called multi-mode cavity (MMC) and single-mode cavity (SMC) microwave reactors. Although these reactors have fundamentally different designs (which will be discussed in the next sections), they possess common components such as a microwave source (generator), waveguide and applicator.

Most of the MW reactors found in the market make use of vacuum tubes as a MW source such as magnetrons<sup>1,2</sup> and travelling-wave tubes (TWTs).<sup>3</sup> Magnetrons are high-powered devices that can generate microwaves at a fixed frequency in an efficient and reliable manner<sup>4</sup> and are usually used in domestic microwave ovens (DMO) and industrial-scale MW apparatus. For a detailed description on how this device works, see Section 1.1. The power output of a magnetron can be controlled by either pulse-width modulation (PWM), that cycles the current on and off for specific periods of time,<sup>5</sup> or by adjusting the cathode current or magnetic field strength. The first method is usually used in most of the domestic microwave ovens commercially available. Travelling-wave tubes are usually used to produce MWs at variable frequencies, though it is beyond the scope of this research to present a detailed description of their design and how they work.

After MWs are produced at the source, they are channelled by the waveguide into the cavity. The waveguide is a hollow metal pipe that confines the microwaves to propagate in one direction with minimal loss of energy. Its design typically affects the specific pattern of electromagnetic radiation that is propagated, also called the mode of MWs. Waveguides usually have a circular or rectangular shape as these generate well understood modes.

The applicator is the MW cavity in which the target load is positioned and MW power is absorbed by this load. Multi- and single-mode cavities (described below) have different MW field structures which is determined by the wavelength of microwaves and the size of the applicator itself. The choice of the cavity depends on a number of variables including sample size, shape and volume. The main difference between the two cavities in terms of the

configuration of synthetic experiments is that single-mode reactors have small chambers that can accommodate only one reaction vessel whereas more vessels can be irradiated simultaneously in a multi-mode reactor.

### 2.1.1 Multi-mode Cavity (MMC) Microwave Reactors

A multi-mode cavity MW reactor is essentially composed of a power supply (and a control mechanism), a MW source (usually a magnetron) connected to a transmission line (waveguide) and an applicator which consists of a large metallic cuboid chamber acting as a Faraday cage. A domestic microwave oven falls into this category and a schematic diagram of its construction is shown in Figure 2-1.

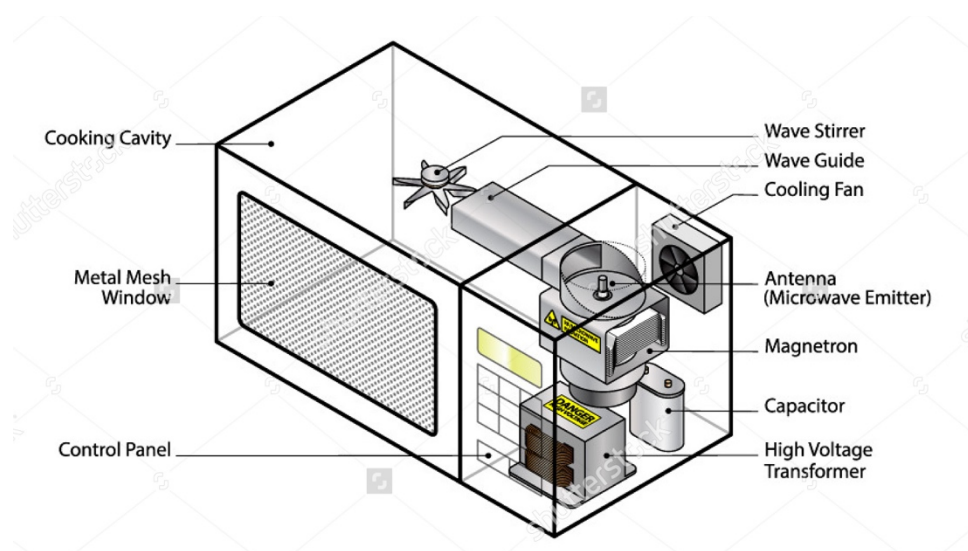


**Figure 2-1** Schematic diagram of a typical microwave oven showing key internal components.<sup>6</sup>

As MWs are reflected by the walls of the cavity, they resonate forming different standing waves. The cavity is several times larger than the wavelength of the MW radiation (12.5 cm) and can therefore support the propagation of multiple modes of MW energy resulting in a heterogeneous distribution of energy.<sup>7</sup> Vollmer *et al.* (2003) studied the physics of microwave ovens by placing a horizontal glass plate covered with a thin film of water within the cavity at a height of about 8 cm and heating it at full power (800 W) for 15 s.<sup>8</sup> As a result, they found the microwave intensity distribution within an oven of 29 x 29 x 19 cm<sup>3</sup> using infrared thermal imaging, as shown in Figure 2-2.

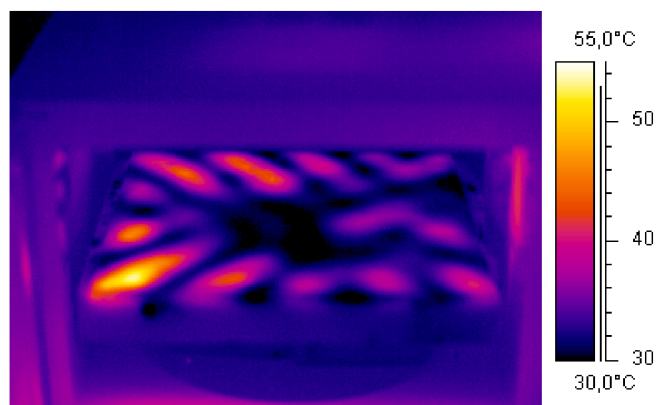


**Figure 2-2** Visualization of the horizontal mode structure in a domestic microwave oven using infrared thermal imaging.<sup>8</sup>

From the picture above, it is possible to observe the uneven heating of the substance due to the so-called ‘hot spots’ (in yellow) and ‘cold spots’ (in black). This is the main reason why microwave ovens employ either a rotating turntable or a wave stirrer. The latter consists of a rotating reflector usually positioned at the top of the cavity [Figure 2-1]. Both methods help to provide a more homogeneous distribution of microwave energy within the cavity but do not entirely overcome the problem. Because of the resulting random MW field pattern,<sup>7,9-11</sup> the reproducibility of MMC synthesis experiments is often low, especially when large loads are employed, and it is hard to calculate the effective power delivered into the sample.<sup>12</sup> In this thesis, MMC experiments were carried out by placing a cylindrical load (quartz tube + pellet + susceptor) consistently at the same position in the cavity to ensure the experimental parameters were as constant as possible and to maximize repeatability. The sample position was determined empirically. Together with a small sample size ( $\sim 2 \text{ cm}^3$ ), microwave reactions in a multi-mode cavity were found to be repeatable and reliable, yielding products with high purity and uniform morphology.

In recent years, the number of commercially available multi-mode cavity MW reactors specifically designed for MW synthesis has increased. Figure 2-3 illustrates the CEM Mars 6 which is equipped with 2 magnetrons and operating with a total power of 1.8 kW.<sup>5</sup> Its waveguides have been strategically designed to disperse MW energy uniformly throughout the cavity.

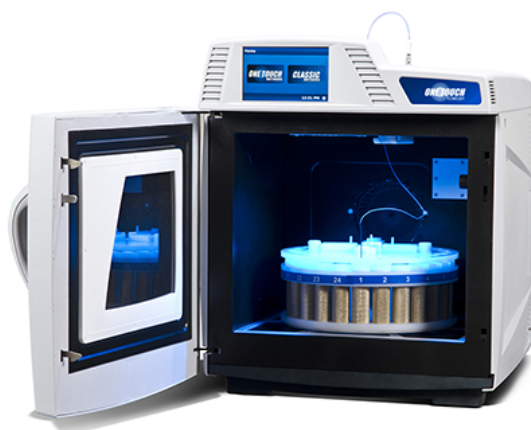


**Figure 2-3** CEM Mars 6 multi-mode cavity MW reactor.<sup>13</sup>

The MMC experiments detailed in Chapter 3, 4 and 5 were conducted in a Sharp R272SLM domestic microwave oven. This model is touch control and operates at a MW frequency of 2.45 GHz and a power of 800 W.

### 2.1.2 Single-mode Cavity (SMC) Microwave Reactors

A single-mode cavity is a small compact chamber (of the order of approximately one half wavelength) that can support the propagation of only one mode of MW energy.<sup>14</sup> This results in a more homogeneous distribution of energy and a higher power density with respect to a MMC and prevents the formation of the hot and cold spots. MWs are directed to the applicator through a rectangular waveguide and a standing wave pattern is formed by superimposition of a forward and reflected wave using a short circuit tuner [Figure 2-4]. This generates points of no MW energy (“nodes”) and points of the highest magnitude of MW energy (“antinodes”).

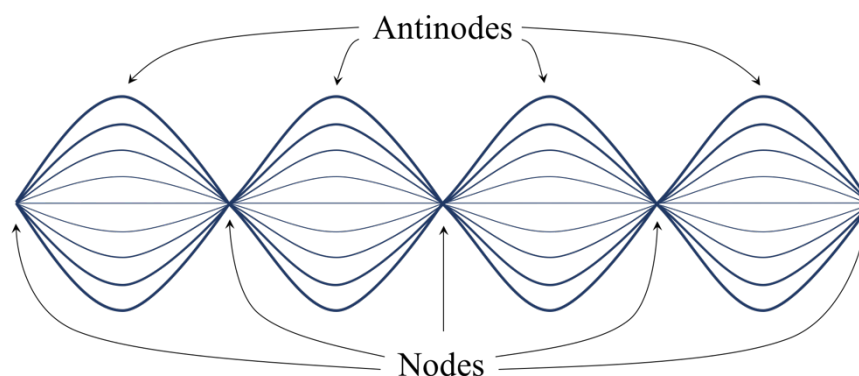


**Figure 2-4** Nodes and antinodes standing wave pattern.

The tuner is finely adjusted so that the antinode of the standing wave and, hence, the point of maximum electric field strength is in correspondence with the sample position. Unlike in a MMC reactor, the electromagnetic distribution is known and so is the power delivered into the sample. However, single-mode MW reactors are far less commonly used than multi-mode MW reactors due, in part, to the complication of having to tune the microwave radiation but, mainly, for reasons of cost. Single-mode systems can indeed cost upwards of £10,000, compared to ~£40/50 for a basic domestic MW oven.

A single-mode MW reactor possesses a number of additional components that MMC reactors usually do not have. Figure 2-5 provides a schematic illustration of the SMC reactor used for the work described in this thesis, its components and the way these are configured.

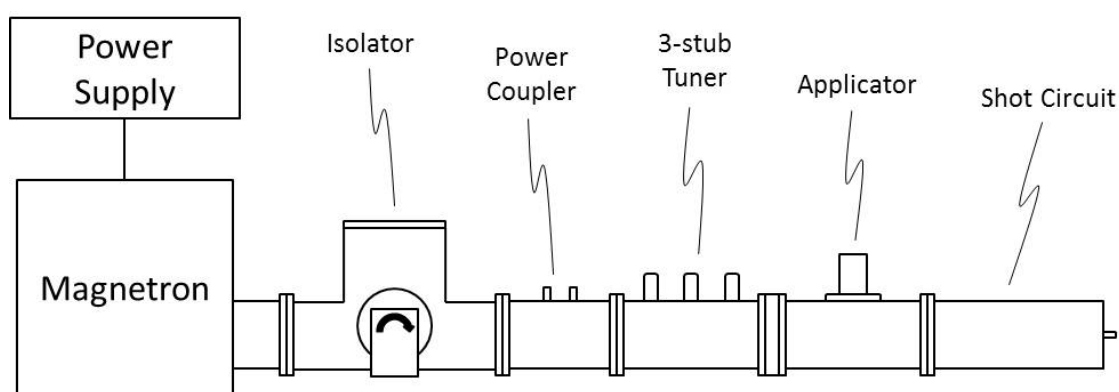


**Figure 2-5** Schematic illustration of the single-mode cavity MW reactor used.

A power supply (0-1 kW) is connected to a magnetron and, together, they generate microwaves at a frequency of 2.45 GHz. The microwaves pass through an isolator (max operating power of 6 kW), which prevents reflected MW power passing back into the magnetron by diverting them to a water load. The isolator is connected to a dual directional coupler that measures the forward and reflected MW power and displays them at a power meter. In this system, microwaves are tuned using an automatic S-TEAM Econotuner (2.45 GHz, max operating power 1 kW), which consists of three stubs that can move up and down all the way through the waveguide. The position of these stubs is controlled by computer software that is designed to maximise the amount of power absorbed by the sample and, hence, minimise the reflected power. The applicator is where the load is positioned, contained within a quartz tube. A quartz window is placed between the applicator and the autotuner to avoid external bodies reaching the magnetron which could otherwise damage it. The system is then terminated by a sliding short circuit that controls the location of the

antinode of the standing wave. All components were connected through 43.3 mm x 86.6 mm WR340 rectangular waveguide and supplied by Gerling Applied Engineering Inc. USA (with the exception of the autotuner as detailed above). The width of the waveguide is equal to  $\lambda/2$  (where  $\lambda$  is the wavelength of the microwave radiation) so that only one mode of microwave radiation can exist.

## 2.2 Synthesis and Processing

This section describes the reagents used and the general procedure for sample preparation as well as the experimental set-up adopted for the synthesis of vanadium carbide (Chapter 3), zirconium carbide and hafnium carbide (Chapter 4) and zirconium nitride (Chapter 5) using multi- and single-mode cavity MW reactors.

### 2.2.1 Sample Preparation

The synthesis of the transition metal carbides ( $V_8C_7$ , ZrC and HfC) was attempted using both elemental metal powders and the corresponding oxides as a source of the transition metal and graphite as a source of carbon atoms. The synthesis of zirconium nitride, ZrN, was only attempted using zirconium metal powder under flowing gas ( $N_2$  or  $NH_3$ ) as experiments using zirconium dioxide,  $ZrO_2$ , led to no reaction with nitrogen or ammonia gas under the experimental conditions used (see Chapter 5). All the starting materials used in this work were of high purity [Table 2-1] and were analysed by powder X-ray diffraction prior to their use. Table 2-2 lists the attempted reactions and the respective stoichiometric ratios used.

For the preparation of the transition metal carbides (TMCs), the required stoichiometric amount of starting materials was weighed out and ground together in an agate mortar and pestle until a homogeneous mixture was obtained. The mixed starting materials (1 g for the metal powder plus graphite, 0.5 g for the metal oxides plus graphite, unless otherwise specified) were then introduced into an 8-mm pellet die and uniaxially cold pressed using a hydraulic press at 5 tonnes of pressure for 5 minutes. The so-obtained pellets were embedded into 0.35 g of graphite powder, which acts as a susceptor material, within a 10-mm inner diameter open quartz tube (transparent to MWs).

A slightly different sample preparation process was employed for the synthesis of zirconium nitride. Zirconium metal powder (0.3 g) was introduced into a 10-mm inner diameter open quartz tube. In this case, the graphite powder used as a susceptor was arranged

around the outside of the tube but not placed into the reaction vessel in direct contact with the starting material (see Section 2.2.2.1).

**Table 2-1** Manufacturer, purity and nominal particle size of the starting materials used.

<b>Reactant</b>	<b>Manufacturer</b>	<b>Purity</b>	<b>Particle size</b>
Graphite (C)	Sigma Aldrich	99.5 %	< 50 $\mu\text{m}$
Vanadium (V)	Alfa Aesar	99.5 %	< 44 $\mu\text{m}$
Vanadium pentoxide ( $\text{V}_2\text{O}_5$ )	Sigma Aldrich	99.6 %	Not provided
Zirconium (Zr)	Alfa Aesar	98.8 %, small Hf impurity	< 45 $\mu\text{m}$
Zirconium dioxide ( $\text{ZrO}_2$ )	M&B	99.6 %	Not provided
Hafnium (Hf)	Alfa Aesar	99.6 %, small Zr impurity	< 45 $\mu\text{m}$
Hafnium dioxide ( $\text{HfO}_2$ )	Alfa Aesar	99.9 %	Not provided

**Table 2-2** List of all the attempted reactions for the synthesis of transition metal carbides and nitrides.

<b>Attempted Reactions</b>	
<b>Metal reactants</b>	<b>Metal oxide reactants</b>
$8 \text{ V} + 7 \text{ C} \rightarrow \text{V}_8\text{C}_7$	$4 \text{ V}_2\text{O}_5 + 27 \text{ C} \rightarrow \text{V}_8\text{C}_7 + 20 \text{ CO}$
$\text{Zr} + \text{C} \rightarrow \text{ZrC}$	$\text{ZrO}_2 + 3 \text{ C} \rightarrow \text{ZrC} + 2 \text{ CO}$
$\text{Hf} + \text{C} \rightarrow \text{HfC}$	$\text{HfO}_2 + 3 \text{ C} \rightarrow \text{HfC} + 2 \text{ CO}$
$2 \text{ Zr} + \text{N}_2 \rightarrow 2 \text{ ZrN}$	—
$2 \text{ Zr} + 2 \text{ NH}_3 \rightarrow 2 \text{ ZrN} + 3 \text{ H}_2$	—

## 2.2.2 Synthesis Using a MMC Reactor

Synthesis experiments in a MMC microwave reactor were performed using sealed quartz tubes under flowing gas, which will be described in more detail in Section 2.2.2.1.

### 2.2.2.1 Experimental Set-up Using a Sealed Quartz Tube Under Flowing Gas

For the synthesis of the TMCs under flowing gas, a sample-containing quartz tube was capped with a Suba-seal® septum and sealed with Parafilm M®, subsequently to the sample preparation. Two syringes were inserted into the septum, to allow the inert gas (Ar, BOC, purity 99.998%) to be delivered into and flow out of the system. The reaction tube was then fed through a stainless steel tube and collar fitted to the ceiling of a modified domestic microwave oven to allow access to the cavity. A 12-mm hole was previously drilled to align with the empirically determined hot-spot. The function of the steel tube + collar is to avoid possible microwave leakage which could otherwise be harmful to users. The quartz tube was placed in the center of a beaker containing silica flour within the cavity. Figure 2-6 and Figure 2-7 provide a schematic illustration and a photograph, respectively, of this reaction set-up.

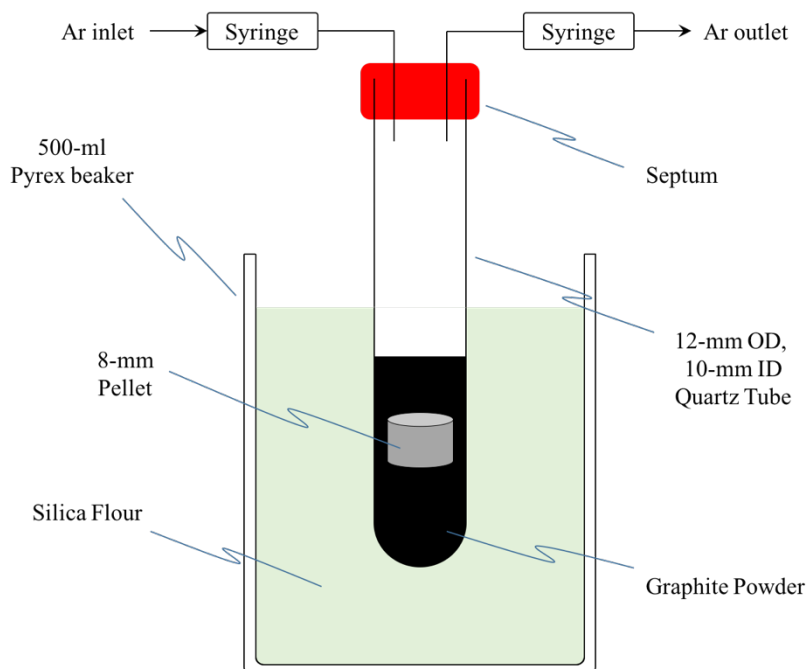


**Figure 2-6** Schematic illustration of the reaction set-up under flowing gas using a capped and sealed quartz tube in an MMC microwave reactor for the synthesis of TMCs.

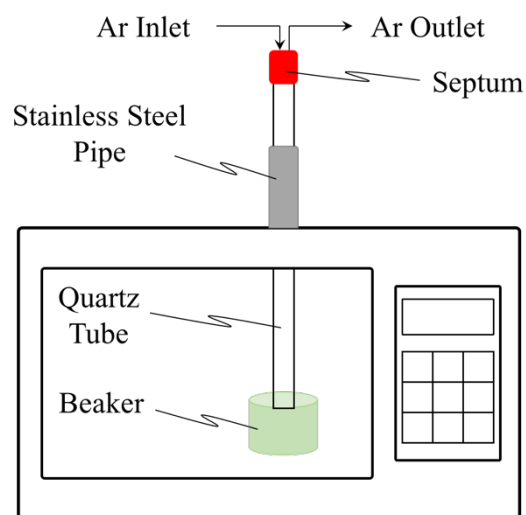


**Figure 2-7** Photograph (*left*) and diagram (*right*) of the reaction set-up under flowing gas using a capped and sealed quartz tube in an MMC microwave reactor for the synthesis of TMCs.

The synthesis of zirconium nitride involved the use of a slightly different set-up in which graphite powder susceptor was placed outside of the reaction vessel replacing the silica flour in the above configuration. After the initial sample preparation, a capped and sealed quartz tube was fed through the stainless steel tube + collar and placed in the center of an alumina crucible containing the susceptor graphite powder, in turn located on a refractory fire brick. Two syringes were inserted into the septum to act as gas inlet and outlet respectively [Figure 2-8 and Figure 2-9] and either nitrogen (BOC, oxygen free) or ammonia (BOC, anhydrous, purity 99.98%) gas was supplied to the sample.

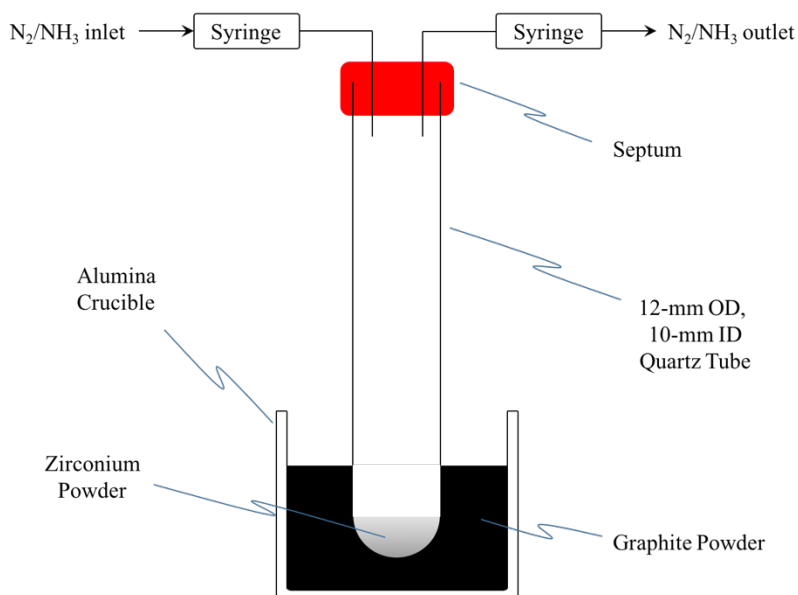


**Figure 2-8** Schematic illustration of the reaction set-up under flowing gas using a capped and sealed quartz tube in an MMC microwave reactor for the synthesis of zirconium nitride.

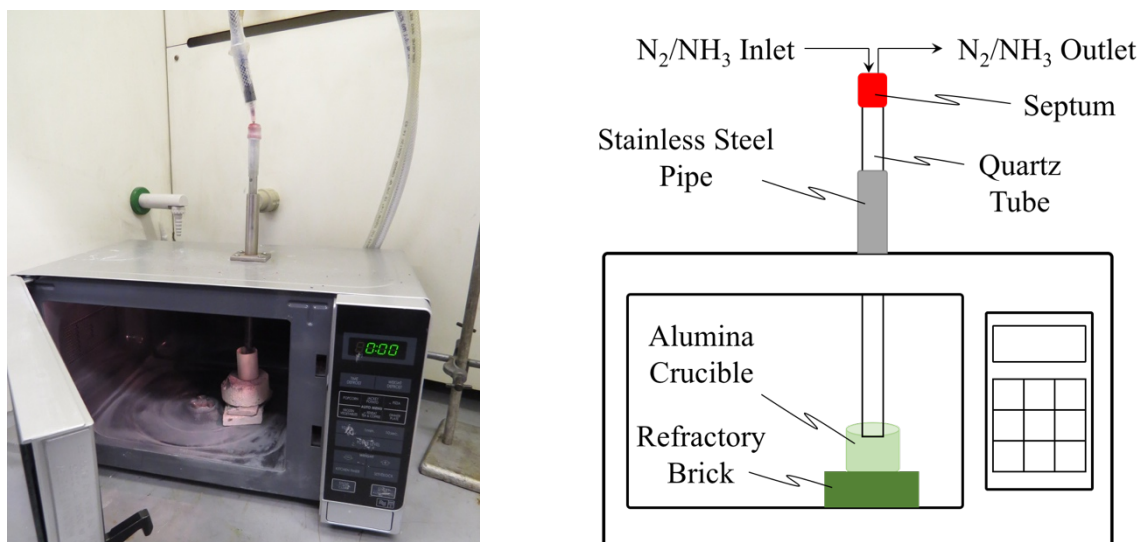


**Figure 2-9** Photograph (*left*) and diagram (*right*) of the reaction set-up under flowing gas using a capped and sealed quartz tube in an MMC microwave reactor for the synthesis of zirconium nitride.

### 2.2.3 Synthesis Using a SMC Reactor

Synthesis experiments in a SMC microwave reactor were conducted using a broadly similar experimental set-up to that used for synthesis in a MMC reactor with the main difference being that no surrounding environment of either  $\text{SiO}_2$  (as thermal insulator) or graphite (as MW susceptor) was required.

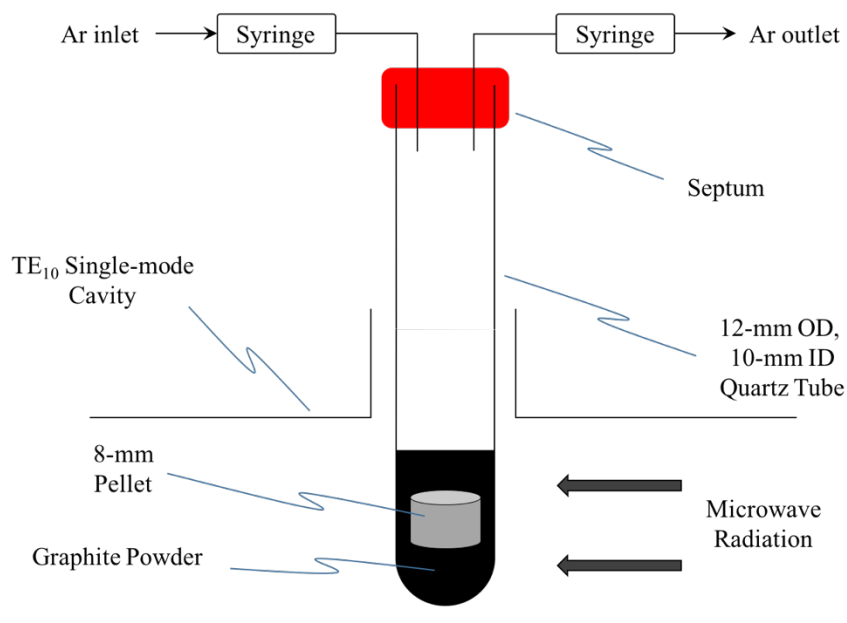


**Figure 2-10** Schematic illustration of the reaction set-up under flowing gas using a capped and sealed quartz tube in an SMC microwave reactor.

After the initial sample preparation, the sealed quartz tube was positioned within the waveguide, held in place by a clamp stand positioned next to the SMC applicator. A schematic illustration and photographs of this set-up is illustrated in Figure 2-10 and Figure 2-11.



**Figure 2-11** Photographs of the reaction set-up under flowing gas using a capped and sealed quartz tube in an SMC microwave reactor.

## 2.3 Characterization Techniques

In this section, the basic concepts of the analytical techniques used throughout this research project are presented. Initially, a theoretical background on crystallography is introduced, followed by information on Powder X-ray Diffraction [2.3.1] and Neutron Diffraction [2.3.2] which were used to identify product phases as well as to determine the crystal structure of the materials prepared in this thesis by Rietveld refinement methods [2.3.3]. The sample morphology and elemental composition was investigated by Scanning Electron Microscopy coupled with Energy-dispersive X-ray Spectroscopy, discussed in Section 2.3.4. Additional characterization was performed by Raman Spectroscopy [2.3.5] and surface analysis was conducted by X-ray Photoelectron Spectroscopy [2.3.6].

## 2.3.1 Powder X-ray Diffraction

Powder X-ray Diffraction (PXRD) is an analytical technique which uses X-rays for the structural characterization of powdered crystalline materials and provides a variety of useful information, including the phase(s) present in the sample, the unit cell dimensions of a particular structure and the average bulk composition in terms of the mass or molar fractions of crystalline phases. This rapid and non-destructive technique is used across several scientific disciplines, such as material science, chemistry, physics, engineering, etc. and was the main method used for the characterization of samples in this thesis.

### 2.3.1.1 Crystallography

Before describing diffraction in detail and discussing how this phenomenon occurs, it is essential to first consider the fundamentals of crystallography.<sup>15-17</sup> Crystallography is the experimental science of determining the arrangement of atoms in crystalline solids. A crystal is a solid material constituted of atoms, molecules or ions arranged in a highly ordered and periodic pattern. The crystal structure is characterized by the smallest symmetric divisible unit, called the unit cell, which make up the crystal if repeated by simple translation in three dimensions. Figure 2-12 illustrates a simple unit cell which can be identified by three vectors (or lengths)  $a$ ,  $b$  and  $c$  and the interaxial angles between them  $\alpha$ ,  $\beta$  and  $\gamma$ .

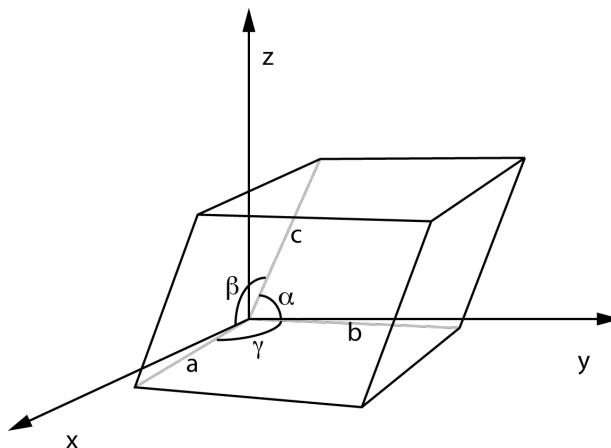


**Figure 2-12** General representation of a simple unit cell showing cell lengths and angles.<sup>18</sup>

Seven crystal systems exist in total (cubic, hexagonal, tetragonal, trigonal, orthorhombic, monoclinic and triclinic), shown in Table 2-3, which are classified according to their fundamental symmetry operations.<sup>19</sup>

The number of lattice points,  $N$ , within a unit cell is given by the following equation:

$$N = N_i + \frac{N_f}{2} + \frac{N_c}{8} + \frac{N_e}{4} \quad (2-1)$$

where  $N_i$ ,  $N_f$ ,  $N_c$  and  $N_e$  are the number of lattice points in cell interior, in cell faces, in cell corners and on cell edges, respectively.

**Table 2-3** The seven crystal systems and corresponding Bravais lattices.<sup>20</sup>

<b>System</b>	<b>Axial lengths and angles</b>	<b>Bravais lattice</b>	<b>Lattice centering</b>
Cubic	Three equal axis at right angles $a = b = c$ , $\alpha = \beta = \gamma = 90^\circ$	Primitive	<i>P</i>
		Body-centered	<i>I</i>
		Face-centered	<i>F</i>
Tetragonal	Three axis at right angles, two equals $a = b \neq c$ , $\alpha = \beta = \gamma = 90^\circ$	Primitive	<i>P</i>
		Body-centered	<i>I</i>
Orthorombic	Three unequal axis at right angles $a \neq b \neq c$ , $\alpha = \beta = \gamma = 90^\circ$	Primitive	<i>P</i>
		Body-centered	<i>I</i>
		Base-centered	<i>C</i>
		Face-centered	<i>F</i>
Trigonal	Three equal axis, equally inclined $a = b = c$ , $\alpha = \beta = \gamma \neq 90^\circ$	Primitive	<i>P</i>
Hexagonal	Two equal coplanar axes at $120^\circ$ , third axis at right angles $a = b \neq c$ , $\alpha = \beta = 90^\circ$ , $\gamma = 120^\circ$	Primitive	<i>P</i>
Monoclinic	Three unequal axes, one pair not at right angles $a \neq b \neq c$ , $\alpha \neq \gamma = 90^\circ \neq \beta$	Primitive	<i>P</i>
		Base-centered	<i>C</i>
Triclinic	Three unequal axes, unequally inclined and none at right angles $a \neq b \neq c$ , $\alpha \neq \beta \neq \gamma \neq 90^\circ$	Primitive	<i>P</i>

Four main different centering types [Figure 2-13] exists as follows: primitive (*P*), base-centered (*A*, *B* or *C*), body-centered (*I*) and face-centered (*F*).<sup>19</sup> In the primitive centering type, there are lattice points on the cell corners only, giving one lattice point per unit cell. The base-centered type has lattice points on the cell corners as well as identical points at the



### 2.3.1.2 Introduction to Diffraction

X-rays are electromagnetic radiation with wavelength ranging from 0.01 to 10 nm and frequencies from  $3 \times 10^{16}$  to  $3 \times 10^{19}$  Hz. The diffraction of X-rays occurs because their wavelength is of the same order of magnitude as the interatomic distances in crystals, ranging from  $\sim 0.5$  to  $\sim 2.5$  Å.<sup>15</sup> X-rays are elastically scattered spherically by the electrons of atoms as these are forced to oscillate with the same frequency as the electric-field component of the incident wave.

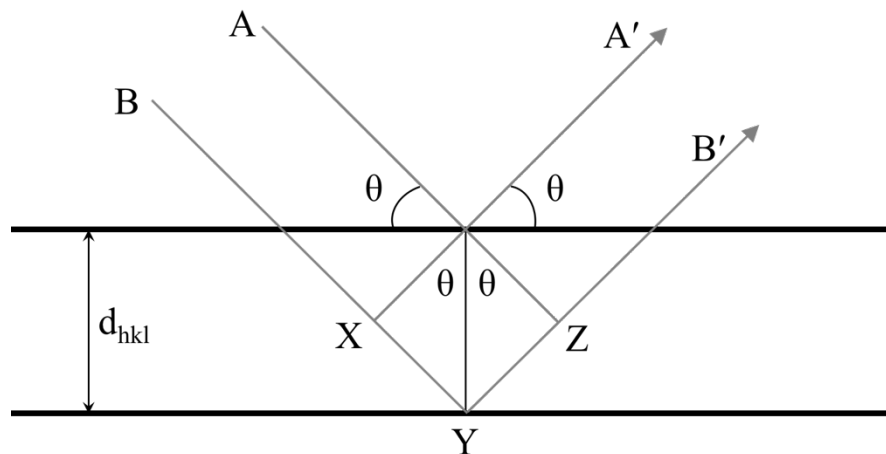


**Figure 2-14** Schematic showing diffraction of X-rays on parallel crystallographic planes within a crystal. A and B are two incident X-ray beams, A' and B' are the corresponding diffracted X-ray beams. The distance between crystallographic planes is  $d_{hkl}$  and  $\theta$  is the angle between the plane and the incident beam.

William Lawrence Bragg, a British physicist and X-ray crystallographer, proposed a law (referred to as Bragg's Law) in 1913 according to which crystals can be thought of as a set of parallel crystallographic planes separated by a constant parameter  $d$  and defined by their Miller indices,  $hkl$ .<sup>22</sup> A diffracted X-ray beam is observed only when the reflections of the incident waves from adjacent crystallographic planes are in phase and interfere constructively [Figure 2-14]. Conversely, if the scattered waves are out of phase, they interfere destructively cancelling each other and no diffracted peak is observed. In other words, the reflections of the incident beams add up in phase when their pathlengths differ by an integer multiple of the wavelength. This is mathematically explained by the following equation:

$$n\lambda = 2d \sin \theta \quad (2-2)$$

where  $n$  is an integer,  $\lambda$  is the wavelength of the incident beam,  $d$  is the interplanar spacing and  $\theta$  is the angle of incident radiation. In crystals, the conditions of Bragg's law are therefore met only at specific diffraction angles which depend upon unit cell type and size as well as the inter-atomic plane spacing.

For powdered (polycrystalline) materials, the random orientation of the crystallites gives rise to continuous cones of intensity of diffracted X-ray radiation (Debye-Scherrer cones) [Figure 2-15] and not to single narrow beams as for single crystals.

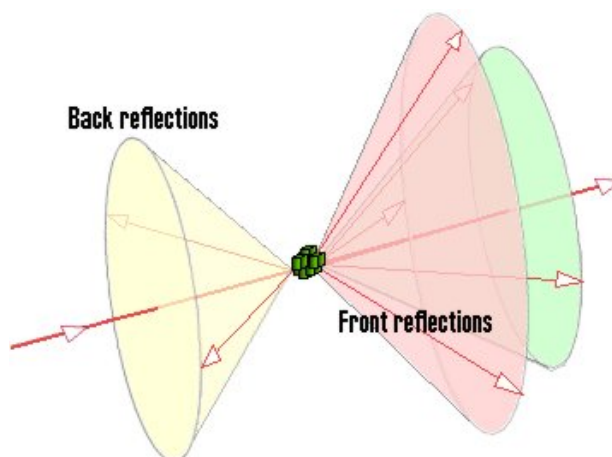


**Figure 2-15** Diffracted X-ray cones from a powder (polycrystalline) sample.<sup>23</sup>

### 2.3.1.3 Sample Preparation, Data Collection and Analysis

After microwave reaction, the pellets were taken from the reaction vessel and excess graphite carefully removed from the surface. The samples were subsequently ground with an agate mortar and pestle until a fine powder is obtained to ensure sample homogeneity and random orientation of crystallites. The resulting powder was then inserted into a circular hollow space on a planar glass sample holder (flat plate) and pressed level using a glass slide [Figure 2-16]. A flattened sample surface is essential for the success of a PXRD structural analysis to prevent displacement errors (often included within the zero-shift error) caused when the sample sits above or below the surface of the sample holder.

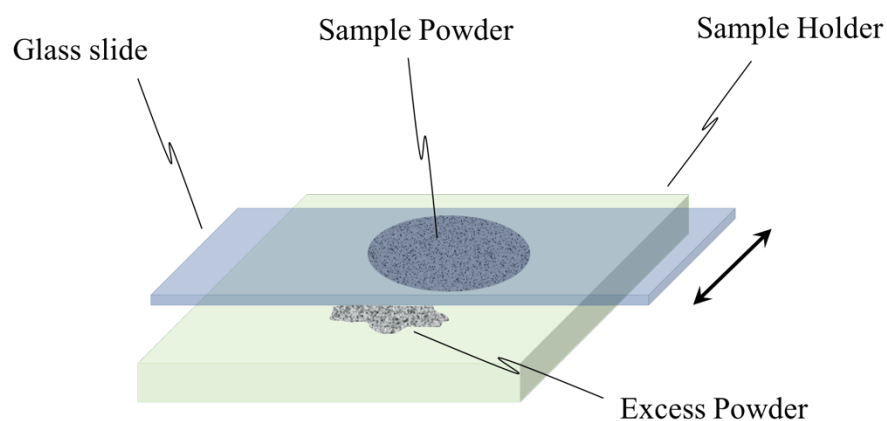


**Figure 2-16** Schematic illustration of a PXRd flat plate sample holder.

All PXRd measurements in this thesis were collected using an X'pert PRO MPD diffractometer in Bragg-Brentano ( $\theta$ - $2\theta$ ) geometry using a Cu  $K\alpha_1$  radiation X-ray source ( $\lambda = 1.5418 \text{ \AA}$ ) and an X'celerator solid-state detector. Figure 2-17 illustrates a schematic of the Bragg-Brentano geometry. In this reflection geometry, the source is fixed (stationary) and the sample and detector are rotated by  $\theta$  and  $2\theta$ , respectively. The X-ray tube operates at a standard power of 40 kV and current of 40 mA. The incident X-ray beam was collimated using a 10-mm beam mask. In order to prevent the divergence of the incident X-ray beam, a series of slits were used such as 0.04 radian Soller slits, a  $1/2^\circ$  divergence slit and a  $1/2^\circ$  anti-scatter slit.

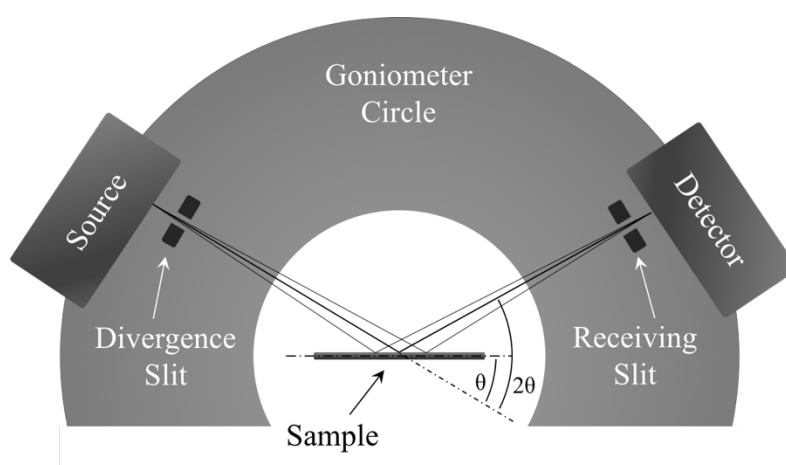


**Figure 2-17** Setup of the diffractometer in a Bragg-Brentano geometry.

For phase identification, PXRd data were collected for 1 h between  $10^\circ \leq 2\theta \leq 85^\circ$ , with a step size of  $0.017^\circ 2\theta$ . For structural refinement, high quality PXRd data were obtained collecting for 12 h scan from  $10^\circ \leq 2\theta \leq 110^\circ$ , with a step size of  $0.017^\circ 2\theta$ .

PXRD patterns were displayed as plots of intensity against  $2\theta$  in PowderCell 2.3 software.<sup>24</sup> This software was used to identify the phases present by comparing PXRD patterns with those of known structures downloaded from the Inorganic Crystal Structure Database (ICSD).<sup>25</sup> The crystal system and unit cell parameters were found by indexing using CELREF (CELREF: Graphical Unit Cell Refinement).<sup>26</sup> Structure refinement by the Rietveld method [Section 2.3.3] was performed on the 12-hour scans using the General Structure Analysis System (GSAS) software and the associated graphical user interface (EXPGUI).<sup>27,28</sup>

### 2.3.2 Powder Neutron Diffraction

Powder Neutron Diffraction (PND) is similar to PXRD in the sense that they are both diffraction experiments used to determine the crystal structure of crystalline materials and the data obtained using the former is complementary to those obtained using the latter. This is due to the different scattering properties of neutrons as compared to X-rays. As previously discussed in Section 2.3.1.2, X-rays interact with the electron cloud surrounding each atoms which means that heavier atoms (large atomic number,  $Z$ ) diffract X-rays more intensely than lighter atoms (small atomic number). This technique is therefore unsuitable for the study of light elements (such as hydrogen with only one valence electron). Conversely, neutrons are scattered by atomic nuclei and can be used to study structures containing low atomic number materials. Moreover, each isotope contributes differently to the diffracted neutron intensity meaning that a distinction can be observed between, for example, protium ( $^1\text{H}$ ) and deuterium ( $^2\text{H}$ ), for instance.

Unfortunately, it is not possible to produce intense neutron beams in the laboratory. Two main methods are currently used for the production of neutron beams with an acceptable intensity: a nuclear reactor and a spallation source. In a nuclear reactor, an intense flux of neutrons is produced by fission of enriched  $^{235}\text{U}$ .<sup>29</sup> This method leads to the production of the so-called “thermal” neutrons with a wavelength ranging from 1 to 2 Å. However, most neutron diffraction experiments require a monochromated beam of neutrons which will necessarily implicate a loss of most of the neutron flux. The Institut Laue-Langevin (ILL) is an example of a nuclear reactor source for constant wavelength diffraction and is situated in Grenoble, France. In this facility, the diffracted neutrons are detected by a bank of 25  $^3\text{He}$  counters at 5 atm and counted and recorded as a function of the angles through which they were scattered by the sample.

At a spallation source, the neutron production process typically begins with negatively charged hydride ions,  $H^-$ , which are accelerated in a linear accelerator (linac).<sup>29</sup> A high-energy proton beam is produced by firing the  $H^-$  ions through a gold foil which removes the electrons from the ions. This beam bombards a heavy metal target (generally tantalum, Ta) which generates a pulse of neutrons which have too short a wavelength for diffraction experiments and therefore must be slowed down by ambient temperature water moderators. Spallation sources use the neutron time-of-flight scattering technique which measures the time (in  $\mu s$ ),  $t_f$ , taken for a neutron to travel a fixed path length,  $L$ , from the source to the detectors via the sample. Combining Bragg's law [Equation (2-2)] and the de Broglie's relationship [Equation (2-3)] yields Equation (2-4).<sup>30</sup>

$$\lambda = \frac{h}{p} = \frac{h}{mv} \quad (2-3)$$

$$n\lambda = n \frac{h}{mv} = n \frac{ht_f}{mL} = 2d \sin \theta \quad (2-4)$$

where  $m$  is the mass of a neutron ( $1.67 \times 10^{-27}$  kg),  $v$  is the velocity of a neutron,  $p$  is the momentum and  $h$  is the Planck's constant ( $6.626176 \times 10^{-34}$  J s). Substitution for  $h$  and  $m$  gives:<sup>30</sup>

$$t_f = 2dL \frac{m}{h} \sin \theta = 505.56dL \sin \theta \quad (2-5)$$

$$d = \frac{h}{2mL \sin \theta} t_f = \frac{1.977 \times 10^{-3}}{L \sin \theta} t_f \quad (2-6)$$

### 2.3.2.1 The POLARIS Powder Diffractometer at ISIS

All PND experiments in this thesis were conducted at the ISIS pulsed neutron and muon source at the Rutherford Appleton Laboratory (RAL) in Oxfordshire using the POLARIS instrument. The POLARIS diffractometer at ISIS is a high intensity, medium resolution time of flight powder diffractometer [Figure 2-18] at the ISIS spallation source.<sup>30</sup> It has a primary flight path of 14 m and a large stainless steel vacuum vessel (~20,000 litres). The instrument consists of six detector banks: bank 1 (very low angle,  $2\theta$  range 6-14°), bank 2 (low angle,  $2\theta$  range 19-34°), bank 3 (low angle,  $2\theta$  range 40-67°), bank 4 (90 degrees,  $2\theta$  range 75-113°), bank 5 (back scattering,  $2\theta$  range 135-143°) and bank 6 (back scattering,  $2\theta$  range 146-168°).

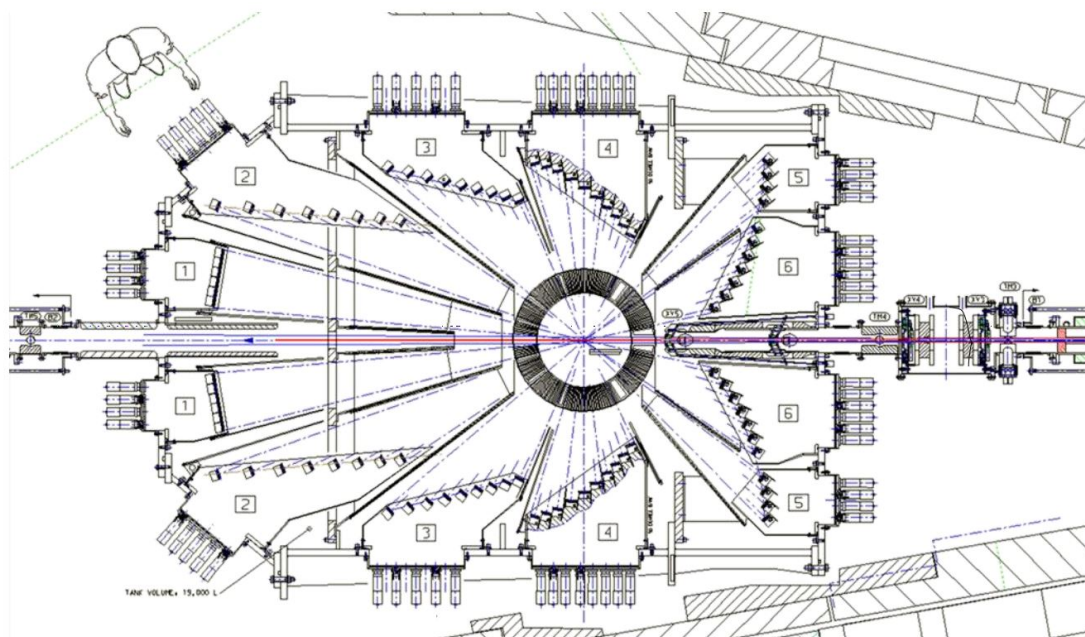


**Figure 2-18** Schematic of the POLARIS diffractometer at ISIS. The numbers indicate the different detector banks.<sup>31</sup>

### 2.3.2.2 Sample Preparation, Data Collection and Analysis

The preparation of the samples for PND analysis were performed according to the appropriate MMC microwave method described in Section 2.2.2.1.

Powdered samples between 1 and 2 g were placed into a 6-mm vanadium sample can which was then attached to a sample rod and lowered into the sample tank of the diffractometer. PND data were collected for a run duration of 350  $\mu\text{A}\cdot\text{h}$  proton beam current (approx. 1.5 hours) for both vanadium carbide and zirconium carbide samples.

Structural refinement by the Rietveld method [Section 2.3.3] was performed on the PND scans using the General Structure Analysis System (GSAS) and the associated graphical user interface (EXPGUI).<sup>27,28</sup>

### 2.3.3 Rietveld Refinement

Rietveld refinement technique was originally developed by Hugo M. Rietveld in the late 1960s for constant wavelength neutron diffraction<sup>32,33</sup> and was subsequently also employed for powder X-ray diffraction data. In this thesis, Rietveld refinement has been used with both PXRD and PND data [Chapter 3 and 4].

Rietveld refinement is a full profile structure method that allows detailed structural information to be extracted from diffraction data. This method is based on a least squares approach and refinement is performed by minimizing the difference in intensity between an experimental diffraction pattern (observed data) and a proposed model for the structure and instrumental parameters (calculated data).<sup>34</sup> The overall goal of a Rietveld refinement is therefore the minimization of the residual function,  $M$ , which is given by the following equation:

$$M = \sum_i w_i (y_i^{obs} - y_i^{calc})^2 \quad (2-7)$$

where  $w_i$  is a weighting factor given by  $1/y_i^{obs}$ ,  $y_i^{obs}$  and  $y_i^{calc}$  are the observed and calculated intensity, respectively, at the  $i^{\text{th}}$  step.

Firstly, a good starting model and a high-quality diffraction pattern need to be used in order to achieve a successful refinement. Scale factors are refined and background parameters are subsequently introduced either manually or calculated from a polynomial expression. For the majority of refinements in this thesis, a shifted Chebyshev function (function type one within GSAS) or a reciprocal interpolation function (function type eight within GSAS) were used to fit the pattern background. The diffraction peak positions are then accurately determined by varying lattice parameters and zero-point error correction (sample displacement from diffractometer centre – see Section 2.3.1.3). Peak intensities are fitted by refining peak shape parameters and varying atomic positions. Unlike constant wavelength PND which produces near Gaussian peaks, time-of-flight PND and PXRD require a combination of Gaussian,  $G$  [Equation (2-8)], and Lorentzian,  $L$  [Equation (2-9)], functions to define the pattern peak shape. This is known as a pseudo-Voigt combination function,  $pV$ , given by Equation (2-10):

$$G = \frac{(4 \ln 2)^{1/2}}{H_k \sqrt{\pi}} \exp\left(\frac{-4 \ln 2 (2\theta_i - 2\theta_k)^2}{H_k^2}\right) \quad (2-8)$$

$$L = \frac{2}{\pi H_k} \left/ \left[ 1 + 4 \frac{(2\theta_i - 2\theta_k)^2}{H_k^2} \right] \right. \quad (2-9)$$

$$pV = \eta L + (1 - \eta)G \quad (2-10)$$

where  $\eta$  is a mixing parameter and  $H_k$  is the peak half width of the  $k^{\text{th}}$  Bragg reflection. Both Gaussian and Lorentzian functions make use of this term which is given by:

$$H^2 = U \tan^2 \theta + V \tan \theta + W \quad (2-11)$$

where  $U$ ,  $V$  and  $W$  are refinable terms that represents the halfwidth (Cagliotti) parameters. The intensity,  $y_i$ , at each point  $i$  in the diffraction pattern is given by:

$$y_i^{calc} = s \sum_k L_k |F_k|^2 \phi(2\theta_i - 2\theta_k) P_k A + y_i^{bg} \quad (2-12)$$

where  $s$  is the scale factor,  $k$  represents a Bragg reflection defined by its Miller indices,  $L_k$  contains Lorentz polarisation and multiplicity factors,  $F_k$  is the structure factor for the  $k^{\text{th}}$  Bragg reflection,  $P_k$  is the preferred orientation function,  $A$  is the absorption factor and  $y_i^{bg}$  is the background intensity for the  $i^{\text{th}}$  step.

Intensity mismatches may still be observed due to the thermal motion of the atoms within the sample in which case temperature factors may be refined too.

The R-factors are the best way to indicate the quality of fit for a Rietveld refinement and offer a quantitative comparison between the observed data and the calculated model. These include:  $R$ -profile ( $R_p$ ) [Equation (2-13)],  $R$ -weighted profile ( $R_{wp}$ ) [Equation (2-14)],  $R$ -Bragg ( $R_B$ ) [Equation (2-15)],  $R$ -Intensity ( $R_I$ ) [Equation (2-16)] and  $R$ -expected ( $R_e$ ) [Equation (2-17)].

$$R_p = \frac{\sum |y_i - y_{ci}|}{\sum y_i} \quad (2-13)$$

$$R_{wp} = \left\{ \frac{\sum w_i (y_i - y_{ci})^2}{\sum w_i (y_i)^2} \right\}^{1/2} \quad (2-14)$$

$$R_B = \frac{\sum |I_k(obs) - I_k(calc)|}{\sum I_k(obs)} \quad (2-15)$$

$$R_I = \frac{\sum |I_k^2(obs) - I_k^2(calc)|}{\sum I_k^2(obs)} \quad (2-16)$$

$$R_e = \left\{ \frac{(N - P + C)}{\sum w_i (y_i)} \right\}^{1/2} \quad (2-17)$$

where  $I_K(obs)$  and  $I_K(calc)$  are the observed and calculated Bragg intensities of reflection  $K$ , respectively,  $N$  is the number of observations,  $P$  is the number of independently refined parameters and  $C$  is the number of constraints. In this thesis, the  $R$ -factors  $R_p$  and  $R_{wp}$  are always used, being the most mathematically important indicators for the evaluation of a refinement.<sup>35</sup> Another factor used in this work and quoted quite often in the literature is the goodness-of-fit,  $\chi^2$  (chi-squared), which is given by:

$$\chi^2 = \left(\frac{R_{wp}}{R_e}\right)^2 = \left(\frac{\sum w_i (y_i - y_{ci})^2}{(N - P + C)}\right) \quad (2-18)$$

For an ideal perfect fit, the goodness-of-fit approaches 1. However, all these parameters strictly depend on the conditions of the data collected and only offer a suggestion of the quality of the refinement. Therefore, a visual inspection of the observed and calculated patterns together with reasonable bond lengths and angles often represents the most objective way to judge a structure model.

### **2.3.4 Scanning Electron Microscopy coupled with Energy-dispersive X-ray**

Scanning Electron Microscopy (SEM) is an analytical technique used to study the surface feature, morphology and texture of solid objects. A common scanning electron microscope uses a high-energy electron beam focused on the sample to generate several types of signals which are then processed to provide a three-dimensional representation of the sample.

Figure 2-19 illustrates the basic component of a SEM microscope. The electron beam is produced by heating a metallic (usually tungsten) filament in an electron gun which passes through a series of electromagnetic lenses so that it is focused on to a portion of the sample. By hitting the sample, the incident beam causes the ejection of the following species: backscattered electrons (BSEs), secondary electrons (SEs), Auger electrons, photons of characteristic X-rays and cathodoluminescence.<sup>36</sup> BSEs are elastically scattered electrons which originates when an electron in the incident beam circles an atomic nucleus in the sample and is reflected out of the specimen. SEs are the product of the ionization resulting from the interaction of the incident beam with the loosely bound outer-shell electrons. Auger electrons originate when an inner-shell electron is ejected by the incident beam and an outer-

shell electron fills the hole, transferring the difference in energy to a second electron which is subsequently ejected as an Auger electron. Photons of characteristic X-rays are originated when an inner-shell electron in the sample is removed by the incident beam and an outer-shell electron fills the vacancy, releasing the energy in the form of X-rays.

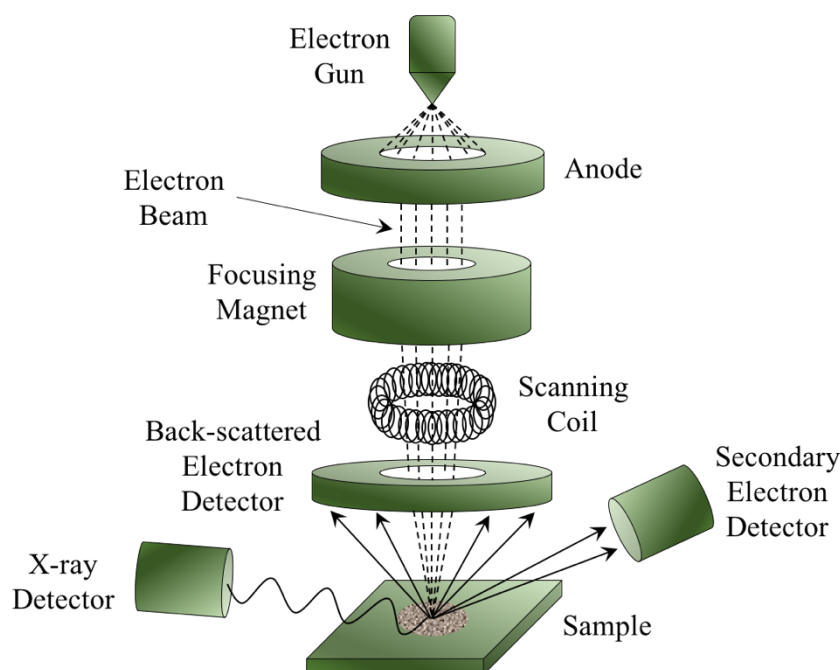


**Figure 2-19** Schematic representation of a SEM microscope.

The backscattered and secondary electrons are then collected by detectors and an image is produced by converting them into signals.<sup>37</sup> BSE images can provide information about the chemical composition of the sample as the intensity of the BSE signal is strongly related to the atomic number ( $Z$ ) of the specimen. The SEs provide the image contrast since these emerge from more superficial locations with respect to BSEs.

Energy-dispersive X-ray Spectroscopy (EDX) is an elemental microanalysis technique that is often used together with SEM. EDX relies on the principle that each element has known characteristic X-ray emission spectra and detects the relative abundance of these emitted photons versus their energy to obtain information about the elemental composition of the sample at specific areas.<sup>38</sup> The drawback of EDX is that, like XRD, the analysis of light elements presents a real challenge and cannot be detected efficiently.

Sample morphology and composition were studied using the Philips XL30 ESEM which was run in high vacuum mode with an applied accelerating voltage of 20 kV and a working distance of 10 mm for imaging. In order to achieve a better quality of the collected images, the powdered sample was dispersed onto a carbon tab stuck on an aluminum stab and

subsequently sputter-coated with a 10 nm layer of gold/palladium alloy to prevent charge building up on the sample surface of the sample. The sample was subsequently loaded into the instrument chamber and SEM micrographs collected. An Oxford Instruments X-act spectrometer using a silicon drift detector was coupled to this microscope for EDX analysis. The instrument was calibrated using the INCA EDX analysis software (Cu used for all calibration measurements).

### 2.3.5 Raman Spectroscopy

Raman spectroscopy is a vibrational spectroscopy technique that provides information about vibrational and rotational transitions in a system. The Raman effect was first observed by and named after the Indian physicist C. V. Raman, who was awarded the Nobel Prize in physics in 1930 for his discovery.<sup>39</sup> As each molecule has a different set of vibrational energy levels, this technique is widely used in chemistry for sample identification. In a Raman spectrometer, a laser beam in the UV-region in the electromagnetic spectrum is focused through a lens on to a sample. The very weak scattered light is deflected by a curved mirror and focused so that it can be measured by a very sensitive detector [Figure 2-20]. A Raman spectrum of the sample is then obtained by plotting the intensity of the scattered light versus the wavenumbers.

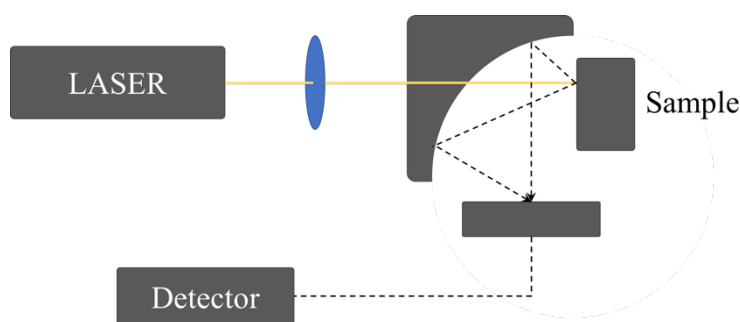


**Figure 2-20** Typical optical configuration in a Raman spectrometer.<sup>40</sup>

When the laser beam hits the sample, three types of light scattering are produced: Rayleigh scattering, Stokes scattering and Anti-stokes scattering.<sup>41</sup> Rayleigh scattering occurs when a photon is absorbed to a higher virtual level and is subsequently scattered back to the initial level, retaining the incident frequency and energy (elastic scattering). Stokes scattering occurs when the scattered photon has a lower energy and frequency (higher wavelength) than that of the initial photon (inelastic scattering). Anti-Stokes scattering

occurs when the scattered photon has a higher energy and frequency (lower wavelength) than that of the initial photon (inelastic scattering).

The three processes described above are illustrated in Figure 2-21. Rayleigh scattering is the predominant mode of scattering. Raman scattering, which include Stokes and Anti-Stokes scattering, is usually much weaker. Only a small portion of photons (one every thirty million) is indeed inelastically scattered.

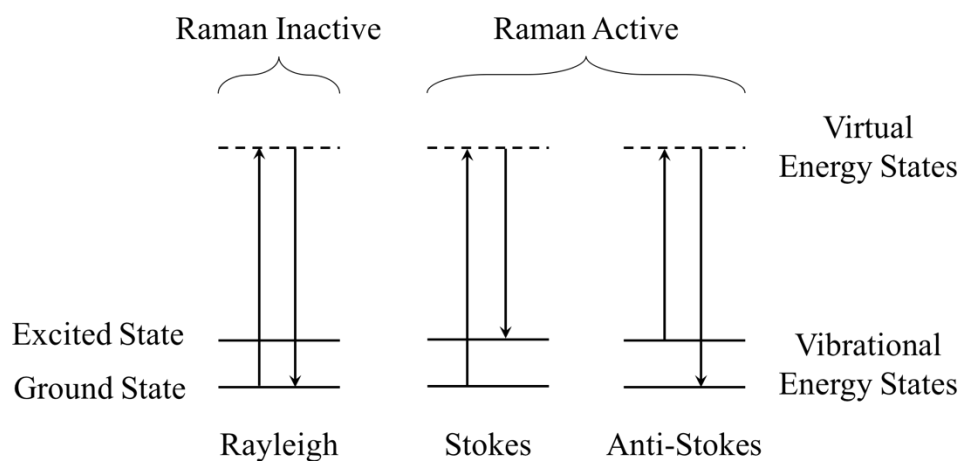


**Figure 2-21** Rayleigh, Stokes and Anti-Stokes scattering in Raman spectroscopy.

Due to the different interactions between the incident electromagnetic wave and the vibrational energy levels of the molecule within the sample, the outgoing photon will scatter with an increased (Stokes scattering) or decreased (Anti-Stokes scattering) energy. The molecule remains in the “excited” state only for a very brief period of time before emitting the photon and returning to the original vibrational level.<sup>41</sup> The primary selection rule for Raman spectroscopy is that the molecular polarizability must change during the molecular vibration ( $\Delta J = 0, \pm 2$ ).

Prior to Raman measurements, samples were prepared by placing a small amount of powder on a glass slide and flattening it with the aid of a second glass slide. The sample was then inserted into the Raman spectrometer, and after adjusting the focus of the microscope lens onto the sample, a Raman spectrum collected.

The Raman spectrometer used for all analysis conducted in this work was a Horiba Jobin Yvon Raman LabRam instrument fitted with a Quantum Venus 532 nm green laser at 150 mW and a confocal microscope (600 grooves mm<sup>-1</sup> grating, 100  $\mu$ m aperture and 10% filter). Spectra were collected through a 50X objective lens in backscattering mode and a

Synapse CCD detector. The software used for data collection/analysis and manipulation was Horiba LabSpec and Microsoft Excel, respectively.

### 2.3.6 X-ray Photoelectron Spectroscopy

X-ray Photoelectron Spectroscopy (XPS) is a characterization technique used for analysing the surface of a material (typically up to a depth of 2-5 nm) and provides information about which elements are present at the surface and their chemical and electronic state.<sup>42,43</sup> This technique functions in a similar way to SEM/EDX (described in Section 2.3.4) and relies on the photoelectric effect [Figure 2-22]. When a sample is irradiated with a mono-energetic Al K $\alpha$  X-ray beam ( $E_{\text{photon}} = 1486.7$  eV), an electron could be ejected from the sample surface. This is called a photoelectron and its binding energy ( $E_{\text{binding}}$ ) is related to its kinetic energy once ejected ( $E_{\text{kinetic}}$ ) and the energy of the initial X-ray photon ( $E_{\text{photon}}$ ) and can be calculated from the following equation:<sup>44</sup>

$$E_{\text{binding}} = E_{\text{photon}} - E_{\text{kinetic}} - \Phi \quad (2-19)$$

where  $\Phi$  is the work function – the minimum thermodynamic energy required to remove an electron from the surface of a solid.

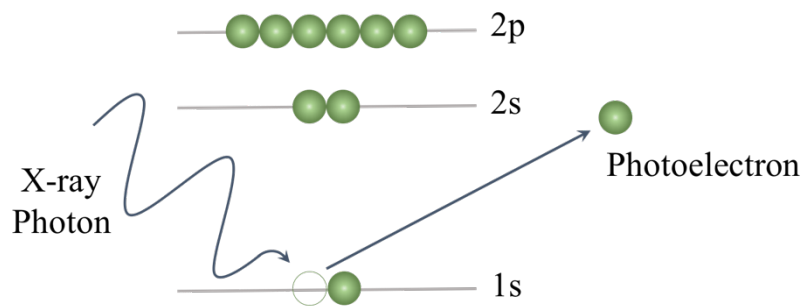


**Figure 2-22** Diagram showing the photoelectric effect. An incident X-ray photon excites the atom and a photoelectron is subsequently emitted.

The kinetic energy of the emitted electrons is measured by an electron analyser [Figure 2-23] and the XPS spectrum is obtained by plotting the intensity (number of photoelectrons versus time) versus the binding energy.

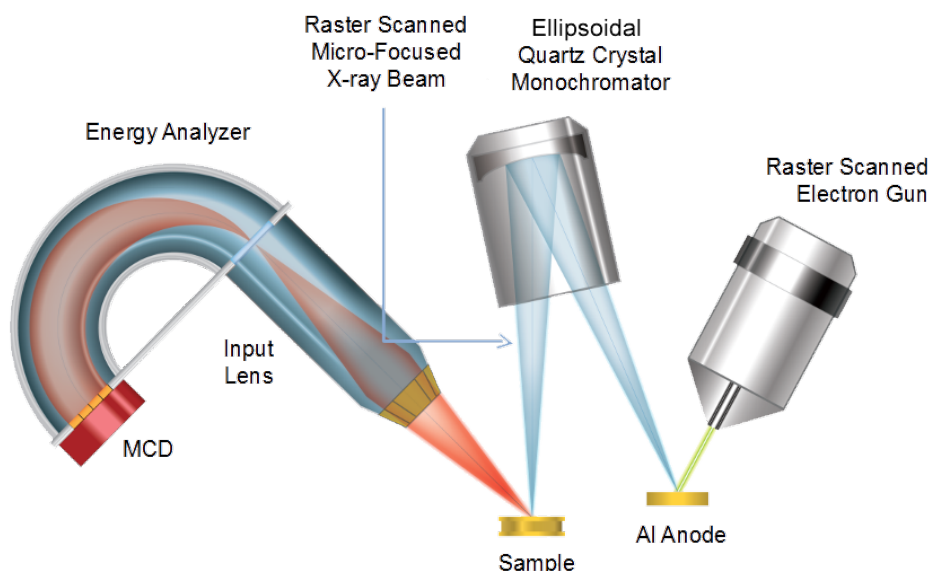


**Figure 2-23** Basic components of a monochromatic XPS system.<sup>45</sup>

Moreover, a few nanometers of surface can be removed from the specimen by Ar ion etching revealing a new layer that can subsequently be characterized by XPS. An ion beam is produced by bombarding a gas with electrons and then directed towards the sample, removing the superficial atoms.

Measurements were run with the assistance of Dr. Sina Saremi-Yarahmadi (Department of Materials, University of Loughborough) using a Thermo Scientific K-Alpha+ X-ray photoelectron spectrometer with monochromatic Al  $K\alpha$  radiation (1486.7 eV), an anode potential of 10 kV and a 20 mA filament emission current. Samples, still in the pellet form, were loaded onto carbon tabs stuck on aluminium stubs and loaded into the instruments for data analysis. Samples were etched using Argon ion sputtering to remove a few layers of surface allowing analysis deeper into the material.

## 2.4 Chapter Summary

This chapter has described the key theoretical concepts and experimental methods used in this thesis. Sample heating was either by single- or multi-mode microwave cavity and characterization was conducted primarily by PXRD (Section 2.3.1), PND (Section 2.3.2), SEM/EDX (Section 2.3.4), Raman spectroscopy (Section 2.3.5) and XPS (Section 2.3.6).

## 2.5 References

1. Boot, H. A. H. & Randall, J. T. Historical notes on the cavity magnetron. *IEEE Trans. Electron Devices* **23**, 51–70 (1976).
2. Hull, A. W. The magnetron. *J. Am. Inst. Electr. Eng.* **40**, 715–723 (1921).
3. Thostenson, E. T. & Chou, T. W. Microwave processing: fundamentals and applications. *Compos. Part A Appl. Sci. Manuf.* **30**, 1055–1071 (1999).
4. Kenji, K., Kanuma, Y., Oguro, T. & Harada, A. The Reliability of Magnetrons for Microwave Ovens. *J. Microw. Power Electromagn. Energy* **21**, 149–158 (1986).
5. Ferguson, J. D. Focused microwave instrumentation from CEM corporation. *Mol. Divers.* **7**, 281–286 (2003).
6. Retrieved from: <https://image.shutterstock.com/z/stock-vector-how-does-it-work-diagram-of-a-microwave-oven-showing-key-internal-components-145849475.jpg>.
7. Ryyänen, S. & Ohlsson, T. Microwave Heating Uniformity of Ready Meals as Affected by Placement, Composition, and Geometry. *J. Food Sci.* **61**, 620–624 (1996).
8. Vollmer, M. Physics of the microwave oven. *Phys. Educ.* **39**, 74–81 (2003).
9. Yang, H. W. & Gunasekaran, S. Comparison of temperature distribution in model food cylinders based on Maxwell's equations and Lambert's law during pulsed microwave heating. *J. Food Eng.* **64**, 445–453 (2004).
10. Vadivambal, R. & Jayas, D. S. Non-uniform temperature distribution during microwave heating of food materials-A review. *Food Bioprocess Technol.* **3**, 161–171 (2010).
11. Oliveira, M. E. C. & Franca, A. S. Microwave heating of foodstuffs. *J. Food Eng.* **53**, 347–359 (2002).
12. Kitchen, H. J. *et al.* Modern microwave methods in solid-state inorganic materials chemistry: From fundamentals to manufacturing. *Chem. Rev.* **114**, 1170–1206 (2014).
13. Retrieved from: <http://cem.com/en/catalogsearch/result/?q=+mars6+>.
14. Asmussen, J., Lin, H. H., Manring, B. & Fritz, R. Single-mode or controlled multimode microwave cavity applicators for precision materials processing. *Rev. Sci. Instrum.* **58**, 1477–1486 (1987).
15. Pecharsky, V. & Zavalij, P. *Fundamentals of Powder Diffraction and Structural Characterization of Materials*. Springer (2009).
16. West, A. R. *Basic solid state chemistry*. (John Wiley & Sons Inc, 1999).

17. Clegg, W. Crystal structure determination. *Oxford Chem. Prim.* **60**, 243–247 (1998).
18. Jenkins, R. & Snyder, R. *Introduction to X-ray powder diffractometry.* **267**, (John Wiley & Sons, 2012).
19. Blake, A. J. & Clegg, W. *Crystal structure analysis: principles and practice.* **13**, (Oxford University Press, 2009).
20. Glusker, J. P., Lewis, M. & Rossi, M. *Crystal structure analysis for chemists and biologists.* **16**, (John Wiley & Sons, 1994).
21. Ashcroft Neil, W. & David, M. N. Solid State Physics, Cornell University. (1976).
22. Braggs, W. H.; Braggs, W. L. The Reflection of X-ray by Crystals. *Proc. R. Soc. London. Ser. A* **88**, 428–438 (1913).
23. Retrieved from: [http://www.matter.org.uk/diffraction/x-ray/powder\\_method.htm](http://www.matter.org.uk/diffraction/x-ray/powder_method.htm).
24. Kraus, W. & Nolze, G. Powder cell 2.3 version. *CPD Newsllett* **20**, 274–280 (1998).
25. Rühl, S. Inorganic Crystal Structure Database (ICSD). *A Focus Crystallogr.* **6**
26. Laugier, J. & Bochu, B. CELREF: Unit Cell Refinement Program from Powder Diffraction Diagram. *Lab. des Matériaux du Génie Phys. Ec. Natl. Supérieure Phys. Grenoble (INPG), Grenoble, Fr.* (2003).
27. Larson, A. C. & Dreele, R. B. Von. General Structure Analysis System (GSAS). *Los Alamos Natl. Lab. Rep. LAUR* 86–748 (2000).
28. Toby, B. H. EXPGUI, a graphical user interface for GSAS. *J. Appl. Crystallogr.* **34**, 210–213 (2001).
29. Sivia, D. S. *Elementary scattering theory: for X-ray and neutron users.* (Oxford University Press, 2011).
30. Smith, R. I.; Hull, S. User Guide for the Polaris powder diffractometer at ISIS. *Rutherford Applet. Lab. Tech. Reports* (1994). at <http://purl.org/net/epubs/manifestation/9341>
31. S.T. Norberg, I. Ahmed, R.I. Smith, S.G. Eriksson, L. C. C. and S. H. The Polaris Diffractometer at ISIS : Planned Upgrade and New Facilities Chapon. **2**, 7
32. Rietveld, H. M. A profile refinement method for nuclear and magnetic structures. *J. Appl. Crystallogr.* **2**, 65–71 (1969).
33. Rietveld, H. M. Line profiles of neutron powder-diffraction peaks for structure refinement. *Acta Crystallogr.* **22**, 151–152 (1967).
34. Young, R. A. The Rietveld Method, IUCr. *Monogr. Crystallogr. Oxford Univ. Press. Oxford* (1993).
35. Mccusker, L. B., Dreele, R. B. Von, Cox, D. E., Loue È R D, D. & Scardi, P. Rietveld refinement guidelines. *Int. Union Crystallogr. J. Appl. Crystallogr. J. Appl. Cryst* **32**, 36–50 (1999).

36. Hawkes, P. & Spence, J. C. H. *Science of microscopy*. (Springer Science & Business Media, 2008).
37. Goldstein, J. I. *et al.* in *Scanning Electron Microscopy and X-ray Microanalysis* 537–564 (Springer, 2003).
38. Attard, G. & Barnes, C. Surfaces. *Oxford Chem. Prim.* **59**, 48–56 (1998).
39. Raman, C. V. A Change of Wave-length in Light Scattering. *Nature* **121**, 619–619 (1928).
40. Atkins, P. & de Paula, J. Chemical equilibrium. *Atkins' Phys. Chem. 7th edn. Oxford Univ. Press. Oxford, UK* 222–251 (2002).
41. Smith, E. & Dent, G. *Modern Raman Spectroscopy - A Practical Approach*. (2005).
42. Van der Heide, P. *X-ray photoelectron spectroscopy: an introduction to principles and practices*. (John Wiley & Sons, 2011).
43. Chusuei, C. C. & Goodman, D. W. X-Ray Photoelectron Spectroscopy. *Encyclopedia of Physical Science and Technology (Third Edition)* 921–938 (2003).
44. Watts, J. F. X-ray photoelectron spectroscopy. *Vacuum* **45**, 653–671 (1994).
45. Retrieved from: <https://www.phis.com/surface-analysis-techniques/xps-esca.html>.

# 3 Microwave Synthesis and Structural Characterization of Carbides in the V-C System – The V<sub>8</sub>C<sub>7</sub> Superstructure

## 3.1 Introduction to Vanadium Carbide

Two different binary phases exist in the V-C system [Figure 3-1], VC (cubic, *Fm-3m*) and V<sub>2</sub>C (orthorhombic, *Pbcn*).<sup>1,2</sup> The first one exhibits a large degree of nonstoichiometry (VC<sub>1-x</sub> where  $x = 0.65-0.90$ ), while the latter has a narrow homogeneity range. Lipatnikov *et al.* (1997) reported that the stoichiometric composition VC cannot be synthesized under equilibrium conditions and has a tendency to form an ordered cubic superstructure V<sub>8</sub>C<sub>7</sub>.<sup>3</sup> This represents the most stable form and carbon-rich limit of  $\delta$ -VC<sub>1-x</sub> and crystallizes in an NaCl-derived cubic structure (space group *P4<sub>3</sub>32*,  $a = 8.3303$  Å), showing a long-range ordering of structural C vacancies.<sup>4,5</sup> Moreover, several ordered nonstoichiometric superstructures have been reported in the literature, such as V<sub>8</sub>C<sub>7</sub> (cubic, *P4<sub>3</sub>32*), V<sub>6</sub>C<sub>5</sub> (hexagonal, *P3<sub>1</sub>*) and V<sub>4</sub>C<sub>3</sub> (hexagonal, *R-3m*)<sup>3,6-9</sup> [Figure 3-2]. Being one of the hardest transition metal carbides – with a hardness of 9-9.5 Mohs – vanadium carbide finds industrial applications in different fields such as metallurgy, electronics and catalysis.<sup>10</sup>

The work presented in this chapter focuses on the synthesis and structural characterization of the highly crystalline, single-phase vanadium carbide V<sub>8</sub>C<sub>7</sub>, in minute timescales in both multi- and single-mode microwave (MW) cavity reactors. The carbide material was prepared by employing vanadium metal (V) or vanadium pentoxide (V<sub>2</sub>O<sub>5</sub>) as a vanadium source and graphite as a carbon source under inert gas (Argon, Ar). In addition, the reaction profile was examined in order to gain a better understanding of both the microwave heating processes in the solid state as well as of the processing of transition metal carbides. To that end, considerable time and effort were invested in optimizing the experimental protocol and configuration. Once an appropriate synthetic procedure had been established, the as-synthesized ceramics were investigated by Powder X-ray Diffraction (PXRD), Scanning Electron Microscopy (SEM) coupled with Energy Dispersive X-ray (EDX) analysis, Raman spectroscopy, X-ray Photoelectron Spectroscopy (XPS) and Powder

Neutron Diffraction (PND). Further structural comparisons were made between multi-mode and single-mode synthesized samples.

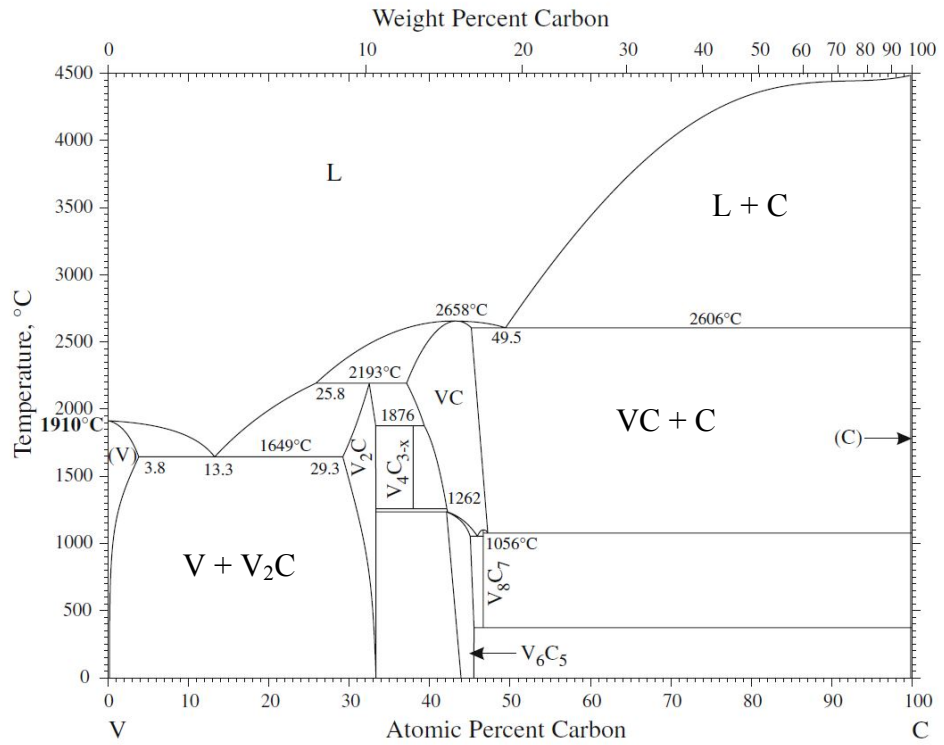
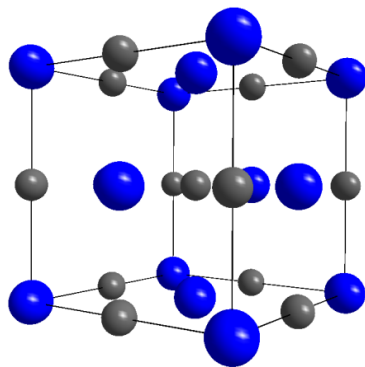
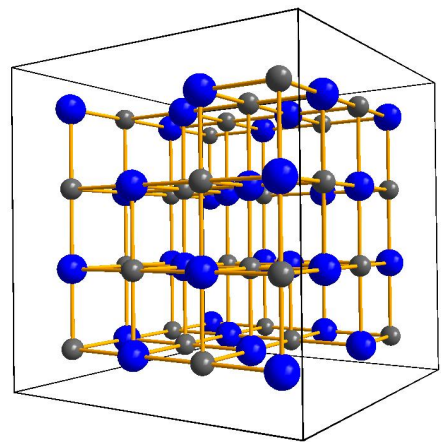


Figure 3-1 Phase diagram of the V-C system.<sup>1</sup>

(a)



(b)



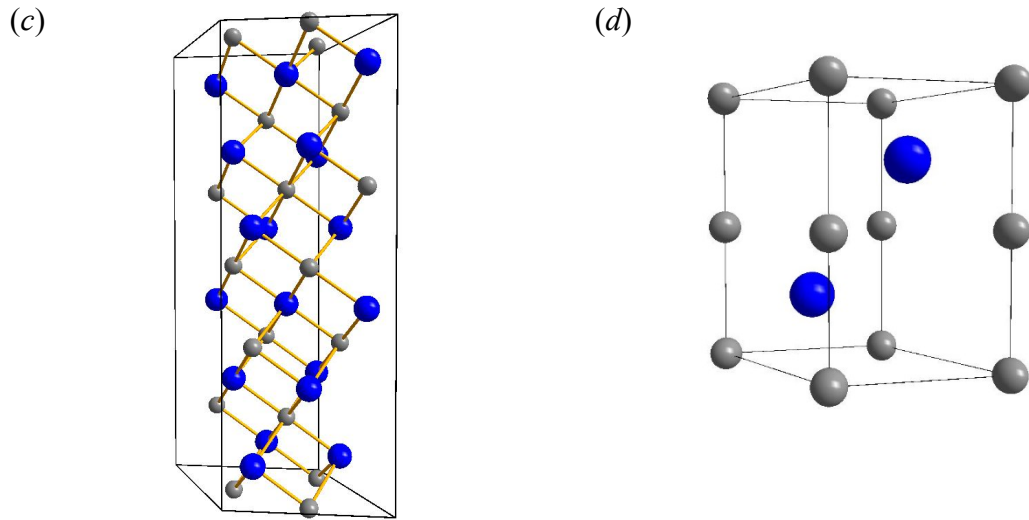


**Figure 3-2** Structures of VC (a),  $V_8C_7$  (b),  $V_6C_5$  (c) and  $V_2C$  (d). V atoms (blue), C atoms (grey).

## 3.2 Microwave Synthesis Studies in the V–C system

This section describes the experimental work that was undertaken towards establishing a synthetic route to vanadium carbide from vanadium metal and carbon in both multimode and single-mode cavity reactors.

### 3.2.1 Introduction

Vanadium carbide has been synthesized using various methods, such as by direct reaction of elemental powders,<sup>2</sup> carbothermal reduction of vanadium oxides ( $V_2O_5$  and  $V_2O_3$ ),<sup>11</sup> mechanical alloying,<sup>12</sup> temperature-programmed reaction<sup>13</sup> and a number of other routes.<sup>14–18</sup> However, these common approaches present several disadvantages, including energy inefficiency, high cost, presence of impurities and low yields.

Storms *et al.* (1962) determined the solid portion of the V-VC phase diagram above 1000 °C and successfully synthesized vanadium carbide using vanadium metal and graphite as starting materials.<sup>2</sup> The precursors were mixed in appropriate stoichiometric ratios and cold-pressed into compacts which were subsequently heated in an induction furnace at temperatures above 1000 °C.

Vanadium carbide was also prepared by Meunier *et al.* (1995) through carbothermal reduction of vanadium pentoxide into a microreactor.<sup>11</sup> The latter was reduced to the  $V_2O_3$  suboxide and subsequently carburized by a 20% mixture  $CH_4/H_2$  gas. The authors used a temperature-programmed reaction process for the synthesis of this compound which was

carried out in two stages. In the first stage, the temperature was rapidly raised to 430 K and maintained for 2 h. In the second stage, the temperature was increased to 1250-1320 K at lower heating rates (0.03-0.2 K s<sup>-1</sup>) and maintained for 4 h.

Prior attempts for synthesizing vanadium carbide using microwave irradiation have relied on starting materials and experimental set up that differ significantly from those reported in the present study. Hossein-Zadeh *et al.* (2014) reported the synthesis of nanocrystalline V<sub>8</sub>C<sub>7</sub> powders in a multi-step process through reduction of V<sub>2</sub>O<sub>5</sub> by carbon and Ca (here used as a reducing metal) using high energy ball milling and subsequent MW heat treatment.<sup>19</sup> V<sub>2</sub>O<sub>5</sub>, calcium and amorphous graphite were initially mixed and reacted according to the following equation:



The reactant powders were high-energy ball milled for 15 h at a rotation speed of 250 rpm and ball-to-powder ratio of 20:1. The mechanical alloying was followed by treatment of the as-milled powder with a 5% acetic acid solution to remove the CaO by-product. The activated powder was then MW heated to complete the reaction and to obtain the desired V<sub>8</sub>C<sub>7</sub> phase. The MW heat treatment was performed in a microwave oven at a power of 900 W and frequency of 2.45 GHz. In this case, a SiC crucible was used as a susceptor instead of graphite powder.

Previous studies conducted within the Gregory Research Group have demonstrated the plausibility of synthesizing refractory ceramic materials in air and/or inert atmosphere over minute or second timescales using MW irradiation.<sup>20-25</sup> The procedures discussed below were carried out by the direct reaction of the elemental starting materials (V + C) using microwave heating, aiming to increase the energy efficiency and, hence, potentially reduce the production cost with respect to the conventional synthesis. The starting materials were mixed according to the following reaction:



Although, theoretically, both starting materials (V metal and C) couple with microwaves, the heating of the reactant pellet alone was unsuccessful and required the use of a microwave susceptor, such as carbon. A susceptor is a material that couples very well with microwaves and converts this energy into thermal energy. Both graphite and activated charcoal are known to be good microwave absorbers, reaching temperatures above 1000 °C in less than 2 minutes.<sup>26</sup> Graphite was used as a susceptor (as well as starting material) to provide additional thermal heating on the outside of the pellet.

The direct reaction of elemental powders is straightforward and proceeds as described by Equation (1-15). This reaction route was more suitable for the reaction set-up used as, unlike in the carbothermal reduction of vanadium(V) oxide discussed in Section 3.3, the pellet would be intact and not fractured by rapid gas evolution.

## 3.2.2 Experimental

### 3.2.2.1 Synthesis

All reactions reported in this section were performed under Ar by mixing and grinding together V metal (Alfa Aesar, < 44  $\mu\text{m}$ , 99.5%) and graphite (Sigma Aldrich, < 50  $\mu\text{m}$ , 99.5%), with a stoichiometric ratio of 8:7 according to Equation (1-15). The so-obtained powder mixture (1 g) was uniaxially cold pressed into a pellet without the use of a binder. The ideal shape of pellets would be spherical, as heat is expected to penetrate homogeneously the sphere and radiate outwards by conduction. Nevertheless, in this study, samples were pressed in a cylindrical shape with a diameter of 8 mm and height of approximately 5 mm. This compact was embedded in ~0.3 grams of graphite powder (here used as a MW susceptor) within a 10-mm quartz tube which is transparent to microwaves. The tube was sealed with a septum cap, parafilm and subsequently connected to an Ar flow. The MW reactions were conducted by using both a multimode and a single-mode cavity reactor.

For multimode cavity experiments, the tube containing the sample was placed in the center of a beaker containing silica powder which acts as a stand for the tube as well as a thermal insulator [Figures 2-7 and 2-8]. The whole apparatus was then inserted into the multimode cavity of a domestic MW oven (DMO) and positioned in the same location within the cavity to keep the experimental parameters as constant as possible. Synthesis was optimized and conducted for 6 minutes at a power of 800 W.

For single-mode cavity experiments, the tube was directly placed into the applicator of the SMC reactor as it is held by a stand [Figures 2-10 and 2-11]. Synthesis was conducted for 2 minutes at a power of 1 kW.

Regardless of the microwave reactor used,  $\text{V}_8\text{C}_7$  was synthesized for the first time on much more rapid timescales than previously reported in the literature. Moreover, the reaction time could be further decreased by employing higher MW powers for the reaction process.

After the reaction went to completion, the pellet was found to be extremely hard due to the fast sintering process of the carbide particles. The surface of the pellet was scratched off

with fine sand paper in order to remove the remaining excess of susceptor. The pellet was then ground, giving a fine, grey powder.

### 3.2.2.2 Characterization

Products were characterized using several analytical techniques. Powder X-ray Diffraction (PXRD) [Section 2.3.1] was used to identify product phases by reference to powder patterns calculated from known structures downloaded from the Inorganic Crystal Structure Database (ICSD)<sup>27</sup> using the PowderCell 2.3 software.<sup>28</sup> The data for phase identification was collected on a PANalytical Xpert MPD, Cu K $\alpha$ 1 radiation, for 1 hour over a range of  $10 < 2\theta/^\circ < 85$ . Crystallographic parameters were obtained by Rietveld refinement [Section 2.3.3] against powder XRD data collected for ca. 12 hours over a range of  $10 < 2\theta/^\circ < 110$  using GSAS and EXPGUI software packages. Sample morphology and elemental composition were investigated by Scanning Electron Microscopy (SEM) and Energy-dispersive X-ray Spectroscopy (EDX) [Section 2.3.4] using a Philips XL30 ESEM microscope coupled with an Oxford Instruments X-act spectrometer. Additional characterization was performed by Raman spectroscopy [Section 2.3.5]. Raman data were collected at room temperature using a Horiba LabRAM confocal microscope system with a 532-nm green laser. Surface analysis was evaluated by X-ray Photoelectron Spectroscopy (XPS) [Section 2.3.6] using a Thermo Scientific K-Alpha+ X-ray photoelectron spectrometer with monochromatic Al K $\alpha$  radiation (1486.7 eV). Finally, Powder Neutron Diffraction (PND) [Section 2.3.2] was used to obtain a definitive model for the defect structure and to establish the amount of any possible oxygen included in the samples. PND experiments were conducted at the ISIS pulsed neutron and muon source at the Rutherford Appleton Laboratory (RAL) in Oxfordshire using the POLARIS instrument.

## 3.2.3 Results and Discussion

### 3.2.3.1 Powder X-ray Diffraction (PXRD)

After a 6-minute reaction in the multimode cavity, the sample was analyzed by *ex-situ* Powder X-ray Diffraction. The PXRD pattern for the so-obtained sample is shown in Figure 3-3. Similar results were obtained after a 2-minute reaction in the single-mode cavity (PXRD pattern shown in the Appendix, Figure 7-1).

In both cases, the product was identified as  $V_8C_7$ , which crystallizes with a cubic sodium chloride superstructure (space group  $P4_332$ ). The PXRD pattern consists of seven sharp, high intensity peaks characteristic of the NaCl-type structure plus several low-intensity superstructure lines. The latter ones (barely visible in Figure 3-3) are not due to the presence of any kind of impurities but are indeed characteristic for the  $V_8C_7$  superstructure.<sup>29</sup> Figure 7-2 in the Appendix shows a magnified image of these superstructure lines in the PXRD pattern shown in Figure 1-3. The seven most intense peaks represent the reflections from the (222), (400), (440), (622), (444), (600) and (662) planes of the cubic structure of vanadium carbide,  $V_8C_7$ . In addition, a weak reflection is observed at  $2\theta \cong 26.5^\circ$  and this was visible in the vast majority of experiments performed under these conditions. This corresponds to the (002) reflection from graphite, which probably originates from residual susceptor that could not be completely physically removed.

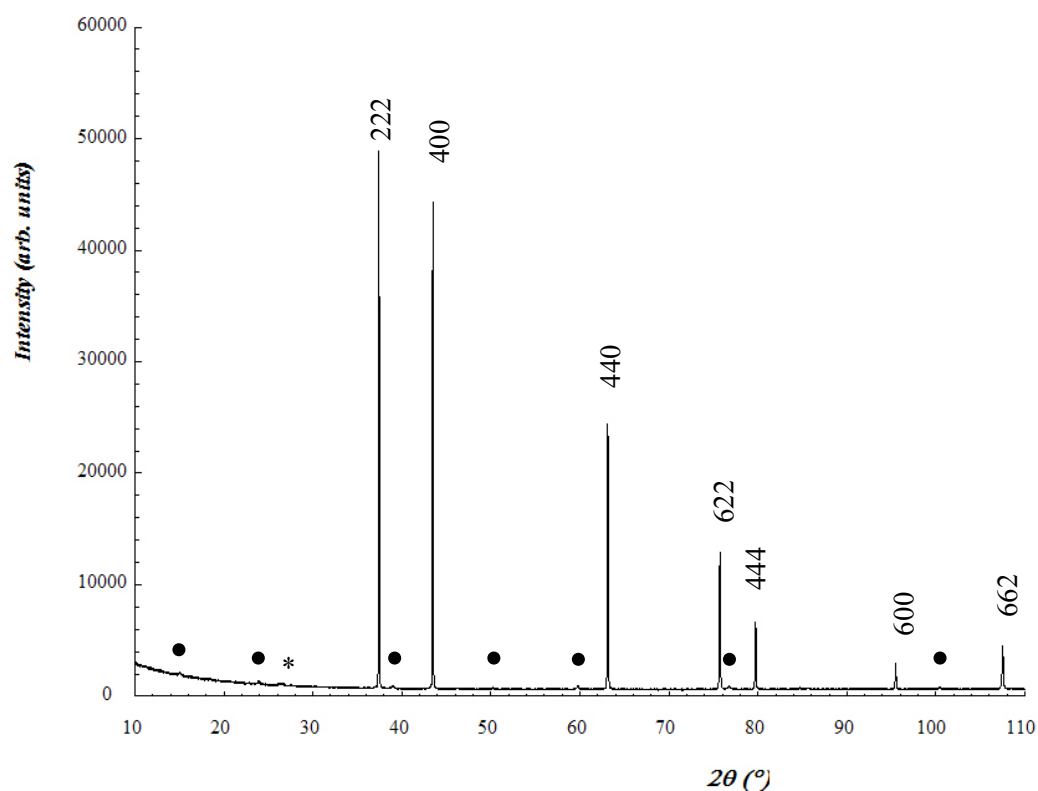


**Figure 3-3** PXRD pattern taken ex-situ from vanadium metal plus graphite (8:7) heated in a MMC reactor for 6 minutes at a power of 800 W. All reflections can be attributed to  $V_8C_7$  except the one marked with \*, which belongs to the (002) reflection from graphite. The reflections marked with • are superstructure lines characteristic of the  $V_8C_7$  phase.

Moreover, the PXRD pattern from the V + C reaction performed in the SMC microwave reactor is essentially indistinguishable from Figure 3-3 and same number of reflections are observed.

### 3.2.3.2 Rietveld Refinement

The structure of the as-obtained  $V_8C_7$  was solved by the Rietveld method against PXRD data, collected for 12 hours over a range of  $10 < 2\theta/^\circ < 110$  with a step size of  $0.017^\circ$  ( $2\theta$ ) using GSAS and EXPGUI software packages.<sup>30,31</sup> The initial model used was the cubic  $P4_332$   $V_8C_7$  structure proposed by de Novion *et al.* (1977)<sup>6</sup> and taken from the ICSD database [Figure 3-4], in which the 32 vanadium atoms occupy the (8c) and (24e) Wyckoff positions and the 28 carbon atoms are located at (4a), (12d) and (12d) Wyckoff positions.

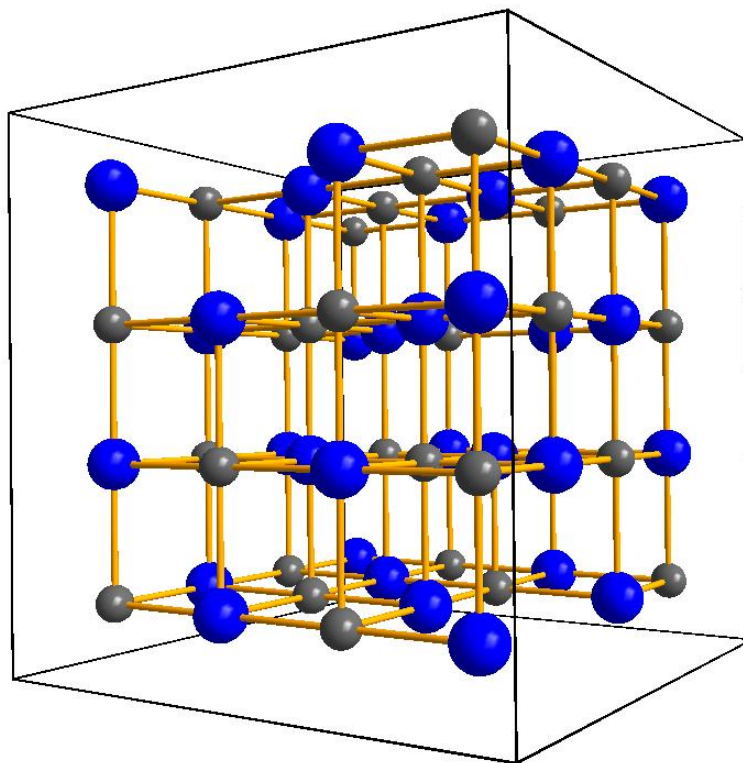


**Figure 3-4** The structure of  $V_8C_7$  as proposed by de Novion *et al.* (1977).<sup>6</sup>

The background was modelled using a shifted Chebyshev function (function 1 within GSAS). Cell parameters, scale factor and zero point were also refined in initial cycles. Peak shape was subsequently modelled using the Thompson-Cox-Hastings pseudo Voigt function (peak shape function 2 within GSAS). Although  $V_8C_7$  crystallizes in a cubic structure (which has fixed atomic positions in the NaCl parent structure), the atomic coordinates of most sites could also be refined due to the presence of the long-range ordering of vacancies at the non-metal positions. Such refinement led to significant improvement of the goodness of fit and showed a small distortion of the vanadium atom positions surrounding the carbon vacancy. These atoms were indeed shifted towards the center of the carbon vacancy as previously reported by Rafaja *et al.* (1998).<sup>5</sup> A corresponding displacement was also observed for the surrounding carbon atoms. The isotropic thermal factors ( $U_{iso}$ ) of the vanadium sites V(1)

and V(2) were constrained to have the same values. The same procedure was repeated for the thermal factors of the carbon sites C(1), C(2) and C(3). This was due to the fact that, if the isotropic thermal factors were refined independently without constraint, the refinement would not achieve convergence. Refinement of the site occupancy factors (SOFs) was also attempted, but resulted in an unstable refinement (with no improvement of the goodness of fit parameters or bond distances) and/or in inconsistent values. All the SOFs were therefore fixed at 1.0 in the final refinement.

Rietveld refinement against PXRD data [Figure 3-5] confirmed that the vanadium carbide superstructure  $V_8C_7$  crystallizes in a cubic NaCl-type superstructure (space group  $P4_332$ ) with a long-range ordering of carbon vacancies at the non-metal positions. The refined lattice parameter was  $a = 8.3312(4) \text{ \AA}$ , consistently with prior reports [de Novion *et al.* (1966)  $a = 8.3340 \text{ \AA}$ <sup>32</sup> and Henfrey *et al.* (1970)  $a = 8.3303 \text{ \AA}$ <sup>4</sup>].

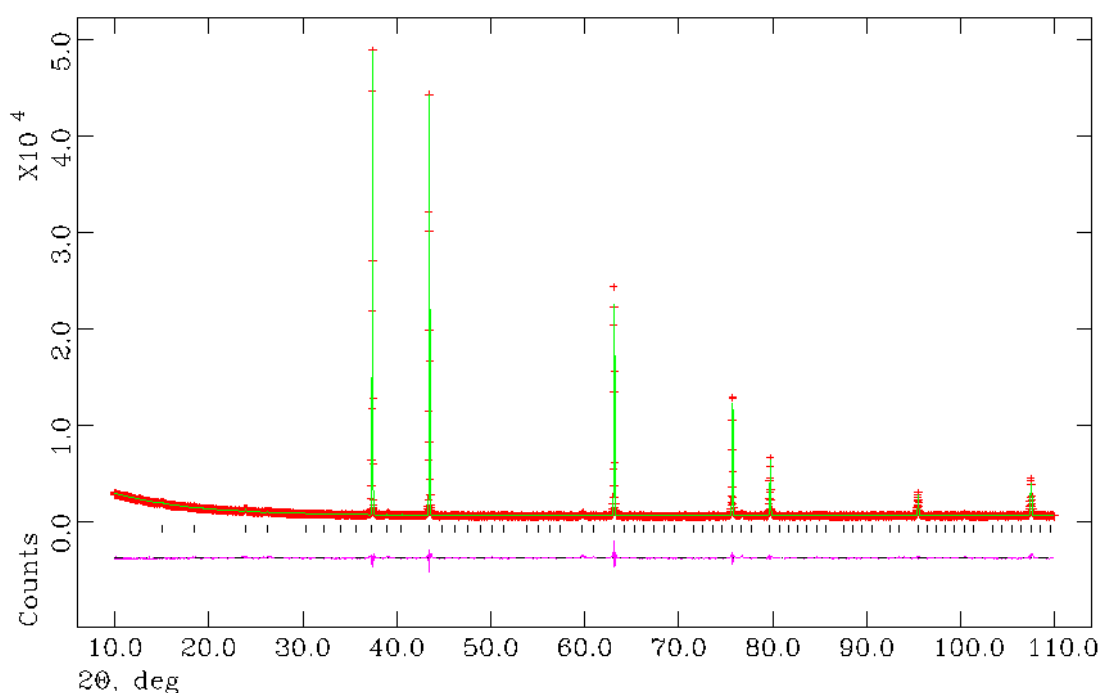


**Figure 3-5** Observed (*plusses*), calculated (*solid green line*), and difference (*solid purple line*) profile plot for the Rietveld refinement against PXRD data for the vanadium carbide superstructure  $V_8C_7$ . Tick marks denote  $V_8C_7$  diffraction peaks. The (002) graphite reflection at  $2\theta = 26.5^\circ$  was excluded from the refinement.

The calculated crystallographic data and atomic parameters are illustrated in Table 3-1 and Table 3-2, respectively.

**Table 3-1** Crystallographic data from Rietveld refinement against PXRD data for  $V_8C_7$  prepared from vanadium metal and carbon in 6 minutes in an MMC reactor at a power of 800 W.

Phase data	
Chemical Formula	V <sub>8</sub> C <sub>7</sub>
Crystal system	Cubic
Space group	<i>P4<sub>3</sub>32</i>
<i>a</i> (Å)	8.3312(4)
Volume (Å <sup>3</sup> )	577.92(1)
<i>Z</i>	4
Formula weight (g mol <sup>-1</sup> )	491.61
Calculated density (g cm <sup>-3</sup> )	5.64984
<i>R</i> <sub>wp</sub>	0.0559
<i>R</i> <sub>p</sub>	0.0370
$\chi^2$	3.459

**Table 3-2** Atomic parameters from Rietveld Refinement against PXRD data for V<sub>8</sub>C<sub>7</sub> prepared from vanadium metal and carbon in 6 minutes in an MMC reactor at a power of 800 W.

Atomic parameters						
Atom Type	Wyckoff Site	Fractional Coordinates			<i>U</i> <sub>iso</sub> (Å <sup>2</sup> )	Site Occupancy
		<i>x/a</i>	<i>y/b</i>	<i>z/c</i>		
V(1)	8c	0.3731(5)	0.3731(5)	0.3731(5)	0.01177(3)	1.0
V(2)	24e	0.1250(3)	0.3784(3)	0.1290(5)	0.01177(3)	1.0
C(1)	4a	0.1250	0.1250	0.1250	0.01028(1)	1.0
C(2)	12d	0.1250	0.6338(1)	0.6161(1)	0.01028(1)	1.0
C(3)	12d	0.1250	0.3787(2)	0.8712(2)	0.01028(1)	1.0

Only the V–V bond distances in vanadium carbide have been reported previously by Gusev *et al.* (2015) which are in the range of 2.883 – 3.058 Å.<sup>33</sup> These values are in good agreement with those determined by Rietveld refinement in the present study and shown in the Appendix, Table 7-1, together with the bond angles. However, Buijink *et al.* (1995) studied the chemistry of vanadium-carbon single and double bonds and reported values for V–C bonds in a number of vanadium complexes.<sup>34</sup> These are in the range of 2.0262 – 2.103 Å, again in agreement with those reported in Table 7-1, Appendix.

### 3.2.3.3 *Ex-situ* Study of the V + C Reaction as a Function of Time

From the *ex-situ* PXRD data, a phase analysis was conducted by monitoring the phase evolution as a function of time for both multimode and single-mode cavity experiments, which revealed information on possible reaction mechanisms.

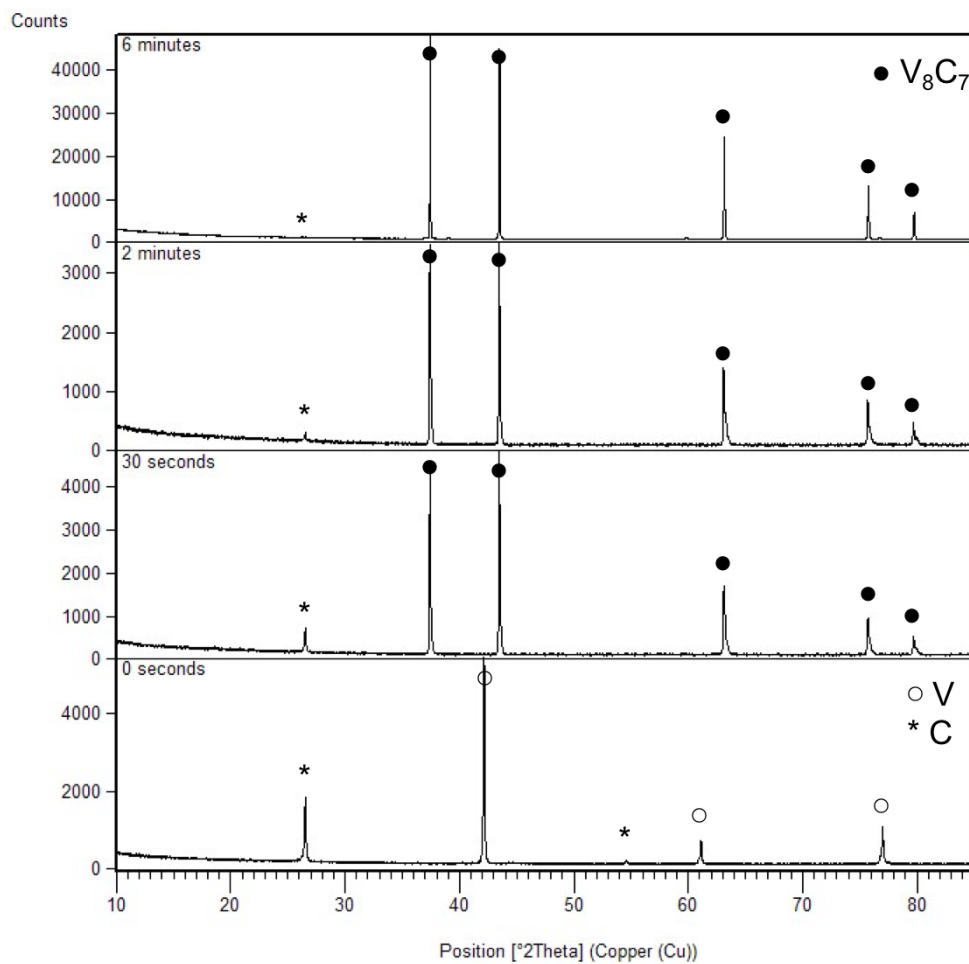


**Figure 3-6** *Ex-situ* patterns for V + C pellets irradiated in an MMC reactor at a power of 800 W from  $t = 0$  (reagents – bottom) to reaction completion (top).

Figure 3-6 illustrates the PXRD patterns collected after the V + C pellets had been irradiated with MWs for 0 s, 30 s, 1 min and 6 mins in the MMC reactor. Immediately before the start of the reaction ( $t = 0$ ), only reflections from the reagents, vanadium metal and graphite, are present. After 30 s of MW irradiation, the amount of free carbon present in the sample had drastically decreased while no evidence for the presence of metallic V is observed. It seems that the starting V metal has all reacted to produce vanadium carbides with a lower carbon content ( $VC_{1-x}$ ) with respect to stoichiometric VC. This is evident from the shape of reflections in the respective PXRD pattern in Figure 3-6. These peaks are highly unsymmetrical with the tail of each reflection at high  $2\theta$  clearly less steep than the

corresponding edge at lower  $2\theta$ . Figure 7-3 in the Appendix shows a magnified image of the PXRD pattern after a 2-minute reaction illustrating the unsymmetrical nature of the reflections at  $75.7^\circ$  and  $79.6^\circ$   $2\theta$  angles. It can therefore be concluded that the primarily formed vanadium carbides have a lower carbon content ( $VC_{1-x}$ ) and, accordingly, a smaller unit cell parameter.<sup>35</sup> In subsequent time points ( $t = 30$  s to  $t = 1$  min), the intensity of the vanadium carbide reflections increases, the peaks become increasingly symmetrical (the high  $2\theta$  tails become steeper and steeper) and peaks corresponding to graphite become less intense. As the reaction approaches completion ( $t = 6$  min), highly crystalline  $V_8C_7$  pellets are obtained as a single carbide phase together with a small impurity of graphite which is likely to originate from residual susceptor. The PXRD patterns for the V + C pellets after 0 sec, 30 sec and 2 min of MW irradiation are shown separately in Figures 7-4 to 7-6 in the Appendix.

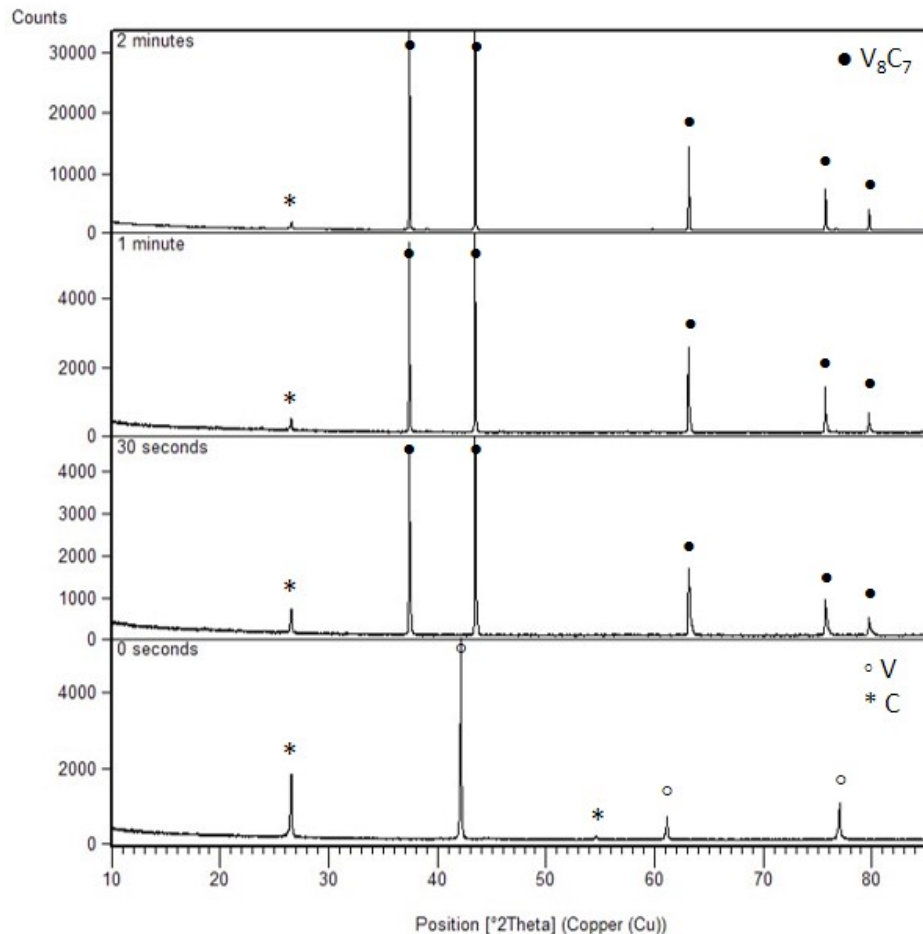


**Figure 3-7** *Ex-situ* patterns for V + C pellets irradiated in an SMC reactor at a power of 1 kW from  $t = 0$  (reagents – *bottom*) to reaction completion (*top*).

The reaction process in the single-mode cavity synthesis is similar to that for the multimode cavity experiments but much shorter reaction times are required. Figure 3-7

illustrates the PXRD patterns collected after the V + C pellets had been irradiated with MWs for 0 s, 10 s, 30 s and 2 mins in a single-mode MW reactor. At  $t = 0$ , only reflections from the reagents, vanadium metal and graphite, are present. After 10 s of MW irradiation, no reflections from the vanadium metal phase are observed, suggesting that it has all reacted with graphite to form carbon-deficient vanadium carbide ( $VC_{1-x}$ ). As the reaction proceeds, the intensity of the vanadium carbide reflections increases until a single carbide phase of  $V_8C_7$  is obtained after 2 minutes of MW irradiation.

From Figure 3-6 and Figure 3-7, it can be seen that although the reaction appears to proceed by the same route in both cases, the single-mode MW experiment is much more rapid than the multimode reactor (equivalent). The reaction time for the synthesis of vanadium carbide from vanadium metal and graphite in a multimode cavity MW reactor operating at 800 W (6 minutes) can thus be reduced by one third (2 minutes) by employing a single-mode MW reactor operating at 1 kW.

This *ex-situ* study of the V + C reaction as a function of time suggests a straightforward mechanism involving direct combination of the elements to form a succession of carbides that become more C-rich. The  $V_8C_7$  phase is indeed obtained through the formation of carbon-deficient vanadium carbides  $VC_{1-x}$ . No other stable, observable intermediates are identified throughout the reaction. For more detailed mechanistic insights, the MW synthesis of V and C should be investigated *in-situ* which would require the development of a customized single-mode MW reactor, specifically designed to perform time-resolved experiments by means of powder X-ray diffraction (PXRD) or, preferably, powder neutron diffraction (PND).

#### **3.2.3.4 Scanning Electron Microscopy (SEM) coupled with Energy-dispersive X-ray Spectroscopy (EDX)**

The MW-synthesized  $V_8C_7$  powders prepared from vanadium metal and graphite were analyzed for particle size and morphology by Scanning Electron Microscopy (SEM). As carbide and nitride materials find industrial applications in abrasives and wear-resistant parts, the particle size, shape and morphology of such materials play an important role in their suitability for specific applications.<sup>10</sup>

SEM micrographs for the  $V_8C_7$  samples synthesized in 6 minutes in a MMC microwave reactor at a power of 800 W are shown in Figure 3-8. The microwave reaction yields to the formation of irregular micron-scale  $V_8C_7$  particles, typically with dimensions of a few microns to a maximum of approximately 70  $\mu\text{m}$ .

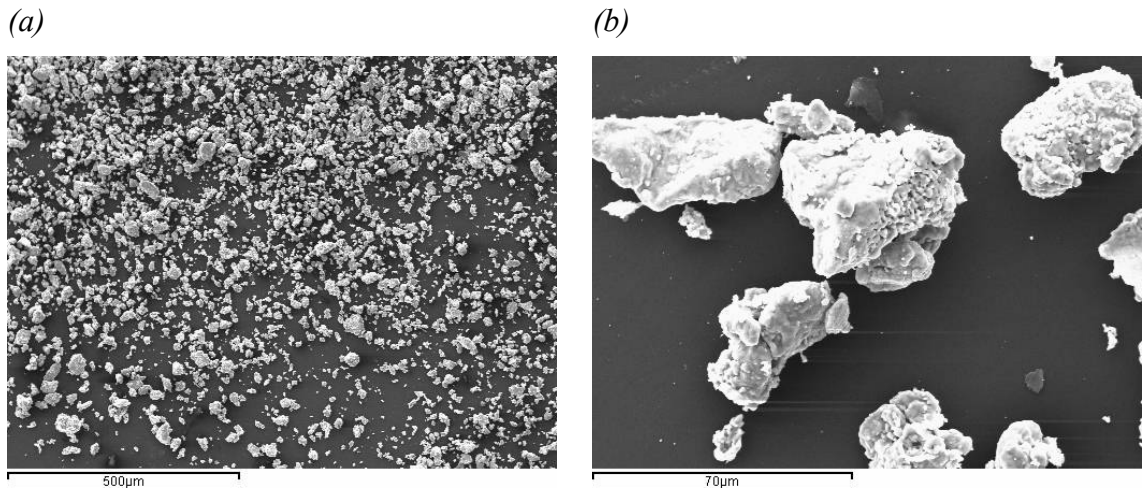


**Figure 3-8** SEM micrographs for the  $V_8C_7$  synthesized from vanadium metal and carbon in 6 minutes in an MMC microwave reactor at a power of 800 W.

SEM micrographs for the  $V_8C_7$  samples synthesized in 2 minutes in the single-mode cavity microwave reactor at a power of 1 kW show similar results to those prepared in the MMC reactor and are shown in Figure 3-9. Also in this case, the microwave reaction yields to the formation of irregular micron-scale  $V_8C_7$  particles, typically with dimensions of a few microns to a maximum of approximately 70 μm.

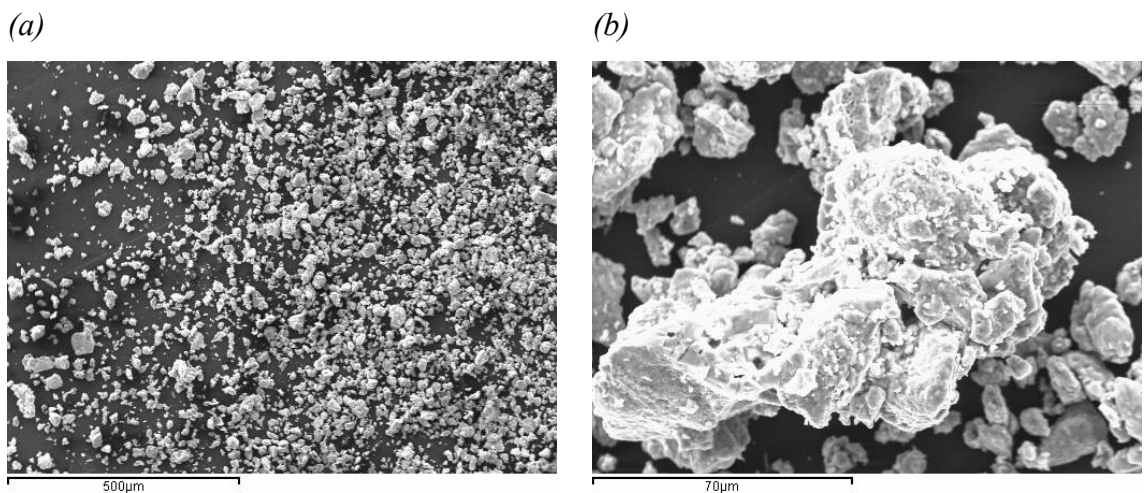


**Figure 3-9** SEM micrographs for the  $V_8C_7$  synthesized from vanadium metal and carbon in 2 minutes in a single-mode cavity (SMC) microwave reactor at a power of 1 kW.

The SEM images obtained for the MMC and SMC samples demonstrate very similar particle sizes and morphologies.  $V_8C_7$  particles exhibit relatively rough surfaces, in both cases. Larger particles are presumably the product of a sintering process undergone between smaller particles, and have remained intact due to incomplete post-reaction pellet grinding.

EDX data were collected for several crystallites and showed slightly different results. Some EDX spectra showed indeed that only vanadium and carbon were present [Figure 3-10] whereas some others suggested that oxygen was also included in the structure either in the surface or in the bulk material [Figure 3-11].

The presence of oxygen in the form of additional bulk oxide phases was excluded beforehand, as PXRD data do not support this last option.

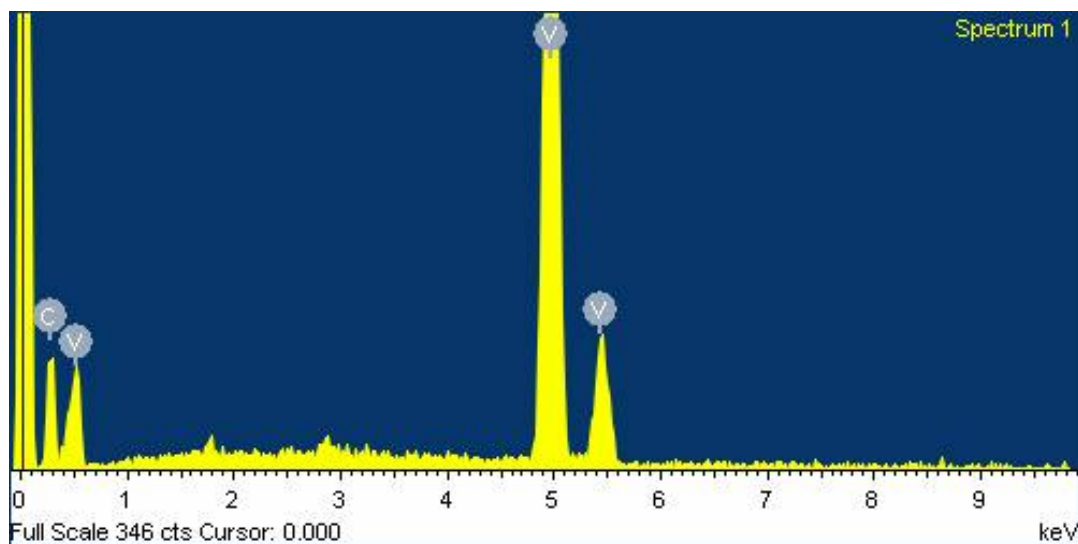


**Figure 3-10** EDX spectrum for the  $V_8C_7$  synthesized from vanadium metal and carbon in 6 minutes in an MMC microwave reactor, showing that only vanadium and carbon were present.

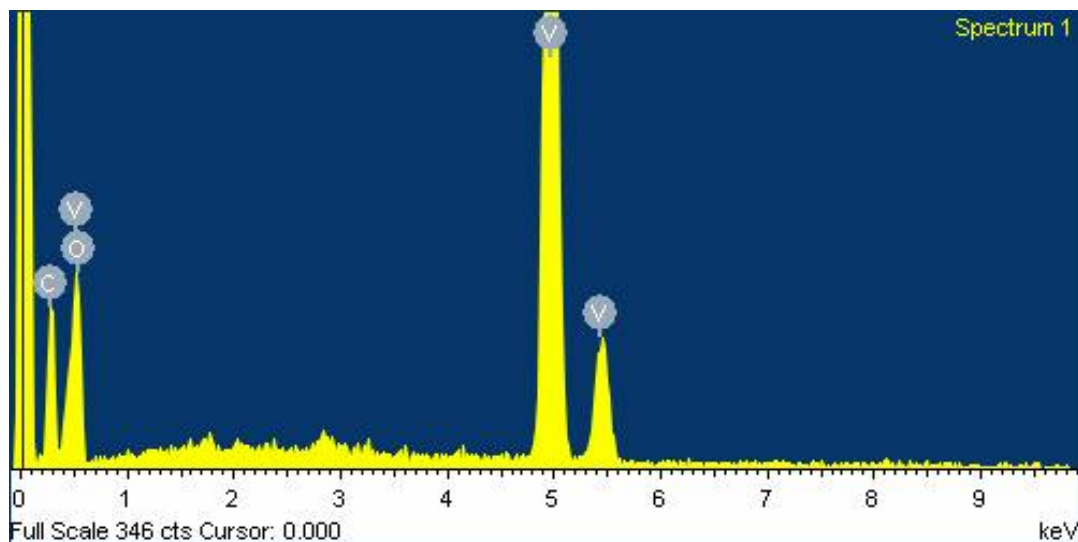


**Figure 3-11** EDX spectrum for the  $V_8C_7$  synthesized from vanadium metal and carbon in 6 minutes in an MMC microwave reactor, showing that oxygen was present as well as vanadium and carbon.

CHN analysis was also performed on the  $V_8C_7$  sample synthesized from vanadium metal and carbon, giving a vanadium content of 82.36 wt. % and a carbon content of 17.64 wt. %.

These values are consistent with the theoretical ones: 82.90 wt. % for V and 17.10 wt. % for C.

### 3.2.3.5 Raman Spectroscopy

Further characterization was undertaken by Raman spectroscopy. Ghimbeu *et al.* (2011) used Raman spectroscopy to characterize their nanostructured vanadium nitride/multiwalled carbon nanotubes (VN/CNTs) composites.<sup>36</sup> This study showed that the vanadium nitride used for the synthesis of the composite material had a similar Raman spectrum when compared to that of  $V_2O_5$ . According to the authors, this is probably due to the presence of surface oxides on the VN particles.

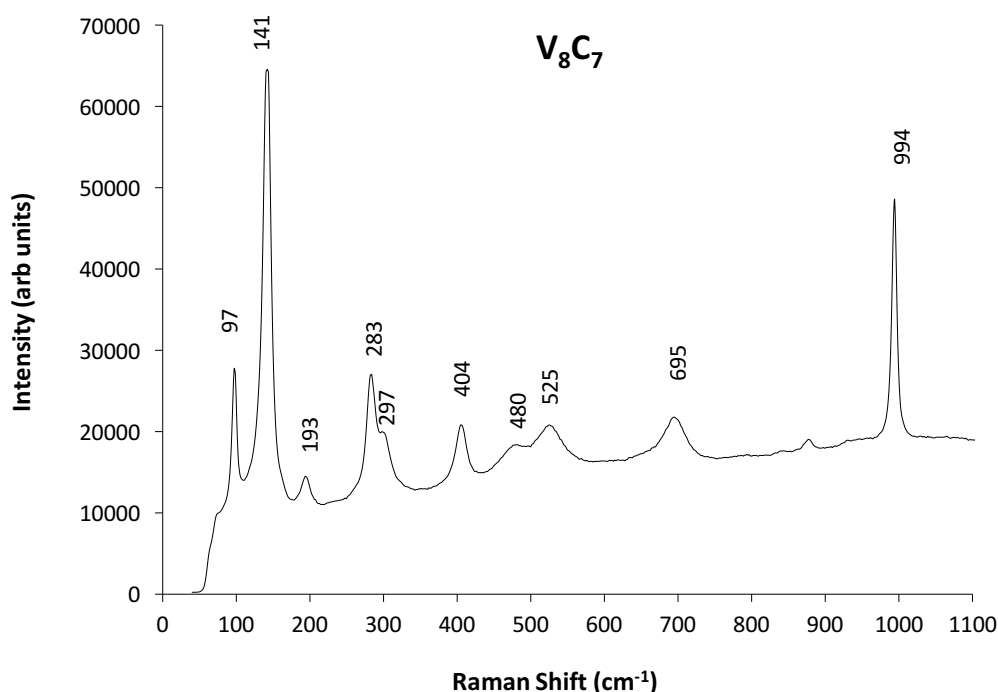


**Figure 3-12** Experimental Raman spectrum for the MW-synthesized  $V_8C_7$  from vanadium metal and carbon in 6 minutes in an MMC microwave reactor.

In Section 3.2.3.4, it was discussed how some EDX spectra showed the possibility of oxygen contamination in the sample. Raman spectroscopy was here used to provide additional supporting information regarding possible oxygen inclusion within the samples. Figure 3-12 illustrates the Raman spectrum of the MW-synthesized  $V_8C_7$  from vanadium metal and graphite in 6 minutes in a multi-mode MW reactor. The spectrum shows the same characteristic bands as  $V_2O_5$ <sup>37-41</sup> [Figure 3-13] although the two compounds have different structures. As previously discussed in Section 3.2.3.2,  $V_8C_7$  crystallizes in a cubic structure

with a space group of  $P4_332$  while  $V_2O_5$  has an orthorhombic structure (space group  $Pmmn$ ). Most of the bands in the  $V_8C_7$  Raman spectrum appear to be slightly shifted towards lower Raman shifts compared to those in the  $V_2O_5$  spectrum and are reported in Table 3-3.

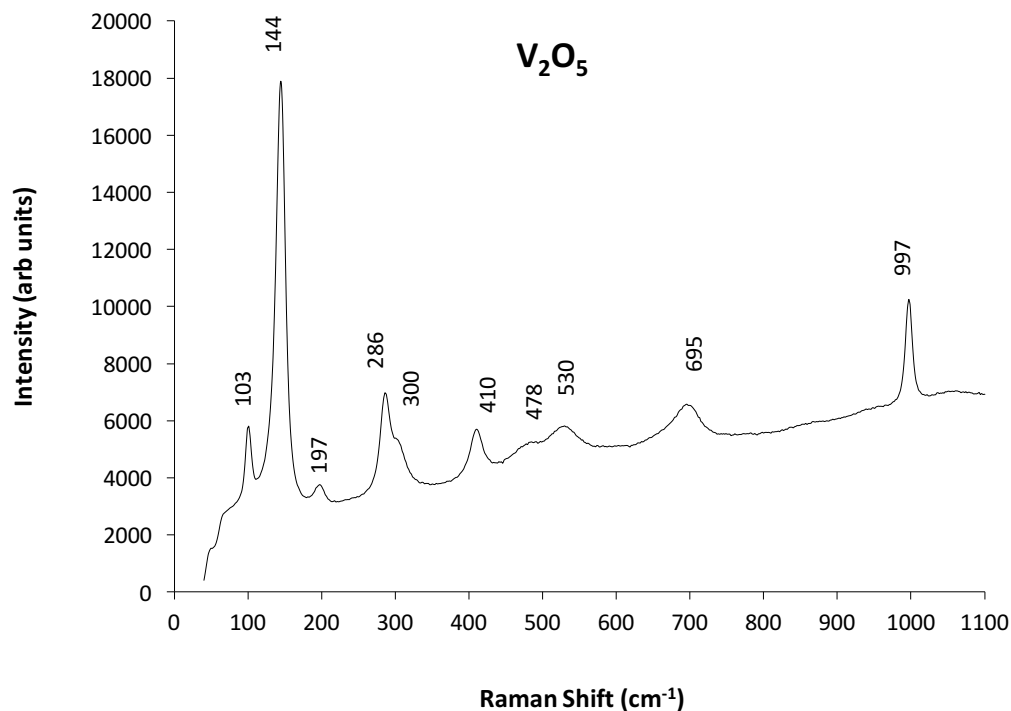


**Figure 3-13** Raman spectrum for commercial  $V_2O_5$ .

Raman spectroscopy experiments were conducted in sealed capillary tubes under Ar to make sure that the characteristic Raman bands of  $V_2O_5$  observed in Figure 3-12 would not arise as a consequence of sample burning due to high laser powers. Moreover, samples were subjected to PXRD scans after Raman experiments, showing no evidence for the formation of oxide phases.

**Table 3-3** Comparison of the Raman shifts of the MW-synthesized  $V_8C_7$  and commercial  $V_2O_5$  and their assigned symmetry modes.

$V_8C_7$ Raman Shift ( $cm^{-1}$ )	$V_2O_5$ Raman Shift ( $cm^{-1}$ )	Assignment
97	103	$A_g$
141	144	$B_{1g} + B_{3g}$
193	197	$A_g$
283	286	$B_{3g}$
297	300	$B_{2g}$
404	410	$A_g$
480	478	$A_g$
525	530	$A_g$
695	695	$B_{2g}$
994	997	$A_g + B_{2g}$

Vanadium pentoxide has been widely investigated due to its intriguing electrochemical properties.<sup>42-48</sup> Several papers have been published in the literature that aimed at studying the Raman spectroscopy of this compound (thin films, nanotubes, etc.).<sup>37-41</sup>  $V_2O_5$  forms an orthorhombic structure (space group  $Pmmn$ ) with lattice parameters  $a = 11.512$ ,  $b = 3.564$  and  $c = 4.368$  Å [Figure 3-14]. Its structure can be described from the packaging of  $V_2O_5$  layers along the  $c$  axis of the unit cell. Distorted  $VO_5$  square pyramids build up each layer and share corners and edges. Three different oxygen atoms can be observed: terminal (vanadyl) oxygen, O1, oxygen coordinated to two vanadium atoms, O2, and oxygen coordinated to three vanadium atoms, O3 [Figure 3-14].

Zhou *et al.* (2008) studied the Raman spectrum of vanadium pentoxide from density-functional perturbation theory<sup>41</sup> and found that the crystal modes can be classified as follows:

$$\begin{aligned} \Gamma(V_2O_5) = & 7A_g(R) + 3B_{1g}(R) + 7B_{2g}(R) + 4B_{3g}(R) \\ & + 3A_u + 6B_{1u}(IR) + 3B_{2u}(IR) + 6B_{3u}(IR) \end{aligned} \quad (3-3)$$

where all the  $g$  modes are Raman active while the  $B_u$  modes are IR active.

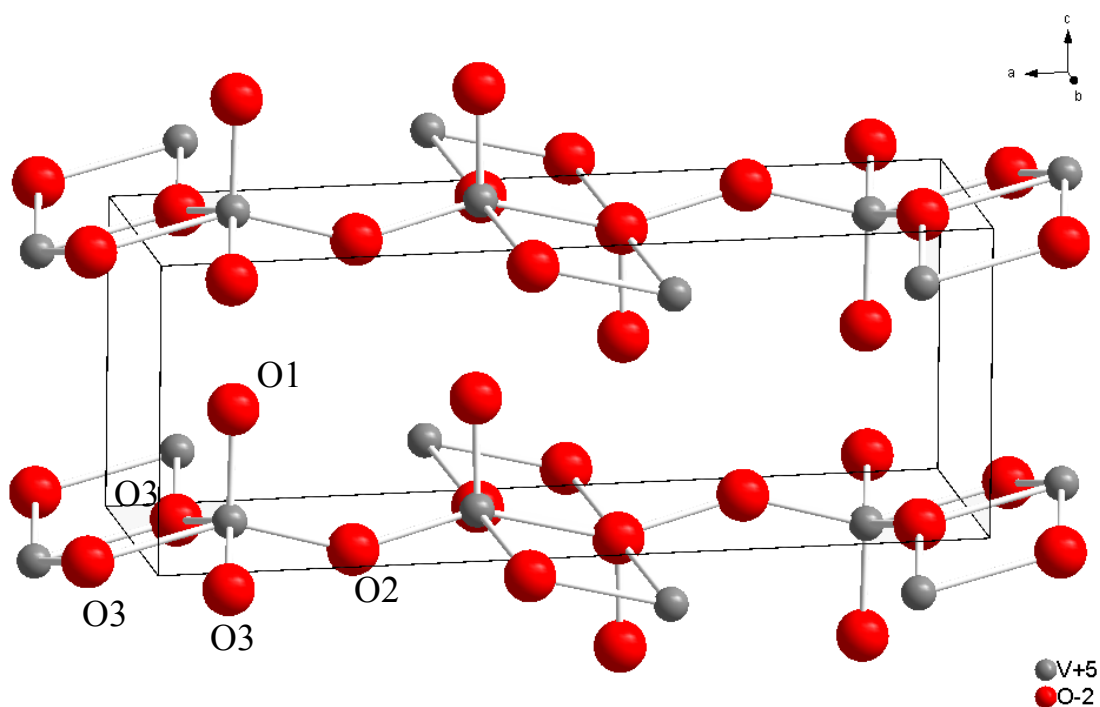


**Figure 3-14** Structure of vanadium pentoxide.

Lee *et al.* (2003) investigated the Raman spectroscopy of vanadium oxide thin films<sup>39</sup> and assigned each Raman peak to the respective stretching mode. The three low-frequency Raman peaks at 103, 144 and 197  $\text{cm}^{-1}$  were attributed to the layered structure and described as corresponding to the lattice vibration. The bending vibration of the V=O bonds was proposed to underlie the detection of the two peaks at 286 and 410  $\text{cm}^{-1}$ , whereas the peaks at 300  $\text{cm}^{-1}$  and 478  $\text{cm}^{-1}$  were ascribed to the bending vibrations of the doubly (V<sub>2</sub>-O) and triply (V<sub>3</sub>-O) coordinated oxygen, respectively. A V<sub>3</sub>-O stretching mode, which results from edge-shared oxygens in common to three pyramids, was thought to lead to the appearance of the 530  $\text{cm}^{-1}$  peak. For the final two peaks, detected at 695 and 997  $\text{cm}^{-1}$ , the suggested causal agent was a V<sub>2</sub>-O stretching mode which result from corner-shared oxygens common to two pyramids and to the V=O (terminal oxygen) stretching mode which results from an unshared oxygen.

In conclusion, the MW-synthesized V<sub>8</sub>C<sub>7</sub> and commercial V<sub>2</sub>O<sub>5</sub> show the same Raman bands in their spectra despite the difference in structure. This could be due to the inclusion of oxygen in the V<sub>8</sub>C<sub>7</sub> samples (see Section 3.2.3.6 and 3.2.3.7) as reported by Ghimbeu *et al.*,<sup>36</sup> even if synthesized under Ar. It is unclear how oxygen could be introduced into the system for reactions under inert atmosphere. A possible explanation could be that the contaminating oxygen is generated during reaction from the quartz tube which, by reacting

with graphite susceptor, forms silicon carbide and releases carbon monoxide.<sup>20,49</sup> O contamination could also be attributed to the presence of the element on the surface of vanadium metal or impurity in the Ar supply. It is rather unlikely that oxygen could be present from a leak in the argon line, as all possible measures were taken to prevent this and the whole procedure takes place under a positive pressure of Ar.

### 3.2.3.6 X-ray Photoelectron Spectroscopy (XPS)

The chemical nature of the  $V_8C_7$  surface was analyzed by XPS. Measurements were run with the assistance of Dr. Sina Saremi-Yarahmadi at the Department of Materials at the University of Loughborough. Figure 3-15 shows the wide survey XPS spectrum for the MW-synthesized  $V_8C_7$  sample prepared from vanadium metal and carbon in 6 minutes in a multi-mode cavity MW reactor.

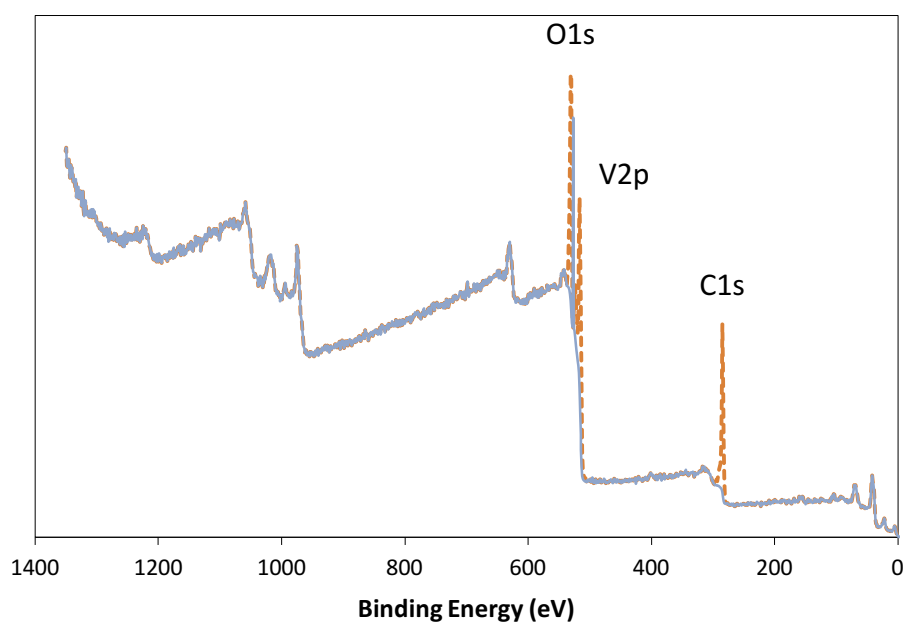


**Figure 3-15** Wide survey X-ray photoelectron spectrum for the MW-synthesized  $V_8C_7$  samples prepared from vanadium metal and carbon in 6 minutes in a MMC microwave reactor.

XPS spectra obtained in the V2p, C1s and O1s regions show peaks that can be ascribed to the presence of vanadium, carbon and oxygen, respectively.

For binding energies ranging from 512 to 527 eV [Figure 3-16], three different vanadium species were observed. The peaks at 513.8 and 521.2 eV are due to the presence of vanadium carbide (VC). The remaining peaks are associated with vanadium oxide species. The peaks at 515.8 and 523.3 eV indicate the presence of vanadium(III) oxide ( $V_2O_3$ ) while the peaks at 517.7 and 525.1 eV support the presence of vanadium(V) oxide ( $V_2O_5$ ). The existence of

these species stands in agreement with the Raman spectra for the  $V_8C_7$  samples and commercial  $V_2O_5$  showing the same characteristic bands (see Section 3.2.3.5).

In the C1s region ranging from 281 to 291 eV [Figure 3-17], four different chemical types of carbon were found. At the lowest energy ( $\sim 283.1$  eV), the peak is associated with the presence of VC, whereas the most intense peak at 284.7 eV is due to the presence of free carbon. This is probably due to the unsuccessful removal of graphite susceptor from sample pellets. Single and double chemical bonding of carbon with oxygen (C–O and C=O) were observed at the highest energies 286.1 and 289.0 eV.

For binding energies ranging from 526 to 534 eV (O1s region), two different types of oxygen species were observed. The peak at 530.2 eV is assigned to the presence of oxides, whereas the peak at 531.8 eV is more indicative of oxygen in an organic compound.

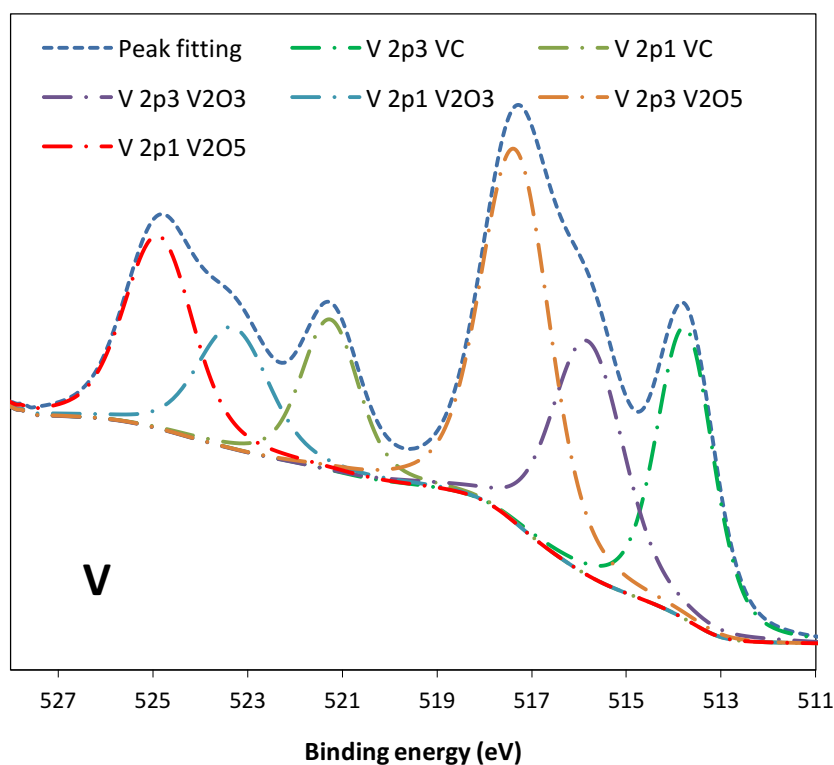


**Figure 3-16** Fitted V2p X-ray photoelectron spectrum for the MW-synthesized  $V_8C_7$  samples prepared from vanadium metal and carbon in 6 minutes in a multi-mode MW reactor.

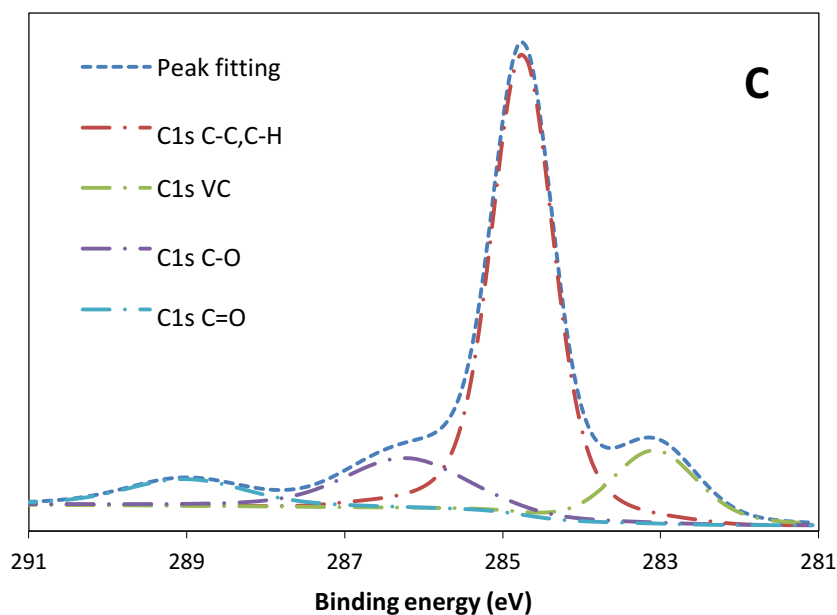


**Figure 3-17** Fitted C1s X-ray photoelectron spectrum for the MW-synthesized  $V_8C_7$  samples prepared from vanadium metal and carbon in 6 minutes in a multi-mode MW reactor.

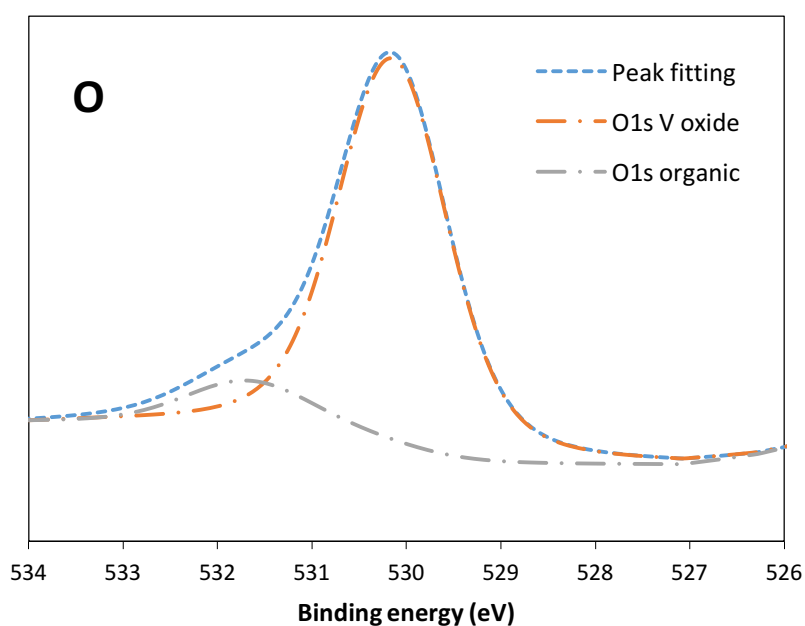


**Figure 3-18** Fitted O1s X-ray photoelectron spectrum for the MW-synthesized  $V_8C_7$  samples prepared from vanadium metal and carbon in 6 minutes in a multi-mode MW reactor.

In light of the XPS results, it is reasonable to conclude that oxygen is indeed present to a depth of 10 nm in the  $V_8C_7$  particles.

The  $V_8C_7$  sample was subsequently subjected to Ar ion etching in order to remove the surface and analyze the bulk of the sample. In this case, a sintered pellet was used rather than loose powder as the etching process is much less effective for the latter. Three etchings

were performed on the same sample. According to the etching rate used, each etching process is expected to remove approximately 3 nm of surface material.<sup>50</sup> It should be noted that prior to the first etching, an additional etching was performed to remove dust from the surface and therefore an additional 3 nm has to be accounted. Therefore, after three etchings 12 nm of surface were in principle removed.

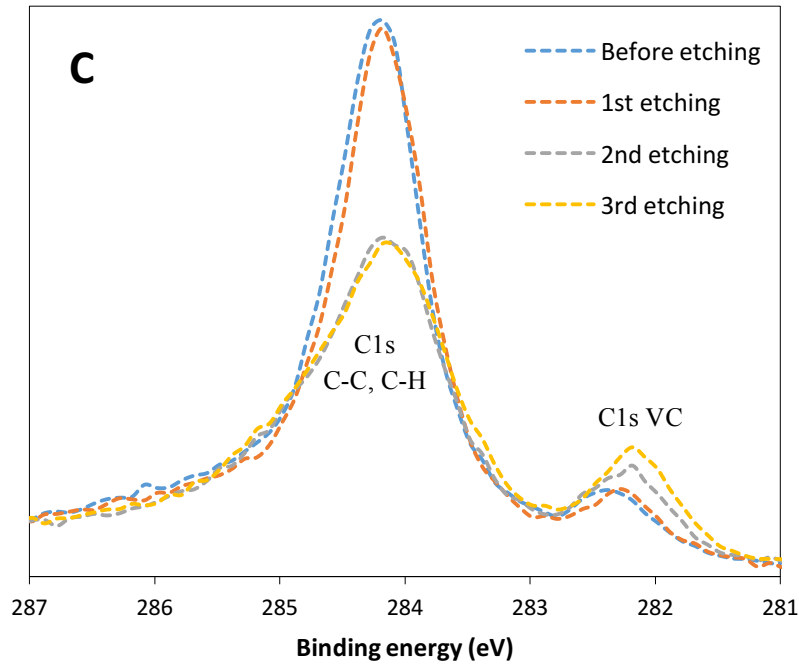


**Figure 3-19** C1s X-ray photoelectron spectrum for the MW-synthesized  $V_8C_7$  prepared from vanadium metal and carbon in 6 minutes in a multi-mode MW reactor after three Ar ion etchings.

Figure 3-19 shows the XPS spectrum of the  $V_8C_7$  samples in the C1s region after each etching. As the etching processes proceed, the peak at ~284 eV (which is assigned to the presence of free carbon) decreases. On the contrary, the peak at ~282 eV (which is assigned to the presence of VC) increases suggesting that the particle surface is surrounded by free carbon from the graphite susceptor.

A similar trend can also be seen in the XPS spectrum of the  $V_8C_7$  sample in the V2p and O1s regions [Figure 3-20]. The peak at ~529 eV in the O1s region (which is associated with the presence of vanadium oxides) decreases with etching. In the V2p region, the peaks at ~515, 523, 517 and 525 eV (which are assigned to the presence of  $V_2O_3$  and  $V_2O_5$ ) decrease after etching, whereas both the peaks due to the presence of VC at ~513 and 521 eV increase.

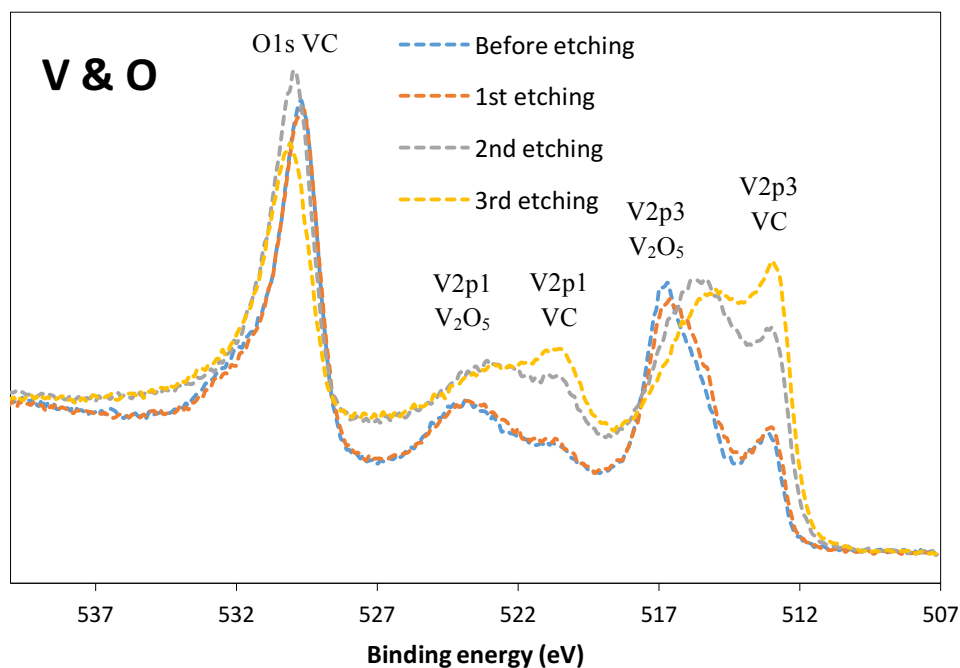


**Figure 3-20** V2p and O1s X-ray photoelectron spectrum for the MW-synthesized  $V_8C_7$  samples prepared from vanadium metal and carbon in 6 minutes in a multi-mode MW reactor after three Ar ion etchings.

In conclusion, XPS measurement confirmed the presence of oxygen at the vanadium carbide surface consistent with Raman spectroscopy. Even after three Ar ion etching processes which removed 12 nm of surface material, vanadium oxide species were still observable although the intensity of the respective peaks was found to decrease, significantly. Thus, oxygen might be present below the 12 nm of surface material removed.

### 3.2.3.7 Powder Neutron Diffraction (PND)

As discussed in the previous section, XPS only gives a measure of the elemental composition at the surface rather than the bulk. A Powder Neutron Diffraction experiment was therefore performed on a powdered  $V_8C_7$  sample synthesized from vanadium metal and carbon in 6 minutes in a MMC reactor at a power of 800 W. PND was used to attempt to establish how much (if any) oxygen was present within the bulk carbide structure as PXRD is not as effective for such purposes. The reason for this lies on the fact that carbon and oxygen are neighboring atoms (6 and 8 electrons in total, respectively) which makes it hard to distinguish them by using X-rays as the latter are diffracted by electrons. On the other hand, neutron diffraction has the ability to discriminate between C and O as neutrons are diffracted by atomic nuclei.

PND data were collected at the ISIS facility on the POLARIS diffractometer. The diffractometer collects data to extremely short d-spacing, as low as 0.3 Å, by utilizing 5 banks of detectors (see Section 2.3.2.1). The sample used for this analysis was prepared from vanadium metal and graphite for 6 minutes under air in a multimode cavity MW reactor at a power of 800 W. The sample was then loaded into a 6-mm vanadium sample can which was centered in the neutron beam for data collection. Data were collected for approximately 2 h at room temperature using 5 detectors banks.

The sample was analyzed by PXRD prior to PND and the structure refined by the Rietveld method against PXRD data [Appendix, Figure 7-7, Tables 7-2, 7-3 and 7-4]. The same data collection parameters and refinement procedure was employed as discussed in Section 3.2.3.2. The structure model used for Rietveld refinements against PXRD data was the cubic  $P4_332$   $V_8C_7$  taken from the ICSD database.<sup>27</sup>

Following the PND scans, the structure was refined by the Rietveld method against PND data, using GSAS<sup>30</sup> and EXPGUI<sup>31</sup> software packages. The structure model used for the Rietveld refinement was again the cubic  $P4_332$   $V_8C_7$  structure.

In initial cycles, the background was refined using a reciprocal interpolation function (function type 8 within GSAS). The unit cell parameter, diffractometer constant DIFA and peak profiles were included. Modelling of the profile parameters was performed using GSAS function type 3, which combines back-to-back exponentials and pseudo-Voigt functions with Lorentzian broadening. The refinement of the V(1) and V(2) atomic coordinates did not lead to any improvement of the goodness of fit parameters but resulted instead in an unstable refinement (convergence not achieved) [Table 3-5]. This is very unusual, though, since those coordinates were always refined in all the previous refinements improving the overall fitting (see Section 3.2.3.2). On the other hand, the C(2) and C(3) atomic coordinates could be refined as usual. Once convergence was achieved, the thermal factors were refined too. Refinement of the site occupancy factors (SOFs) was also attempted, but resulted in an unstable refinement (with no improvement of the goodness of fit parameters or bond distances) and/or in inconsistent values. All the SOFs were therefore fixed at 1.0 in the final refinement.

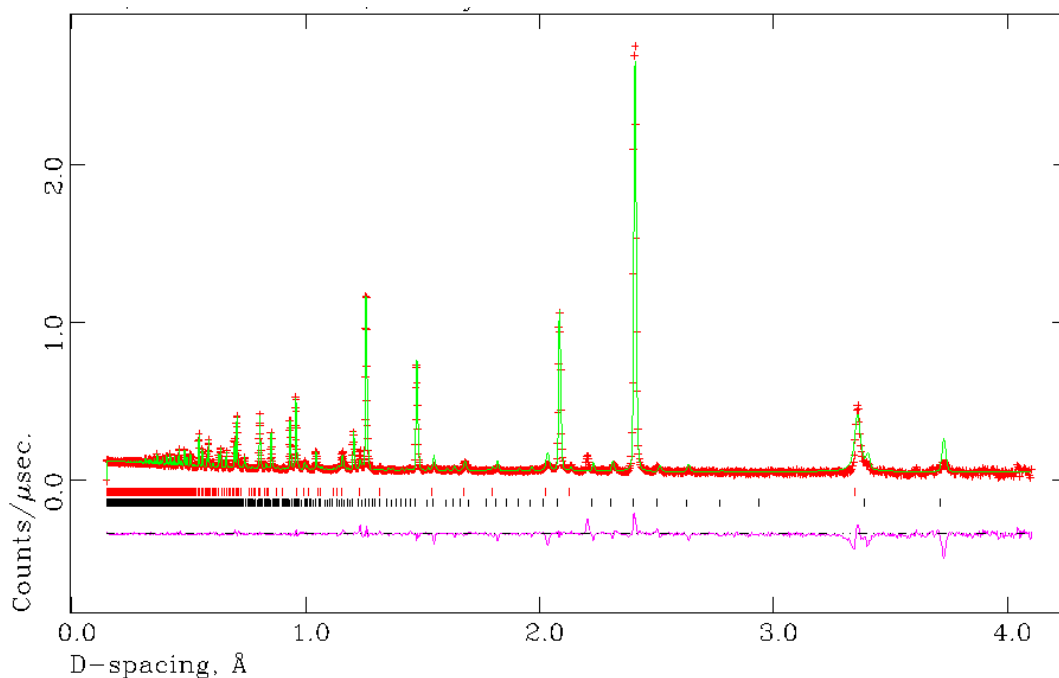


**Figure 3-21** OCD plot from POLARIS bank 4 generated by Rietveld refinement against vanadium carbide PND data using the cubic  $P4_332$   $V_8C_7$  structure model taken from the ICSD database. Data collected at room temperature for approx. 2 hours. The red tick marks indicate reflections from graphite and the black tick marks indicate reflections from  $V_8C_7$ .

**Table 3-4** Crystallographic data from Rietveld refinement against PND data for  $V_8C_7$  synthesized from vanadium metal and graphite heated in a MMC for 6 minutes at a power of 800 W.

<b>Phase data</b>	
Chemical Formula	$V_8C_7$
Crystal system	Cubic
Space group	$P4_332$
$a$ (Å)	8.33053(6)
Volume (Å <sup>3</sup> )	576.40(1)
$Z$	4
Formula weight (g mol <sup>-1</sup> )	491.61
Calculated density (g cm <sup>-3</sup> )	5.6121
$R_{wp}$	0.0597
$R_p$	0.0968
$\chi^2$	6.366

**Table 3-5** Atomic parameters from Rietveld refinement against PND data for  $V_8C_7$  synthesized from vanadium metal and graphite heated in a MMC for 6 minutes at a power of 800 W.

Atomic parameters						
Atom Type	Wyckoff Site	Fractional Coordinates			$U_{iso}$ ( $\text{\AA}^2$ )	Site Occupancy
		$x/a$	$y/b$	$z/c$		
V(1)	8c	0.3750	0.3750	0.3750	0.00453(5)	1.0
V(2)	24e	0.1250	0.3750	0.1250	0.00453(5)	1.0
C(1)	4a	0.1250	0.1250	0.1250	0.00278(3)	1.0
C(2)	12d	0.1250	0.6260(4)	0.6240(2)	0.00278(3)	1.0
C(3)	12d	0.1250	0.3753(2)	0.8747(5)	0.00278(3)	1.0

Figure 3-21 shows the Rietveld refinement against PND data for the MW-synthesized  $V_8C_7$ . It can be seen that there are a small number of weaker reflections which are not fitted by the  $V_8C_7$  model. A mismatch in position is observed for the peak at  $d \sim 2.14$   $\text{\AA}$  which was initially thought to be vanadium metal from either the sample can or an impurity in the sample. This was then added to the refinement as a third phase and subsequently excluded as it did not improve the peak fitting. Moreover, some problems with the peak width fitting at  $\sim 18$  milliseconds and an intensity mismatch for the reflection at  $\sim 20$  milliseconds are observed. These issues suggest that the cubic  $V_8C_7$  structure model used may not be completely correct. The PND data was then indexed using to establish whether the  $P4_332$  space group proposed by de Novion *et al.* (1977)<sup>6</sup> is indeed correct or not. Unfortunately, no other space groups were found to match up with the PND data. The V–V and V–C atomic distances are consistent with values derived from PXRD data (Section 3.2.3.2) and are shown in the Appendix, Table 7-5, together with the bond angles.

Gusev *et al.* (2015) recently studied the crystal structure of the  $V_8C_7$  phase through Neutron and X-ray diffraction in both macro- and nanocrystalline powders.<sup>33</sup> They found and confirmed what previous studies from other authors had shown,<sup>4,5</sup> that is  $V_8C_7$  crystallizes with a cubic NaCl-type superstructure in space group  $P4_332$ .

In summary, although the refinement is not satisfactory, it would appear that the space group is likely correct. Further structural characterization is needed to provide a definite model and, unfortunately, it was not possible to measure the amount of oxygen inclusion within the sample from the PND data.

### 3.3 Microwave Synthesis Studies in the V<sub>2</sub>O<sub>5</sub>–C system

This section describes experimental work undertaken to establish a synthetic route to vanadium carbide from vanadium(V) oxide and carbon in both a MMC and a SMC.

#### 3.3.1 Introduction

The reactions discussed in this section were carried out by carbothermal reduction of vanadium(V) oxide (V<sub>2</sub>O<sub>5</sub> + C) using microwave heating. The starting materials were mixed according to the following reactions:



In the carbothermal reduction of V<sub>2</sub>O<sub>5</sub>, a significant amount of carbon monoxide (CO) is released [Equation (3-4)]. It was observed that the rapid gas evolution led to fracturing of the pellet or, in some cases, delamination. It was found that a direct reaction of elemental powders was more suitable for the reaction set-up, preventing this fracturing and the subsequent loss of material.

#### 3.3.2 Experimental

##### Synthesis

All reactions reported in this section were performed in air by mixing and grinding together vanadium(V) oxide (Sigma Aldrich, 99.6%) and graphite (Sigma Aldrich, < 50 μm, 99.5%), in a stoichiometric ratio of 4:27 according to Equation (3-4). The so-obtained powder mixture (0.5 g) was uniaxially cold pressed into a pellet and the use of a binder was found to be crucial. The binder consisted of a 5% PVA (polyvinyl alcohol) solution in distilled water. 0.5 ml portions of the binder solution were used for each pellet. The compact was embedded in graphite powder (used as a MW susceptor) within a 10-mm quartz tube. The tube was sealed with a red rubber stopper, parafilm and subsequently connected to Ar flow. The MW reactions were conducted by using either a multi-mode or a single-mode cavity reactors.

For multimode cavity experiments, the tube containing the sample was placed in the center of a beaker containing silica powder which stabilizes the tube and acts as a thermal

insulator [Figures 1-6 and 1-7]. The whole apparatus was then inserted into the multimode cavity of a domestic MW oven (DMO) and positioned in a consistent location within the cavity to keep the experimental parameters as constant as possible. Synthesis was conducted for 6 minutes at a power of 800 W.

For single-mode cavity experiments, the tube was placed directly into the applicator of the SMC reactor and held by a stand [Figures 1-10 and 1-11]. Synthesis was conducted for 2 minutes at a power of 1 kW.

After the reaction went to completion, the pellet was found to be fractured or disintegrated. This made it impossible to collect among the graphite susceptor. As the microwave reaction proceeds fast, so does the carbon monoxide (CO) evolution. Once released, the gas tends to break the pellet contributing to the aforementioned problem. Nonetheless, despite these issues, the carbothermal reduction of  $V_2O_5$  using microwave heating showed similar reaction times to those found in the direct reaction of elemental starting materials (V + C) [Section 3.2.2].

### **Characterization**

Products were characterized using several analytical techniques. Powder X-ray Diffraction (PXRD) [Section 2.3.1] was used to identify product phases by reference to calculated patterns from known structures downloaded from the Inorganic Crystal Structure Database (ICSD)<sup>27</sup> using the PowderCell 2.3 software.<sup>28</sup> The data was collected on a PANalytical Xpert MPD, Cu  $K\alpha$ 1 radiation, for 1 hour over a range of  $10 < 2\theta^\circ < 85$ . Crystallographic parameters were obtained by Rietveld refinement [Section 2.3.3] against powder XRD data collected for ca. 12 hours over a range of  $10 < 2\theta^\circ < 110$  using GSAS and EXPGUI software packages. Sample morphology and elemental composition were investigated by Scanning Electron Microscopy (SEM) and Energy-dispersive X-ray Spectroscopy (EDX) [Section 2.3.4]. Additional characterization was performed by Raman spectroscopy [Section 2.3.5]. Raman data were collected at room temperature using a Horiba LabRAM confocal microscope system with a 532-nm green laser. Surface analysis was evaluated by X-ray Photoelectron Spectroscopy (XPS) [Section 2.3.6] using a Thermo Scientific K-Alpha+ X-ray photoelectron spectrometer with monochromatic Al  $K\alpha$  radiation (1486.7 eV).

### 3.3.3 Results and Discussion

#### 3.3.3.1 Powder X-ray Diffraction (PXRD)

After a 6-minute reaction in the multimode cavity, the sample was analyzed by *ex-situ* Powder X-ray Diffraction. The PXRD pattern for the so-obtained sample is shown in Figure 3-22. Similar results were obtained after a 2-minute reaction in the single-mode cavity (PXRD pattern shown in the Appendix, Figure 7-8).

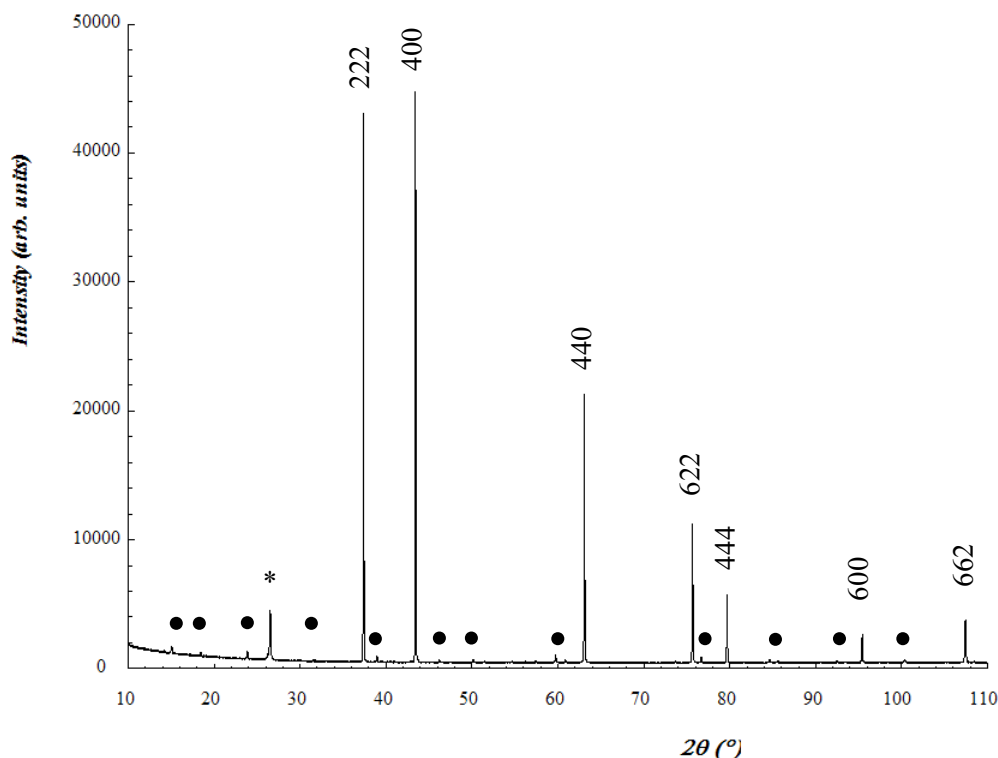


**Figure 3-22** PXRD pattern taken *ex-situ* from vanadium(V) oxide plus graphite (4:27) heated for 6 minutes in an MMC microwave reactor at a power of 800 W. All reflections can be attributed to  $V_8C_7$  except the one marked with \*, which belongs to the (002) reflection from graphite. The reflections marked with • are superstructure lines characteristic of the  $V_8C_7$  phase.

As was observed for the vanadium metal + carbon reactions, the product was identified as the vanadium carbide,  $V_8C_7$  (cubic, space group  $P4_332$ ), in each case. The PXRD pattern consists of seven intense, sharp peaks characteristic of a NaCl-type structure plus several low-intensity superstructure lines characteristics for the  $V_8C_7$  phase. It was noted that, for  $V_2O_5 + C$  reactions, the intensity of the graphite reflection (marked with \* in Figure 3-22) is higher than that for the  $V + C$  reactions. Presumably, this is a consequence of the fracturing of the  $V_2O_5 + C$  pellet as CO gas evolves during the microwave reaction. Therefore, the graphite susceptor becomes integrated with the fractured pellet which makes its removal

harder. Consequently, during the carbothermal reduction of  $V_2O_5$ , a greater amount of unremoved graphite susceptor is seen.

### 3.3.3.2 Rietveld Refinement

The structure of the  $V_8C_7$  product prepared from vanadium(V) oxide and graphite was solved by the Rietveld method against PXD data, collected for 12 hours over a range of  $10 < 2\theta/^\circ < 110$  with a step size of  $0.017^\circ$  ( $2\theta$ ) using GSAS and EXPGUI software packages.<sup>30,31</sup> The structure model used is the same as that one in Section 3.2.3.2 proposed by de Novion *et al.*<sup>6</sup> [Figure 3-4].

The procedure used for these refinements is essentially the same as that used for the  $V_8C_7$  samples synthesized from V + C powders (see Section 3.2.3.2). The background was refined first, followed by cell parameters, scale factors and zero point. Subsequently, peak shape parameters and atomic parameters were modelled. A similar displacement is observed for the vanadium and carbon atoms surrounding the carbon vacancy which are shifted towards the center of the non-metal position. Also in this case, the isotropic thermal factors ( $U_{iso}$ ) of the vanadium sites V(1) and V(2) and carbon sites C(1), C(2) and C(3) were constrained to have the same values as the refinement would not achieve convergence otherwise. Refinement of the site occupancy factors (SOFs) resulted in an unstable refinement (with no improvement of the goodness of fit parameters or bond distances) and/or in inconsistent values. All the SOFs were therefore fixed at 1.0 in the final refinement.

The Rietveld refinement against PXRD data is illustrated in Figure 3-23. The calculated lattice parameter is  $a = 8.3362(1) \text{ \AA}$  which is slightly higher than that one obtained for  $V_8C_7$  from the V + C reactions. Henfrey *et al.* (1970) suggested that a higher unit cell parameter can arise from oxygen content in the sample.<sup>4</sup> The presence of residual oxide in the carbide lattice could be one reason why the  $V_2O_5 + C$  samples show a slightly higher unit cell parameter than the V + C samples.

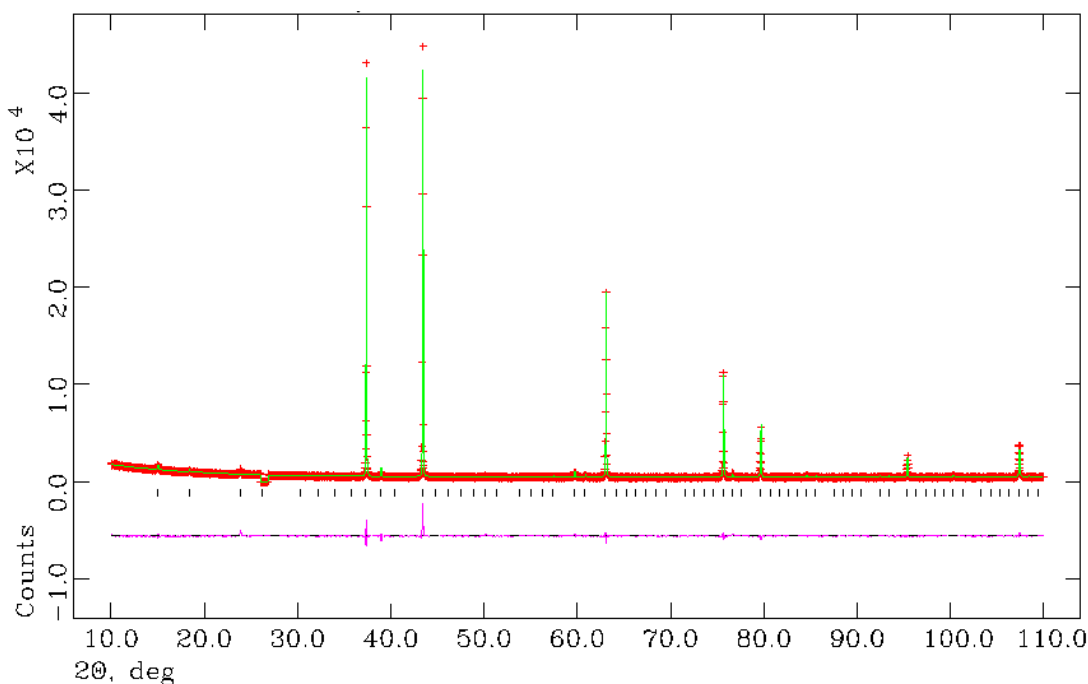


**Figure 3-23** Observed (*plusses*), calculated (*solid green line*), and difference (*solid purple line*) profile plot for the Rietveld refinement against PXRD data for the vanadium carbide superstructure  $V_8C_7$ . Tick marks denote  $V_8C_7$  diffraction peaks. The (002) graphite reflection at  $2\theta = 26.5^\circ$  was excluded from the refinement.

The calculated crystallographic data and atomic parameters are illustrated in Table 3-6 and Table 3-7, respectively.

**Table 3-6** Crystallographic data from Rietveld refinement against PXRD data for  $V_8C_7$  prepared from vanadium(V) oxide and carbon in 6 minutes in an MMC reactor at a power of 800 W.

<b>Phase data</b>	
Chemical Formula	$V_8C_7$
Crystal system	Cubic
Space group	$P4_332$
$a$ (Å)	8.33615(3)
Volume (Å <sup>3</sup> )	578.68(2)
$Z$	4
Formula weight (g mol <sup>-1</sup> )	491.61
Calculated density (g cm <sup>-3</sup> )	5.6365
$R_{wp}$	0.0608
$R_p$	0.0440
$\chi^2$	2.559

**Table 3-7** Atomic parameters from Rietveld Refinement against PXRD data for  $V_8C_7$  prepared from vanadium(V) oxide and carbon in 6 minutes in an MMC reactor at a power of 800 W.

<b>Atomic parameters</b>						
Atom Type	Wyckoff Site	Fractional Coordinates			$U_{iso}$ ( $\text{\AA}^2$ )	Site Occupancy
		$x/a$	$y/b$	$z/c$		
V(1)	8c	0.3701(4)	0.3701(4)	0.3701(4)	0.0117(3)	1.0
V(2)	24e	0.1270(1)	0.3821(1)	0.1310(4)	0.0117(3)	1.0
C(1)	4a	0.1250	0.1250	0.1250	0.0102(1)	1.0
C(2)	12d	0.1250	0.6088(4)	0.6411(2)	0.0102(1)	1.0
C(3)	12d	0.1250	0.3543(2)	0.8956(3)	0.0102(1)	1.0

The bond lengths and angles of the  $V_8C_7$  sample obtained from vanadium(V) oxide and graphite in 6 minutes in a MMC reactor are listed in Table 7-6 in the Appendix. These values are slightly different to those reported for the  $V_8C_7$  prepared from V + C in Section 3.2.3.2 but in good agreement with V–V and V–C bond lengths reported in previous studies.<sup>33,34</sup>

### 3.3.3.3 *Ex-situ* Study of the $V_2O_5 + C$ Reaction as a Function of Time

The phase evolution as a function of time for both multimode and single-mode cavity experiments, which revealed information on possible reaction mechanisms, was investigated by *ex-situ* PXRD experiments. The data provided useful information on the progress of the reactions in each case.

Figure 3-24 illustrates the PXRD patterns collected after the  $V_2O_5 + C$  pellets had been irradiated with MWs for 0 s, 30 s, 1 min, 2 mins and 6 mins in an MMC reactor. At the start of the reaction ( $t = 0$ ), only the reflections from the vanadium(V) oxide and graphite starting materials are detectable. After 30 s of MW irradiation, the amount of free carbon present in the sample has slightly decreased while almost all the starting vanadium(V) oxide ( $V_2O_5$ ) has reacted to produce vanadium(III) oxide ( $V_2O_3$ ). Also, a few extra low-intensity peaks (unlabeled) are observed which could not be characterized. As time proceeds from  $t = 30$  s to  $t = 1$  min, vanadium carbide reflections start to appear while the peaks belonging to free carbon continues to decrease in intensity. From  $t = 1$  min to  $t = 2$  min, the intensity of the vanadium carbide reflections increases, the peak widths become narrower and the remaining graphite is diminished. Unlike in the direct reaction of the elemental powders (V metal + C)

discussed in Section 3.2.3.3, the  $V_8C_7$  reflections seem to be symmetrical in the carbothermal reduction of vanadium pentoxide. As the reaction goes to completion ( $t = 6$  min), highly crystalline  $V_8C_7$  is obtained together with a small impurity of graphite which likely originates from residual susceptor. The PXRD patterns for the  $V_2O_5 + C$  pellets after 0 sec, 30 sec, 1 min and 2 min of MW irradiation are shown separately in Figures 7-9 to 7-12 in the Appendix.

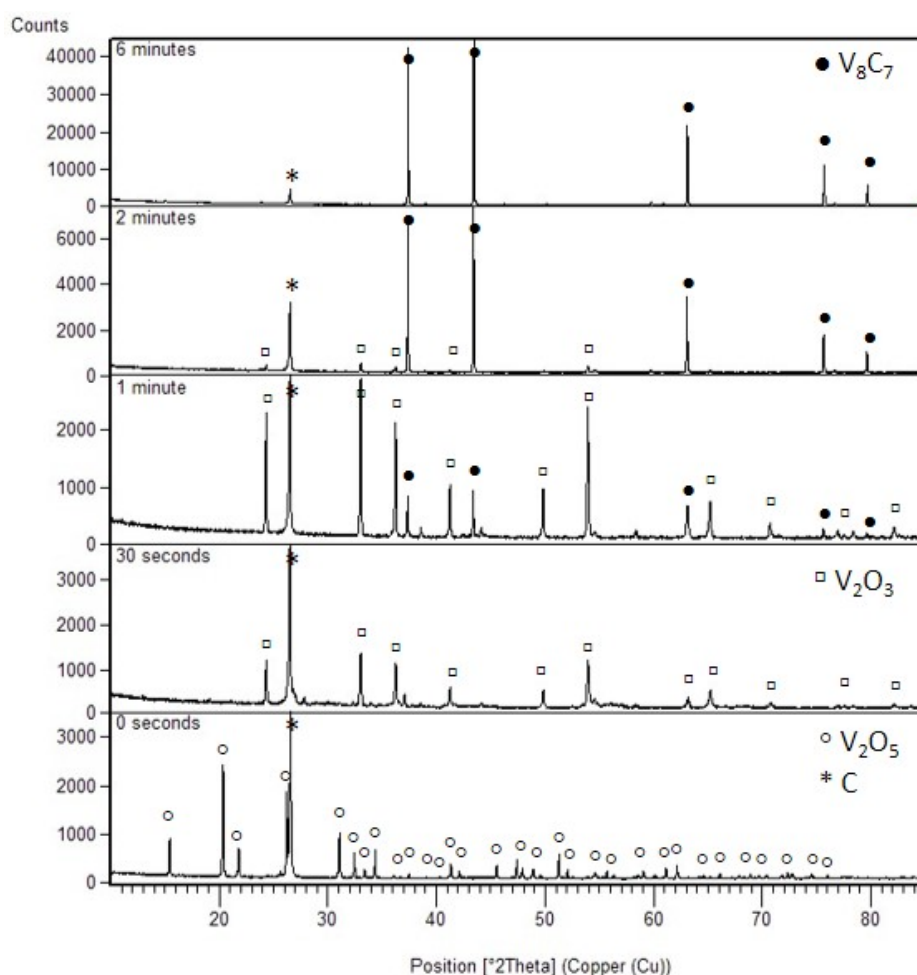


**Figure 3-24** Ex-situ patterns for  $V_2O_5 + C$  pellets heated for 6 minutes in an MMC reactor at a power of 800 W from reagents (bottom) to reaction completion (top).

The reaction mechanism for the single-mode cavity synthesis is similar to that for the multimode cavity experiments, but shorter reaction times are observed. Figure 3-25 illustrates the PXRD patterns collected after the  $V_2O_5 + C$  pellets had been irradiated with MWs for 0 s, 10 s, 1 min and 2 mins in a single-mode MW reactor. At  $t = 0$ , only reflections from reagents vanadium(V) oxide and graphite starting materials are present. After 10 s of MW irradiation, almost all  $V_2O_5$  has been converted to  $V_2O_3$ . As the reaction proceeds, the intensity of the vanadium(III) oxide reflections decreases while the intensity of the vanadium

carbide reflections increases until a single phase of  $V_8C_7$  is obtained after just 2 minutes of MW irradiation.

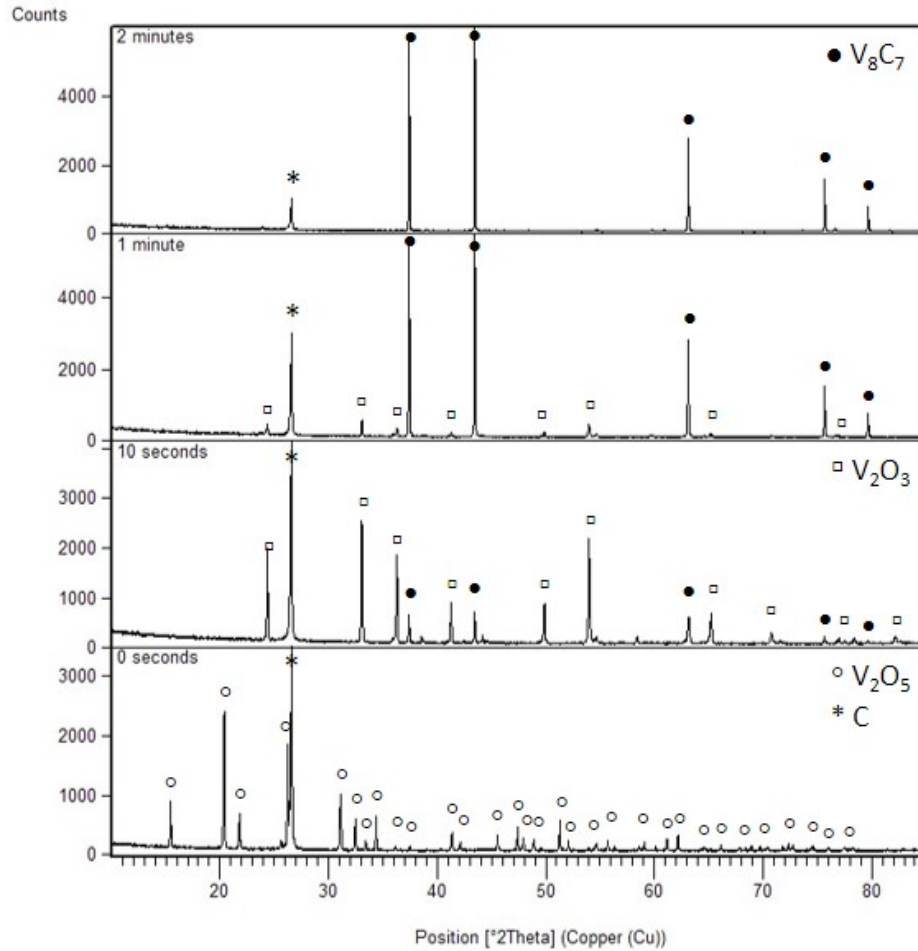


**Figure 3-25** Ex-situ patterns for  $V_2O_5 + C$  pellets heated for 2 minutes in a SMC reactor at a power of 1kW from reagents (bottom) to reaction completion (top).

As discussed in Section 3.3.3.1, the amount of carbon impurity is lower for the  $V_8C_7$  samples synthesized from  $V + C$  pellets compared to those prepared from  $V_2O_5 + C$  pellets probably due the CO evolution, during reaction which fractures the pellets and allows the graphite susceptor to enter the cracks.

Taking together the results presented in Figure 3-24 and Figure 3-25, the single-mode MW reactor appears evidently much faster compared to its multimode counterpart (a domestic MW oven in this case). The reaction time for the synthesis of vanadium carbide from vanadium(V) oxide and graphite in a multimode cavity MW reactor (6 minutes) can be reduced by one third (2 minutes) by employing a single-mode MW reactor, although these reactors are not directly comparable since it is not possible to measure effective power absorbed by the sample in the MMC reactor.

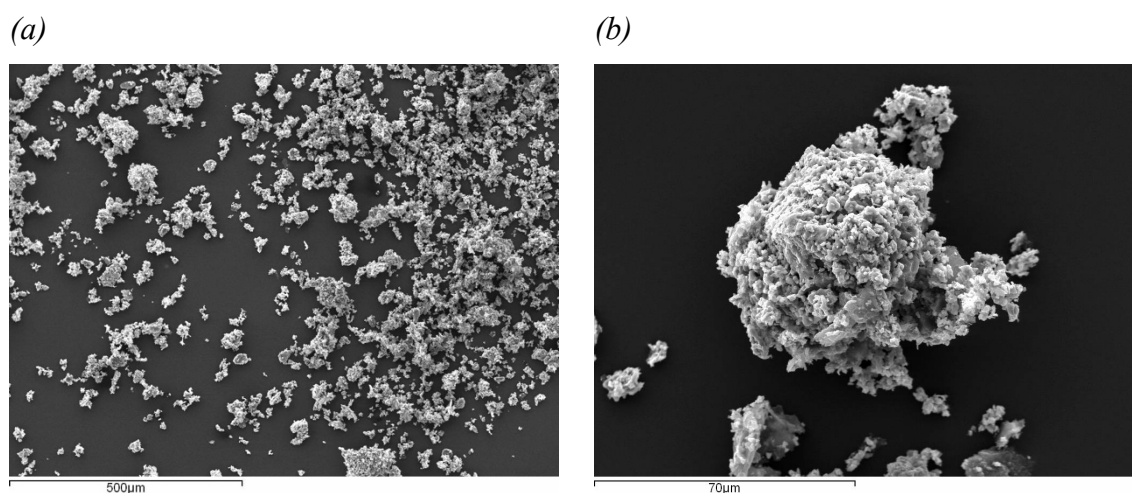
This *ex-situ* study of the  $V_2O_5 + C$  reaction as a function of time suggests that the reaction mechanism involves the reduction of the vanadium atom from  $V_2O_5$  to  $V_2O_3$  to VC. No other stable, observable intermediates are identified throughout the reaction.

As already explained, acquisition of more detailed mechanistic information would require investigation *in-situ*. The latter relies on the development of a customized single-mode MW reactor, specifically designed to perform time-resolved experiments by means of powder X-ray diffraction (PXRD) or, even better, powder neutron diffraction (PND).

### 3.3.3.4 Scanning Electron Microscopy (SEM) coupled with Energy-dispersive X-ray Spectroscopy (EDX)

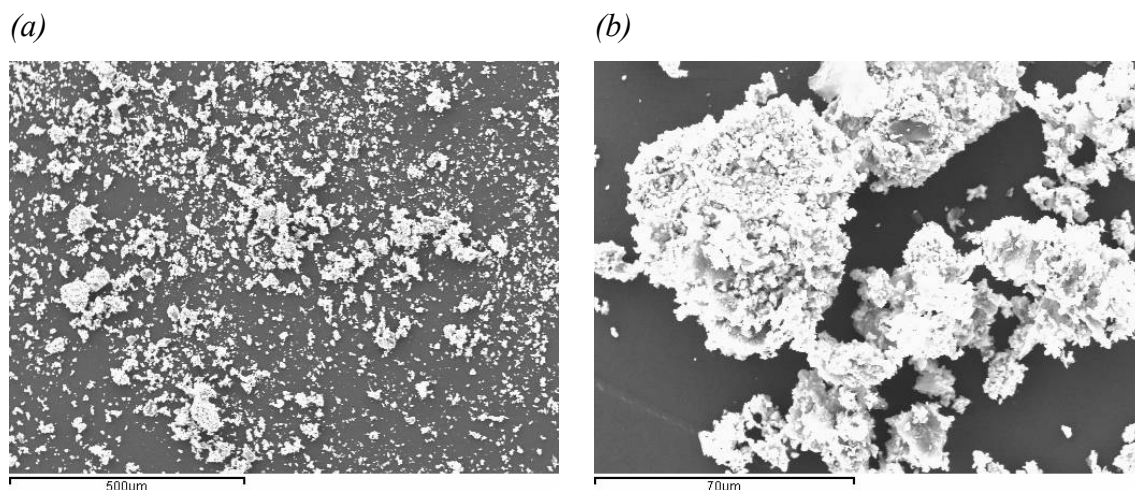
The MW-synthesized  $V_8C_7$  powders prepared from vanadium(V) oxide and graphite were also analyzed for particle size, particle morphology and distribution by Scanning Electron Microscopy (SEM).

Figure 3-26 illustrates the SEM micrographs for the  $V_8C_7$  samples synthesized in an MMC reactor at a power of 800 W. Similarly to the equivalent  $V + C$  reaction, the microwave reaction between  $V_2O_5$  and carbon yields irregular micron-scale  $V_8C_7$  particles, typically with dimensions of a few microns to a maximum of approximately 100  $\mu\text{m}$ . The main difference between the products from the direct reaction of elemental powders ( $V + C$ ) and those from the carbothermal reduction of vanadium(V) oxide ( $V_2O_5 + C$ ) is that the latter reaction produces more porous particles with rougher surfaces. This might be due to the fact that CO gas is released during the reaction (see Equation (3-4)) which hence causes the more porous microstructure observed by SEM.



**Figure 3-26** SEM micrographs for the MW-synthesized  $V_8C_7$  from vanadium(V) oxide and carbon in a MMC reactor at a power of 800 W.

Figure 3-27 shows the SEM micrographs for the  $V_8C_7$  samples synthesized in the single-mode cavity microwave reactor at a power of 1 kW. Particles are very similar to those obtained from the MMC reaction, with dimensions ranging from a few microns to 100  $\mu m$ .



**Figure 3-27** SEM micrographs for the MW-synthesized  $V_8C_7$  from vanadium(V) oxide and carbon in a single-mode cavity (SMC) microwave reactor at a power of 1 kW.

EDX data were also collected for the particles obtained after the carbothermal reduction/carburization of  $V_2O_5$ . In Section 3.2.3.4, it was shown how some EDX spectra suggested that the only elements present in the samples were vanadium and carbon whereas some others supported the inclusion of oxygen within the  $V_8C_7$  particles. Similar results were obtained for the carbothermal reduction/carburization of  $V_2O_5$ .

### 3.3.3.5 Raman Spectroscopy

Raman spectroscopy was employed to perform further characterization. Figure 3-28 shows the Raman spectrum of the  $V_8C_7$  synthesized from vanadium(V) oxide and graphite in a multi-mode cavity MW reactor. Like the samples synthesized from V and C, the Raman spectrum is very similar to that for  $V_2O_5$  (see Section 3.2.3.5) which, again, suggests the presence of oxygen in the samples.

Table 3-8 shows the Raman shifts for both  $V_8C_7$  and commercial  $V_2O_5$  (used as a starting material) and the respective assignments. For a description of the assignment of each Raman band to the respective stretching mode, see Section 3.2.3.5.

The Raman spectra for the  $V_8C_7$  samples synthesized from  $V_2O_5$  and C suggests that oxygen is included either within the bulk structure or just on the surface of particles. Such

results were expected since the samples synthesized from vanadium oxide (which obviously contains oxygen) were treated under the same conditions as the samples synthesized from vanadium metal.

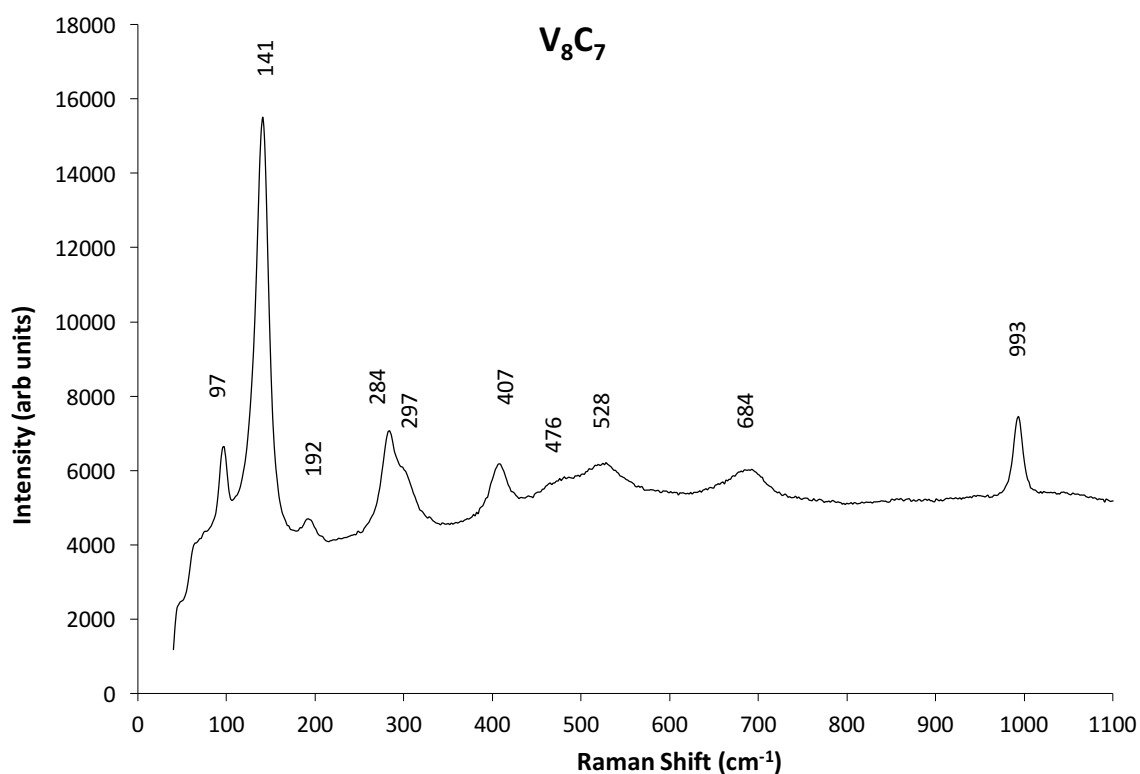


**Figure 3-28** Experimental Raman spectrum for the MW-synthesized  $V_8C_7$  from vanadium(V) oxide and carbon in an MMC at a power of 800 W.

**Table 3-8** Raman shifts of the MW-synthesized  $V_8C_7$  from vanadium(V) oxide and carbon in an MMC at a power of 800 W and commercial  $V_2O_5$  and their assigned symmetry modes.

$V_8C_7$ Raman Shift ( $cm^{-1}$ )	$V_2O_5$ Raman Shift ( $cm^{-1}$ )	Assignment
97	103	$A_g$
141	144	$B_{1g} + B_{3g}$
192	197	$A_g$
284	286	$B_{3g}$
297	300	$B_{2g}$
407	410	$A_g$
476	478	$A_g$
528	530	$A_g$
684	695	$B_{2g}$
993	997	$A_g + B_{2g}$

### 3.3.3.6 X-ray Photoelectron Spectroscopy (XPS)

The chemical nature of the  $V_8C_7$  surface was analyzed by XPS. The wide survey XPS spectrum for the MW-synthesized  $V_8C_7$  samples prepared from vanadium metal and carbon in both multimode and single-mode MW reactors is shown in Figure 3-29. As suggested by Raman spectroscopy, XPS spectra obtained in the V2p, C1s and O1s regions have shown peaks ascribed to the presence of vanadium, carbon and oxygen, respectively. Figure 3-30, Figure 3-31 and Figure 3-32 show the binding energies from 512-527 eV (V2p), 281-291 eV (C1s) and 526-534 eV (O1s), respectively.

In the V2p region (binding energies ranging from 512 to 527 eV) [Figure 3-30], three different vanadium species were observed. The peaks at 513.8 and 521.2 eV are due to the presence of vanadium carbide (VC) whereas the remaining peaks are associated with vanadium oxide species. The peaks at 515.8 and 523.3 eV indicate the presence of vanadium(III) oxide ( $V_2O_3$ ) while the peaks at 517.7 and 525.1 eV support the presence of vanadium(V) oxide ( $V_2O_5$ ). The existence of these species stands in agreement with the

Raman spectra for the  $V_8C_7$  samples and commercial  $V_2O_5$  showing the same characteristic bands (see Section 3.2.3.5).

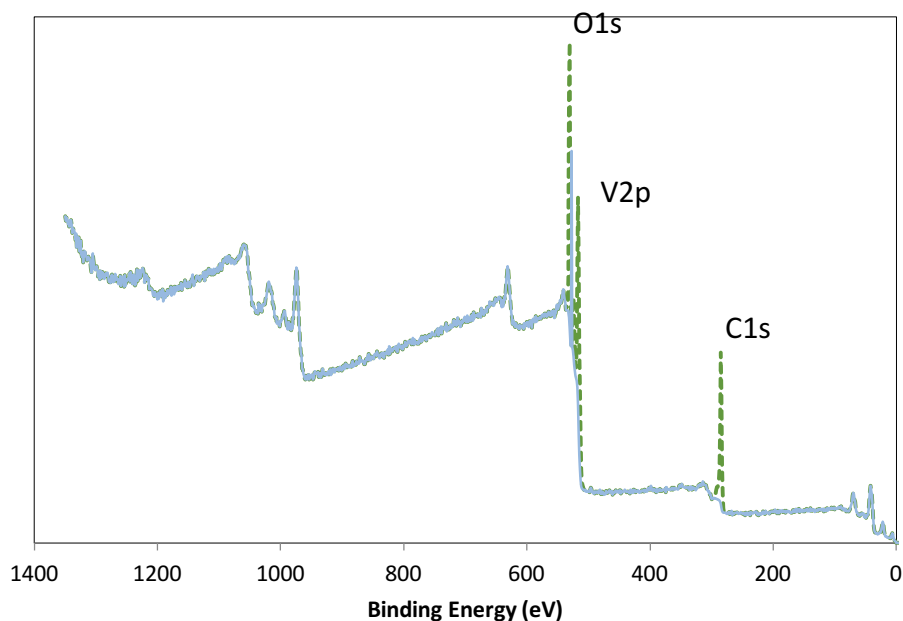


**Figure 3-29** Wide survey X-ray photoelectron spectrum for the MW-synthesized  $V_8C_7$  sample prepared from  $V_2O_5 + C$  powders in an MMC reactor at a power of 800 W.

In the C1s region ranging from 281 to 291 eV [Figure 3-31], four different chemical types of carbon were found. At the lowest energy ( $\sim 283.1$  eV), the peak is associated with the presence of VC, whereas the most intense peak at 284.7 eV is due to the presence of free carbon. This is probably due to the unsuccessful removal of graphite susceptor from sample pellets. Single and double chemical bonding of carbon with oxygen (C–O and C=O) were observed at the highest energies 286.1 and 289.0 eV.

For binding energies ranging from 526 to 534 eV (O1s region) [Figure 3-32], two different types of oxygen species were observed. The peak at 530.2 eV is assigned to the presence of oxides, whereas the peak at 531.8 eV is more indicative of oxygen in an organic compound.

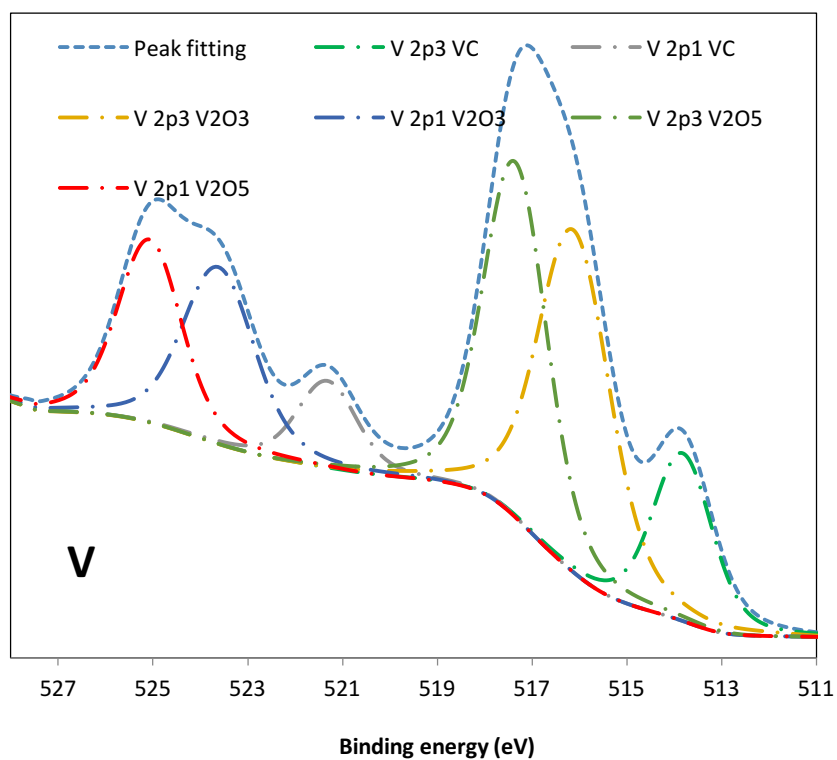


**Figure 3-30** Fitted V2p X-ray photoelectron spectrum for the MW-synthesized  $V_8C_7$  sample prepared from  $V_2O_5 + C$  powders in an MMC reactor at a power of 800 W.

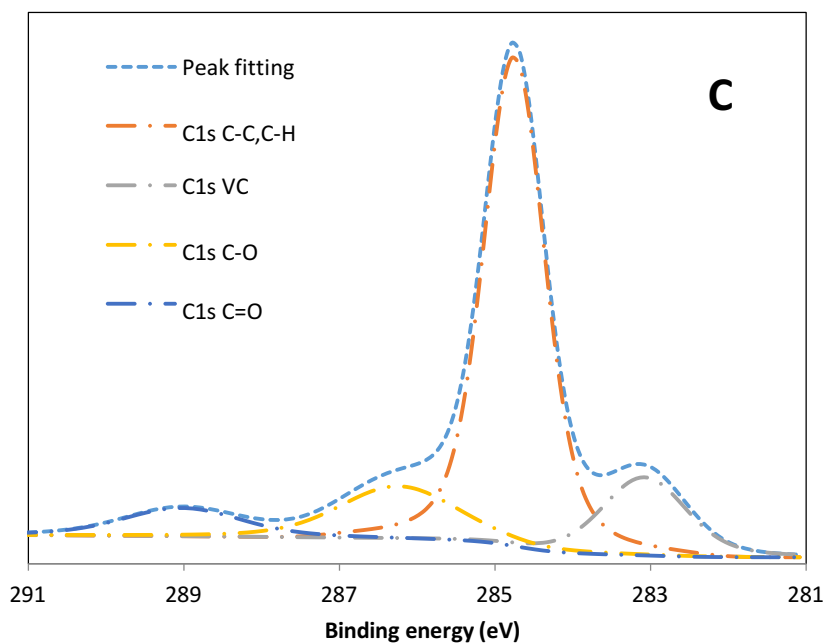


**Figure 3-31** Fitted C1s X-ray photoelectron spectrum for the MW-synthesized  $V_8C_7$  samples prepared from  $V_2O_5 + C$  powders in an MMC reactor at a power of 800 W.

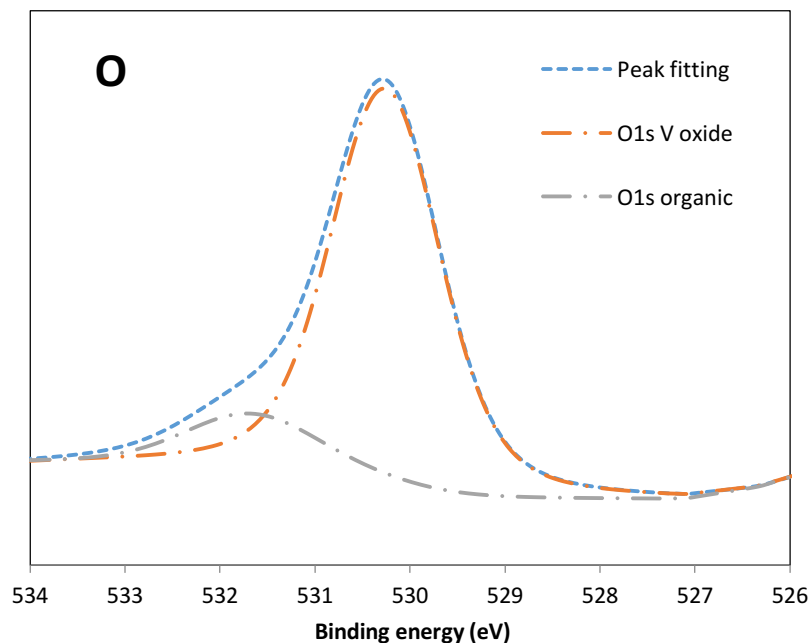


**Figure 3-32** Fitted O1s X-ray photoelectron spectrum for the MW-synthesized  $V_8C_7$  samples prepared from  $V_2O_5 + C$  powders in an MMC reactor at a power of 800 W.

The  $V_8C_7$  sample was also subjected to Ar ion etching in order to remove the surface and analyze the core of the sample. Three etchings were performed on the same sample which removed 12 nm of surface in total. After this process, vanadium oxide species were still observed although the intensities of the respective oxide-associated peaks slightly decrease as the surface layers are removed. It appears therefore that oxygen is present on the surface of particles and its amount gradually decreases in deeper layers. Unfortunately, it was not possible to run any neutron diffraction experiments on the  $V_8C_7$  sample obtained from vanadium pentoxide and carbon due to time limitations, but this will also be the subject of future works. Once a PND pattern of such sample is collected, this will be compared to that of the  $V_8C_7$  sample obtained from the direct reaction of the elemental powders (V metal + C) to establish whether the two samples have different or comparable amount of oxygen (if any) dissolved in them.

### 3.4 Chapter Summary

The scope of this work was to synthesize vanadium carbide by direct reaction of elemental powders (V + C) and carbothermal reduction/carburization of vanadium(V) oxide ( $V_2O_5 + C$ ) using either a multi- or a single-mode MW reactors. Once an appropriate

synthetic route and reaction conditions were established, the resulting products were characterized by PXRD, SEM/EDX, Raman Spectroscopy, XPS and PND.

Vanadium carbide can be synthesized from vanadium metal and carbon or vanadium(V) oxide and carbon under Ar in 6 minutes using an MMC reactor at a power of 800 W and in 2 minutes using a SMC reactor at a power of 1 kW. Rietveld refinement against PXRD data confirmed the formation of the vanadium carbide superstructure,  $V_8C_7$ , as a single phase (together with a small amount of graphite, originating from susceptor) which crystallizes in a cubic structure (space group  $P4_332$ ) with lattice parameter  $a = 8.3312(4)$  Å (for the V + C reaction) and  $a = 8.33615(3)$  Å (for the  $V_2O_5$  + C reaction). SEM micrographs and EDX spectra showed the formation of irregular micron-scale particles with dimensions ranging from a few microns to a maximum of 100  $\mu\text{m}$  with a relatively rough surface containing vanadium, carbon and, at times, oxygen (although an inert atmosphere of Ar was employed). The oxygen inclusion evidence was also supported by Raman Spectroscopy. Raman spectra of the MW-synthesized products showed indeed bands which could be attributed to vanadium(V) oxide ( $V_2O_5$ ). XPS analysis together with Ar ion etching confirmed the presence of oxygen in the  $\sim 12$  nm of the surface material removed. PND investigation of the V + C sample synthesized in a MMC reactor aiming at evaluating the C and O occupancies of the final products was unfortunately unsuccessful and needs therefore to be repeated as part of future works.

### 3.5 References

1. Okamoto, H. C-V (Carbon-Vanadium). *J. Phase Equilibria Diffus.* **31**, 91–92 (2010).
2. Storms, E. K. & McNeal, R. J. The Vanadium-Vanadium Carbide System. *J. Phys. Chem.* **66**, 1401–1408 (1962).
3. Lipatnikov, V. N. *et al.* Effects of vacancy ordering on structure and properties of vanadium carbide. *J. Alloys Compd.* **261**, 192–197 (1997).
4. Henfrey, A. W. & Fender, B. E. F. A neutron diffraction investigation of  $V_8C_7$ . *Acta Crystallogr. Sect. B* **26**, 1882–1883 (1970).
5. Rafaja, D., Lengauer, W., Ettmayer, P. & Lipatnikov, V. N. Rietveld analysis of the ordering in  $V_8C_7$ . *J. Alloys Compd.* **269**, 60–62 (1998).
6. De Novion, C. H. & Maurice, V. Order and Disorder in Carbides and Nitrides. *J. Phys. Colloq.* **38**, 211–220 (1977).
7. Wang, B., Liu, Y. & Ye, J. Mechanical properties and electronic structures of VC,

- V4C3 and V8C7 from first principles. *Phys. Scr.* **88**, 1–9 (2013).
8. Tashmetov, M. Y. *et al.* Neutron Diffraction Study of Ordered Structures and Phase Transitions in Vanadium Subcarbide. *J. Nano- Electron. Phys.* **5**, 4–7 (2013).
  9. Lipatnikov, V. N. Phase equilibria, phases and compounds in the V-C system. *Russ. Chem. Rev.* **74**, 697–723 (2005).
  10. Toth, L. E. *Transition Metal Carbides and Nitrides*. (Elsevier, 2014).
  11. Meunier, F. *et al.* Synthesis and Characterization of High Specific Surface Area Vanadium Carbide; Application to Catalytic Oxidation. *J. Catal.* **44**, 33–44 (1997).
  12. Zhang, B. & Li, Z. Q. Synthesis of vanadium carbide by mechanical alloying. *J. Alloys Compd.* **392**, 183–186 (2005).
  13. Kapoor, R. & Oyama, S. T. Synthesis of Vanadium Carbide by Temperature Programmed Reaction. *Journal of Solid State Chemistry* **120**, 320–326 (1995).
  14. Li, C., Yang, X., Yang, B. & Qian, Y. A Chemical Co-Reduction Route to Synthesize Nanocrystalline Vanadium Carbide. *J. Am. Ceram. Soc.* **89**, 320–322 (2006).
  15. Liu, F. *et al.* Synthesis and characterization of vanadium carbide nanoparticles by thermal refluxing-derived precursors. *J. Mater. Sci.* **46**, 3693–3697 (2011).
  16. Ma, J. *et al.* Low temperature synthesis of vanadium carbide (VC). *Mater. Lett.* **63**, 905–907 (2009).
  17. Ma, S., Liang, J., Zhao, J. & Xu, B. Synthesis, characterization and growth mechanism of flower-like vanadium carbide hierarchical nanocrystals. *CrystEngComm* **12**, 750–754 (2010).
  18. Zhang, Y. *et al.* Exploring a novel approach to fabricate vanadium carbide encapsulated into carbon nanotube (VC@C) with large specific surface area. *Bull. Mater. Sci.* **36**, 345–351 (2013).
  19. Hossein-Zadeh, M. & Mirzaee, O. Synthesis and characterization of V8C7 nanocrystalline powder by heating milled mixture of V2O5, C and Ca via mechanochemical activation. *Adv. Powder Technol.* **25**, 978–982 (2014).
  20. Carassiti, L. *et al.* Ultra-rapid, sustainable and selective synthesis of silicon carbide powders and nanomaterials via microwave heating. *Energy Environ. Sci.* **4**, 1503–1510 (2011).
  21. Kennedy, J. L., Drysdale, T. D. & Gregory, D. H. Rapid, energy-efficient synthesis of the layered carbide, Al4C3. *Green Chem.* **17**, 285–290 (2015).
  22. Kitchen, H. J. *et al.* Modern microwave methods in solid-state inorganic materials chemistry: From fundamentals to manufacturing. *Chem. Rev.* **114**, 1170–1206 (2014).
  23. Vallance, S. R., Kingman, S. & Gregory, D. H. Ultra-rapid processing of refractory carbides; 20 s synthesis of molybdenum carbide, Mo2C. *Chem. Commun. (Camb)*.

- 742–744 (2007).
24. Vallance, S. R., Kingman, S. & Gregory, D. H. Ultrarapid materials processing: Synthesis of tungsten carbide on subminute timescales. *Adv. Mater.* **19**, 138–142 (2007).
  25. Vallance, S. R. *et al.* Ultrarapid microwave synthesis of superconducting refractory carbides. *Adv. Mater.* **21**, 4502–4504 (2009).
  26. McGill, B. S. L. & Walkiewicz, W. Microwave Heating of Chemical and Minerals. *Dep. Inter. Bur. Mines* **95**, 1–28 (1995).
  27. Rühl, S. Inorganic Crystal Structure Database (ICSD). *A Focus Crystallogr.* **6**
  28. Kraus, W. & Nolze, G. Powder cell 2.3 version. *CPD Newslett* **20**, 274–280 (1998).
  29. Lipatnikov, V. N. *et al.* Effects of vacancy ordering on structure and properties of vanadium carbide. *J. Alloys Compd.* **261**, 192–197 (1997).
  30. Larson, A. C. & Dreele, R. B. Von. General Structure Analysis System (GSAS). *Los Alamos Natl. Lab. Rep. LAUR* 86–748 (2000).
  31. Toby, B. H. EXPGUI, a graphical user interface for GSAS. *J. Appl. Crystallogr.* **34**, 210–213 (2001).
  32. De Novion, C. H.; Lorenzelli, R.; Costa, P. Superlattice structure in vanadium carbide VC<sub>1-x</sub>. *C. R. Acad. Sci. Paris* **263**, 775–778 (1966).
  33. Gusev, A. I., Kurlov, A. S., Bobrikov, I. A. & Balagurov, A. M. V<sub>8</sub>C<sub>7</sub> superstructure in nonstoichiometric vanadium carbide powders. *JETP Lett.* **102**, 179–185 (2015).
  34. Buijink, J. K. F. Chemistry of vanadium-carbon single and double bonds. 49–73 (1995).
  35. Epicier, T., Blanchin, M. G., Ferret, P. & Fuchs, G. High-resolution electron microscopy imaging of the carbon vacancy superlattice in the ordered carbide VC<sub>1-x</sub>. *Philos. Mag. A* **59**, 885–906 (1989).
  36. Ghimbeu, C. M., Raymundo-Piñero, E., Fioux, P., Béguin, F. & Vix-Guterl, C. Vanadium nitride/carbon nanotube nanocomposites as electrodes for supercapacitors. *J. Mater. Chem.* **21**, 13268 (2011).
  37. Chen, W., Mai, L., Peng, J., Xu, Q. & Zhu, Q. Raman spectroscopic study of vanadium oxide nanotubes. *J. Solid State Chem.* **177**, 377–379 (2004).
  38. Gilson, T. R., Bizri, O. F. & Cheetham, N. Single-crystal Raman and Infrared Spectra of Vanadium(V) Oxide. *J. Chem. Soc., Dalt. Trans.* **3**, 291–294 (1973).
  39. Lee, S. *et al.* Raman spectroscopic studies of amorphous vanadium oxide thin films. *Solid State Ionics* **165**, 111–116 (2003).
  40. Su, Q., Liu, X. Q., Ma, H. L., Guo, Y. P. & Wang, Y. Y. Raman spectroscopic characterization of the microstructure of V<sub>2</sub>O<sub>5</sub> films. *J. Solid State Electrochem.* **12**,

919–923 (2008).

41. Zhou, B. & He, D. Raman spectrum of vanadium pentoxide from density-functional perturbation theory. *J. Raman Spectrosc.* **39**, 1475–1481 (2008).
42. Aita, C. R., Liu, Y. L., Kao, M. L. & Hansen, S. D. Optical behavior of sputter-deposited vanadium pentoxide. *J. Appl. Phys.* **60**, 749–753 (1986).
43. Cogan, S. F., Nguyen, N. M., Perrotti, S. J. & Rauh, R. D. Optical properties of electrochromic vanadium pentoxide. *J. Appl. Phys.* **66**, 1333–1337 (1989).
44. Hirashima, H.; Ide, M.; Yoshida, T. Memory Switching of V<sub>2</sub>O<sub>5</sub>-TeO<sub>2</sub> Glasses. *J. Non-Cryst. Solids* **86**, 327–335 (1986).
45. Legrouri, A.; Baird, T.; Fryer, J. R. Electron Optical Studies of Fresh and Reduced Vanadium Pentoxide-Supported Rhodium Catalysts. *J. Catal.* **140**, 173–183 (1993).
46. Nadkarni, G. S.; Shirodkar, V. S. Experiment and Theory for Switching in Al/V<sub>2</sub>O<sub>5</sub>/Al Devices. *Thin Solid Films* **105**, 115–129 (1983).
47. Park, H. K.; Smyrl, W. H.; Ward, M. D. V<sub>2</sub>O<sub>5</sub> Xerogel Films as Intercalation Hosts for Lithium. *J. Electrochem. Soc.* **2**, 63–67 (1996).
48. Ramirez, R., Casal, B., Utrera, L. & Ruiz-Hitzky, E. Oxygen Reactivity in Vanadium Pentoxide: Electronic Structure and Infrared Spectroscopy Studies. *J. Phys. Chem.* **94**, 8960–8965 (1990).
49. Satapathy, L. N., Ramesh, P. D., Agrawal, D. & Roy, R. Microwave synthesis of phase-pure, fine silicon carbide powder. *Mater. Res. Bull.* **40**, 1871–1882 (2005).
50. Watts, J. F. & Wolstenholme, J. *An Introduction to Surface Analysis by XPS and AES*. (John Wiley & Sons, Ltd, 2003).

## 4 Microwave Synthesis and Structural Characterization of Carbides in the Zr-C and Hf-C Systems

### 4.1 Introduction to Zirconium and Hafnium Carbide

Zirconium and hafnium carbide are metal carbides of the Group 4 of the periodic table and are both extremely hard ceramic materials.

Unlike the V-C system [Chapter 3], no evidence of the existence of superstructures was found in the literature for the Zr-C and Hf-C systems. However, ZrC and HfC both occur over a considerable range of composition. Sara *et al.* studied the phase relations in the zirconium-carbon system in 1965<sup>1</sup> and established that only one phase, a monocarbide ZrC, was found. The low-carbon and carbon-rich boundaries for this phase were determined to be 38.5 and 48.9 at.% carbon, respectively, which suggested that zirconium carbide has a broad compositional field and can exist as  $ZrC_{1-x}$  (where  $x = 0.77-0.98$ ). Therefore,  $ZrC_{0.98}$  represents the carbon-rich limit of  $ZrC_{1-x}$  and crystallizes in the NaCl-type cubic structure (space group  $Fm-3m$ ,  $a = 4.6986 \text{ \AA}$ ) [Figure 4-3].

The Hf-C system behaves similarly to the Zr-C system. Deardorff *et al.* investigated the hafnium-carbon phase diagram in 1967 and found that the composition range of  $HfC_{1-x}$  exists from 37.0 to 48.5 at.% carbon.<sup>2</sup> In this case, the carbon-rich limit for hafnium carbide is then represented by  $HfC_{0.97}$  which also crystallizes in the NaCl-type cubic structure (space group  $Fm-3m$ ,  $a = 4.6425 \text{ \AA}$ ). Figure 4-1 and Figure 4-2 illustrate the phase diagram for the Zr-C and Hf-C systems, respectively.

The work presented in this chapter focuses on the microwave synthesis and structural characterization of single-phase ZrC and HfC in both multi- and single-mode MW cavity reactors of which only the work on the Zr-C system was successful. The zirconium carbide material has been prepared by employing zirconium metal (Zr) as a zirconium source and graphite as a carbon source under Ar. Once an appropriate synthetic procedure was established, the so-synthesized ceramics were investigated by Powder X-ray Diffraction (PXRD), Scanning Electron Microscopy (SEM) coupled with Energy Dispersive X-ray (EDX) analysis, Raman Spectroscopy, X-ray Photoelectron Spectroscopy (XPS) and

Powder Neutron Diffraction (PND). The carbothermal reduction of zirconium dioxide ( $\text{ZrO}_2 + \text{C}$ ) was also investigated using microwave heating but did not lead to the formation of any products.

Attempts to synthesize HfC from Hf metal and graphite under Ar were also carried out but a partial oxidation of the Hf phase during reaction was observed and prevented reactions completion under the experimental conditions employed. This suggested the presence of oxygen in the system (although all the reactions were carried under Ar) which contaminated the samples. As per the  $\text{ZrO}_2 + \text{C}$  reactions, the carbothermal reduction of hafnium oxide was also investigated but did not lead to the formation of any products as well.

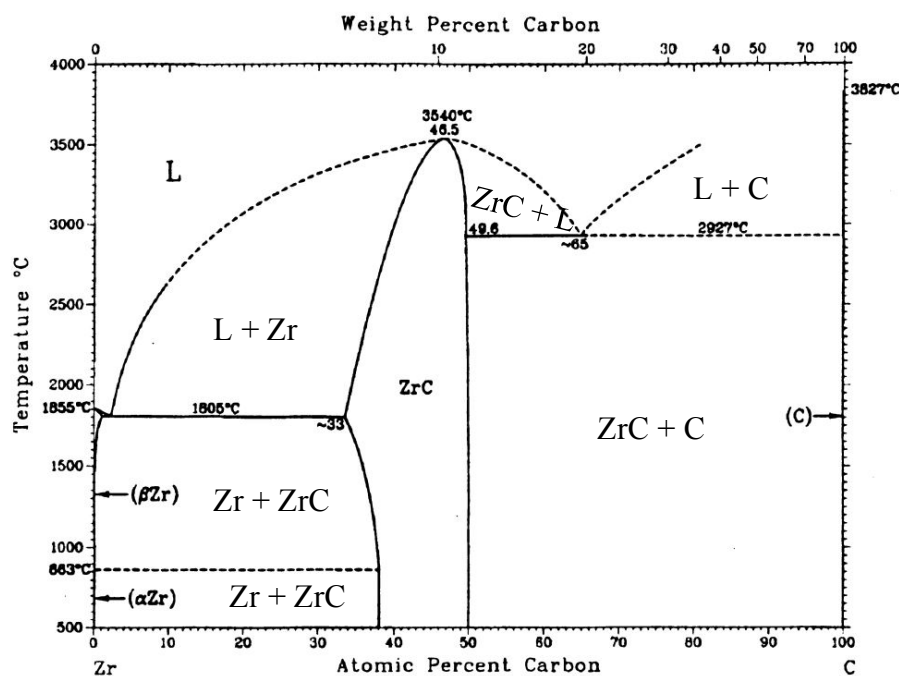


Figure 4-1 Phase diagram of the Zr-C system.<sup>1</sup>

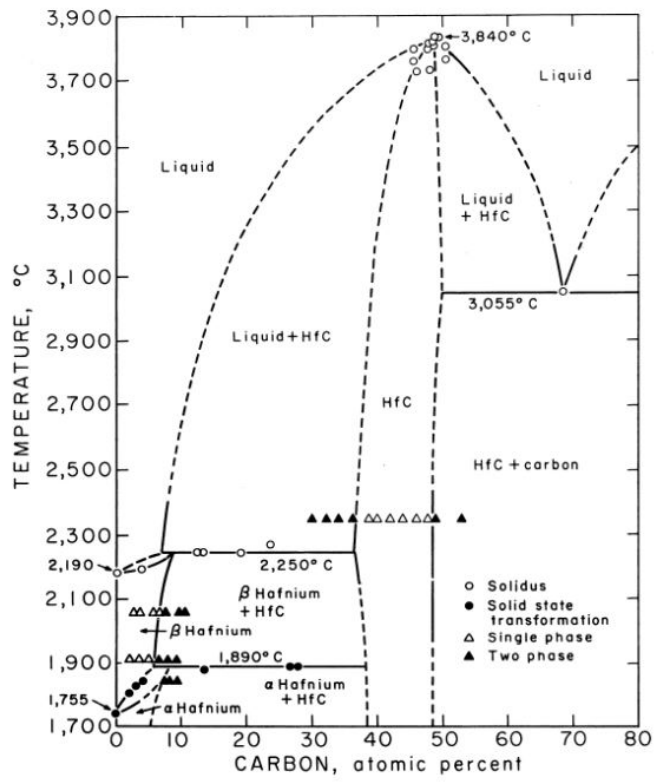


Figure 4-2 Phase diagram of the Hf-C system.<sup>2</sup>

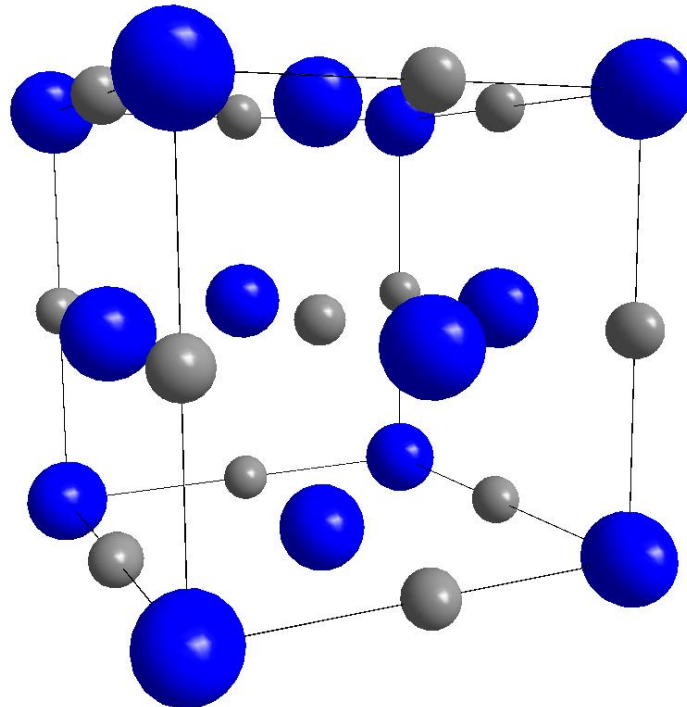


Figure 4-3 Crystal structure of ZrC and HfC. Zr/Hf atoms (blue), C atom (grey).

## 4.2 Microwave Synthesis Studies in Zr–C system

This section describes experimental work undertaken to establish a synthetic route to zirconium carbide from zirconium metal and carbon in both a MMC and a SMC.

### 4.2.1 Introduction

Zirconium carbide has been synthesized using various synthetic methods such as direct reaction of elemental powders,<sup>3</sup> carbothermal reduction of zirconium oxide ( $\text{ZrO}_2$ ),<sup>4-7</sup> mechanical activation assisted self-propagating high-temperature synthesis,<sup>8,9</sup> sol-gel route,<sup>10,11</sup> laser pyrolysis route<sup>12</sup> and some other synthetic methods.<sup>13,14</sup> However, as discussed in Section 1.6.1, these common methods face several challenges like energy inefficiency, high cost, impurities and/or low yields.

The synthesis of zirconium carbide from elemental powders was investigated by Nachiappan *et al.* (2010) by reactive hot pressing.<sup>3</sup> This synthetic method is often used to decrease the reaction temperature and time by applying a relatively high pressure with significant improvements in densification. The authors of the study mixed stoichiometric and nonstoichiometric amounts of zirconium and graphite which were reactively hot pressed to produce monolithic  $\text{ZrC}_x$  (where  $x = 0.5$  to 1). Reactions were conducted in a vacuum hot press at a pressure of 40 MPa and temperatures of up to 1400 °C (held for 1 h).

The carbothermal reduction of  $\text{ZrO}_2$  represents the most common industrial process for the synthesis of ZrC and was extensively investigated in previous studies. Maitre *et al.* (1997) studied the solid-state reaction between zirconia and graphite under flowing argon.<sup>5</sup>  $\text{ZrO}_2$ -C mixtures (with a stoichiometric ratio of 1:3) were put in a vitreous carbon crucible and heated in a furnace by a graphite heating element at temperatures of up to 1823 K for 24 h.

Zirconium carbide has been previously synthesized using microwave irradiation but the experimental set up is slightly different from that used in the present study. Das *et al.* reported the microwave synthesis of ZrC-SiC composites by carbothermal reduction of zircon sand powder.<sup>15</sup> The chemical composition of zircon sand reported by the authors is illustrated in Table 4-1.

**Table 4-1** Chemical composition of zircon sand.<sup>15</sup>

<b>Compound</b>	<b>Composition (wt%)</b>
ZrO <sub>2</sub>	62.0
HfO <sub>2</sub>	8.0
SiO <sub>2</sub>	28.0
TiO <sub>2</sub>	0.2
Al <sub>2</sub> O <sub>3</sub>	1.2
Fe <sub>2</sub> O <sub>3</sub>	0.2
CaO	0.4

Stoichiometric mixtures of zircon sand and amorphous carbon were ground together, pelletized and embedded in a SiC crucible. Pellets were irradiated with 2.45 GHz microwaves in a domestic microwave oven at a power of 700 W under Ar for 30 minutes. Unfortunately, this study did not find positive confirmation from our own experiments, as further discussed in Section 4.3.

The reactions discussed in this section were carried out by direct reaction of the elemental starting materials (Zr + C). The starting materials were mixed according to the following reaction:



Although both starting materials (Zr and C) theoretically couple with microwaves, the heating of reactant pellet alone was unsuccessful and required the use of a microwave susceptor, such as carbon. Both graphite and activated charcoal are known to be good microwave absorbers, reaching temperatures above 1000 °C in less than 2 minutes. Graphite was used as a susceptor (as well as a starting material) to provide additional thermal heating to the outside of the pellet.

The direct reaction of elemental powders is straightforward and proceeds as described by Equation (1-15). This reaction route is suitable for the reaction set-up used and the collected pellet should be intact, hard and not fractured.

## 4.2.2 Experimental

#### 4.2.2.1 Synthesis

All reactions reported in this section were performed under Ar by mixing and grinding together Zr metal (Alfa Aesar, < 45  $\mu\text{m}$ , 98.8%) and graphite (Sigma Aldrich, < 50  $\mu\text{m}$ , 99.5%), in a 1:1 stoichiometric ratio according to Equation (1-15). The so-obtained powder mixture (1 g) was uniaxially cold pressed into a pellet without the use of a binder. Samples were pressed into a cylindrical shape with a diameter of 8 mm and height of approximately 5 mm. This compact was embedded in graphite powder (here used as a MW susceptor) within a 10-mm quartz tube which is transparent to microwaves. The tube was sealed with a septum cap, parafilmed and subsequently connected to an Ar flow. The MW reactions were conducted in either a multi-mode or a single-mode cavity microwave reactor.

For multimode cavity experiments, the tube containing the sample was placed in the center of a beaker containing silica powder which acts as a stand for the tube as well as a thermal insulator. The whole apparatus was then inserted into the multimode cavity of a domestic MW oven (DMO) and positioned in the same location within the cavity to keep the experimental parameters as constant as possible. Synthesis was conducted for 6 minutes at a power of 800 W.

For single-mode cavity experiments, the tube was directly placed into the applicator of the SMC reactor and held in place by a stand. Synthesis was conducted for 2 minutes at a power of 1 kW.

As per  $\text{V}_8\text{C}_7$  [Chapter 3], ZrC was synthesized for the first time on much more rapid timescales than previously reported in the literature. Moreover, the reaction time could be further decreased by employing higher MW powers for the reaction process.

After the reaction went to completion, the pellet was found to be extremely hard due to the fast sintering process of the carbide particles. The surface of the pellet was physically cleared with fine sand paper in order to remove the remaining excess of susceptor. The pellet was then ground, giving a fine, grey powder.

#### 4.2.2.2 Characterization

Products were characterized using several analytical techniques. Powder X-ray Diffraction (PXRD) [Section 2.3.1] was used to identify product phases by reference to known structures downloaded from the Inorganic Crystal Structure Database (ICSD)<sup>16</sup> using the PowderCell 2.3 software.<sup>17</sup> The data collected on a PANalytical Xpert MPD diffractometer, Cu  $\text{K}\alpha_1$  radiation, for 1 hour over a range of  $10 < 2\theta^\circ < 85$ . Crystallographic parameters were obtained by Rietveld refinement [Section 2.3.3] against powder XRD data collected for ca. 12 hours over a range of  $10 < 2\theta^\circ < 110$  using GSAS and EXPGUI software

packages.<sup>18,19</sup> Sample morphology, elemental composition and mapping were investigated by Scanning Electron Microscopy (SEM) and Energy-dispersive X-ray Spectroscopy (EDX) [Section 2.3.4]. Additional characterization was performed by Raman spectroscopy [Section 2.3.5]. Raman data were collected at room temperature using a Horiba LabRAM confocal microscope system with a 532-nm green laser. Surface analysis was evaluated by X-ray Photoelectron Spectroscopy (XPS) [Section 2.3.6] using a Thermo Scientific K-Alpha+ X-ray photoelectron spectrometer with monochromatic Al K $\alpha$  radiation (1486.7 eV). Finally, Powder Neutron Diffraction (PND) [Section 2.3.2] was used to obtain a definitive crystal structure and to establish the oxygen stoichiometry with precision. PND experiments were conducted at the ISIS pulsed neutron and muon source at the Rutherford Appleton Laboratory (RAL) in Oxfordshire using the POLARIS instrument.

## 4.2.3 Results and Discussion

### 4.2.3.1 Powder X-ray Diffraction (PXRD)

After a 20-minute reaction in the multimode cavity, the sample was analyzed by ex-situ Powder X-ray Diffraction. The PXRD pattern for the so-obtained samples is shown in Figure 4-4. Similar results were obtained after a 6-minute reaction in the single-mode cavity reactor and the PXRD pattern is shown in the Appendix, Figure 7-13.

The product in each of the MMC and SMC synthesis experiments was identified as zirconium carbide, ZrC, which crystallizes in the expected cubic structure (space group *Fm-3m*). The PXRD pattern consists of nine intense, sharp peaks characteristic of a salt-like structure, which represent the reflections from the (111), (200), (220), (311), (222), (400), (331), (420) and (422) planes of the structure of zirconium carbide. An additional low intensity reflection is also observed in most of the experiments at  $2\theta \cong 26.5^\circ$  which corresponds to the (002) reflection from graphite, which probably originates from the unsuccessful removal of residual graphite.

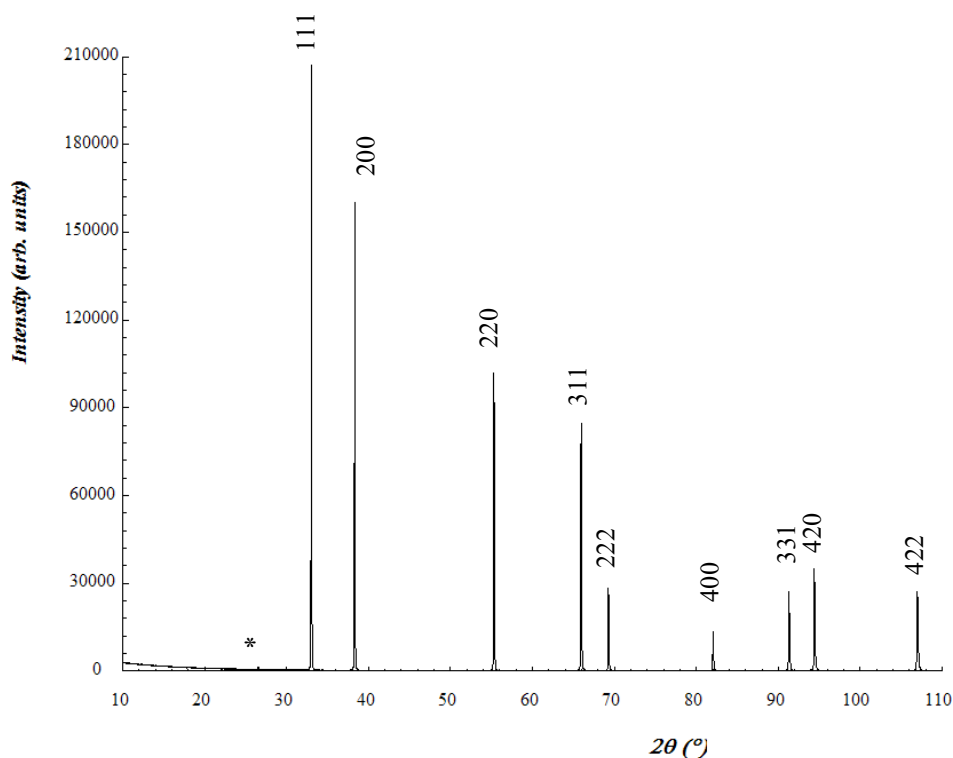


**Figure 4-4** PXR D pattern taken *ex-situ* from zirconium metal plus graphite (1:1) heated in an MMC reactor for 20 minutes at a power of 800 W under Ar. All reflections can be attributed to ZrC except the one marked with \*, which belongs to the (002) reflection from graphite.

The same reaction using the same experimental parameters was also investigated under air but the formation of undesired products (such as  $\text{ZrO}_2$ ) was observed which indicated that the use of an inert environment was likely essential. The so-formed oxide phase did not subsequently react with free carbon to produce ZrC under this conditions (see Section 3.3.3.1 for further details).

#### 4.2.3.2 Rietveld Refinement

The structure of the so-obtained ZrC was refined by the Rietveld method against PXR D data, collected for 12 hours over a range of  $10 < 2\theta^\circ < 110$  with a step size of  $0.017^\circ$  ( $2\theta$ ) using the GSAS and EXPGUI software packages.<sup>18,19</sup> The structure model used was for cubic  $Fm-3m$  ZrC taken from the ICSD database<sup>16</sup> [Figure 4-3], in which the 4 zirconium atoms occupy the Wyckoff position (4a) whereas the 4 carbon atoms are located at the Wyckoff position (4b).

The background was modelled using a shifted Chebyshev function (function 1 within GSAS). The cell parameters, scale factor and zero point were also refined in initial cycles. Peak shape was subsequently modelled using the Thompson-Cox-Hastings pseudo Voigt

function (peak shape function 2 within GSAS). The isotropic thermal factors ( $U_{\text{iso}}$ ) of the zirconium and carbon atoms were refined independently. Refinement of the carbon site occupancy factor was also attempted giving a value of 0.98. This probably suggests that the MW-synthesized zirconium carbide ( $\text{ZrC}_{1-x}$  – where  $x = 0.98$ ) has a carbon content which is close to that of stoichiometric zirconium monocarbide  $\text{ZrC}$ .

Rietveld refinement against PXRD data [Figure 4-5] confirmed that the  $\text{ZrC}$  crystallizes in a cubic rock-salt structure (space group  $Fm-3m$ ) with a cubic lattice parameter  $a = 4.69645(1) \text{ \AA}$  which is consistent with those previously reported by Bittner *et al.* in 1962 ( $a = 4.691 \text{ \AA}$ )<sup>20</sup> and by Samsonov *et al.* in 1956 ( $a = 4.683 \text{ \AA}$ ).<sup>21</sup>

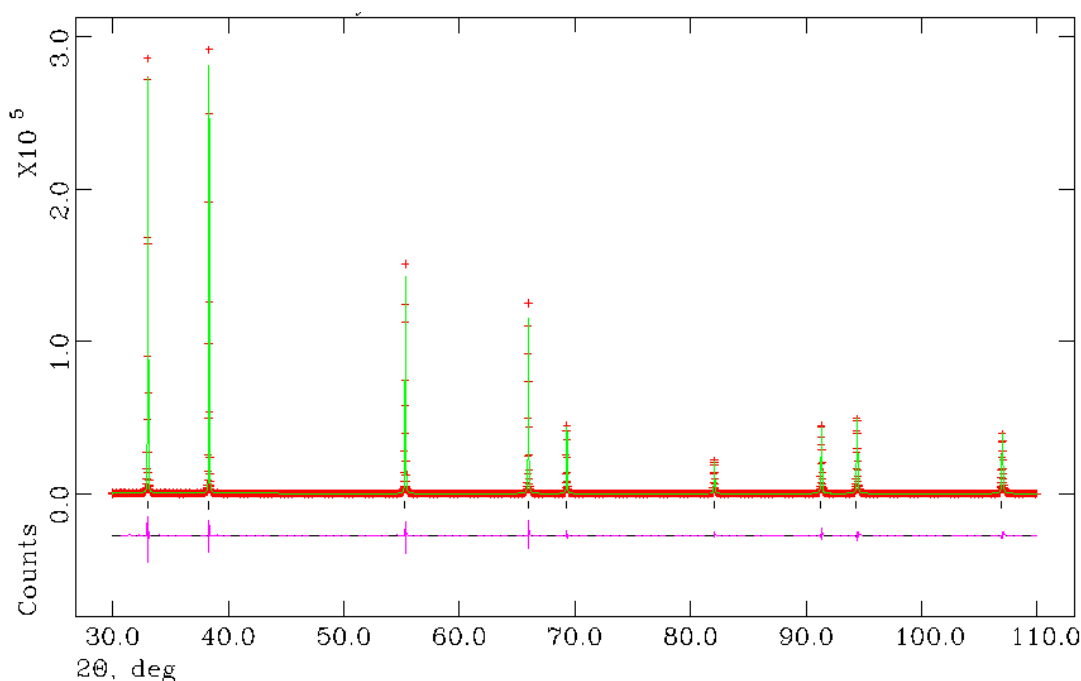


**Figure 4-5** Observed (*plusses*), calculated (*solid green line*), and difference (*solid purple line*) profile plot for the Rietveld refinement against PXRD data for the zirconium carbide  $\text{ZrC}$ . Tick marks denote  $\text{ZrC}$  diffraction peaks. The (002) graphite reflection at  $2\theta = 26.5^\circ$  was excluded from the refinement.

The calculated crystallographic data and atomic parameters are illustrated in Table 4-2 and Table 4-3, respectively.

**Table 4-2** Crystallographic data from Rietveld refinement against PXRD data for ZrC.

<b>Phase data</b>	
Chemical Formula	ZrC
Crystal system	Cubic
Space group	<i>Fm -3 m</i>
<i>a</i> (Å)	4.69645(1)
Volume (Å <sup>3</sup> )	103.59(7)
<i>Z</i>	4
Formula weight (g mol <sup>-1</sup> )	101.84
Calculated density (g cm <sup>-3</sup> )	6.5297
<i>R</i> <sub>wp</sub>	0.0981
<i>R</i> <sub>p</sub>	0.0746
$\chi^2$	12.41

**Table 4-3** Atomic parameters from Rietveld Refinement against PXRD data for ZrC.

<b>Atomic parameters</b>						
Atom Type	Wyckoff Site	Fractional Coordinates			<i>U</i> <sub>iso</sub> (Å <sup>2</sup> )	Site Occupancy
		<i>x/a</i>	<i>y/b</i>	<i>z/c</i>		
Zr(1)	8c	0.0000	0.0000	0.0000	0.00618(4)	1.0
C(1)	12d	0.5000	0.5000	0.5000	0.00502(2)	0.983(1)

#### 4.2.3.3 *Ex-situ* Study of the Zr + C Reaction as a Function of Time

From the ex-situ PXRD data, the phase evolution was monitored as a function of time and a phase analysis was conducted for both multimode and single-mode cavity experiments.

The Zr + C pellets were irradiated with MWs in a DMO for 0 s, 5 mins, 10 mins and 20 mins and the respective PXRD patterns are shown in Figure 4-6. At *t* = 0 (before reaction), only reflections from the reagents are present (zirconium metal and graphite). After 5 minutes of microwave irradiation, only a small amount of zirconium carbide is formed (broad small peaks are observed) and reflections from reagents are still present. At *t* = 10 minutes, the latter reflections have mostly disappeared and only reflections from the products are observed. By evaluating the peak shape, it can be noticed that the reflections

are non-symmetrical (tail less steep than the leading edge). Figure 7-14 in the Appendix shows a magnified image of the PXRD pattern after a 10-minute reaction illustrating the unsymmetrical nature of the reflections at  $66^\circ$  and  $69.5^\circ$   $2\theta$  angles. This suggests that zirconium carbides with a lower carbon content ( $ZrC_{1-x}$ ) and, hence, a smaller unit cell (higher  $2\theta$  angles) are formed first.<sup>1</sup> As time proceeds, the intensity of the zirconium carbide reflections increases and the peaks become sharper and more symmetrical while the amount of graphite decreases, as indicated by its (002) reflection at  $26.5^\circ$ . At  $t = 20$  minutes, the reaction approaches completion. Only reflections from products are observed and highly crystalline ZrC pellets are obtained as a likely single phase. Nonetheless, a small impurity of graphite is observed in the powder patterns from most of the experiments which is likely to originate from residual susceptor on the outer surface of the pellet. The PXRD patterns for the Zr + C pellets after 0 sec, 5 min and 10 min of MW irradiation are shown separately in Figures 7-15 to 7-17 in the Appendix.

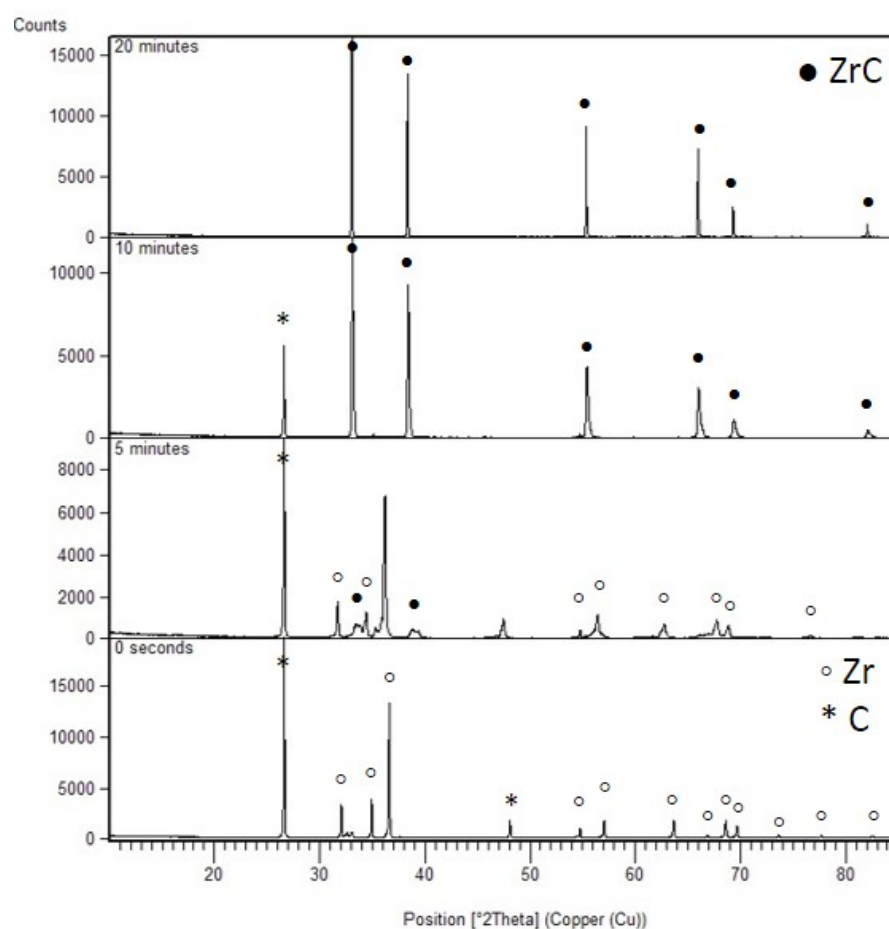


**Figure 4-6** *Ex-situ* patterns for Zr + C pellets heated in an 800 W domestic MW oven from reagents (*bottom*) to reaction completion (*top*).

The same phase analysis was conducted for the single-mode cavity experiments and similar results over significantly shorter reaction times were observed (as expected). Figure 4-7 illustrates the PXRD patterns collected after the Zr + C pellets had been irradiated with MWs for 0 s, 2 minutes, 4 minutes and 6 minutes in a single-mode MW reactor. Before MW irradiation ( $t = 0$ ), once again, only Zr and graphite are present. After only 2 minutes, the starting materials are still present but zirconium carbide starts forming although at this stage the observed peaks are of relatively low intensity. From 2 to 4 minutes, almost all the starting materials have reacted and the intensity of the ZrC reflections increases giving ZrC<sub>1-x</sub> as the major product(s). As per the MMC experiments, a non-symmetrical peak shape is also observed for SMC experiments. The tail of peaks is indeed less steep than the leading edge. As the reaction goes to completion ( $t = 6$  minutes), the intensity of peaks reaches a maximum value and a single ZrC phase is obtained.

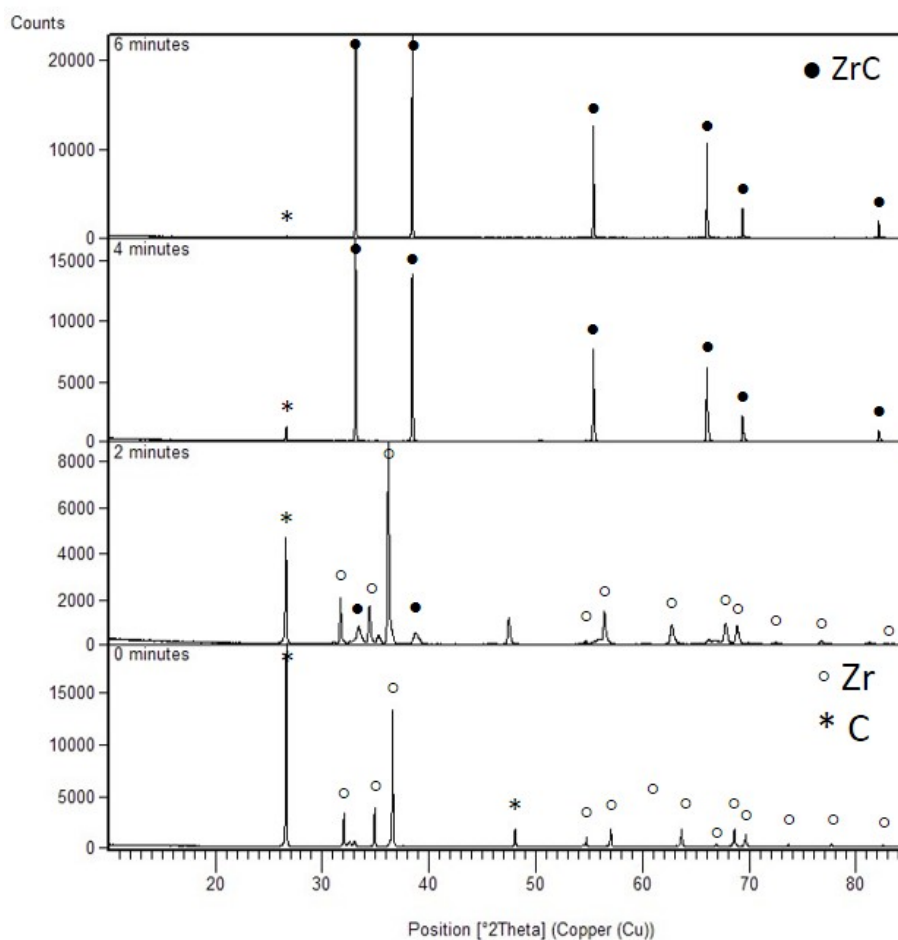


**Figure 4-7** *Ex-situ* patterns for Zr + C pellets heated in a single-mode cavity MW reactor at a power of 1 kW from reagents (*bottom*) to reaction completion (*top*).

In light of the results shown in Figure 4-6 and Figure 4-7, it is evident that a single-mode MW reactor leads to significantly faster ZrC synthesis than a multimode reactor (a domestic

MW oven was used in this study) and reaction times can be drastically cut by approximately one third. The microwave synthesis of zirconium carbide from zirconium metal and graphite takes indeed 20 minutes to go to completion in a DMO at a power of 800 W, whereas it takes only 6 minutes to achieve the same results using a single-mode cavity reactor at a power of 1 kW.

To summarise, the ex-situ study of the Zr + C reaction as a function of time suggests that the reaction mechanism is straightforward and involves the direct combination of the elements. The ZrC phase is apparently obtained through the formation of carbon-deficient zirconium carbide(s)  $ZrC_{1-x}$ . No other stable, observable intermediates are identified throughout the reaction. In order to have detailed mechanistic information, the MW synthesis of Zr and C should be investigated *in-situ*. However, such investigation requires the development of a customized single-mode MW reactor, specifically designed to perform time-resolved experiments by means of powder X-ray diffraction (PXRD) or, even better, powder neutron diffraction (PND).

#### 4.2.3.4 Scanning Electron Microscopy (SEM) coupled with Energy-dispersive X-ray Spectroscopy (EDX)

The MW-synthesized ZrC powders prepared from zirconium metal and graphite were analyzed by Scanning Electron Microscopy (SEM) coupled with Energy-dispersive X-ray Spectroscopy (EDX) for particle size and morphology. As discussed in Section 3.2.3.4, the particles size, shape and morphology of ceramic materials represent an important aspect because of their industrial application as abrasives and in wear-resistant parts.<sup>22</sup>

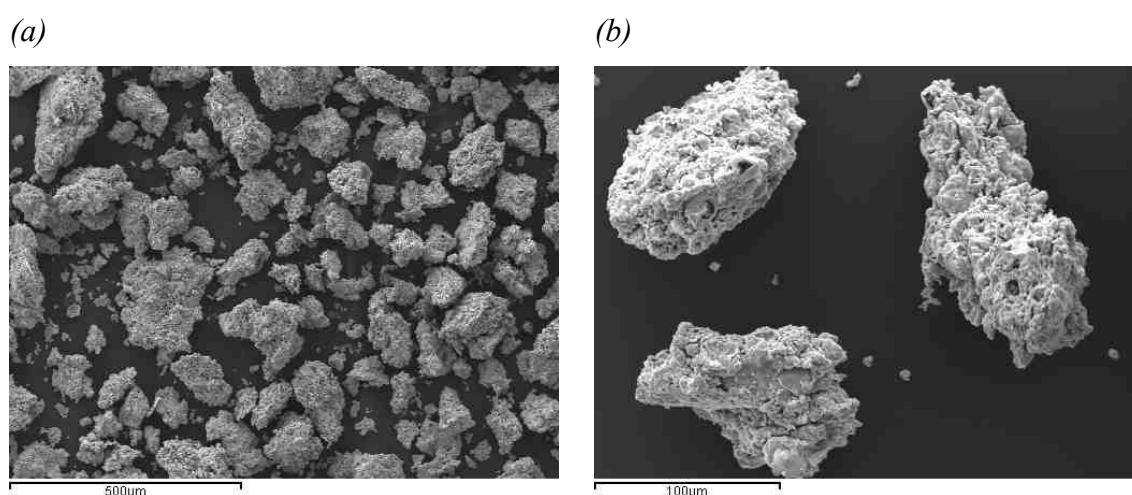


**Figure 4-8** SEM micrographs at (a) low and (b) higher magnification for the MW-synthesized ZrC from zirconium metal and carbon in 20 minutes in an MMC reactor at a power of 800 W.

SEM micrographs for the ZrC samples synthesized from zirconium metal and graphite in 20 minutes in an MMC reactor at a power of 800 W are shown in Figure 4-8. The microwave reaction yields irregular micron-scale ZrC particles, typically with from a few microns to a maximum of approximately a couple of hundred microns across.

SEM/EDX experiments were also conducted for ZrC samples synthesized in a single-mode cavity microwave reactor at a power of 1 kW [Figure 4-9] and show similar results to those shown in Figure 4-8. Irregular micron-scale ZrC particles are observed, ranging from a few microns to a maximum of 150  $\mu\text{m}$ .

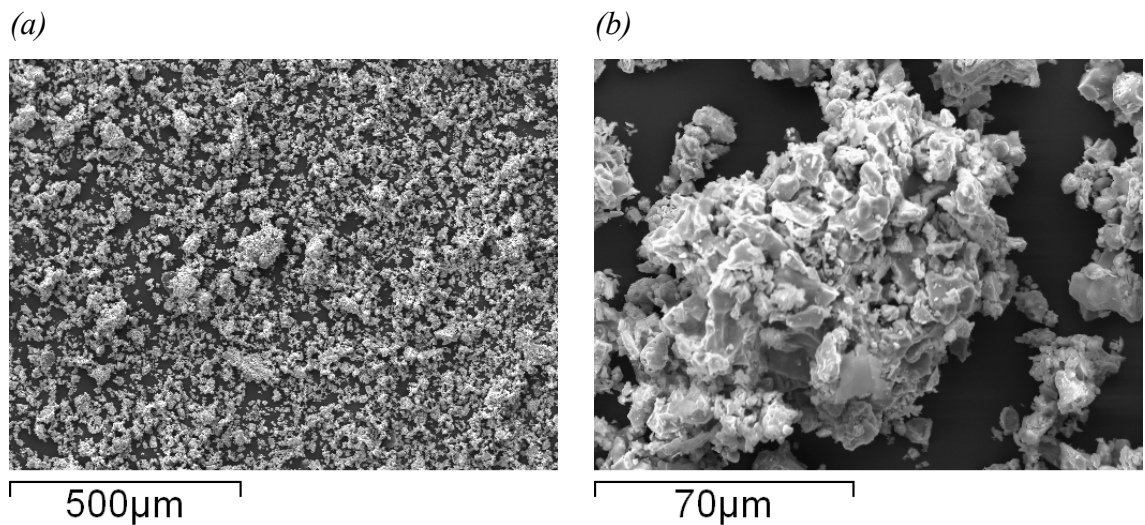


**Figure 4-9** SEM micrographs at (a) low and (b) higher magnification for the MW-synthesized ZrC from zirconium metal and carbon in 6 minutes in a SMC microwave reactor at a power of 1 kW.

The SEM results obtained for the MMC and SMC samples are in agreement with each other and show similar particle size and morphology. ZrC particles have, in both cases, a quite rough surface and the bigger particles are the product of the sintering process undergone between smaller particles and remain intact even after grinding the product pellet.

EDX data were collected for several crystallites and they all show the presence of mainly zirconium and carbon as expected [Figure 4-10]. However, some EDX spectra also showed that oxygen or hafnium impurities were contained in the samples [Figure 4-11 and Figure 4-12], respectively. The Hf impurity is assumed to originate from the zirconium powder used as a starting material and as purchased from Alfa Aesar. According to the product specification, the Zr powder indeed contains ca. 2% of Hf which was not visible by PXRD.

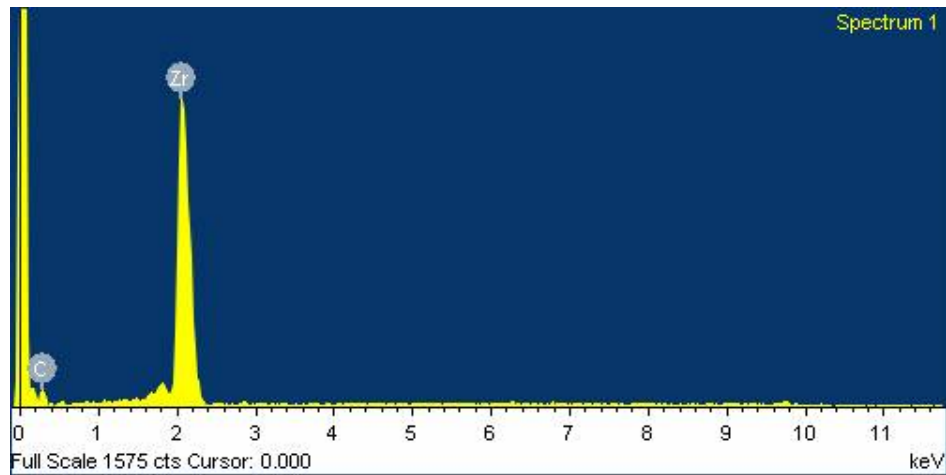


**Figure 4-10** EDX spectrum for the MW-synthesized ZrC from zirconium metal and carbon in 20 minutes in an MMC microwave reactor, showing that only zirconium and carbon were present.

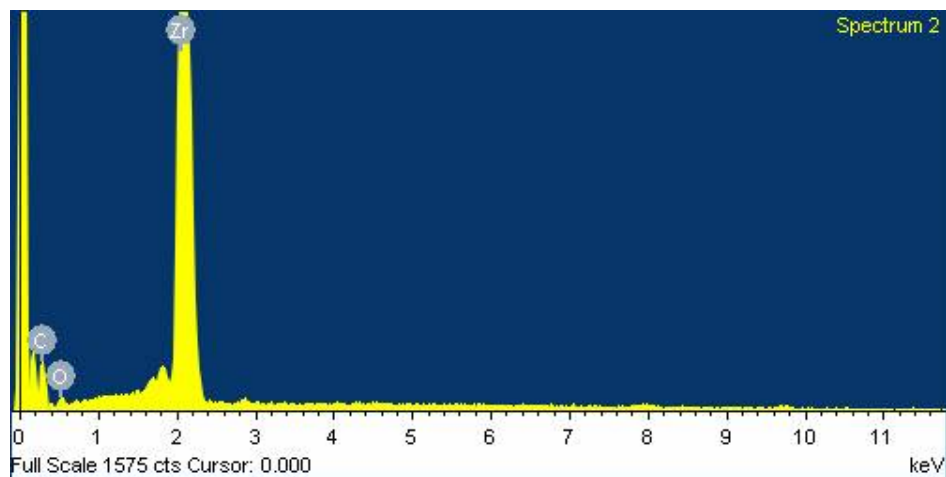


**Figure 4-11** EDX spectrum for the MW-synthesized ZrC from zirconium metal and carbon in 20 minutes in an MMC microwave reactor, showing that oxygen was present as well as zirconium and carbon.

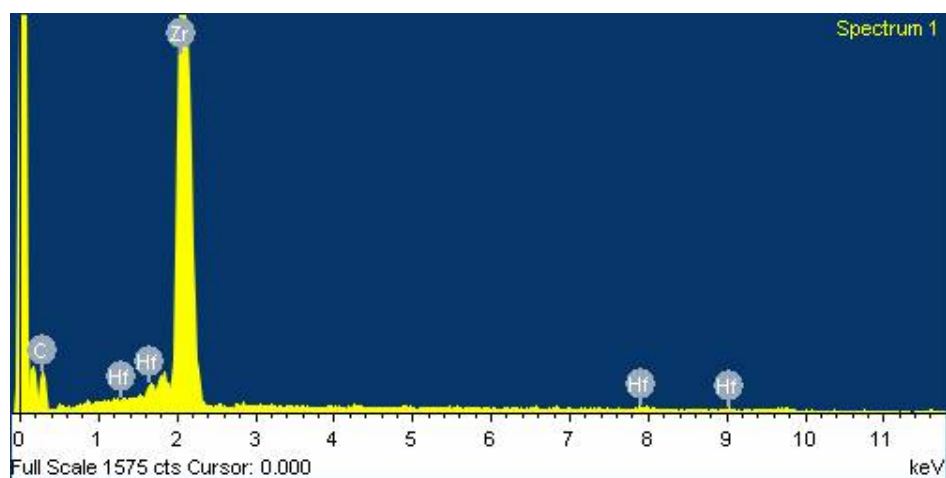


**Figure 4-12** EDX spectrum for the MW-synthesized ZrC from zirconium metal and carbon in 20 minutes in an MMC microwave reactor, showing that hafnium impurities were present as well as zirconium and carbon.

In light of the EDX data, it was assumed that some of the MW-synthesized ZrC samples could contain a small amount of oxygen, as seen for the  $V_8C_7$  samples and discussed in Section 3.2.3.4. The presence of oxygen in the form of additional bulk oxide phases was excluded beforehand, as PXRD data do not support this last option.

#### 4.2.3.5 Raman Spectroscopy

Raman spectroscopy proved to be an effective tool for the present research and provided further evidence of likely oxygen inclusion in the MW-synthesized  $V_8C_7$  particles [see Section 3.2.3.5]. On this evidence in the V-C system, further characterization of the MW-synthesized ZrC samples was performed by Raman spectroscopy. The Raman spectrum of ZrC synthesized from zirconium metal and graphite in 20 minutes in an MMC reactor is shown in Figure 4-13.

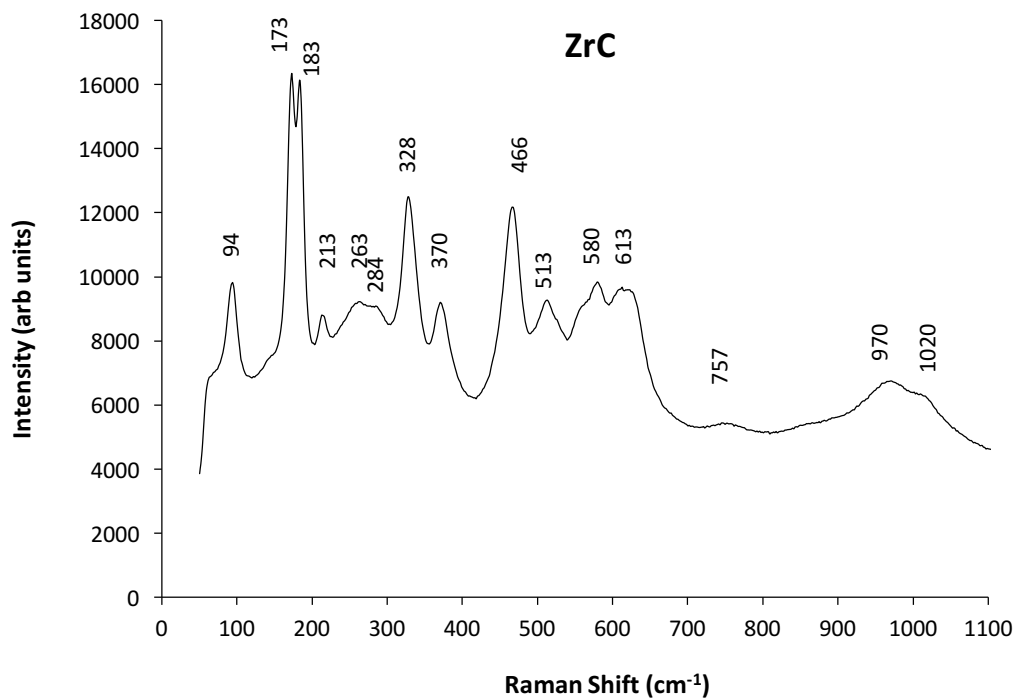


**Figure 4-13** Experimental Raman spectrum for the MW-synthesized ZrC from zirconium metal and carbon in 20 minutes in an MMC microwave reactor.

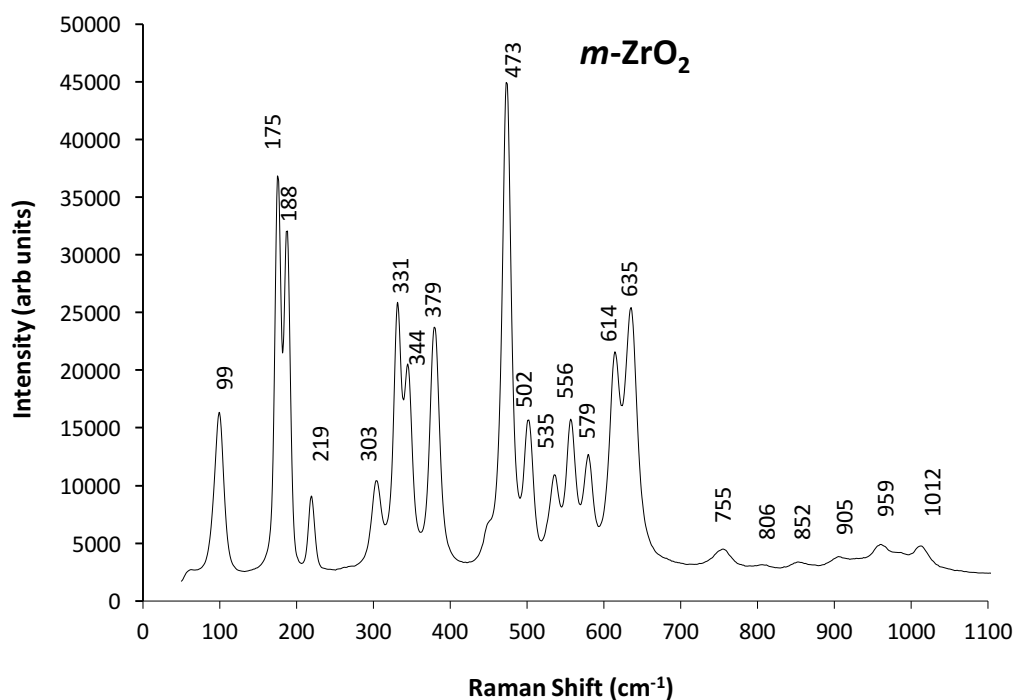


**Figure 4-14** Experimental Raman spectrum for commercial *m*-ZrO<sub>2</sub>.

By comparison with the Raman spectrum for commercial monoclinic ZrO<sub>2</sub> shown in Figure 4-14, it can be seen that the MW-synthesized ZrC shares some common bands at similar Raman shifts with *m*-ZrO<sub>2</sub> although the two compounds have completely different crystal structures.

Zirconium dioxide (or zirconia, ZrO<sub>2</sub>) is a chemically unreactive white compound. Three phases are known for zirconia: monoclinic (< 1,170 °C – most naturally occurring form), tetragonal (1,170-2,370 °C) and cubic (> 2,370 °C).<sup>23</sup> Figure 4-15 shows the crystal structures for these three polymorphs.

As they have different crystal structures, these three polymorphs also have different Raman spectra. The spectrum of the MW-synthesized ZrC from zirconium metal and graphite shows some characteristic modes of both *m*-ZrO<sub>2</sub> and *t*-ZrO<sub>2</sub> which are summarized in Table 4-4.

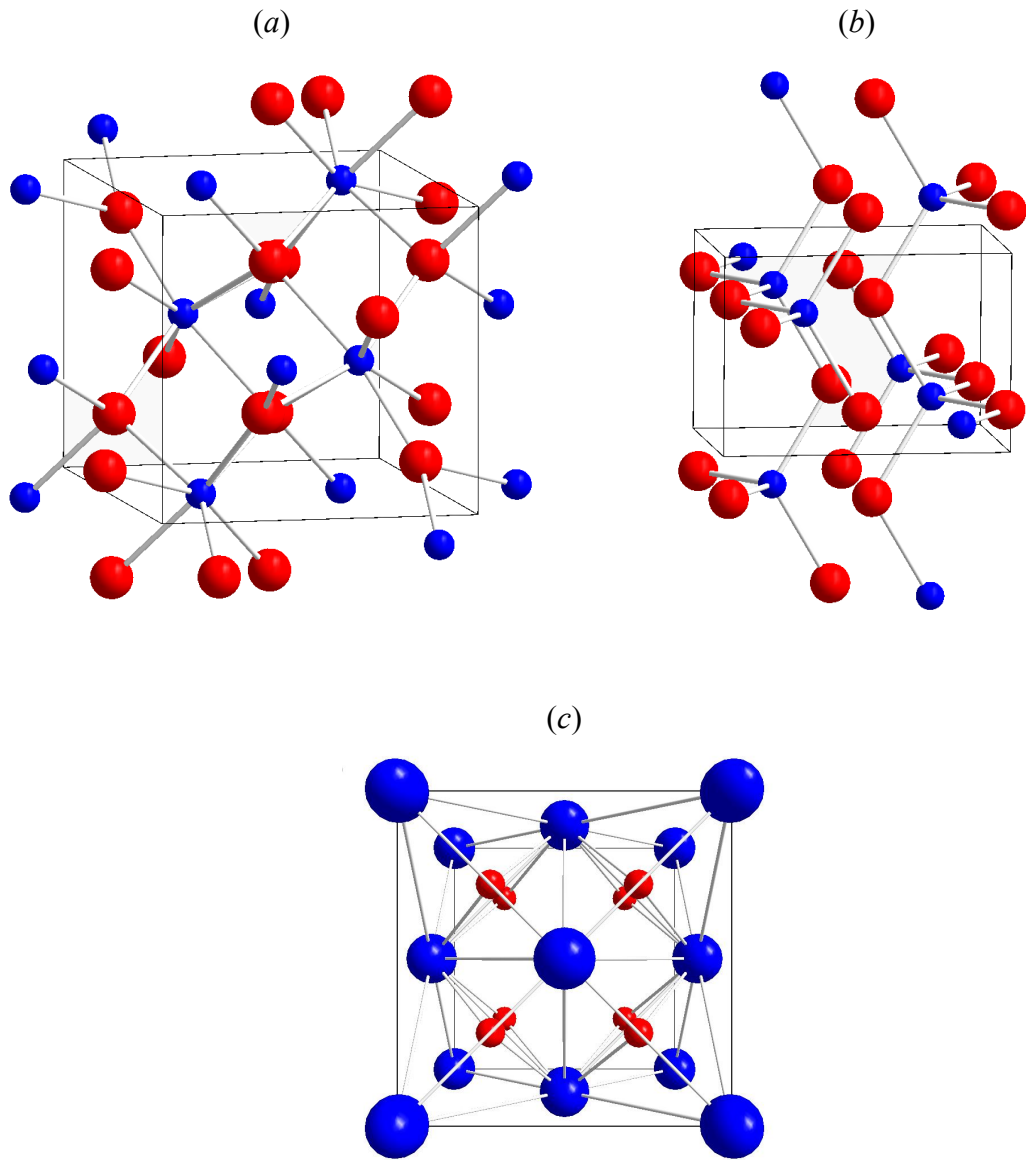


**Figure 4-15** Crystal structures for *m*-ZrO<sub>2</sub> (a), *t*-ZrO<sub>2</sub> (b) and *c*-ZrO<sub>2</sub> (c). Zr atoms (blue), O atoms (red).

The Raman spectroscopy of both monoclinic and tetragonal zirconia has been extensively studied over the years and several investigations can be found in the literature<sup>24-34</sup>. However, the mode assignments of the Raman spectra are incomplete. Keramidas *et al.* performed a Raman scattering study of ZrO<sub>2</sub> and its phase transformations (monoclinic → tetragonal).<sup>30</sup> Factor-group analysis of ZrO<sub>2</sub> polymorphs predicted that eighteen modes (the *A<sub>g</sub>* and *B<sub>g</sub>* modes) are expected to be Raman-active. The distribution of normal modes in *m*-ZrO<sub>2</sub> is as follows:

$$\Gamma(\text{ZrO}_2) = 9A_g(R) + 9B_g(R) + 8A_u(ir E \parallel b) + 7B_u(E \perp b) \quad (4-2)$$

All the eighteen Raman bands predicted in the study are seen in the commercial Raman spectrum of ZrO<sub>2</sub> [Figure 4-14], with the exception of the bands with wavenumbers of 800 cm<sup>-1</sup> and above which are not mentioned in the previous publication.

**Table 4-4** Raman shifts of the MW-synthesized ZrC compared to those of *m*-ZrO<sub>2</sub> and *t*-ZrO<sub>2</sub> with their respective assignments. “*m*” stands for monoclinic, “*t*” for tetragonal.

ZrC Raman Shift (cm <sup>-1</sup> )	<i>m</i> -ZrO <sub>2</sub> Raman Shift (cm <sup>-1</sup> ) <sup>30</sup>	<i>t</i> -ZrO <sub>2</sub> Raman Shift (cm <sup>-1</sup> ) <sup>34</sup>	Assignment
94	99	–	<i>A<sub>g</sub></i>
173	175	–	<i>A<sub>g</sub> + B<sub>g</sub></i>
183	188	–	<i>A<sub>g</sub></i>
213	219	–	<i>B<sub>g</sub></i>
263	–	264	<i>A<sub>1g</sub></i>
284 (?)	–	–	–
–	303	–	<i>A<sub>g</sub></i>
328	331/334	320	<i>B<sub>1g</sub></i>
370	379	–	<i>B<sub>g</sub></i>
466	473	–	<i>A<sub>g</sub></i>
513	502	–	<i>B<sub>g</sub></i>
–	535	–	<i>A<sub>g</sub></i>
580	579	606	<i>B<sub>1g</sub></i>
613	615	–	<i>B<sub>g</sub></i>
757	755	–	<i>B<sub>g</sub></i>
970	959	–	–
1020	1012	–	–

The Raman spectrum of the MW-synthesized ZrC contains many similar bands to those observed for *m*-ZrO<sub>2</sub> and overlap has made some bands difficult to distinguish in the ZrC spectrum. However, some additional bands are observed in the Raman spectrum for ZrC

which cannot be assigned to monoclinic  $ZrO_2$  and might match more closely to bands from the tetragonal phase of  $ZrO_2$ . The Raman spectrum of  $t$ - $ZrO_2$  contains six bands which are assigned as follows:<sup>34</sup>

$$\Gamma = 2B_{1g}(R) + 3E_g(R) + A_{1g}(R) \quad (4-3)$$

Only three of these bands are visible in the Raman spectrum of ZrC as illustrated in Table 4-4. Moreover, the latter shows one extra low intensity band at  $284\text{ cm}^{-1}$  which does not seem to belong to either of the two  $ZrO_2$  polymorphs and, hence, has not been assigned (although in principle, it could well be the band from  $m$ - $ZrO_2$  at  $303\text{ cm}^{-1}$ ).

#### 4.2.3.6 X-ray Photoelectron Spectroscopy (XPS)

XPS was employed to analyze the chemical nature of the ZrC surface. Measurements were taken with the assistance of Dr. Sina Saremi-Yarahmadi at the Department of Materials at the University of Loughborough. Figure 4-16 displays the wide survey XPS spectrum for the MW-synthesized ZrC sample, which was prepared from zirconium metal and carbon in 20 minutes in a multi-mode cavity MW reactor.

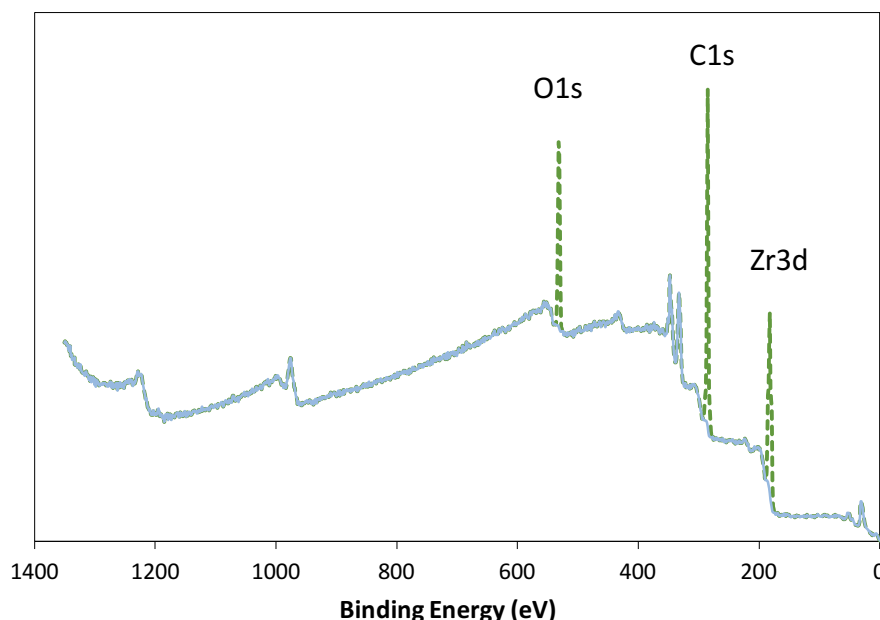


**Figure 4-16** Wide survey X-ray photoelectron spectrum for the MW-synthesized ZrC samples prepared from zirconium metal and carbon in 20 minutes in a multi-mode MW reactor.

The obtained XPS spectra suggest the presence of zirconium, carbon and oxygen, as corresponding peaks in the Zr3d, C1s and O1s regions could be detected.

Four different zirconium species can be distinguished for binding energies ranging from 176 to 189 eV [Figure 4-17]. The peaks at 179.2 and 181.5 eV are due to the presence of zirconium carbide (ZrC). The remaining peaks at 182.4 and 184.5 eV are associated with zirconium oxide species. The presence of such species stands in agreement with the Raman spectra for the ZrC samples (see Section 3.2.3.5).

In the C1s region ranging from 281 to 291 eV [Figure 4-18], four distinct chemical types of carbon were found. The lowest energy peak (~281.5 eV) is associated with the presence of ZrC, whereas the most intense peak at 284.9 eV corresponds to free carbon, arguably as a consequence of remaining traces of graphite susceptor on the sample pellets. Single and double chemical bonding of carbon with oxygen (C–O and C=O) were visible at the highest energies 286.1 and 289.0 eV.

For binding energies ranging from 526 to 536 eV [Figure 4-19], two different types of oxygen species were detected. The peak at 530.2 eV is attributed to the presence of ZrO<sub>2</sub> species, whereas the peak at 531.9 eV is rather indicative of oxygen in an organic compound.

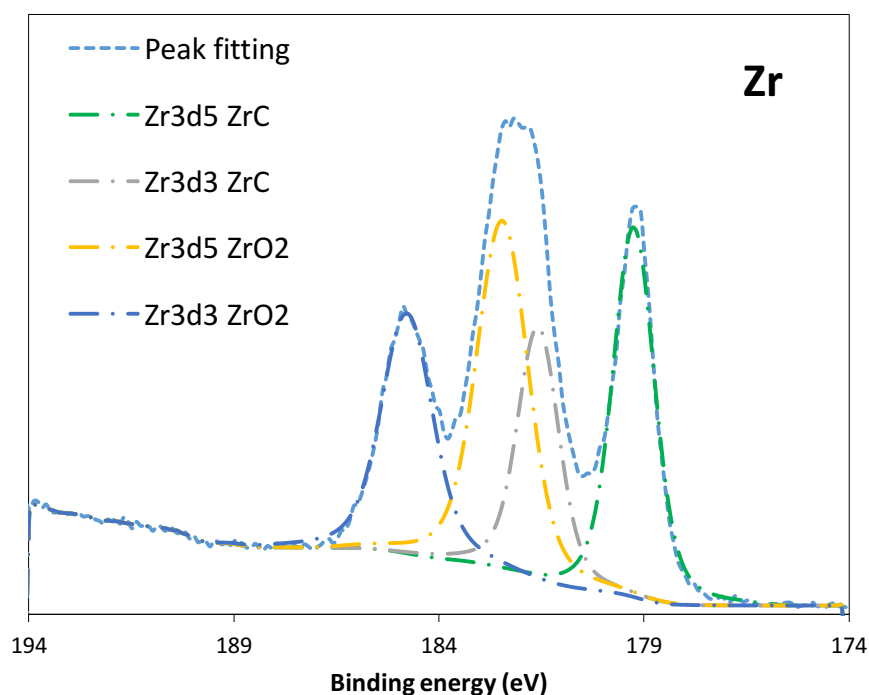


**Figure 4-17** Fitted Zr3d X-ray photoelectron spectrum for the MW-synthesized ZrC samples prepared from zirconium metal and carbon in 20 minutes in a multi-mode MW reactor.

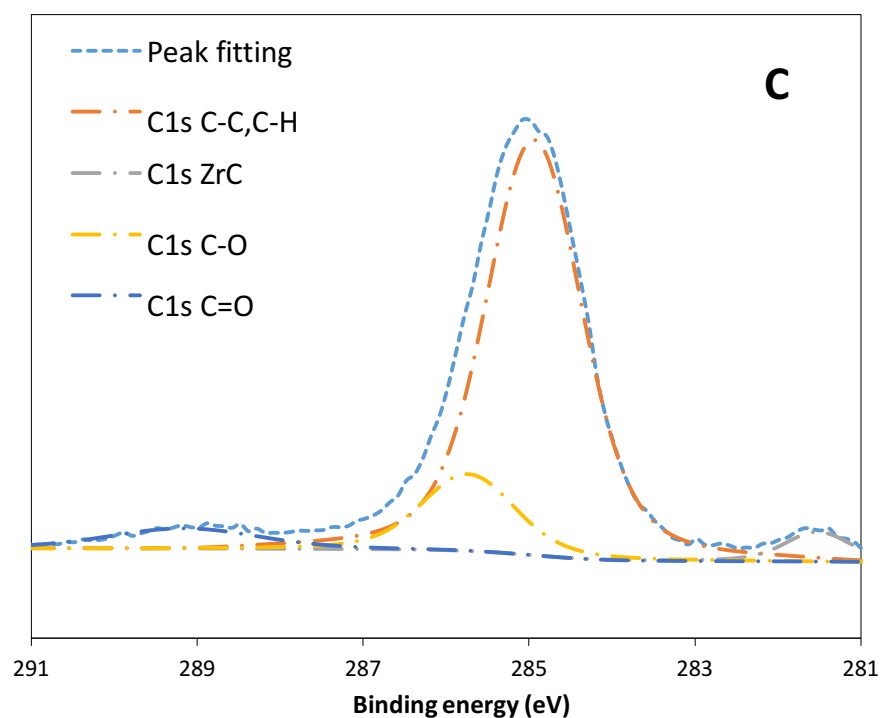


**Figure 4-18** Fitted C1s X-ray photoelectron spectrum for the MW-synthesized ZrC samples prepared from zirconium metal and carbon in 20 minutes in a multi-mode MW reactor.

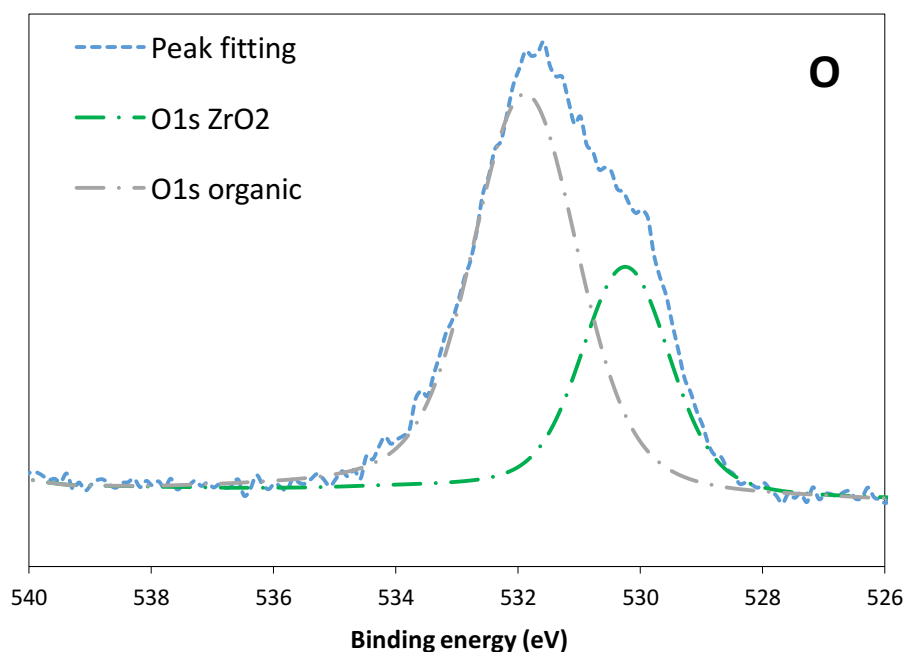


**Figure 4-19** Fitted O1s X-ray photoelectron spectrum for the MW-synthesized ZrC samples prepared from zirconium metal and carbon in 20 minutes in a multi-mode MW reactor.

In light of the XPS results, it is reasonable to conclude that oxygen is indeed present to a depth of 10 nm in the ZrC particles.

The ZrC sample was subsequently subjected to Ar ion etching in order to expose the bulk of the sample for analysis. A sintered pellet was used rather than loose powder as the etching process is much less effective for the latter. Three etchings were performed on the sample, with an etching rate expected to yield removal of approximately 3 nm of surface material per etching. Notably, a pre-etching step was performed to remove surface dust, hence additional 3 nm have to be accounted for. Therefore, after three etchings 12 nm of surface were in principle removed.

Figure 4-20 shows the XPS spectrum of the ZrC samples in the Zr3d region before and after the etching treatment. All the four peaks appear equally intensified following the etching process. This might be due to the presence of free carbon at the surface of particles which decreases after the etching process, as shown in Figure 4-21. The peak at 284.9 eV appears considerably decreased in amplitude after etching, meaning that part of the free carbon has been removed from the material surface. The remaining three peaks at 281.5, 286.1 and 289.0 eV associated with the chemical bonding of carbon with zirconium and oxygen (Zr-C, C-O and C=O, respectively) remain largely unchanged.

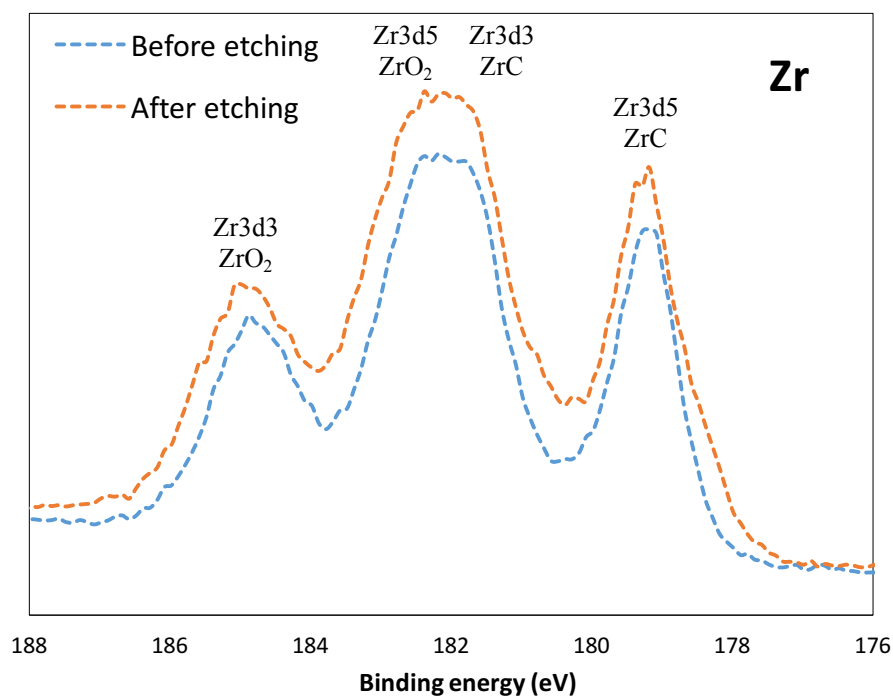


**Figure 4-20** Zr3d X-ray photoelectron spectrum for the MW-synthesized ZrC samples prepared from zirconium metal and carbon in 20 minutes in a multi-mode MW reactor before and after Ar ion etching.

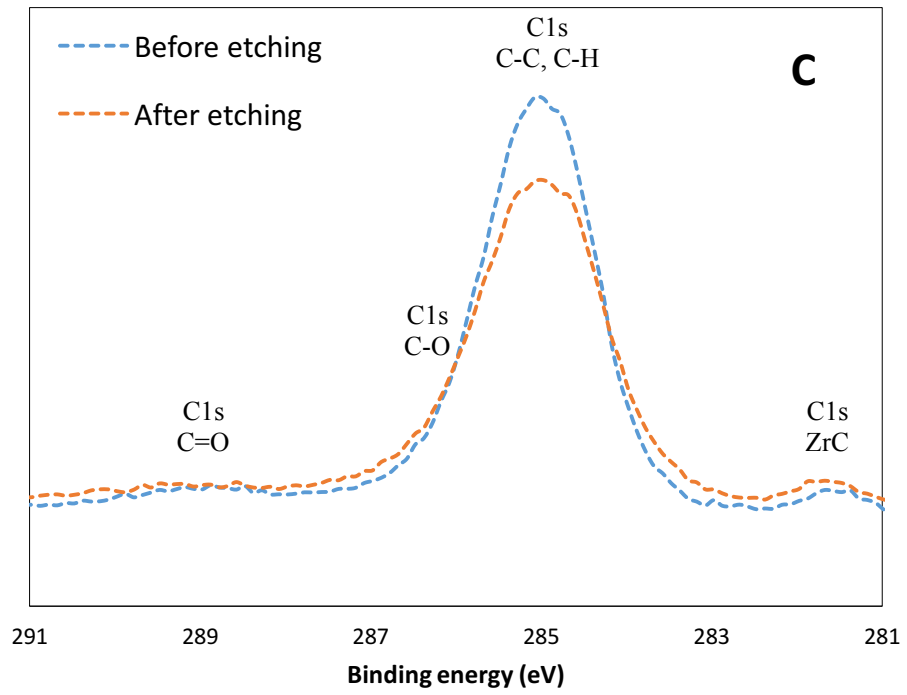


**Figure 4-21** C1s X-ray photoelectron spectrum for the MW-synthesized ZrC samples prepared from zirconium metal and carbon in 20 minutes in a multi-mode MW reactor before and after Ar ion etching.

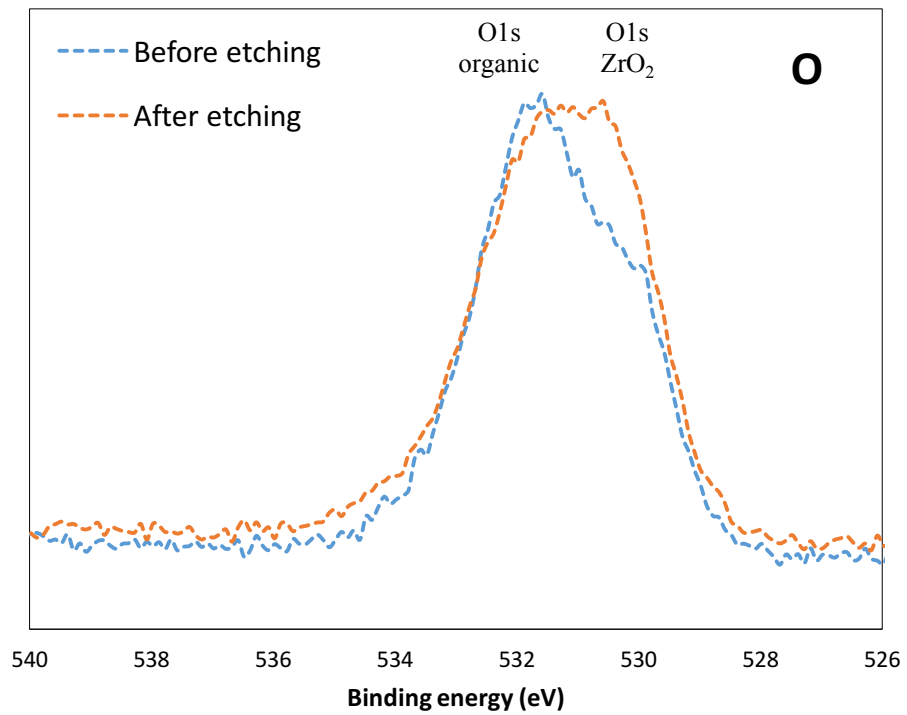


**Figure 4-22** O1s X-ray photoelectron spectrum for the MW-synthesized ZrC samples prepared from zirconium metal and carbon in 20 minutes in a multi-mode MW reactor before and after Ar ion etching.

The XPS spectrum of the O1s region before and after etching is shown in Figure 4-22. The peak at 531.9 eV associated with the presence of oxygen in an organic compound (which could result from the oxidation of graphite) does vary in intensity, whereas the peak at 530.2 eV is assigned to the presence of ZrO<sub>2</sub> increases in intensity in agreement with Figure 4-20.

In summary, XPS measurement confirmed the presence of oxygen at the zirconium carbide surface, consistently with EDX and Raman spectroscopy. Progressive Ar ion etching treatments, removing 12 nm of surface material in total, were found insufficient to remove zirconium oxide species.

#### 4.2.3.7 Powder Neutron Diffraction (PND)

A Powder Neutron Diffraction experiment was performed on a ZrC sample in order to determine the bulk crystal structure more accurately and to establish the stoichiometry of carbon and the existence of oxygen in the material.

PND data were collected at the ISIS facility on the POLARIS diffractometer. For a description of the diffractometer, see Section 2.3.2.1. The sample used for this analysis was prepared by the same method discussed previously, from zirconium metal and graphite for 20 minutes under Ar in a MMC reactor at a power of 800 W. The sample was then loaded into a 6-mm vanadium sample can which was centered in the neutron beam for data collection. Data were collected for approximately 2 h at room temperature using all 5 detector banks.

The sample was analyzed by PXRD prior to PND and the structure refined by the Rietveld method against PXRD data [Appendix, Figure 7-18, Tables 7-5 and 7-6]. The same data collection parameters and refinement procedure was employed as discussed in Section 3.2.3.2. The structure model used for both Rietveld refinements against PXRD data and PND data was the cubic *Fm-3m* ZrC taken from the ICSD database.

Following the PND scans, two Rietveld refinements against the PND data were carried out using different structure models. The first neutron refinement, shown in Figure 4-23, was carried out using the same structure model employed for the X-ray refinement described in Section 3.2.3.2. For the second neutron refinement [Figure 4-24], an oxygen atom was added at the same position where the carbon atom sits (ZrC<sub>x</sub>O<sub>y</sub>) and the occupancy factor of the two atoms was refined. The crystallographic data for both the ZrC and ZrC<sub>x</sub>O<sub>y</sub> refinements are shown in Table 4-5 and Table 4-7, respectively, and the atomic parameters in Table 4-6 and Table 4-8.

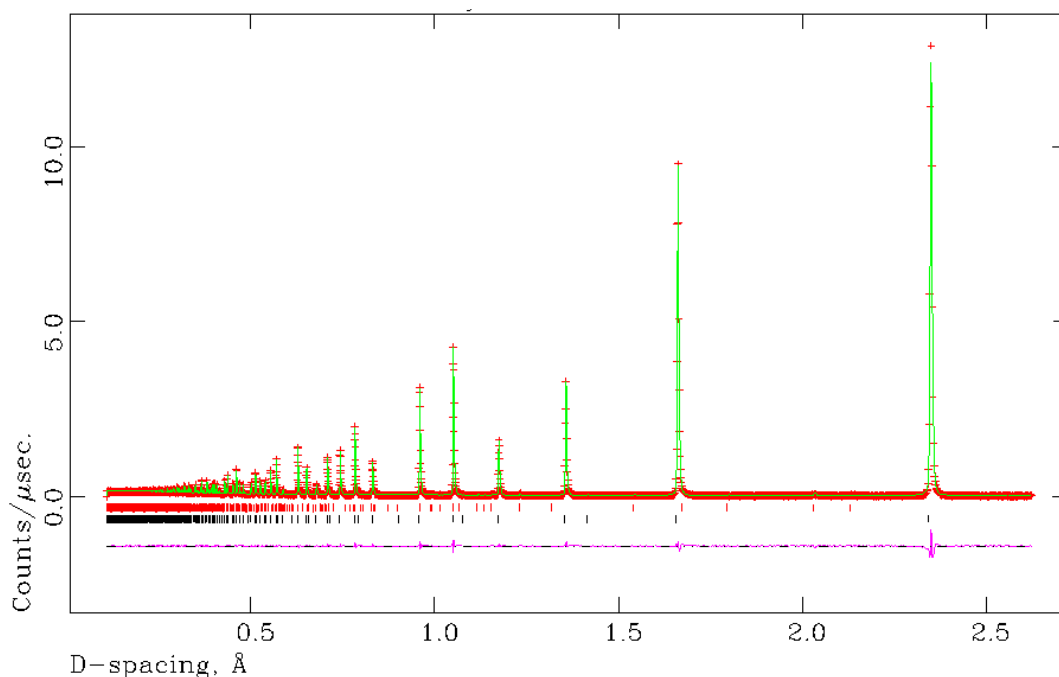


**Figure 4-23** OCD plot from POLARIS bank 5 generated by Rietveld refinement against PND data using the cubic  $Fm-3m$  ZrC structure model taken from the ICSD database. Data were collected at room temperature for approx. 2 h. The red tick marks indicated reflections from graphite and the black tick marks indicate reflections from ZrC.

**Table 4-5** Crystallographic data for Rietveld refinement against PND data for  $ZrC_{0.98}$  using the cubic  $Fm-3m$  ZrC structure model taken from the ICSD database.<sup>16</sup>

<b>Phase data</b>	
Chemical Formula	$ZrC_{0.98}$
Crystal system	Cubic
Space group	$Fm-3m$
$a$ (Å)	4.69862(1)
Volume (Å <sup>3</sup> )	103.73(4)
$Z$	4
Formula weight (g mol <sup>-1</sup> )	103.02
Calculated density (g cm <sup>-3</sup> )	6.5962
$R_{wp}$	0.0537
$R_p$	0.0656
$\chi^2$	4.294

**Table 4-6** Atomic parameters from Rietveld refinement against PND data for  $\text{ZrC}_{0.98}$  using the cubic using the cubic  $Fm-3m$  ZrC structure model taken from the ICSD database.<sup>16</sup>

Atomic parameters					
Name	Fractional coordinates			$U_{\text{iso}}$	Occup.
	$x/a$	$y/b$	$z/c$		
Zr1	0.0000	0.0000	0.0000	0.00332(2)	1.000(0)
C1	0.5000	0.5000	0.5000	0.00293(4)	0.982(2)

In initial cycles, the background was refined using a reciprocal interpolation function (function type 8 within GSAS). The unit cell parameter, diffractometer constant DIFA and peak profiles were included. Modelling of the profile parameters was carried out using GSAS function type 3, which combines back-to-back exponentials and pseudo-Voigt combination with Lorentzian broadening. Once convergence was achieved, the thermal factors and occupancies were also refined.

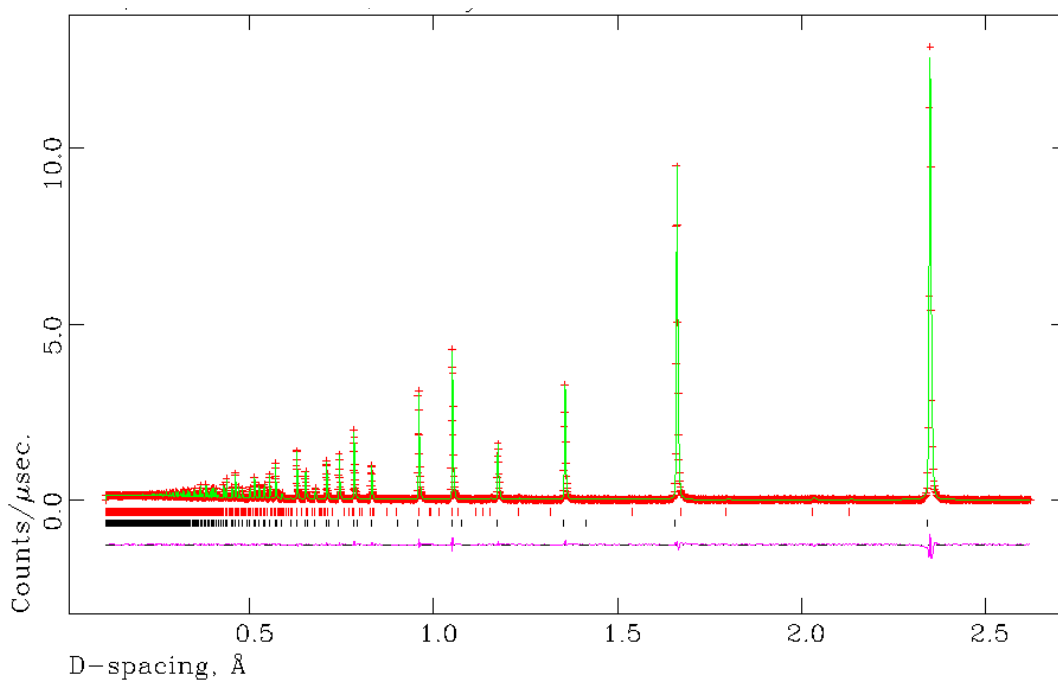


**Figure 4-24** OCD plot from POLARIS bank 5 generated by Rietveld refinement against PND data using the cubic  $Fm-3m$   $\text{ZrC}_x\text{O}_y$  structure model derived from the ZrC structure model taken from the ICSD database. Data collected at room temperature for approx. 2 h. The red tick marks indicated reflections from graphite and the black tick marks indicate reflections from ZrC.

**Table 4-7** Crystallographic data for Rietveld refinement against PND data for  $\text{ZrC}_{0.97}\text{O}_{0.03}$  using the cubic  $Fm\text{-}3m$   $\text{ZrC}_x\text{O}_y$  structure model derived from the ZrC structure model taken from the ICSD database.<sup>16</sup>

<b>Phase data</b>	
Chemical Formula	$\text{ZrC}_{0.97}\text{O}_{0.03}$
Crystal system	Cubic
Space group	$Fm\text{-}3m$
$a$ (Å)	4.69861(1)
Volume (Å <sup>3</sup> )	103.73(2)
$Z$	4
Formula weight (g mol <sup>-1</sup> )	103.38
Calculated density (g cm <sup>-3</sup> )	6.61929
$R_{\text{wp}}$	0.0531
$R_{\text{p}}$	0.0654
$\chi^2$	4.198

**Table 4-8** Atomic parameters for Rietveld refinement against PND data for  $\text{ZrC}_{0.97}\text{O}_{0.03}$  using the cubic  $Fm\text{-}3m$   $\text{ZrC}_x\text{O}_y$  structure model derived from the ZrC structure model taken from the ICSD database.

<b>Atomic parameters</b>					
Name	Fractional coordinates			$U_{\text{iso}}$	Occup.
	$x/a$	$y/b$	$z/c$		
Zr1	0.0000	0.0000	0.0000	0.00238(4)	1.0000
C1	0.5000	0.5000	0.5000	0.00377(1)	0.969(3)
O1	0.5000	0.5000	0.5000	0.00377(1)	0.032(3)

Gendre *et al.* (2011) studied seven different stoichiometries of zirconium oxycarbide powders synthesized by carbothermal reduction of zirconia using conventional heating.<sup>35</sup> The samples were analyzed by PXRD and the lattice parameters were refined by the Rietveld method, which are shown in Table 4-9. The study showed that the lattice parameter of the zirconium oxycarbide phase decreases as the amount of oxygen increases.

**Table 4-9** Stoichiometry and respective lattice parameter for the different zirconium oxycarbide specimens synthesized by Gendre *et al.*<sup>35</sup>

<b>Stoichiometry</b>	<b>Lattice Parameter (Å) (<math>\pm 0.001</math>)</b>
ZrC <sub>1.00</sub>	4.698
ZrC <sub>0.95</sub> O <sub>0.05</sub>	4.695
ZrC <sub>0.90</sub> O <sub>0.10</sub>	4.688
ZrC <sub>0.80</sub> O <sub>0.20</sub>	4.680
ZrC <sub>0.70</sub> O <sub>0.30</sub>	4.679 + ZrO <sub>2</sub>
ZrC <sub>0.60</sub> O <sub>0.40</sub>	4.679 + ZrO <sub>2</sub>
ZrC <sub>0.50</sub> O <sub>0.50</sub>	4.679 + ZrO <sub>2</sub>

Both models refined in this thesis seem to be reasonable and show similar chi-squared and R-factor values. Also, the lattice parameters for the two models are almost identical ( $\sim 4.698$  Å), which is the same value Gendre *at al.* obtained for the ZrC<sub>1.00</sub> specimen. However, if oxygen is present in the bulk of the material, the amount is obviously very small and, hence, difficult to detect and quantify. In light of this consideration, the oxygen-containing model does not find an undisputable confirmation without any further investigations. In light of this, there is no conclusive evidence for oxygen inclusion and the stoichiometry for the MW-synthesized zirconium carbide is probably ZrC<sub>0.98</sub>.

### **4.3 Microwave Synthesis Studies in the ZrO<sub>2</sub>–C system**

This section describes experimental work undertaken to establish a synthetic route to zirconium carbide from zirconium oxide and carbon in both a MMC and a SMC microwave reactors.

#### **4.3.1 Introduction**

The reactions discussed in this section were performed on the basis of the premise of carbothermal reduction of zirconium dioxide followed by carburization (ZrO<sub>2</sub> + C) using microwave heating. The starting materials were mixed according to the following equation:



(4-4)

### 4.3.2 Experimental

#### Synthesis

All reactions reported in this section were performed under Ar by mixing and grinding together zirconium dioxide (M&B, 99.6%) and graphite (Sigma Aldrich, < 50  $\mu\text{m}$ , 99.5%), in a 1:3 stoichiometric ratio according to Equation (3-4). The so-obtained powder mixture (0.5 g) was uniaxially cold pressed into a pellet without the use of a binder. The compact was embedded in graphite powder (here used as a MW susceptor) within a 10-mm quartz tube which is transparent to microwave. The latter was sealed with a septum cap, parafilm and subsequently connected to an Ar flow. The MW reactions were conducted using either a multimode or a single-mode cavity reactor.

For multimode cavity experiments, the tube containing the sample was placed in the center of a beaker containing silica powder which acts as a stand for the tube as well as a thermal insulator. The whole apparatus was then inserted into the multimode cavity of a domestic MW oven (DMO) and positioned in the same location within the cavity to keep the experimental parameters as constant as possible. Synthesis was attempted with an irradiation time of up to 30 min at a power of 800 W.

For single-mode cavity experiments, the tube was directly placed into the applicator of the SMC reactor and held in place by a stand. Synthesis was conducted for a maximum of 10 minutes at a power of 1 kW as the reaction tube was observed to melt for longer reaction times.

#### Characterization

Products were characterized using only Powder X-ray Diffraction as no reaction was observed to occur between  $\text{ZrO}_2$  and carbon. PXRD [Section 2.3.1] was used to identify possible product phases by reference with known structures downloaded from the Inorganic Crystal Structure Database (ICSD)<sup>16</sup> using the PowderCell 2.3 software.<sup>17</sup> The data were collected on a PANalytical Xpert MPD diffractometer, Cu  $\text{K}\alpha_1$  radiation, for 1 h over a range of  $10 < 2\theta^\circ < 85$ .

### 4.3.3 Results and Discussion

#### 4.3.3.1 Powder X-ray Diffraction (PXRD)

After microwave irradiation, the pellet was found to be intact and no color change had occurred as if no reaction took place which was then confirmed by PXRD.

As shown in Figure 4-25, after 20 minutes of microwave irradiation in a domestic MW oven at a power of 800 W, no change in PXRD patterns was observed. In both cases, only the starting materials  $ZrO_2$  and C were found to be present.

Zirconia is known to be a chemically unreactive material. Its remarkable stability has been exploited over the years and makes  $ZrO_2$  a relevant material for refractory applications (such as laboratory crucibles, grinding media, etc.).

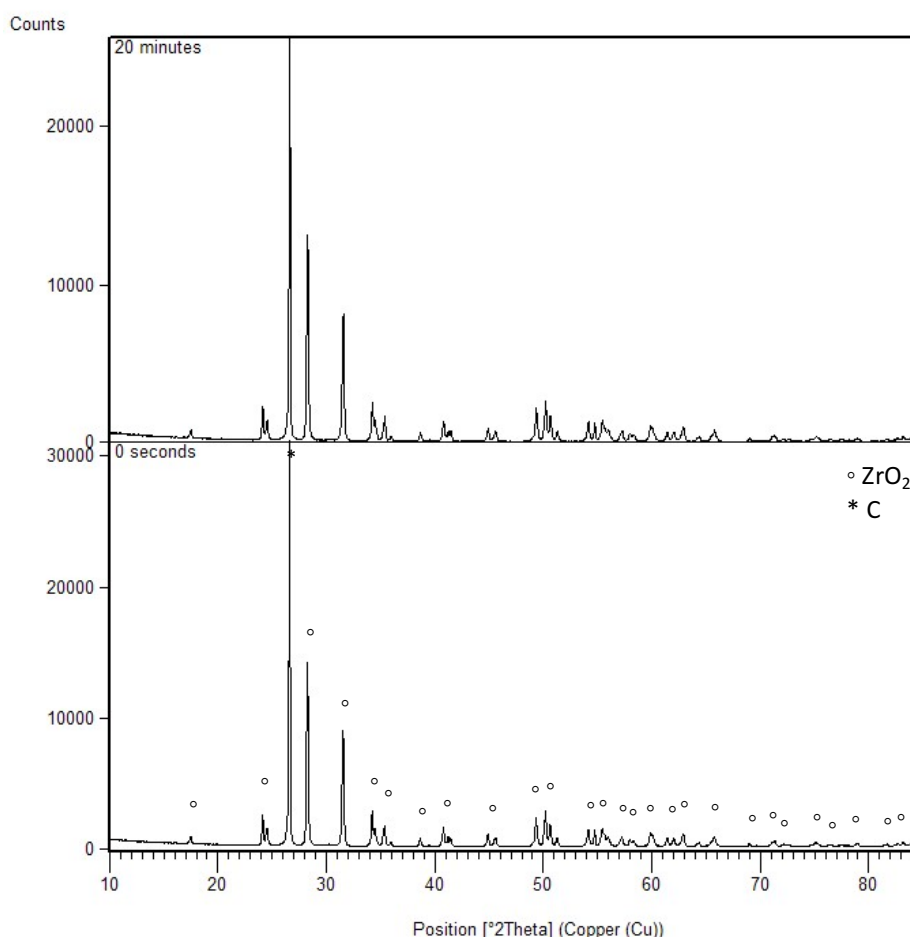


**Figure 4-25** *Ex-situ* PXRD patterns for the  $ZrO_2 + C$  pellets heated in a domestic MW oven at a power of 800 W from reagents (bottom) to products (top).

Nawrocki *et al.* studied the chemistry of zirconium dioxide and its use in chromatography.<sup>36</sup> The review describes both the physical and chemical properties of zirconia and silica from a chromatographic point of view. The study showed that, although

both compounds have similar bond strengths [shown in Table 4-10], they have different chemical reactivity.

**Table 4-10** Bond energies for SiO<sub>2</sub> and ZrO<sub>2</sub>.<sup>36</sup>

<b>Bond</b>	<b>Energy of Dissociation (kcal/mol)</b>	<b>Bond Strength (kcal/mol)</b>	<b>Metal Coordination Number</b>
Si–O	185 ± 7	193 ± 2.6	4
Zr–O	180 ± 5	181.6 ± 2	7

The reason for this difference in reactivity lies in the fact that, in monoclinic zirconia, each zirconium atom is bonded to seven oxygen atoms whereas, in silica, each silicon atom is tetracoordinated to oxygen. These properties combine to make zirconia a chemically unreactive material and silica less stable (more reactive) than the former. This difference in reactivity is relevant in terms of carbide synthesis. Previous studies conducted within our group have shown how it is possible to synthesize silicon carbide (SiC) from silica and graphite via microwave heating in minute timescales.<sup>37</sup> Unfortunately, similar attempts with zirconia and carbon were not successful in this study.

On the other hand, in Section 4.2.1, it was mentioned that Das *et al.* successfully synthesized ZrC-SiC composites by carbothermal reduction of zircon sand [Table 4-1] via microwave heating<sup>15</sup> using a similar experimental set-up to that used in this study. The success of this microwave synthesis might be due to the fact that zircon sand contains a relatively high amount of SiO<sub>2</sub> (28 wt. % for the study in question) which produces SiC by reacting with carbon. Among its wealth of applications, silicon carbide is also known to be a strong absorber of microwaves which induce a flow of free electrons in the semiconducting structure of SiC that heats up the material very quickly via a ohmic resistance heating mechanism.<sup>38</sup> This is likely to be the driving force that enables ZrO<sub>2</sub> and carbon to react in the presence of SiO<sub>2</sub>.

Maitre *et al.* (1997) reported the synthesis of ZrC from zirconia and carbon under flowing Ar using conventional heating. Zirconium carbide was obtained after heating the starting materials for 24 h at a temperature of 1823 K, which could be a too high to be reached under the experimental conditions employed in this study. Unfortunately, it was not possible to record temperature measurements during the microwave reactions for a comparison with the above cited study.

## 4.4 Microwave Synthesis Studies in Hf–C system

This section describes experimental work undertaken to establish a synthetic route to hafnium carbide from hafnium metal and carbon in either a MMC or a SMC reactor. Unfortunately, the use of the latter was attempted but, because of the fast melting of the reaction tubes in initial irradiation times, no further experiments were performed. Only MMC experiments are therefore presented in this section.

### 4.4.1 Introduction

Hafnium carbide has very similar chemical and physical properties to ZrC (as they are both group IV transition metal carbides) and has been synthesized using direct reaction of elemental powders, carbothermal reduction of hafnium dioxide,<sup>39,40</sup> mechanically activated solid-state synthesis,<sup>41,42</sup> sol-gel route,<sup>43</sup> electrochemical synthesis,<sup>44</sup> chemical vapour deposition<sup>45</sup> and several other methods.<sup>46–49</sup> However, energy inefficiency, high cost, impurities and/or low yields are issues that normally occur in these common synthetic methods.

As per the production of ZrC, HfC is industrially synthesized by carbothermal reduction of HfO<sub>2</sub>. The synthesis and densification of nano-crystalline hafnium carbide powders was previously investigated by Feng *et al.* (2015).<sup>39</sup> The starting materials used in this study were hafnium dioxide and a phenolic resin with char yield of 49 wt% as a hafnium and carbon source, respectively. These compounds were mixed in a polyethylene bottle for 4 h using yttria-stabilized ZrO<sub>2</sub> balls and ethanol as the mixing media. The mixture was dried at 120 °C for 12 h and granulated to obtain a fine powder. The latter was subsequently uniaxially cold pressed into 30-mm pellets which were placed in a graphite crucible and heated under vacuum using a spark plasma sintering (SPS) apparatus at a temperature of 1650 °C for 90 min.

There are no previous studies which investigate the microwave synthesis of hafnium carbide either from direct reaction of elemental powders or by carbothermal reduction of HfO<sub>2</sub>. The reactions discussed in this section were performed by direct reaction of the elemental starting materials (Hf + C). The starting materials were mixed in a 1:1 stoichiometric ratio according to the following equation:



By microwave heating the reactant pellet alone, no reaction was observed although both starting materials (Hf + C) theoretically couple with microwaves. This required instead the use of graphite as a microwave susceptor to provide additional thermal heating on the outside of the pellet.

## 4.4.2 Experimental

### 4.4.2.1 Synthesis

All reactions reported in this section were performed under Ar by mixing and grinding together Hf metal (Alfa Aesar, < 45  $\mu\text{m}$ , 99.6%) and graphite (Sigma Aldrich, < 50  $\mu\text{m}$ , 99.5%), in a 1:1 stoichiometric ratio according to Equation (4-5). The so-obtained powder mixture (1 g) was uniaxially cold pressed into a pellet without the use of a binder. Samples were pressed in a cylindrical shape with a diameter of 8 mm and height of approximately 5 mm. This compact was embedded in graphite powder (here used as a MW susceptor) within a 10-mm quartz tube which is transparent to microwave. The tube was then sealed with a septum cap, parafilm and subsequently connected to an Ar flow. The MW reactions were conducted by using both multi-mode and single-mode cavity reactors.

For multimode cavity experiments, the tube containing the sample was placed in the center of a beaker containing silica powder which acts as a stand for the tube as well as a thermal insulator. The whole apparatus was then inserted into the multimode cavity of a domestic MW oven (DMO) and positioned in the same location within the cavity to keep the experimental parameters as constant as possible.

For single-mode cavity experiments, the tube was directly placed into the applicator of the SMC reactor and held in place by a stand.

### 4.4.2.2 Characterization

Products were characterized using only Powder X-ray Diffraction as hafnium carbide was not successfully synthesized as a single-phase. PXRD [Section 2.3.1] was used to identify possible product phases by reference with known structures downloaded from the Inorganic Crystal Structure Database (ICSD)<sup>16</sup> using the PowderCell 2.3 software.<sup>17</sup> The data were collected on a PANalytical Xpert MPD diffractometer, Cu K $\alpha$ 1 radiation, for 1 hour over a range of  $10 < 2\theta/^\circ < 85$ .

## 4.4.3 Results and Discussion

### 4.4.3.1 Powder X-ray Diffraction (PXRD)

After using different irradiation times for the microwave synthesis of HfC, it was found that the best results were obtained after a 20-minute reaction in a MMC reactor at a power of 800 W. Samples was then analyzed ex-situ by Powder X-ray Diffraction. The PXRD pattern for a so-obtained sample is shown in Figure 4-26.

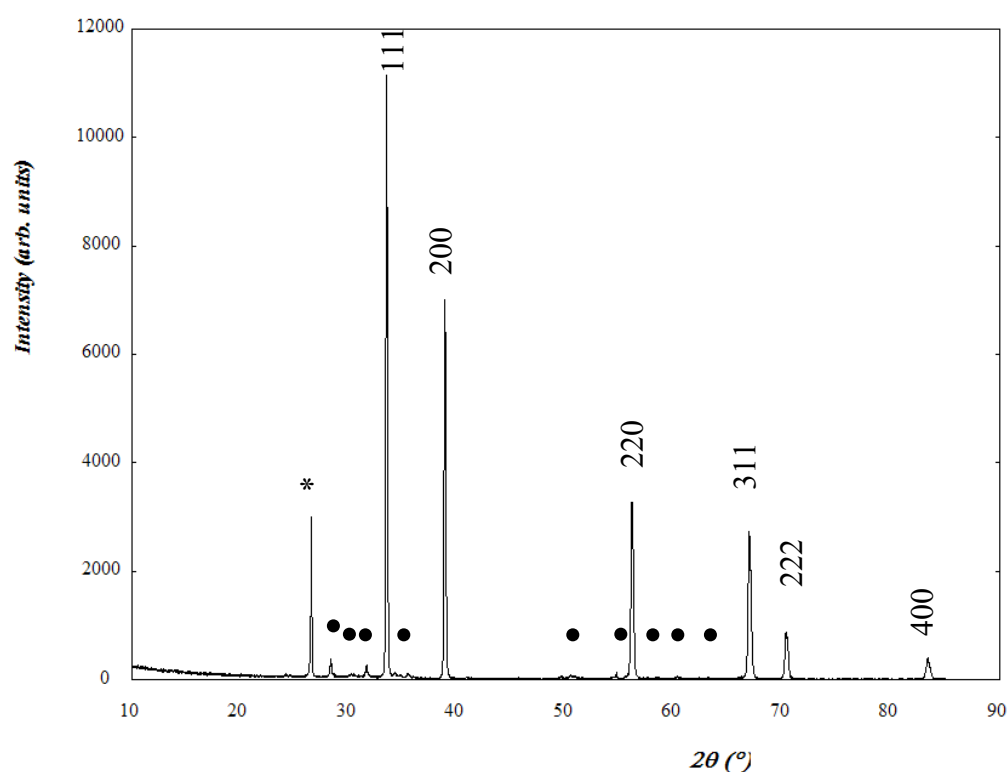


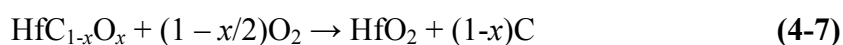
**Figure 4-26** PXRD pattern taken *ex-situ* from hafnium metal plus graphite (1:1) heated in a DMO for 20 minutes at a power of 800 W under Ar. The reflection marked \* can be attributed to the (002) reflection from graphite whereas the low intensity reflections marked • belong to the hafnium dioxide phase.

The products were identified as hafnium carbide (HfC), which crystallizes in a cubic structure (space group  $Fm-3m$ ), hafnium dioxide (HfO<sub>2</sub>) and unreacted graphite. The PXRD pattern consists of six sharp peaks characteristic of the salt-like structure which represent the reflection from the (111), (200), (220), (311), (222) and (400) planes plus an extra reflection at  $2\theta = 26.5^\circ$  (which belongs to the (002) reflection from graphite). Additionally, several weak peaks (marked with “•”) can be attributed to HfO<sub>2</sub>.

In Figure 4-26, it can be seen that the graphite reflection is relatively intense, especially when compared to the other post-reaction carbide systems discussed in this thesis. This suggests that there is considerable unreacted carbon remaining after reaction and that some hafnium metal reacts with oxygen to form HfO<sub>2</sub>. As per the V-C and Zr-C system, the oxygen contamination is thought to be coming from the presence of oxygen on the surface of the metal particles or impurity in the Ar supply. All possible measures were taken to prevent that oxygen could get into from a leak in the argon line.

For reaction times longer than 20 minutes, it is observed that the intensity of HfC reflections decreases as those of HfO<sub>2</sub> increase, suggesting that hafnium carbide is gradually oxidized to hafnium dioxide.

The oxidation of HfC has been the subject of investigations of high-temperature structural materials for some years.<sup>50-53</sup> Shimada *et al.* studied the isothermal oxidation of HfC single crystals at temperatures of 700° - 1500°C and at oxygen pressures of 0.08-80 kPa for 4 h.<sup>53</sup> It was found that during and after the initial rapid oxidation of HfC with the formation of the oxycarbide phase, HfC<sub>x</sub>O<sub>1-x</sub>, carbon is released according to equations (4-6) and (4-7):



Such temperatures (700°C - 1000°C) are easily reached during the microwave reactions described in this thesis.<sup>54</sup> It is reasonable to propose that hafnium carbide (and/or the starting hafnium metal) undergoes oxidation during the MW reactions above due to the presence of oxygen in the system.

In summary, the PXRD pattern shown in Figure 4-26 confirms the successful formation of HfC as a major product but the formation of the oxide phase prevents the reaction to go to completion as HfO<sub>2</sub> does not react with carbon at temperatures reached within the microwave cavity. Unfortunately, it was not possible to measure the temperature reached during reactions because no such instrumentation was available.

#### 4.4.3.2 Ex-situ Study of the Hf + C Reaction as a Function of Time

From the ex-situ PXRD data, a phase analysis was conducted by monitoring the phase evolution as a function of time for both multimode and single-mode cavity experiments.

Figure 4-27 shows the PXRD patterns collected after the Hf + C pellets were irradiated with MWs for 0 s, 5 mins, 10 mins, 15 mins and 20 mins in the MMC reactor at a power of

800 W. At  $t = 0$  s (when the magnetron was still off), only reflections from hafnium metal and graphite are present as might be expected (but demonstrating that no  $\text{HfO}_2$  could be detected in the starting materials). After 5 minutes of microwave irradiation, hafnium carbide starts to form as the amount of Hf and C decreases. Also, peaks from the hafnium oxide phase are observed after 5 min of irradiation (although the reactions were run under Ar). No other phases/intermediates are observed during the conversion to  $\text{HfC}$ . At  $t = 10$  and 15 minutes, hafnium metal and graphite continues to react and  $\text{HfC}$  becomes the major phase. At this point, only a small amount of hafnium remains which then disappears as the reaction time reaches 20 minutes. No more  $\text{HfC}$  is observed from this point onwards.

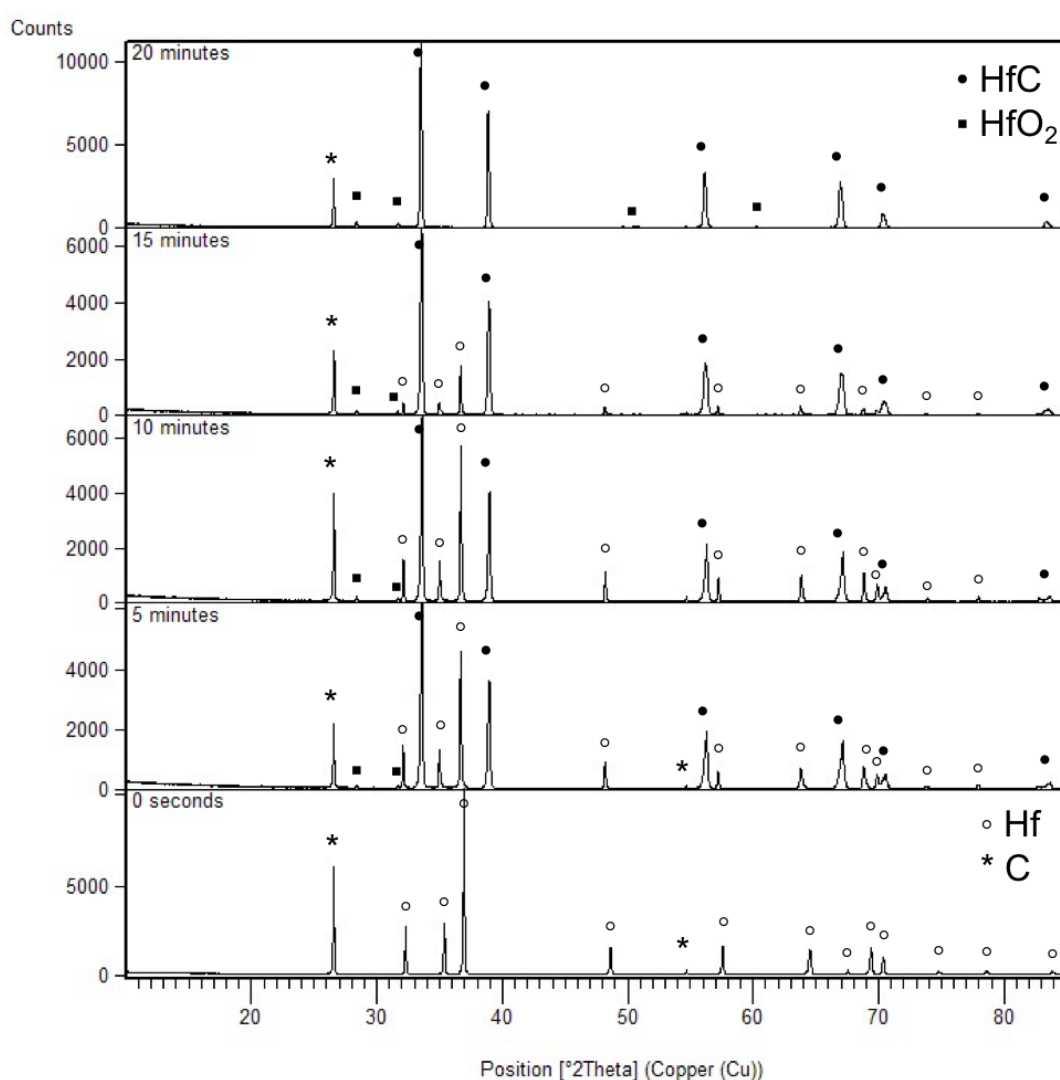


**Figure 4-27** Ex-situ patterns for Hf + C pellets heated in an MMC reactor at a power of 800 W for 0 seconds (bottom) to 20 minutes (top).

The carbothermal reduction/carburization of hafnium dioxide was also investigated in this study and was not successful. No reaction between reactants ( $\text{HfO}_2 + \text{C}$ ) was observed.

The experiments were carried out using the same procedure used for the carbothermal reduction of zirconia, described in Section 4.3. Both synthetic routes turned out to be unsuccessful using microwave irradiation as the two oxide materials are known to be chemically unreactive.

## 4.5 Chapter Summary

This work aimed at synthesizing zirconium and hafnium carbides by direct reaction of elemental powders ( $\text{Zr/Hf} + \text{C}$ ) and carbothermal reduction/carburization of zirconium/hafnium dioxide ( $\text{ZrO}_2/\text{HfO}_2 + \text{C}$ ) using both multi- and single-mode MW reactors. Upon establishing appropriate synthetic route and reaction conditions, the resulting products were characterized by PXRD, SEM/EDX, Raman Spectroscopy, XPS and PND.

Direct reactions of elemental powders under air resulted in the oxidation of the starting metal powder (Zr or Hf) and the subsequent formation of the respective oxide phase ( $\text{ZrO}_2$  or  $\text{HfO}_2$ ) which posed as a barrier to the formation of the carbide phase. Indeed, the carbothermal reduction of neither zirconia nor hafnia was successful, as the starting materials do not couple with microwaves.

Zirconium carbide can be synthesized from zirconium metal and carbon under Ar in 20 minutes using an MMC reactor at a power of 800 W and in 6 minutes using a SMC reactor at a power of 1 kW. Rietveld refinement against PXRD data confirmed the formation of zirconium carbide as a single phase (together with a small amount of graphite, originating from susceptor) which crystallizes in a cubic structure (space group  $Fm-3m$ ) with lattice parameter  $a = 4.69645(1) \text{ \AA}$ . SEM micrographs and EDX spectra revealed the formation of irregular micron-scale particles with a relatively rough surface containing zirconium, carbon and, occasionally, oxygen as indicated by Raman Spectroscopy. Raman spectra of the MW-synthesized products showed indeed bands which could be attributed to both  $m\text{-ZrO}_2$  and  $t\text{-ZrO}_2$ . XPS analysis taken together with Ar ion etching confirmed the presence of oxygen in the  $\sim 12 \text{ nm}$  of the surface material removed. A PND investigation of the ZrC sample was performed using two different structure models. The first model, taken from the ICSD database, was the cubic  $Fm-3m$  ZrC structure. This neutron refinement supports a zirconium carbide sample with a Zr:C stoichiometry of 1:0.98 ( $\text{ZrC}_{0.98}$ ). The second structure model used was obtained by adding an oxygen atom at the same position where the carbon atom sits and the occupancy factors for the two non-metal atoms were refined. The obtained Zr:C:O stoichiometry was 1:0.97:0.03, leading to the formula  $\text{ZrC}_{0.97}\text{O}_{0.03}$ . Although both

refinements lead to plausible ZrC compositions, the presence of oxygen traces can be very challenging to detect. Conceivably, the bulk particle composition is  $\text{ZrC}_{0.98}$  with some oxygen present at the surface of the particles.

Lastly, the direct reaction of hafnium metal and carbon under Ar using either a multi-mode or a single-mode MW reactor led to the formation of hafnium carbide as a major product together with unreacted C and a small amount of  $\text{HfO}_2$ . Once  $\text{HfO}_2$  had formed in this system, further production of HfC appeared impossible under the conditions employed. The source of this oxygen contamination is unfortunately still unclear. However, the Hf-C system behaves similarly to the Zr-C system and it is believed that hafnium carbide might be obtained as a single phase, if only oxygen could be excluded.

## 4.6 References

1. Sara, R. V. The System Zirconium-Carbon. *J. Am. Ceram. Soc.* **48**, 243–247 (1965).
2. Deardorff, D. K.; Copeland, M. I.; Adams, R. P. The Hafnium-Carbon Phase Diagram. *U.S. Dept. Inter. Bur. Mines* (1967).
3. Nachiappan, C., Rangaraj, L., Divakar, C. & Jayaram, V. Synthesis and densification of monolithic zirconium carbide by reactive hot pressing. *J. Am. Ceram. Soc.* **93**, 1341–1346 (2010).
4. Chu, A. *et al.* Carbothermal synthesis of ZrC powders using a combustion synthesis precursor. *Int. J. Refract. Met. Hard Mater.* **36**, 204–210 (2013).
5. Maitre, A. & Lefor, P. Solid state reaction of zirconia with carbon. *Solid State Ionics* **104**, 109–122 (1997).
6. Sondhi, A., Morandi, C., Reidy, R. F. & Scharf, T. W. Theoretical and experimental investigations on the mechanism of carbothermal reduction of zirconia. *Ceram. Int.* **39**, 4489–4497 (2013).
7. Wang, L., Si, L., Zhu, Y. & Qian, Y. Solid-state reaction synthesis of ZrC from zirconium oxide at low temperature. *Int. J. Refract. Met. Hard Mater.* **38**, 134–136 (2013).
8. Tsuchida, T. & Yamamoto, S. Mechanical activation assisted self-propagating high-temperature synthesis of ZrC and ZrB<sub>2</sub> in air from Zr/B/C powder mixtures. *J. Eur. Ceram. Soc.* **24**, 45–51 (2004).
9. Xiang, J. Y. *et al.* Mechanochemically activated synthesis of zirconium carbide nanoparticles at room temperature: A simple route to prepare nanoparticles of

- transition metal carbides. *J. Eur. Ceram. Soc.* **31**, 1491–1496 (2011).
10. Ang, C., Williams, T., Seeber, A., Wang, H. & Cheng, Y. B. Synthesis and evolution of zirconium carbide via Sol-Gel route: Features of nanoparticle oxide-carbon reactions. *J. Am. Ceram. Soc.* **96**, 1099–1106 (2013).
  11. Dollé, M. *et al.* Synthesis of nanosized zirconium carbide by a sol-gel route. *J. Eur. Ceram. Soc.* **27**, 2061–2067 (2007).
  12. Combemale, L., Leconte, Y., Portier, X., Herlin-Boime, N. & Reynaud, C. Synthesis of nanosized zirconium carbide by laser pyrolysis route. *J. Alloys Compd.* **483**, 468–472 (2009).
  13. Seo, M., Kang, S., Kim, Y. & Ryu, S. S. Preparation of highly dispersed ultra-fine ZrC by combination of carbothermal reduction of ball-milled ZrO<sub>2</sub> and C mixture and bead milling. *Int. J. Refract. Met. Hard Mater.* **41**, 345–350 (2013).
  14. Yan, C., Liu, R., Cao, Y., Zhang, C. & Zhang, D. Synthesis of submicrometer zirconium carbide formed from inorganic-organic hybrid precursor pyrolysis. *J. Sol-Gel Sci. Technol.* **64**, 251–256 (2012).
  15. Das, B. P., Panneerselvam, M. & Rao, K. J. A novel microwave route for the preparation of ZrC-SiC composites. *J. Solid State Chem.* **173**, 196–202 (2003).
  16. Rühl, S. Inorganic Crystal Structure Database (ICSD). *A Focus Crystallogr.* **6**
  17. Kraus, W. & Nolze, G. Powder cell 2.3 version. *CPD Newslett* **20**, 274–280 (1998).
  18. Larson, A. C. & Dreele, R. B. Von. General Structure Analysis System (GSAS). *Los Alamos Natl. Lab. Rep. LAUR* 86–748 (2000).
  19. Toby, B. H. EXPGUI, a graphical user interface for GSAS. *J. Appl. Crystallogr.* **34**, 210–213 (2001).
  20. Bittner, H.; Goretzki, H. Magnetische Untersuchungen der Carbide TiC, ZrC, HfC, VC, NbC und TaC. *Monatshefte fuer Chemie* **5**, 1000–1004 (1962).
  21. Samsonov, G. V.; Rozinova, N. S. Some physicochemical properties of alloys of zirconium with carbon. *Izv. Sekt. Platny Drugikh Blagoronykh Met. Inst. Obs. i Neorg. Khimii, Akad. Nauk. SSSR* p126–p132 (1956).
  22. Toth, L. E. *Transition Metal Carbides and Nitrides*. (Elsevier, 2014).
  23. Stevens, R. *An introduction to zirconia. Magnesium Elektron Publication* **113**, (1986).
  24. Anastassakis, E., Papanicolaou, B. & Asher, I. M. Lattice dynamics and light scattering in Hafnia and Zirconia. *J. Phys. Chem. Solids* **36**, 667–676 (1975).
  25. Barberis, P., Merle-Méjean, T. & Quintard, P. On Raman spectroscopy of zirconium oxide films. *J. Nucl. Mater.* **246**, 232–243 (1997).
  26. Feinberg, A. & Perry, C. H. Structural disorder and phase transitions in ZrO<sub>2</sub>-Y<sub>2</sub>O<sub>3</sub>

- system. *J. Phys. Chem. Solids* **42**, 513–518 (1981).
27. Hirata, T. Raman-active modes and the tetragonal-monoclinic phase-transition in ZrO<sub>2</sub> doped with 12 mol-percent CeO<sub>2</sub>. *J. Phys. Chem. Solids* **56**, 951–957 (1995).
  28. Hirata, T., Asari, E. & Kitajima, M. Infrared and Raman Spectroscopic Studies of ZrO<sub>2</sub> Polymorphs Doped with Y<sub>2</sub>O<sub>3</sub> or CeO<sub>2</sub>. *Journal of Solid State Chemistry* **110**, 201–207 (1994).
  29. Ishigame, M. & Yoshida, E. Study of the defect-induced Raman spectra in cubic zirconia. *Solid State Ionics* **23**, 211–218 (1987).
  30. Keramidis, V. & White, W. Raman scattering study of the crystallization and phase transformations of ZrO<sub>2</sub>. *J. Am. Ceram. Soc.* **57**, 22–24 (1974).
  31. Kim, B. & Hamaguchi, H. Mode Assignments of the Raman Spectrum of Monoclinic Zirconia by Isotopic Exchange Technique. *Phys. Status Solidi* **203**, 557–563 (1997).
  32. Kim, B.-K., Hahn, J.-W. & Han, K. R. Quantitative phase analysis in tetragonal-rich tetragonal/monoclinic two phase zirconia by Raman spectroscopy. *J. Mater. Sci. Lett.* **16**, 669–671 (1997).
  33. Phillippi, C. M. & Mazdiyasi, K. S. Infrared and Raman Spectra of Zirconia Polymorphs. *J. Am. Ceram. Soc.* **54**, 254–258 (1971).
  34. Quintard, P. & Barbéris, P. Comparative Lattice-Dynamical Study of the Raman Spectra of Monoclinic and Tetragonal Phases of Zirconia and Hafnia. *J. Am. Ceram. Soc.* **85**, 1745–1749 (2002).
  35. Gendre, M., Maître, A. & Trolliard, G. Synthesis of zirconium oxycarbide (ZrC<sub>x</sub>O<sub>y</sub>) powders: Influence of stoichiometry on densification kinetics during spark plasma sintering and on mechanical properties. *J. Eur. Ceram. Soc.* **31**, 2377–2385 (2011).
  36. Nawrocki, J., Rigney, M., McCormick, A. & Carr, P. W. Chemistry of zirconia and its use in chromatography. *J. Chromatogr. A* **657**, 229–282 (1993).
  37. Carassiti, L. *et al.* Ultra-rapid, sustainable and selective synthesis of silicon carbide powders and nanomaterials via microwave heating. *Energy Environ. Sci.* **4**, 1503–1510 (2011).
  38. Gutmann, B. *et al.* Sintered silicon carbide: A new ceramic vessel material for microwave chemistry in single-mode reactors. *Chem. - A Eur. J.* **16**, 12182–12194 (2010).
  39. Feng, L., Lee, S. H., Wang, H. & Lee, H. S. Synthesis and densification of nanocrystalline hafnium carbide powder. *J. Eur. Ceram. Soc.* **35**, 4073–4081 (2015).
  40. Liu, J. X., Kan, Y. M. & Zhang, G. J. Synthesis of ultra-fine hafnium carbide powder and its pressureless sintering. *J. Am. Ceram. Soc.* **93**, 980–986 (2010).
  41. Barraud, E., Bégin-Colin, S., Le Caër, G., Barres, O. & Villieras, F. Mechanically

- activated solid-state synthesis of hafnium carbide and hafnium nitride nanoparticles. *J. Alloys Compd.* **456**, 224–233 (2008).
42. Matteazzi, P. Room-Temperature Mechanosynthesis of Carbides. 1382–1390 (1991).
  43. Matović, B. *et al.* Synthesis and characterization of hafnium carbide fine powders. *Ceram. Int.* **39**, 719–723 (2013).
  44. Abdelkader, A. M. & Fray, D. J. Electrochemical synthesis of hafnium carbide powder in molten chloride bath and its densification. *J. Eur. Ceram. Soc.* **32**, 4481–4487 (2012).
  45. Ache, H. F. *et al.* Chemical vapour deposition of hafnium carbide and characterization of the deposited layers by secondary-neutral mass spectrometry. *Thin Solid Films* **241**, 356–360 (1994).
  46. Patra, N., Nasiri, N. Al, Jayaseelan, D. D. & Lee, W. E. Low-temperature solution synthesis of nanosized hafnium carbide using pectin. *Ceram. Int.* **42**, 1959–1963 (2016).
  47. Sacks, M. D., Wang, C. A., Yang, Z. & Jain, A. Carbothermal reduction synthesis of nanocrystalline zirconium carbide and hafnium carbide powders using solution-derived precursors. *J. Mater. Sci.* **39**, 6057–6066 (2004).
  48. Sevastyanov, V. G. *et al.* Low-Temperature Synthesis of Nanodispersed Titanium, Zirconium, and Hafnium Carbides. *Russ. J. Inorg. Chem.* **56**, 661–672 (2011).
  49. Carbide, H. Dynamic Compaction of Combustion-Synthesized Hafnium Carbide. **87**, 383–387 (1990).
  50. Bargeron, C. B.; Benson, R. C. X-ray Microanalysis of a Hafnium Carbide Film Oxidized at High Temperature. *Surf. Coat. Technol.* **36**, 111–115 (1988).
  51. Bargeron, C. B., Benson, R. C., Jette, A. N. & Phillips, T. E. Oxidation of Hafnium Carbide in the Temperature Range 1400° to 2060°C. *J. Am. Ceram. Soc.* **76**, 1040–1046 (1993).
  52. Shimada, S., Inagaki, M. & Matsui, K. Oxidation Kinetics of Hafnium Carbide in the Temperature Range of 480°C to 600°C. *J. Am. Ceram. Soc.* **10**, 2671–78 (1992).
  53. Shimada, S. & Yunazar, F. Oxidation of Hafnium Carbide and Titanium Carbide Single Crystals with the Formation of Carbon at High Temperatures and Low Oxygen Pressures. *J. Am. Ceram. Soc.* **28**, 721–728 (2000).
  54. McGill, B. S. L. & Walkiewicz, W. Microwave Heating of Chemical and Minerals. *Dep. Inter. Bur. Mines* **95**, 1–28 (1995).

## 5 Preliminary Studies on the Microwave Synthesis and Structural Characterization of Nitrides in the Zr-N System

### 5.1 Introduction to Zirconium Nitride

Zirconium nitride is a hard ceramic material and, as such, finds myriad applications in refractories, cermets and laboratory crucibles. Gribaudo et al. (1994) studied the phase relations in the zirconium-nitrogen system<sup>1</sup> and assessed the Zr-N phase diagram which is illustrated in Figure 5-1.

Stoichiometric ZrN is the only stable phase in the zirconium-nitrogen system<sup>2</sup> although other non-stoichiometric metastable phases have been previously reported in the literature, such as Zr<sub>3</sub>N<sub>4</sub>,<sup>3</sup> ZrN<sub>2</sub><sup>4</sup> and Zr<sub>2</sub>N.<sup>5</sup> ZrN crystallizes in the NaCl-type cubic structure (space group *Fm-3m*,  $a = 4.585 \text{ \AA}$ ) [Figure 5-2] and occurs over a considerable range of composition and can exist as ZrN<sub>*x*</sub> (where  $0 < x < 1$ ).<sup>2</sup> Zerr et al. (2003) prepared Zr<sub>3</sub>N<sub>4</sub> through a high-pressure synthesis.<sup>6</sup> Experiments were performed in a laser-heated diamond anvil cell at pressures up to 18 GPa and temperatures up to 3,000 K. The compound crystallizes in a cubic structure (space group *I-43d*) and shows a unit cell parameter of  $a = 6.740 \text{ \AA}$ .

The work presented in this chapter illustrates a preliminary study on the microwave synthesis and structural characterization of ZrN in a multi-mode cavity microwave reactor. No single-mode cavity experiments were attempted for this system, due to time limitations. The zirconium nitride material has been prepared by reacting zirconium metal powder with nitrogen (N<sub>2</sub>) or ammonia (NH<sub>3</sub>) gas at atmospheric pressure. Once an appropriate synthetic procedure was established, the MW-synthesized samples were investigated by Powder X-ray Diffraction (PXRD), Scanning Electron Microscopy (SEM) coupled with Energy Dispersive X-ray (EDX) analysis and Raman Spectroscopy.

The microwave reaction under N<sub>2</sub> led to the formation of ZrN together with the apparent presence of unreacted Zr metal, which is more likely a nitride ZrN<sub>*x*</sub> with *x* close to zero. The same reaction run under NH<sub>3</sub> led again to the formation of ZrN but the formation of a cubic phase is also observed which appear to be the nitride-stabilized cubic form of ZrO<sub>2</sub>.

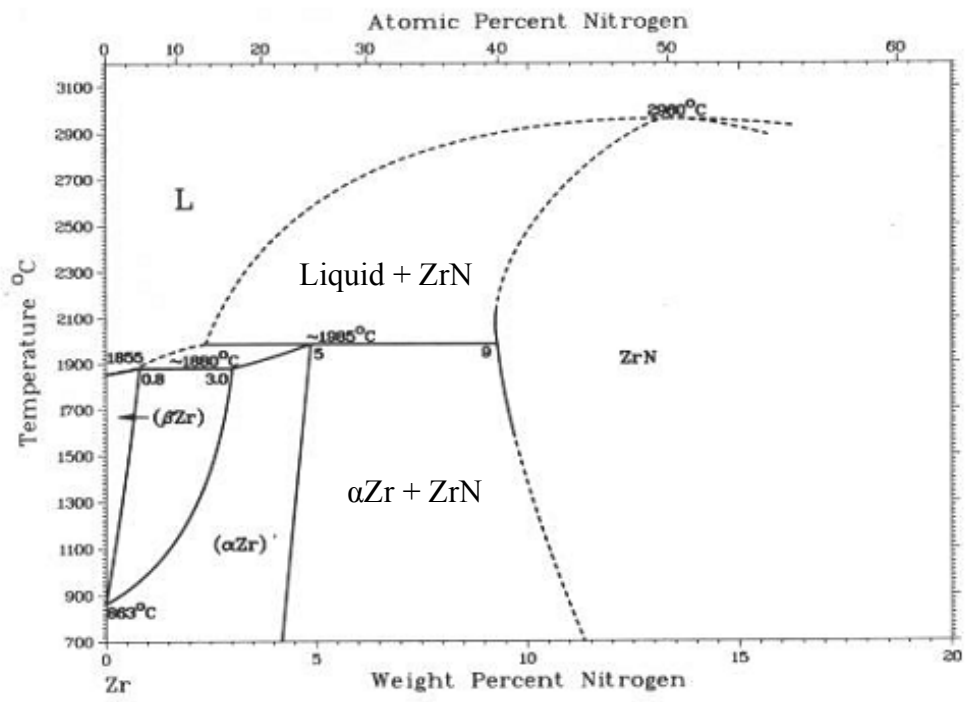


Figure 5-1 Phase diagram of the Zr-N system.<sup>1</sup>

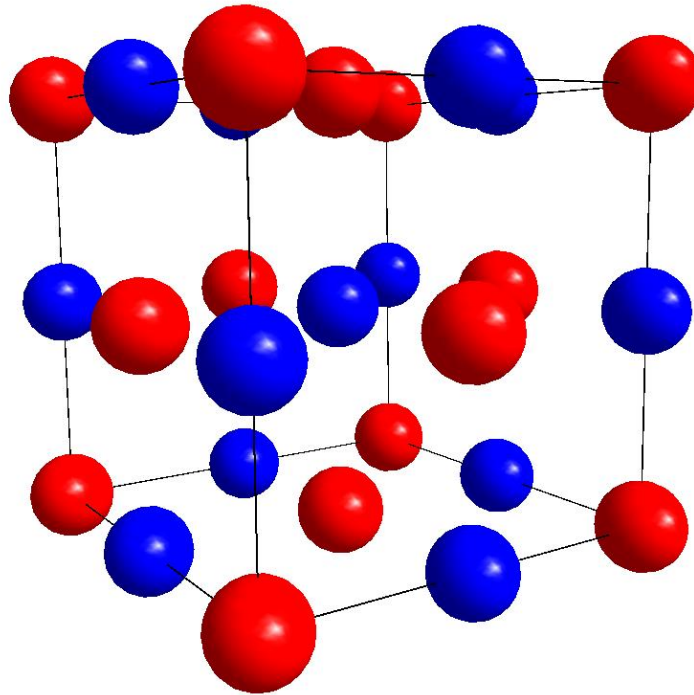


Figure 5-2 Crystal structure of ZrN. Zr atoms (red), N atoms (blue).

## 5.2 Microwave Synthesis Studies in Zr-N system

This section describes experimental work undertaken to establish a synthetic route to zirconium nitride from zirconium metal under nitrogen or ammonia gas in a multimode cavity MW reactor.

### 5.2.1 Introduction

Zirconium nitride is conventionally normally synthesized by reacting zirconium metal with either nitrogen or ammonia gas<sup>7</sup> but numerous reports on the preparation of zirconium nitride using different techniques have been published over the years, such as carbothermal reduction-nitridation of zirconium oxide,<sup>8,9</sup> mechanical alloying of Zr powders in N<sub>2</sub> atmosphere,<sup>10,11</sup> chemical vapour deposition from tetrakis(dialkylamido)zirconium complexes and ammonia,<sup>12</sup> dc-reactive sputtering<sup>4,13,14</sup> and benzene-thermal synthesis.<sup>15</sup>

This material has never been prepared by employing microwave irradiation. The reactions discussed in this section were carried out by direct reaction of zirconium metal powder and nitrogen/ammonia, according to the following reactions:



Although zirconium metal powder theoretically couples with microwaves, the heating of the reactant alone was unsuccessful and required the use of a microwave susceptor, such as graphite. Unlike in the microwave synthesis of V<sub>8</sub>C<sub>7</sub> (Chapter 3) and ZrC (Chapter 4), the susceptor was placed on the outside of the quartz tube and not in contact with the starting material, as discussed in Chapter 3 and 4. This provided enough additional thermal heating for the reaction to occur.

### 5.2.2 Experimental

#### 5.2.2.1 Synthesis

All reactions reported in this section were performed under N<sub>2</sub> by placing loose Zr metal powder (Alfa Aesar, < 45 μm, 98.8%) within a 10-mm quartz tube which is transparent to microwaves. The powder (0.5 g) was not cold pressed in order to allow the reacting gas to penetrate the entire mass. The tube was then sealed with a septum cap, parafilm and

subsequently connected to nitrogen flow. The MW reactions were conducted in a multimode cavity microwave reactor.

For multimode cavity experiments, the sample-containing tube was placed in the center of an alumina crucible containing graphite powder, used as a microwave susceptor [Figures 1-8 and 1-9], on top of a refractory fire brick. The whole apparatus was then inserted into the multimode cavity of a DMO and positioned in the same location within the cavity to keep the experimental parameters as constant as possible. Synthesis was conducted for 20 minutes (with 10-minute intervals) at a power of 800 W.

After each reaction, a yellow-brown powder was found to be compact and reduced in volume due to the fast sintering process of the nitride particles. The product was subsequently ground with the use of a mortar and pestle.

### 5.2.2.2 Characterization

Products were characterized using several analytical techniques. Powder X-ray Diffraction (PXRD) [Section 2.3.1] was used to identify product phases by reference with known structures downloaded from the Inorganic Crystal Structure Database (ICSD)<sup>16</sup> using the PowderCell 2.3 software.<sup>17</sup> The data were collected on a PANalytical Xpert MPD diffractometer, Cu K $\alpha$ 1 radiation, for 1 hour over a range of  $10 < 2\theta/^\circ < 85$ . Crystallographic parameters were obtained by Rietveld refinement [Section 2.3.3] against powder XRD data collected for ca. 12 hours over a range of  $10 < 2\theta/^\circ < 110$  using GSAS and EXPGUI software packages.<sup>18,19</sup> Sample morphology and elemental composition were investigated by Scanning Electron Microscopy (SEM) and Energy-dispersive X-ray Spectroscopy (EDX) [Section 2.3.4]. Additional characterization was obtained from Raman spectroscopy. Raman data were collected at room temperature using a Horiba LabRAM confocal microscope system with a 532-nm green laser.

## 5.2.3 Results and Discussion

### 5.2.3.1 Powder X-ray Diffraction (PXRD)

After 20-minute multimode cavity experiments, the samples were analyzed by *ex-situ* Powder X-ray Diffraction. The PXRD pattern for the MW-synthesized sample under nitrogen gas is shown in Figure 5-3.

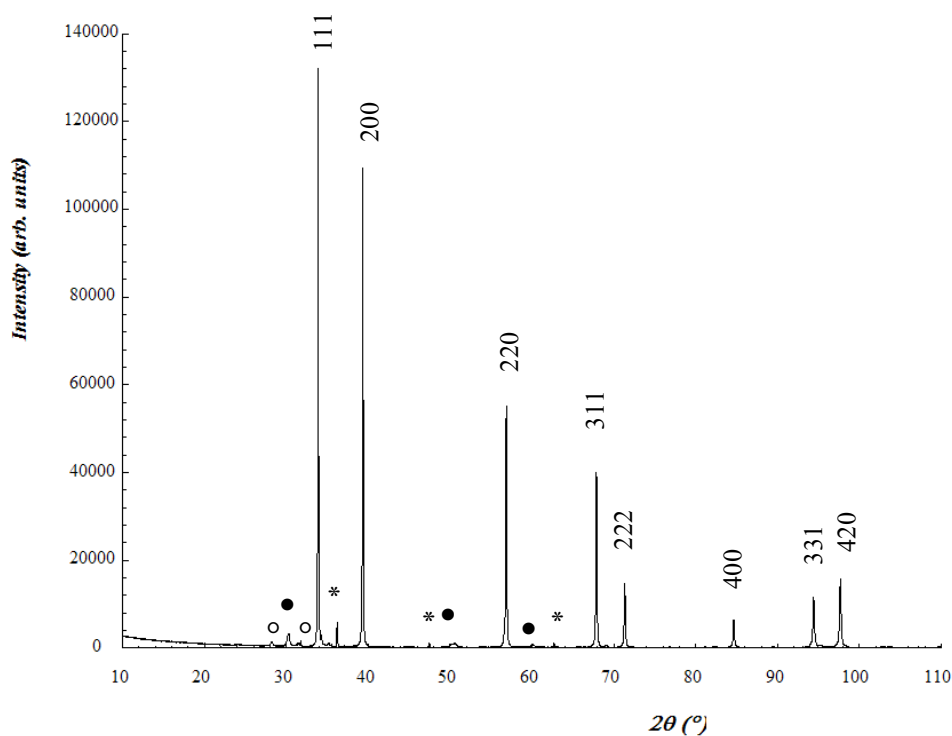


**Figure 5-3** PXR D pattern taken ex-situ from zirconium metal under nitrogen gas heated in a DMO for 20 minutes at a power of 800 W. Reflections marked with the  $hkl$  indices belong to the zirconium nitride phase, the ones marked with “ \* ” to zirconium metal, “ ° ” to  $m\text{-ZrO}_2$  and “ • ” to an unknown cubic phase. The unmarked extra reflections could not be characterized.

The major product was identified as zirconium nitride,  $\text{ZrN}$ , which crystallizes with the rock salt structure (space group  $Fm\text{-}3m$ ). The PXR D pattern consists of eight intense, sharp peaks characteristic of the NaCl-type structure which represent the reflections from the (111), (200), (220), (311), (222), (400), (331) and (420) planes. Extra reflections from secondary phases are also observed. The peaks marked with “ \* ” in Figure 5-3 belong to zirconium metal (hexagonal structure – space group  $P6_3/mmc$ ) whereas the ones marked with “ ° ” can very likely be attributed to  $m\text{-ZrO}_2$  and the ones marked with “ • ” can be indexed to a cubic phase. Two space groups can be attributed to this unknown phase:  $I\text{-}43d$  with lattice parameter  $a = 7.233 \text{ \AA}$  and  $Fm\text{-}3m$  with lattice parameter  $a = 5.114 \text{ \AA}$ . The first space group ( $I\text{-}43d$ ) is the same as in  $\text{Zr}_3\text{N}_4$  but this compound has a much smaller unit cell parameter ( $a = 6.740 \text{ \AA}$ ),<sup>6</sup> hence, its presence was excluded beforehand. The cubic form of zirconia ( $c\text{-ZrO}_2$ ) crystallizes in a space group  $Fm\text{-}3m$  with a lattice parameter which is similar to that one for the unknown phase. Table 5-1 illustrates the phase data for both the uncharacterized phase and  $c\text{-ZrO}_2$  taken from literature.

**Table 5-1** Crystallographic data for the uncharacterized cubic phase (obtained as a by-product during the microwave reaction) and *c*-ZrO<sub>2</sub> taken from literature. \*Range of values for the lattice parameter of the *c*-ZrO<sub>2</sub> phase reported in literature.

Phase data		
Chemical Formula	<i>c</i> -ZrO <sub>2</sub>	<i>Unknown phase</i>
Crystal system	Cubic	
Space group	<i>Fm -3 m</i>	
<i>a</i> /Å	4.916 <sup>20</sup> – 5.145 <sup>21*</sup>	5.113

It is unusual, though, that cubic zirconium dioxide would be formed under the conditions seen during our microwave reactions. Indeed, zirconium oxide would naturally form monoclinic crystals during synthesis.<sup>22</sup> However, cubic zirconia crystals can be obtained and require the use of a stabilizer (usually oxides, such as MgO and CaO) to remain stable at room temperature.<sup>23</sup> On the other hand, Claussen *et al.* (1978) investigated the formation of nitride-stabilized cubic zirconia by mixing various nitrides (such as ZrN) with *m*-ZrO<sub>2</sub> and hot-pressing the mixtures at 1700°C for 1 h under nitrogen gas.<sup>24</sup> The results showed that a fraction of the starting *m*-ZrO<sub>2</sub> underwent a heat-dependent transformation to the cubic form with a lattice parameter  $a = 5.115 \text{ \AA}$  which is consistent with the one obtained for the uncharacterized cubic phase [Table 5-1]. Obviously, at the time of writing this thesis, it is still not possible to confirm the presence of *c*-ZrO<sub>2</sub> in the MW-synthesized samples without further investigations – which will be the subject of future works.

By further increasing the reaction time, PXRD data showed no significant change from the pattern in Figure 5-3, which means that the reaction does not reach completion (see Section 5.2.3.3 for further details). The unreacted zirconium metal does not indeed further react with nitrogen gas to produce zirconium nitride.

A similar reaction was investigated under ammonia gas which gave a slightly different outcome. The PXRD pattern for the MW-synthesized sample under ammonia gas is shown in Figure 5-4.

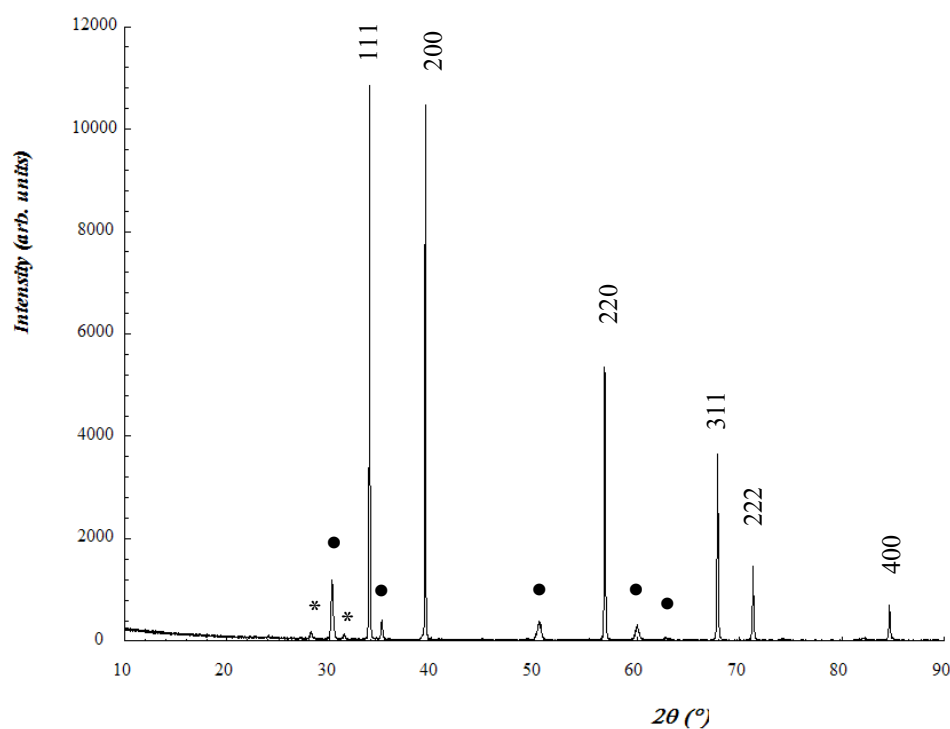


**Figure 5-4** PXRD pattern taken ex-situ from zirconium metal under ammonia gas heated in an MMC reactor for 20 minutes at a power of 800 W. Reflections marked with the  $hkl$  indices belong to the zirconium nitride phase, the ones marked with “ \* ” to zirconium oxide and the extra reflections marked with “ • ” can be attributed to an uncharacterized cubic phase.

The major product was again identified as cubic zirconium nitride,  $ZrN$ , together with small quantities of  $m\text{-}ZrO_2$  (marked with “ \* ”), a similar uncharacterized cubic phase (marked with “ • ”) as the one seen for the microwave reactions under nitrogen gas. Unlike the reactions under nitrogen gas, however, no zirconium metal is observed and so all the starting material appears to have been consumed.

### 5.2.3.2 Rietveld Refinement

The structure of the  $ZrN$  sample obtained from zirconium metal under nitrogen gas was solved by the Rietveld method against PXRD data, collected for 12 hours over a range of  $10 < 2\theta / ^\circ < 110$  with a step size of  $0.017^\circ$  ( $2\theta$ ) using GSAS and EXPGUI software packages.<sup>18,19</sup> The structure model used for zirconium nitride was the cubic  $Fm\text{-}3m$   $ZrN$ , in which the 4 zirconium atoms occupy the Wyckoff position (4a) and the 4 carbon atoms are located at the Wyckoff position (4b). The hexagonal  $Zr$  metal (space group  $P63/mmc$ ) and the monoclinic (space group  $P2/c$ ) and cubic (space group  $Fm\text{-}3m$ )  $ZrO_2$  structure models were also used. All the structure models were taken from the ICSD database.<sup>16</sup>

The background was modelled using a shifted Chebyshev function (function 1 within GSAS). Cell parameters, scale factor and zero point were also refined in initial cycles. Peak shape was subsequently modelled using the Thompson-Cox-Hastings pseudo Voigt function (peak shape function 2 within GSAS). The isotropic thermal factors ( $U_{\text{iso}}$ ) of the zirconium and nitrogen atoms were also refined independently. Refinement of the nitrogen site occupancy factor was also attempted which further improved the goodness of fit parameters. Zirconium metal and the two oxide phases ( $m\text{-ZrO}_2$  and  $c\text{-ZrO}_2$ ) were subsequently added to the refinement and a much better fit was obtained.

Rietveld refinement against PXRD data [Figure 5-5] confirmed that ZrN crystallizes with a cubic NaCl-type structure (space group  $Fm\text{-}3m$ ) and the calculated lattice parameter is  $a = 4.57689(4) \text{ \AA}$ , consistent with previous reports [Christensen *et al.* in 1975 ( $a = 4.585 \text{ \AA}$ )<sup>7</sup>].

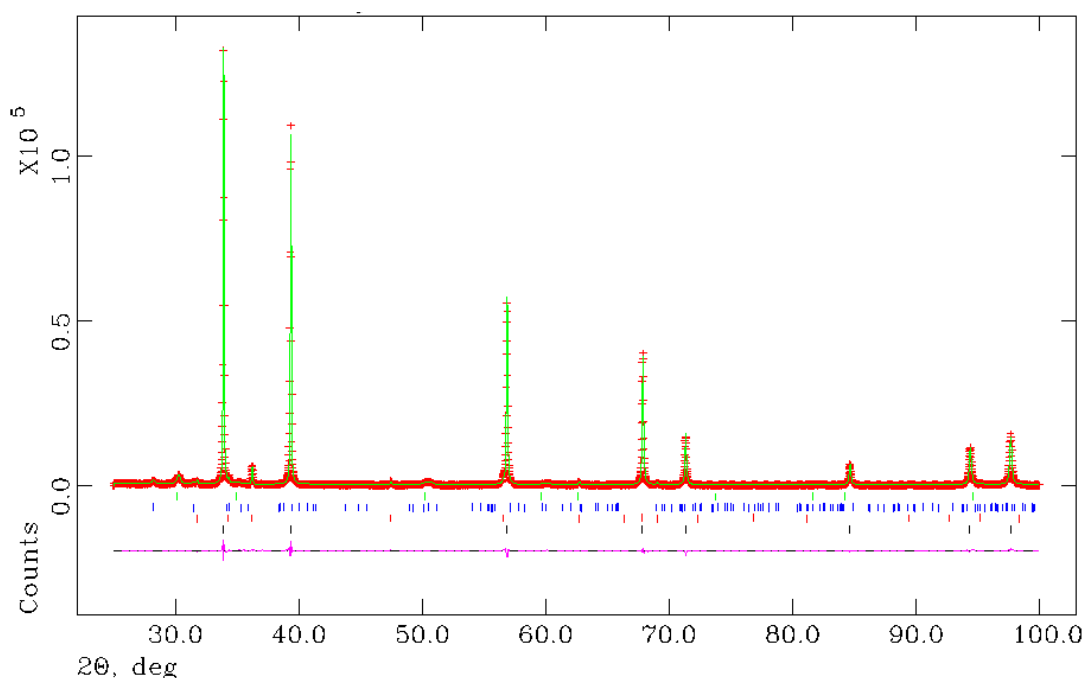


**Figure 5-5** Observed (*plusses*), calculated (*solid green line*), and difference (*solid purple line*) profile plot for the Rietveld refinement against PXRD data for the zirconium nitride ZrN synthesized under nitrogen gas. Tick marks denote ZrN (*bottom*), Zr,  $m\text{-ZrO}_2$  and  $c\text{-ZrO}_2$  (*top*) diffraction peaks.

The calculated crystallographic data and atomic parameters are illustrated in Table 5-2 and Table 5-3, respectively.

**Table 5-2** Crystallographic data from Rietveld refinement against PXRD data for ZrN synthesized from zirconium metal under nitrogen gas.

<b>Phase data</b>	
Chemical Formula	ZrN <sub>0.90</sub>
Crystal system	Cubic
Space group	<i>Fm -3 m</i>
<i>a</i> (Å)	4.57689(4)
Volume (Å <sup>3</sup> )	95.88(3)
<i>Z</i>	4
Formula weight (g mol <sup>-1</sup> )	103.57
Calculated density (g cm <sup>-3</sup> )	7.17473
<i>R</i> <sub>wp</sub>	0.0773
<i>R</i> <sub>p</sub>	0.0523
$\chi^2$	5.880

**Table 5-3** Atomic parameters from Rietveld Refinement against PXRD data for ZrN synthesized under nitrogen gas.

<b>Atomic parameters</b>					
Name	Fractional coordinates			Uiso	Occup.
	<i>x/a</i>	<i>y/b</i>	<i>z/c</i>		
Zr1	0.0000	0.0000	0.0000	0.00955(5)	1.0
N1	0.5000	0.5000	0.5000	0.00728(2)	0.8994(9)

Also the structure of the ZrN sample obtained from zirconium metal under ammonia gas was solved by the Rietveld method against PXRD data [Figure 5-6]. As the idea behind this experiment was conceived relatively late in this project, time allowed for refinement of PXRD data collected only up to 90°. The same structural model was used as for the previous refinement and the same refinement procedure was followed. The only difference was that attempted variation of the N site occupancy factors resulted in an unstable refinement in which both R-factors and the goodness of fit parameter increased and/or unrealistic values of the SOF were obtained. The SOFs for both Zr and N sites were fixed at 1.0.

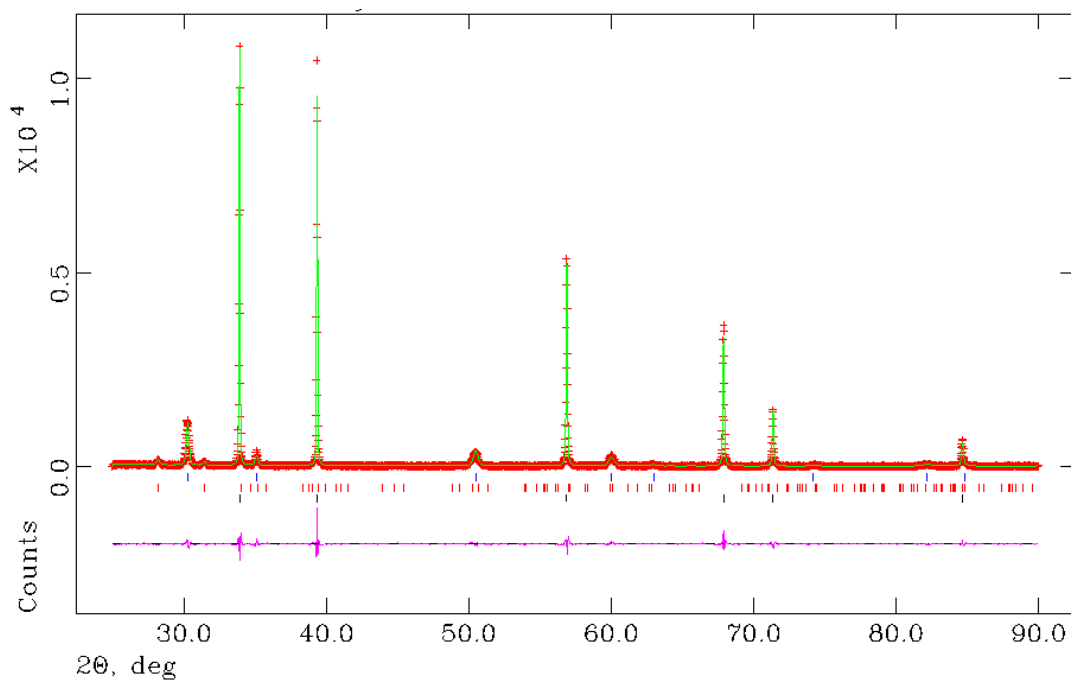


**Figure 5-6** Observed (*plusses*), calculated (*solid green line*), and difference (*solid purple line*) profile plot for the Rietveld refinement against PXRD data for the zirconium nitride ZrN synthesized under ammonia gas. Tick marks denote ZrN (*bottom*), *m-ZrO<sub>2</sub>* and *c-ZrO<sub>2</sub>* (*top*) diffraction peaks.

Table 5-4 and Table 5-5 illustrate the calculated crystallographic data and atomic parameters, respectively, for the Zr + NH<sub>3</sub> sample.

**Table 5-4** Crystallographic data from Rietveld refinement against PXRD data for ZrN synthesized from zirconium metal under ammonia gas.

<b>Phase data</b>	
Chemical Formula	ZrN
Crystal system	Cubic
Space group	<i>Fm -3 m</i>
<i>a</i> (Å)	4.57687(5)
Volume (Å <sup>3</sup> )	95.88(5)
<i>Z</i>	4
Formula weight (g mol <sup>-1</sup> )	105.42
Calculated density (g cm <sup>-3</sup> )	7.30264
<i>R</i> <sub>wp</sub>	0.1575
<i>R</i> <sub>p</sub>	0.1035
$\chi^2$	2.296

**Table 5-5** Atomic parameters from Rietveld Refinement against PXRD data for ZrN synthesized under ammonia gas. The fractional coordinates were not refined, as they are fixed by the structure.

<b>Atomic parameters</b>					
Name	Fractional coordinates			Uiso	Occup.
	$x/a$	$y/b$	$z/c$		
Zr1	0.0000	0.0000	0.0000	0.00917(2)	1.0
N1	0.5000	0.5000	0.5000	0.00344(6)	1.0

The refined lattice parameters for the *c*-ZrO<sub>2</sub> phase in the Zr + N<sub>2</sub> and Zr + NH<sub>3</sub> samples are  $a = 5.1122(1) \text{ \AA}$  and  $a = 5.1095(2) \text{ \AA}$ , respectively. These values are close to each other and consistent with those of previous studies [Table 5-1].

### 5.2.3.3 *Ex-situ* Study of the Zr + N<sub>2</sub> and Zr + NH<sub>3</sub> Reactions as a Function of Time

From the ex-situ PXRD data, the phase evolution was monitored as a function of time and a phase analysis was conducted.

The Zr metal powder was irradiated with MWs under nitrogen or ammonia gas in a MMC reactor using 5 or 10-minute heating cycles. Figure 5-7 shows the phase analysis for the ZrN samples synthesized under nitrogen gas. At  $t = 0$  (before MW irradiation), only reflections from zirconium metal are present. After the first 10-minute heating cycle ( $t = 10$  minutes), zirconium nitride is formed as a major phase (sharp, high intensity peaks are observed) and reflections from zirconium metal have drastically decreased in intensity but still present. No formation of other phases is observed. After two heating cycles ( $t = 10 + 10$  minutes), peaks from the starting material have almost disappeared (a few low intensity reflections remain visible) and the ZrN reflections increase in intensity. Moreover, the formation of a few extra peaks is observed which probably belong to *m*- and *c*-ZrO<sub>2</sub>. However, as discussed in Section 5.2.3.1, the presence of cubic zirconia still needs further evidence to be confirmed. A third heating cycle ( $t = 10 + 10 + 10$  minutes) was also performed in an attempt to eliminate the remaining starting material, but the PXRD pattern remain essentially unchanged from that obtained after two MW-heating cycles (20 minutes).

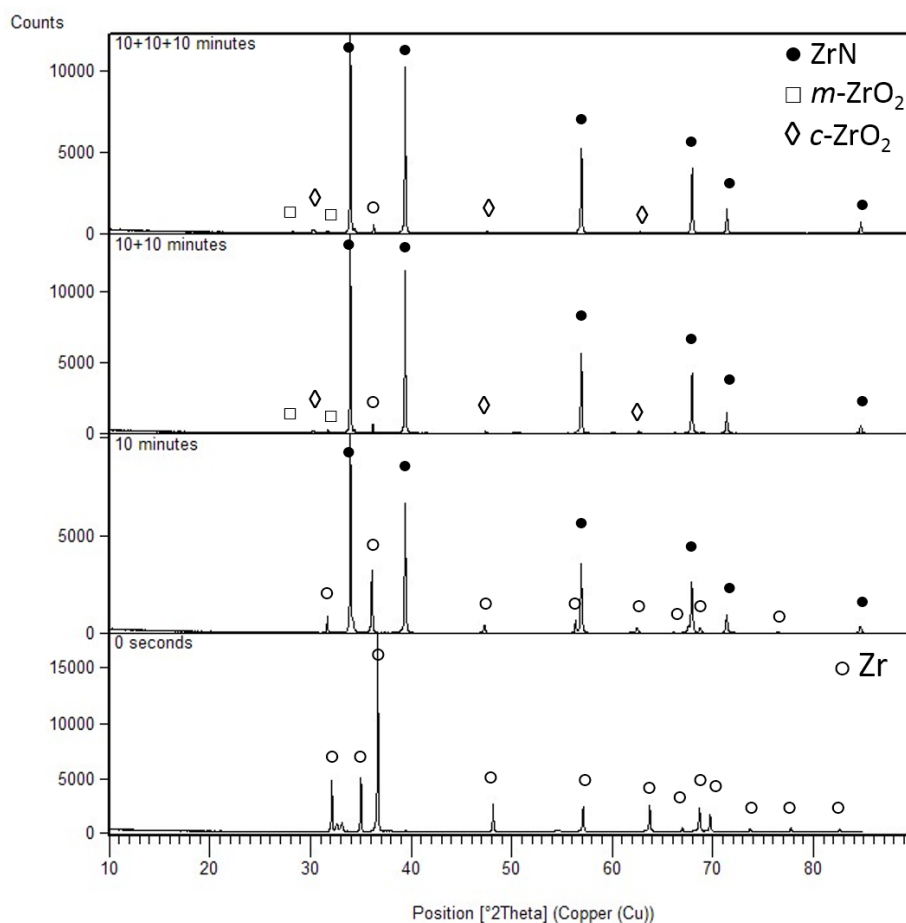


**Figure 5-7** *Ex-situ* PXR D patterns for Zr powder heated under nitrogen gas in a multi-mode cavity MW reactor at a power of 800 W from reagents (*bottom*) to reaction completion (*top*).

A similar PXR D analysis was carried out for the ZrN samples synthesized under ammonia gas and is shown in Figure 5-8. At  $t = 0$  (before MW irradiation), only reflections from zirconium metal are present. After the first 5-minute heating cycle ( $t = 5$  minutes), the starting Zr metal has drastically decreased in intensity and been partially converted to zirconium hydride ( $ZrH_2$ ) and zirconium hydronitrides ( $ZrN_xH_y$ ). After two 5-minute heating cycles, the starting Zr metal is totally consumed when reacting with ammonia, unlike the microwave reactions under nitrogen gas in which a small amount of starting Zr metal is always present. Also, the amount of the  $ZrH_2$  and  $ZrN_xH_y$  decreases as the compounds are consumed and converted to ZrN (nitride reflections increase in intensity). Finally, after 20 minutes of MW irradiation, ZrN is present together with a small amount of  $m\text{-ZrO}_2$  and the uncharacterized  $c\text{-ZrO}_2$  cubic phase, whose reflections have a higher intensity than those seen in patterns from the MW reactions performed under  $N_2$ .

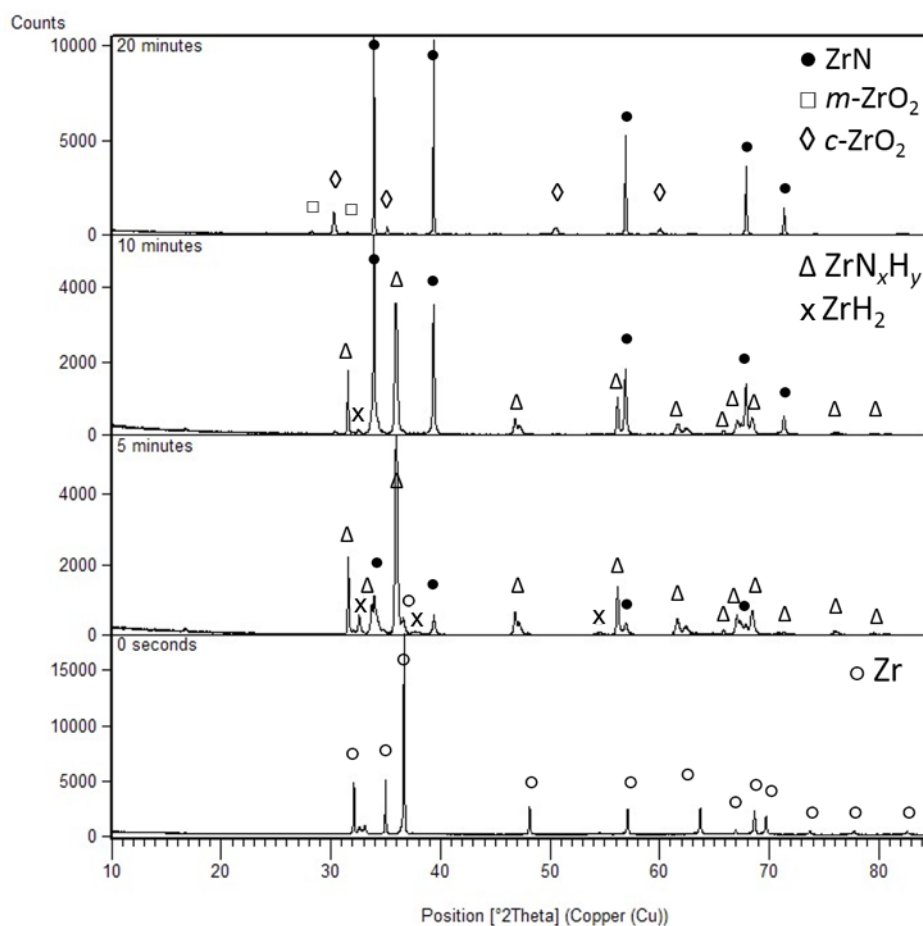


**Figure 5-8** *Ex-situ* patterns for Zr powder heated under ammonia gas in a multimode cavity MW reactor at a power of 800 W from reagents (*bottom*) to reaction completion (*top*).

In light of the PXR, if the presence of oxygen within the reaction system could be prevented, the ZrN product could probably be obtained as a single-phase in experiments under both nitrogen and ammonia gas. The source of this oxygen contamination is unfortunately still unclear, but it might be due to the presence of the element on the surface of zirconium metal or as an impurity in the Ar supply.

#### 5.2.3.4 Scanning Electron Microscopy (SEM) coupled with Energy-dispersive X-ray Spectroscopy (EDX)

As discussed in Section 1.7.1, refractory carbides and nitrides show remarkable properties such as high melting points, high hardness, etc. Because of all these features, they find several applications in industry as cutting tools, abrasives and wear-resistant parts.<sup>25</sup> The size and shape of particles for such compounds as well as their morphology are therefore important factors to take into account when considering the suitability of these materials for specific applications.

The MW-synthesized ZrN powders prepared from zirconium metal under nitrogen and ammonia gases were analyzed by Scanning Electron Microscopy (SEM) coupled with Energy-dispersive X-ray Spectroscopy (EDX) to investigate particle size and morphology.

Figure 5-9 shows the SEM micrographs for the ZrN samples synthesized under nitrogen gas in a MMC reactor for 20 minutes at a power of 800 W. The microwave reaction yields clusters of irregular micron-scale ZrN particles, typically from a few microns to a maximum of approximately a couple of hundreds microns across.

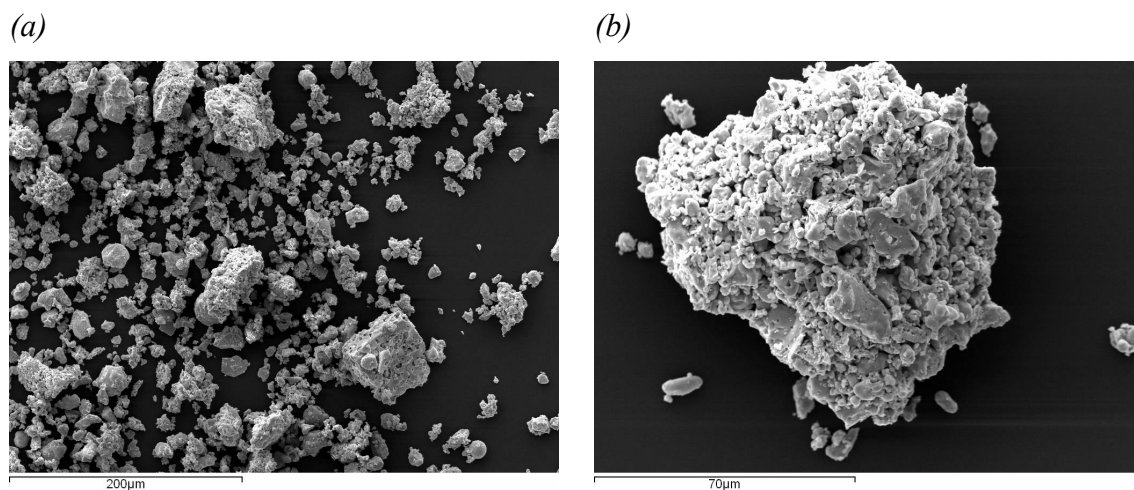


**Figure 5-9** SEM micrographs for the ZrN synthesized from zirconium metal under nitrogen gas in 20 minutes in a MMC microwave reactor at a power of 800 W.

The SEM micrographs for the ZrN samples synthesized under ammonia gas in a MMC reactor for 20 minutes at a power of 800 W are illustrated in Figure 5-10 and show a broadly similar morphology to that of the ZrN samples synthesized under N<sub>2</sub>. The size of the individual particles in the ammonia sample are smaller than those in the nitrogen-synthesized nitride (of the order of  $\leq 10 \mu\text{m}$ ) but as for the nitrogen-synthesized sample, these particles cluster together to form larger agglomerates.

EDX data were collected for several crystallites for both the nitrogen- and ammonia-synthesized samples and showed similar results. Some EDX spectra showed that only zirconium, nitrogen and oxygen were present [Figure 5-11]. The presence of oxygen in the form of additional oxide phases is supported by PXRD data (see Section 5.2.3.1, 3.2.3.2 and 5.2.3.3). Some other EDX spectra suggested instead that carbon and/or hafnium impurities were also detected [Figure 5-12]. However, no source of carbon was used as a starting material and, hence, its presence might be due to carbon-based adhesive discs used as a sample holder during the SEM/EDX measurements. The hafnium impurity presumably comes from the zirconium powder used as a starting material and purchased from Alfa

Aesar, as declared by the manufacturer. According to the product specification, the Zr powder contains indeed ca. 2% of Hf.

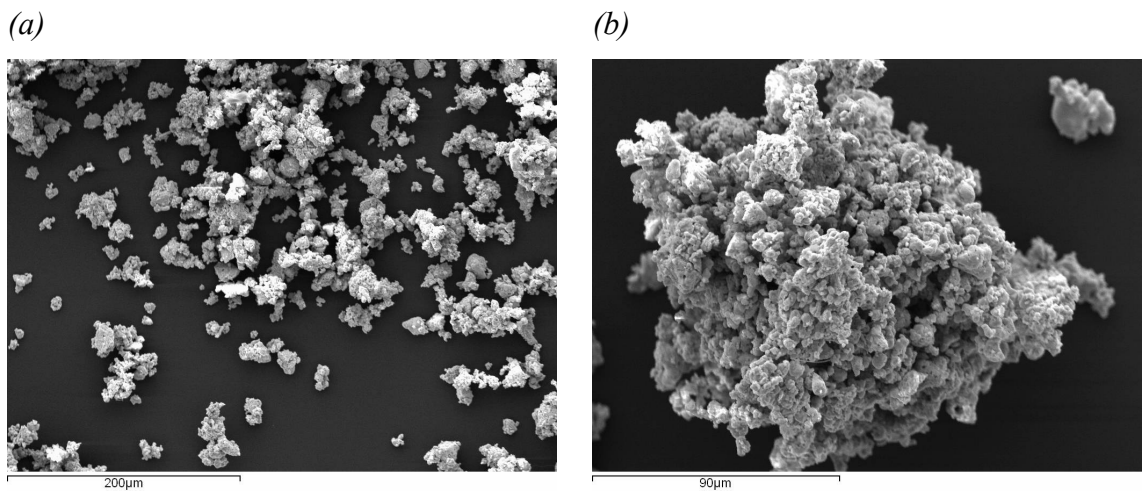


**Figure 5-10** SEM micrographs for the ZrN synthesized from zirconium metal under ammonia gas in 20 minutes in a MMC microwave reactor at a power of 800 W.

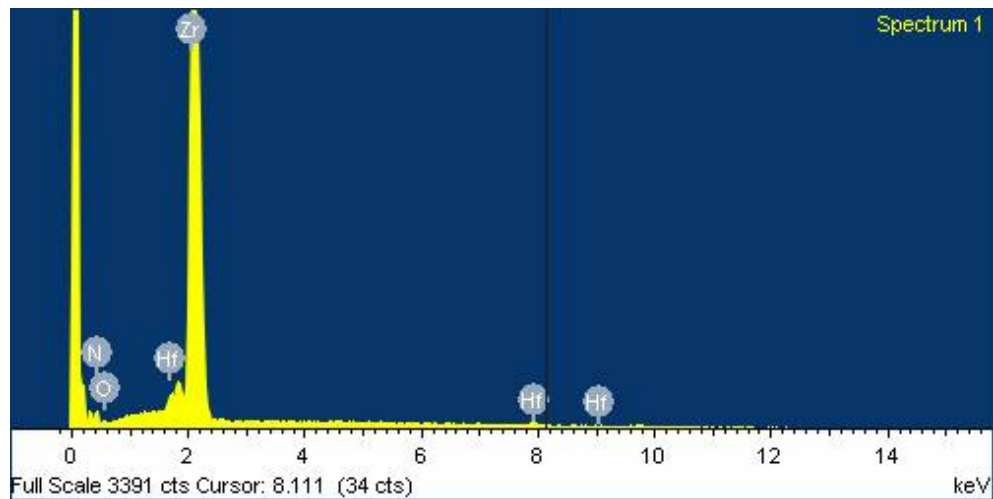


**Figure 5-11** EDX spectrum for the ZrN sample synthesized from zirconium metal under nitrogen gas in 20 minutes in a MMC microwave reactor, showing that zirconium, nitrogen, oxygen and hafnium were present.

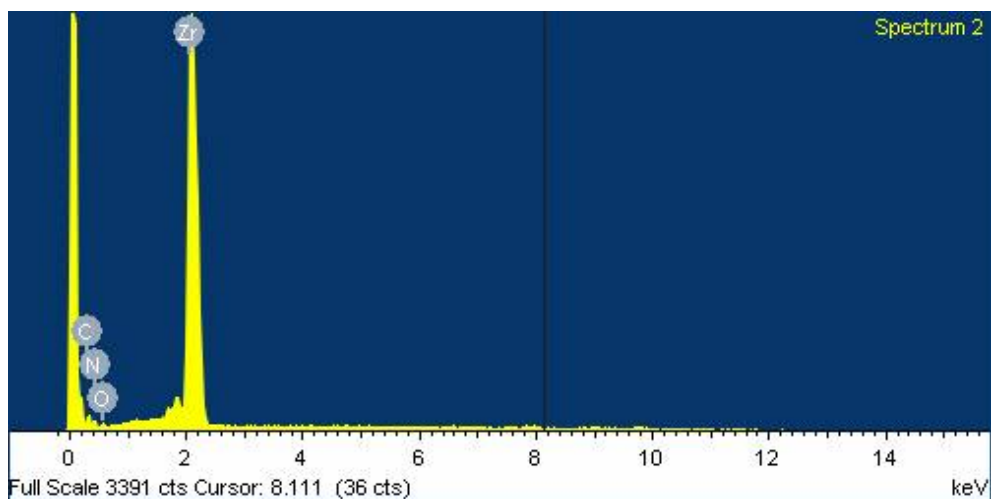


**Figure 5-12** EDX spectrum for the ZrN samples synthesized from zirconium metal under nitrogen gas in 20 minutes in a MMC microwave reactor, showing that zirconium, nitrogen, oxygen and carbon were present.

### 5.2.3.5 Raman Spectroscopy

Raman spectroscopy experiments were carried out for the ZrN samples as an attempt to further characterize the unknown cubic phase discussed above in the previous sections.

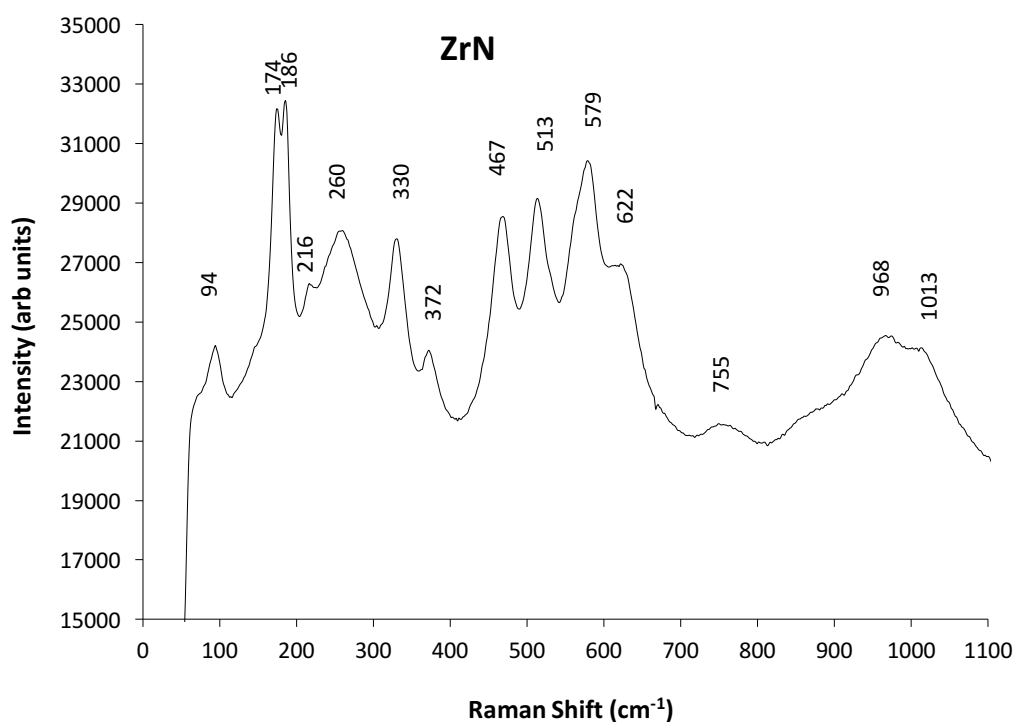


**Figure 5-13** Experimental Raman spectrum for the MW-synthesized ZrN from zirconium metal under nitrogen and gas in 20 minutes in a MMC microwave reactor at a power of 800 W.

Figure 5-13 illustrates the Raman spectrum of the MW-synthesized ZrN from zirconium metal under nitrogen gas.

In Chapter 4 (Section 4.2.3.5), it was noted how MW-synthesized ZrC samples appear to show very similar characteristic Raman bands to combination of monoclinic and tetragonal ZrO<sub>2</sub>. Similar results were obtained for the Raman spectrum of the MW-synthesized ZrN under nitrogen gas [Figure 5-13], whose band assignments are illustrated in Table 5-6. The ZrN spectrum contains bands at almost the same Raman shifts as the MW-synthesized ZrC samples but with slightly different intensities. For a description of the assignment of each Raman band to the respective stretching mode, see Section 4.2.3.5.

**Table 5-6** Raman shifts of the MW-synthesized ZrN compared to those from *m*-ZrO<sub>2</sub> and *t*-ZrO<sub>2</sub> and their assignments. The bands in the experimental spectrum closely resemble a combination of these seen for the 2 phases of ZrO<sub>2</sub>.

ZrN Raman Shift (cm <sup>-1</sup> )	<i>m</i> -ZrO <sub>2</sub> Raman Shift (cm <sup>-1</sup> ) <sup>26</sup>	<i>t</i> -ZrO <sub>2</sub> Raman Shift (cm <sup>-1</sup> ) <sup>27</sup>	Assignment
94 (M)	99	–	<i>A<sub>g</sub></i>
174 (M)	175	–	<i>A<sub>g</sub> + B<sub>g</sub></i>
186 (M)	188	–	<i>A<sub>g</sub></i>
216 (M)	219	–	<i>B<sub>g</sub></i>
260 (T)	–	264	<i>A<sub>1g</sub></i>
330 (T)	–	320	<i>B<sub>1g</sub></i>
372 (M)	379	–	<i>B<sub>g</sub></i>
467 (M)	473	–	<i>A<sub>g</sub></i>
513 (M)	502	–	<i>B<sub>g</sub></i>
579 (T)	–	606	<i>B<sub>1g</sub></i>
622 (M)	615	–	<i>B<sub>g</sub></i>
755 (M)	755	–	<i>B<sub>g</sub></i>
968 (M)	959	–	–
1013 (M)	1012	–	–

Phillippi *et al.* (1971) studied the Raman spectroscopy of zirconia polymorphs, including the cubic form of the material.<sup>28</sup> The authors found that the Raman spectrum of a pure

metastable cubic  $\text{ZrO}_2$  showed only a weak broad line at  $490 \pm 20 \text{ cm}^{-1}$  whereas  $\text{Y}_2\text{O}_3$ -stabilized cubic  $\text{ZrO}_2$  has a distinct asymmetrical line at  $625 \text{ cm}^{-1}$  and several other weak broad lines at 480, 360, 250 and  $150 \text{ cm}^{-1}$ , respectively. However, none of these bands are observed in the Raman spectrum of the MW-synthesized ZrN sample, which suggests that either the indexed cubic phase is not *c*- $\text{ZrO}_2$  or the weak Raman bands of cubic zirconia are actually not visible due to their overlapping with stronger monoclinic and tetragonal bands.

In conclusion, the Raman spectroscopy of the ZrN samples would support the presence of monoclinic zirconium dioxide phase in the sample as indicated by PXRD. However, the evidence is less compelling that the cubic form of zirconia is present and does not suggest the presence of other additional phases.

### 5.3 Chapter Summary

The aim of this work was to perform a preliminary study on the synthesis of zirconium nitride by direct reaction of zirconium metal with nitrogen or ammonia gas using a DMO. Once an appropriate synthetic route and reaction conditions were established, the resulting products were characterized by PXRD, SEM/EDX and Raman Spectroscopy.

It was found that zirconium nitride can be synthesized in 20 minutes using a domestic microwave oven at a power of 800 W under either nitrogen or ammonia gas. The main difference between these two environments is that the reaction under nitrogen gas does not entirely consume the starting zirconium metal which remains unreacted in very small amounts. In the reaction under ammonia gas, this phase is not observed by PXRD. Using either gas sources, however, leads to formation of zirconium dioxide due to the presence of oxygen within the system. Two oxide phases are suggested from PXRD data: *m*- $\text{ZrO}_2$  and, probably, nitride-stabilized *c*- $\text{ZrO}_2$ . The formation of the cubic form of zirconia is a phenomenon that deserves further investigation, due to its gemological and economic importance as a diamond competitor. SEM micrographs and EDX spectra showed the formation of irregular micron-scale particles with a relatively rough surface containing zirconium, nitrogen and oxygen. Hf impurities were also observed which almost certainly originate from the Zr powder used as a starting material (as declared by the manufacturer). Raman spectra of products showed bands which could be attributed to ZrN, but equally might be assigned to both *m*- $\text{ZrO}_2$  and *t*- $\text{ZrO}_2$ . Unfortunately, no bands relating to the *c*- $\text{ZrO}_2$  phase were observed, maybe due to their very weak nature and overlap with more intense *m*- and *t*- $\text{ZrO}_2$  Raman bands. Further investigations are needed, though, in order to confirm

whether the observed cubic phase is actually the cubic form of zirconia or a different compound. However, no other known Zr compounds possess similar crystallographic characteristic to *c*-ZrO<sub>2</sub>.

## 5.4 References

1. Gribaudo, L., Arias, D. & Abriata, J. The N-Zr (Nitrogen-Zirconium) System. *J. Phase Equilibria* **15**, 441–449 (1994).
2. Rizzo, A., A. Signore, M., Mirengi, L. & Dimaio, D. Deposition and properties of ZrN<sub>x</sub> films produced by radio frequency reactive magnetron sputtering. *Thin Solid Films* **515**, 1486–1493 (2006).
3. Pichon, L. *et al.* Zirconium nitrides deposited by dual ion beam sputtering: physical properties and growth modelling. *Appl. Surf. Sci.* **150**, 115–124 (1999).
4. Dauchot, J. P., Edart, S., Wautelet, M. & Hecq, M. Synthesis of zirconium nitride films monitored by in situ soft X-ray spectrometry. *Vacuum* **46**, 927–930 (1995).
5. Liu, C. Systematic study of the evolution of texture and electrical properties of ZrN<sub>x</sub> thin films by reactive DC magnetron sputtering. *Thin Solid Films* **444**, 111–119 (2003).
6. Zerr, A., Mieke, G. & Riedel, R. Synthesis of cubic zirconium and hafnium nitride having Th3P4 structure. *Nat. Mater.* **2**, 185–189 (2003).
7. Christensen, A. N. A Neutron Diffraction Investigation on Single Crystals of Titanium Oxide, Zirconium Carbide and Hafnium Nitride. *Acta Chem. Scand.* **44**, 563–564 (1990).
8. Fu, B. & Gao, L. Synthesis of Nanocrystalline Zirconium Nitride Powders by Reduction–Nitridation of Zirconium Oxide. *Society* **98**, 696–698 (2004).
9. Li, J. Y. *et al.* Zirconium nitride (ZrN) fibers prepared by carbothermal reduction and nitridation of electrospun PVP/zirconium oxychloride composite fibers. *Chem. Eng. J.* **144**, 149–152 (2008).
10. Calka, A. Formation of titanium and zirconium nitrides by mechanical alloying. *Appl. Phys. Lett.* **59**, 1568–1569 (1991).
11. Li-Xia, Q. *et al.* Reactive Mechanical Alloying Synthesis of Nanocrystalline Cubic Zirconium Nitride. *Chinese Phys. Lett.* **25**, 1898–1901 (2008).
12. Fix, R., Gordon, R. G. & Hoffman, D. M. Chemical Vapor-Deposition of Titanium, Zirconium, and Hafnium Nitride Thin-Films. *Chem. Mater.* **3**, 1138–1148 (1991).

13. Rizzo, A. *et al.* Sputtering deposition and characterization of zirconium nitride and oxynitride films. *Thin Solid Films* **520**, 3532–3538 (2012).
14. Wu, D., Zhang, Z., Fu, D., Fan, W. & Guo, H. Structure, electrical and chemical properties of zirconium nitride films deposited by dc reactive magnetron sputtering. *Appl. Phys. A* **64**, 593–595 (1997).
15. Gu, Y., Guo, F., Qian, Y., Zheng, H. & Yang, Z. A benzene-thermal synthesis of powdered cubic zirconium nitride. *Mater. Lett.* **57**, 1679–1682 (2003).
16. Rühl, S. Inorganic Crystal Structure Database (ICSD). *A Focus Crystallogr.* 6
17. Kraus, W. & Nolze, G. Powder cell 2.3 version. *CPD Newslett* **20**, 274–280 (1998).
18. Larson, A. C. & Dreele, R. B. Von. General Structure Analysis System (GSAS). *Los Alamos Natl. Lab. Rep. LAUR* 86–748 (2000).
19. Toby, B. H. EXPGUI, a graphical user interface for GSAS. *J. Appl. Crystallogr.* **34**, 210–213 (2001).
20. Bouvier, P., Djurado, E., Lucazeau, G. & Le Bihan, T. High-pressure structural evolution of undoped tetragonal nanocrystalline zirconia. *Phys. Rev. B - Condens. Matter Mater. Phys.* **62**, 8731–8737 (2000).
21. Wang, D., Guo, Y., Liang, K. & Tao, K. Crystal structure of zirconia by Rietveld refinement. *Sci. China Ser. A Math.* **42**, 80–86 (1999).
22. Stevens, R. *An introduction to zirconia. Magnesium Elektron Publication* **113**, (1986).
23. Alper, A. M. High Temperature Oxides: Oxides of Rare Earths, Titanium, Zirconium, Hafnium, Niobium and Tantalum. *Elsevier* **5**, 117–275 (1970).
24. Claussen, N., Wagner, R., Gauckler, L. J. & Petzow, G. Nitride-Stabilized Cubic Zirconia. *J. Am. Ceram. Soc.* **61**, 369–370 (1978).
25. Santhanam, A. T. *Application of transition metal carbides and nitrides in industrial tools BT - The Chemistry of Transition Metal Carbides and Nitrides.* (Springer Netherlands, 1996).
26. Keramidas, V. & White, W. Raman scattering study of the crystallization and phase transformations of ZrO<sub>2</sub>. *J. Am. Ceram. Soc.* **57**, 22–24 (1974).
27. Quintard, P. & Barbéris, P. Comparative Lattice-Dynamical Study of the Raman Spectra of Monoclinic and Tetragonal Phases of Zirconia and Hafnia. *J. Am. Ceram. Soc.* **85**, 1745–1749 (2002).
28. Phillippi, C. M. & Mazdiyasi, K. S. Infrared and Raman Spectra of Zirconia Polymorphs. *J. Am. Ceram. Soc.* **54**, 254–258 (1971).

## 6 Conclusions and Future Work

The work described in this thesis focuses on the MW synthesis of the Group 4 and 5 transition metal carbides and nitrides,  $V_8C_7$ , ZrC, HfC and ZrN and their subsequent structural characterization by PXRD, PND, SEM-EDX, Raman spectroscopy and XPS.

The study of carbides in the V–C system (Chapter 3) resulted in the successful synthesis of the vanadium carbide,  $V_8C_7$ , in both MMC and SMC microwave reactors. The material was prepared from combining carbon with either vanadium metal and vanadium(V) pentoxide under Ar in 6 minutes using a MMC reactor at a power of 800 W and in 2 minutes using a SMC reactor at a power of 1 kW. Rietveld refinement against PXRD data confirmed the formation of the vanadium carbide as a single phase (together with a small amount of graphite, originating from susceptor) which crystallizes in a cubic superstructure (space group  $P4_332$ ). The *ex-situ* PXRD study of the V + C reaction as a function of time shows that the reaction mechanism is straightforward and involves the direct combination of the elements to form a succession of carbides that become more C-rich. In the carbothermal reduction of vanadium(V) oxide,  $V_2O_5$  is first converted to  $V_2O_3$  and then to  $V_8C_7$ . SEM micrographs and EDX spectra showed the formation of irregular micron-scale particles from a few microns to a maximum of 100  $\mu\text{m}$  across with a relatively rough surface containing vanadium, carbon and oxygen. Raman spectra provided supporting information regarding possible oxygen inclusion within the structure of the products. XPS spectra together with Ar ion etching confirmed the presence of oxygen in the first  $\sim 20$  nm of the product surface. PND investigation of the V + C sample synthesized in a MMC reactor aiming at evaluating the C and O occupancies of the final products was unfortunately unsuccessful and needs therefore to be repeated in future.

The study of carbides in the Zr-C and Hf-C systems (Chapter 4) focused on the microwave synthesis of zirconium and hafnium carbides (which are similar in terms of physical and chemical properties) from either oxide or elemental precursors using both a MMC and SMC reactors. Only ZrC was obtained successfully as a single phase from zirconium metal and carbon under Ar in 20 minutes using a MMC reactor at a power of 800 W and in 6 minutes using a SMC reactor at a power of 1 kW. Rietveld refinement against PXRD data confirmed the formation of zirconium carbide as a single phase (together with a

small amount of graphite, originating from susceptor) which crystallizes in a cubic structure (space group  $Fm-3m$ ) with lattice parameter  $a = 4.69645(1) \text{ \AA}$ . As per  $V_8C_7$ , SEM micrographs and EDX spectra showed the formation of irregular micron-scale particles from a few microns up to  $\sim 200$  microns across with a relatively rough surface containing zirconium and carbon. Oxygen inclusion was confirmed as well by EDX. Raman spectra of the MW-synthesized products showed bands which could be attributed to both  $m\text{-ZrO}_2$  and  $t\text{-ZrO}_2$ , providing additional supporting information about oxygen inclusion. The presence of oxygen (at least in the first  $\sim 20$  nm of particle surface) was confirmed by XPS coupled with Ar ion etching. PND investigations of the ZrC samples were also performed using two different structure models. The first model used was the cubic  $Fm-3m$  ZrC structure as taken from the ICSD database. This neutron refinement supports a zirconium carbide sample with a Zr:C stoichiometry of 1:0.98 ( $\text{ZrC}_{0.98}$ ). The second structure model used was obtained by adding an oxygen atom at the same position where the carbon atom sits and the occupancy factor for the two non-metal atoms were refined. The Zr:C:O stoichiometry found in this refinement was 1:0.97:0.03 which leads to the formula  $\text{ZrC}_{0.97}\text{O}_{0.03}$ . Although both refinements show acceptable results and the difference in quality to the two structural fits is negligible, the presence of this very small amount of oxygen can be very challenging to detect. A more appropriate explanation is that the bulk particle composition is  $\text{ZrC}_{0.98}$  together with some oxygen present at the surface of the particles.

The direct reaction of hafnium metal and carbon under Ar using either a MMC or a SMC microwave reactor led to the formation of hafnium carbide as a major product together with unreacted C and a small amount of  $\text{HfO}_2$  which prevented the reaction reaching completion. Once  $\text{HfO}_2$  had formed in this system, further production of HfC appeared impossible under the conditions employed.

The microwave synthesis of both ZrC and HfC from the oxide precursors ( $\text{ZrO}_2$  and  $\text{HfO}_2$ ) and carbon was not successful as no reaction was observed between the starting materials under the conditions employed.

In light of the results obtained for this system, it is necessary to prevent oxygen entering the system in order to produce single phase compounds. To do so, high-purity starting materials that do not contain any trace of oxygen (at the surface, for instance) are highly recommended. However, it is extremely difficult to completely avoid oxygen contamination in this family of compounds (in the form of oxycarbide phases) but the formation of unwanted oxide phase can be certainly avoided by reducing/removing the amount of oxygen present in the system.

The study of nitrides in the Zr-N system discussed in this thesis represents a preliminary investigation on the microwave synthesis of cubic zirconium nitride. ZrN can be synthesized by direct reaction of zirconium metal with either nitrogen or ammonia gas in 20 minutes using a MMC microwave reactor at a power of 800 W. The  $Zr + N_2$  reaction does not entirely consume the starting zirconium powder which remains unreacted in very small amounts. This phase is not observed in the  $Zr + NH_3$  reaction by PXRD suggesting that the starting Zr is totally consumed. Using either gas sources, however, leads to the formation of zirconium dioxide due to the presence of oxygen within the system. Two oxide phases are suggested from PXRD data: *m*-ZrO<sub>2</sub> and, probably, nitride-stabilized *c*-ZrO<sub>2</sub>. SEM micrographs and EDX spectra showed the formation of irregular micron-scale particles from a few microns to approx. 200 μm across with a relatively rough surface containing zirconium, nitrogen and oxygen. As per ZrC, Raman spectra of ZrN products showed bands which could be attributed to ZrN but equally might be assigned to both *m*-ZrO<sub>2</sub> and *t*-ZrO<sub>2</sub>. Unfortunately, due to the lack of time towards the end of this work, further experiments would be repeated to form further conclusions. Firstly, the use of high-purity starting materials is strictly required since the oxygen contamination might well come from the presence of the element at the Zr particle surface. Once oxygen is excluded from the system, ZrN might be obtained as a single phase and subsequently characterized by further analytical techniques such as those used for the V-C and Zr-C systems (XPS, PND, etc.). Further investigations are also needed, though, in order to confirm whether the observed cubic phase is actually the cubic form of zirconia or a different compound. However, no other known Zr compounds possess similar crystallographic characteristics to *c*-ZrO<sub>2</sub>. In case this aspect finds a positive confirmation, the formation of cubic zirconia represents a phenomenon that deserves further investigations, due to its gemological and economic importance as a diamond competitor. Another interesting observation in the  $Zr + NH_3$  reaction is the formation of the zirconium hydronitride phases (ZrN<sub>x</sub>H<sub>y</sub>) that is not seen in the  $Zr + N_2$  system (as no hydrogen is present). These phases have not been extensively studied previously. Further investigations on these compounds would therefore be undertaken to understand the composition and structure of these mixed anion compounds.

In conclusion, this work has proven the feasibility of microwave heating processes in the production of selected non-oxide ceramics and shown them to be viable alternatives to conventional methods. Further studies focused on the measurement of physical properties (such as microhardness, Young's modulus, electrical properties, etc.) of the MW-synthesized materials would be informative. These data could then be compared with those of conventionally synthesized materials to see whether (and how) microwave synthesis

might influence the microstructural physical (and chemical) properties of non-oxide ceramics.

## 7 Appendix

### Tables and Figures for Chapter 3:

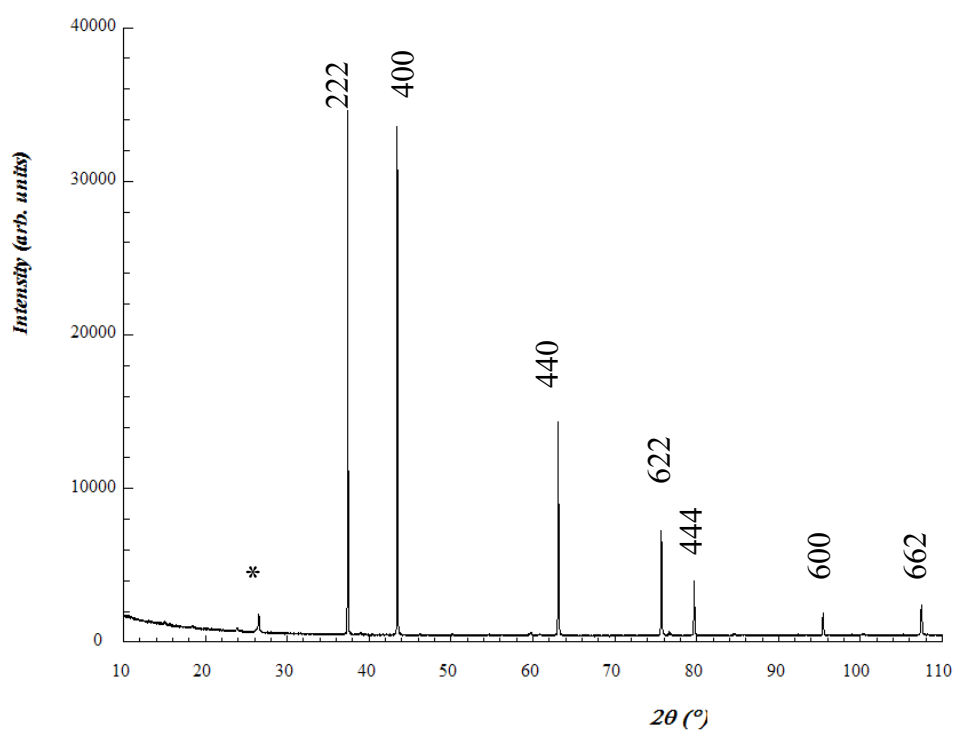


**Figure 7-1** PXRD pattern taken ex-situ from vanadium metal plus graphite (8:7) heated in a SMC reactor for 2 minutes at a power of 1 kW. All reflections can be attributed to  $V_8C_7$  except the one marked with \*, which belongs to the (002) reflection from graphite.

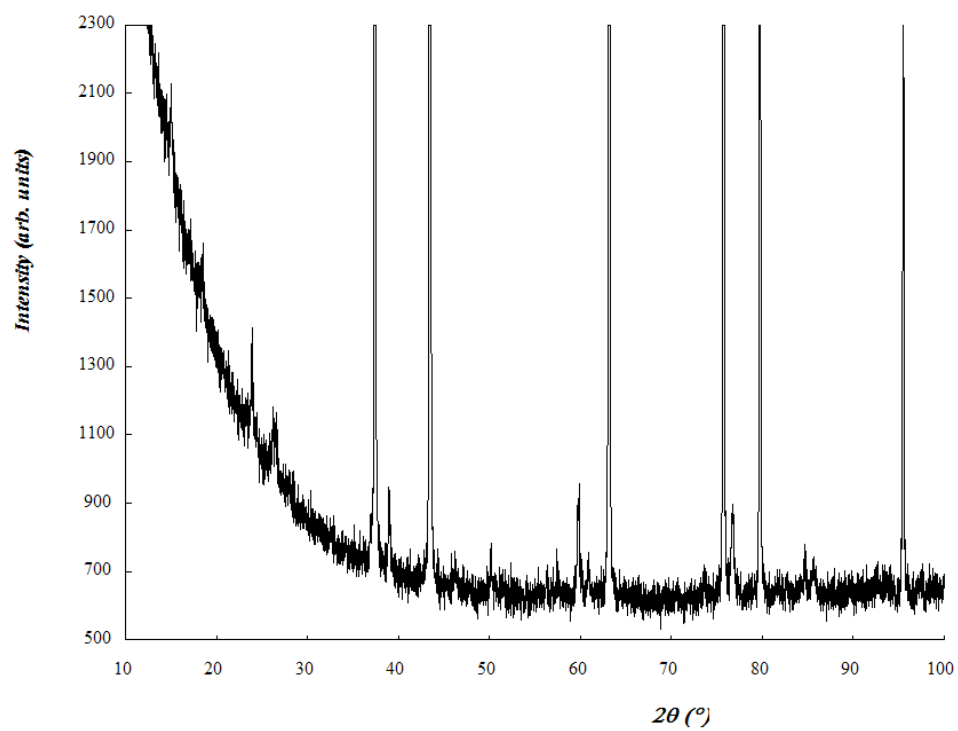


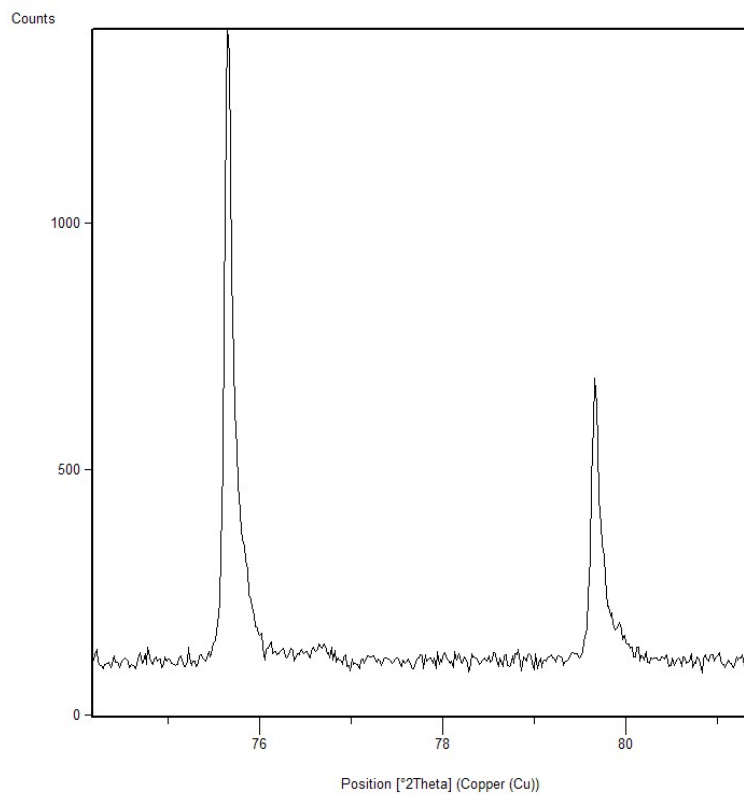
**Figure 7-2** Magnified image of the superstructure lines found in the PXRD pattern taken ex-situ from vanadium metal plus graphite (8:7) heated in a MMC reactor for 6 minutes at a power of 800 W

**Table 7-1** Selected atomic lengths (Å) and angles (°) from Rietveld refinement against PXRD data for V<sub>8</sub>C<sub>7</sub>.

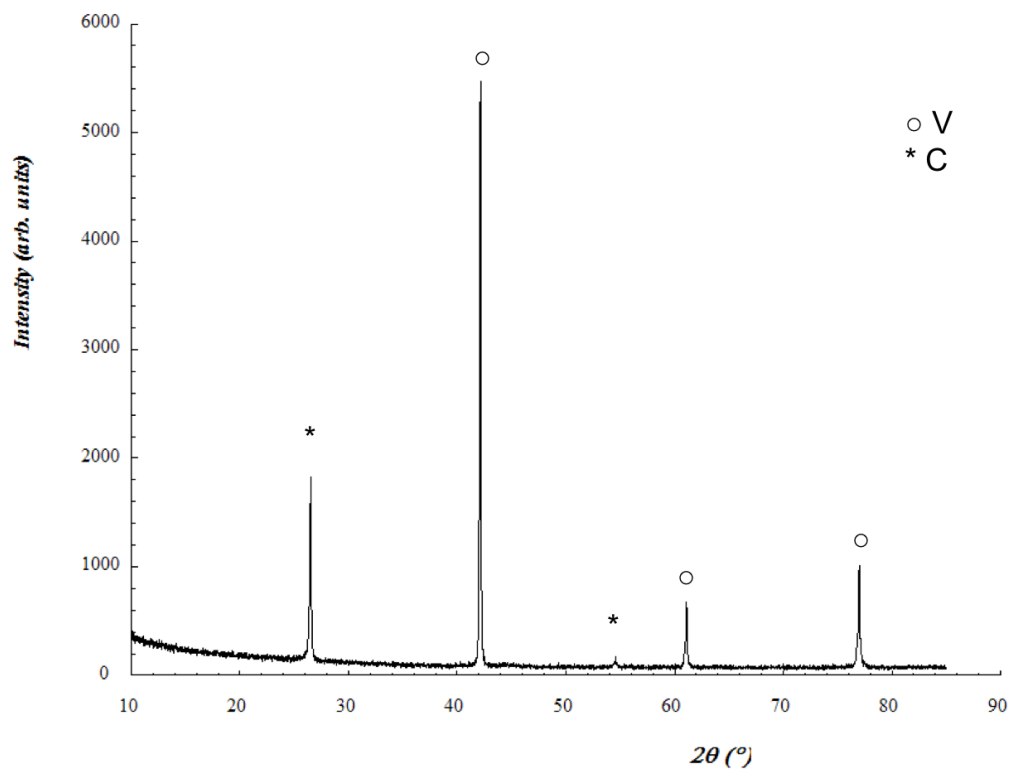
<b>Bond Lengths (Å)</b>			
V(1)–V(1)	2.94529(2)	V(2)–C(3)	2.08278(5)
V(1)–V(2)	2.94529(2)	C(1)–V(2)	2.08263(2)
V(1)–C(2)	2.1076(25)	C(2)–V(1)	2.1076(25)
V(1)–C(3)	2.0656(26)	C(2)–V(2)	2.08293(6)
V(2)–V(2)	2.94529(2)	C(2)–V(2)	2.0580(25)
V(2)–C(1)	2.08263(2)	C(3)–V(1)	2.0656(26)
V(2)–C(2)	2.0580(25)	C(3)–V(2)	2.0999(26)
V(2)–C(2)	2.08293(6)	C(3)–V(2)	2.08278(5)
V(2)–C(3)	2.0999(26)		

<b>Bond Angles (°)</b>			
C(2)–V(1)–C(2)	89.33(7)	V(2)–C(1)–V(2)	180.0(0)
C(2)–V(1)–C(3)	90.20(11)	V(1)–C(2)–V(1)	88.65(13)
C(2)–V(1)–C(3)	179.18(6)	V(1)–C(2)–V(2)	89.31(7)
C(2)–V(1)–C(3)	89.994(1)	V(1)–C(2)–V(2)	178.64(14)
C(3)–V(1)–C(3)	90.48(7)	V(1)–C(2)–V(2)	89.984(3)
C(1)–V(2)–C(2)	90.0(0)	V(2)–C(2)–V(2)	90.67(7)
C(1)–V(2)–C(2)	89.32(7)	V(2)–C(2)–V(2)	178.07(19)
C(1)–V(2)–C(3)	90.47(7)	V(2)–C(2)–V(2)	91.38(14)
C(1)–V(2)–C(3)	180.0(0)	V(1)–C(3)–V(1)	90.95(15)
C(2)–V(2)–C(2)	91.37(14)	V(1)–C(3)–V(2)	179.06(14)
C(2)–V(2)–C(3)	179.17(6)	V(1)–C(3)–V(2)	90.47(7)
C(2)–V(2)–C(3)	90.48(7)	V(1)–C(3)–V(2)	89.992(2)
C(2)–V(2)–C(3)	89.32(7)	V(2)–C(3)–V(2)	89.52(7)
C(2)–V(2)–C(3)	90.20(11)	V(2)–C(3)–V(2)	89.06(14)
C(3)–V(2)–C(3)	89.06(14)	V(2)–C(3)–V(2)	178.66(20)
V(2)–C(1)–V(2)	90.0(0)		



**Figure 7-3** Magnified image of the  $V_8C_7$  PXRD pattern after a 2-minute reaction illustrating the unsymmetrical nature of the reflections at  $75.7^\circ$  and  $79.6^\circ$   $2\theta$  angles.



**Figure 7-4** PXRd pattern taken ex-situ from vanadium metal plus graphite (8:7) heated in a MMC reactor for 0 seconds at a power of 800 W.

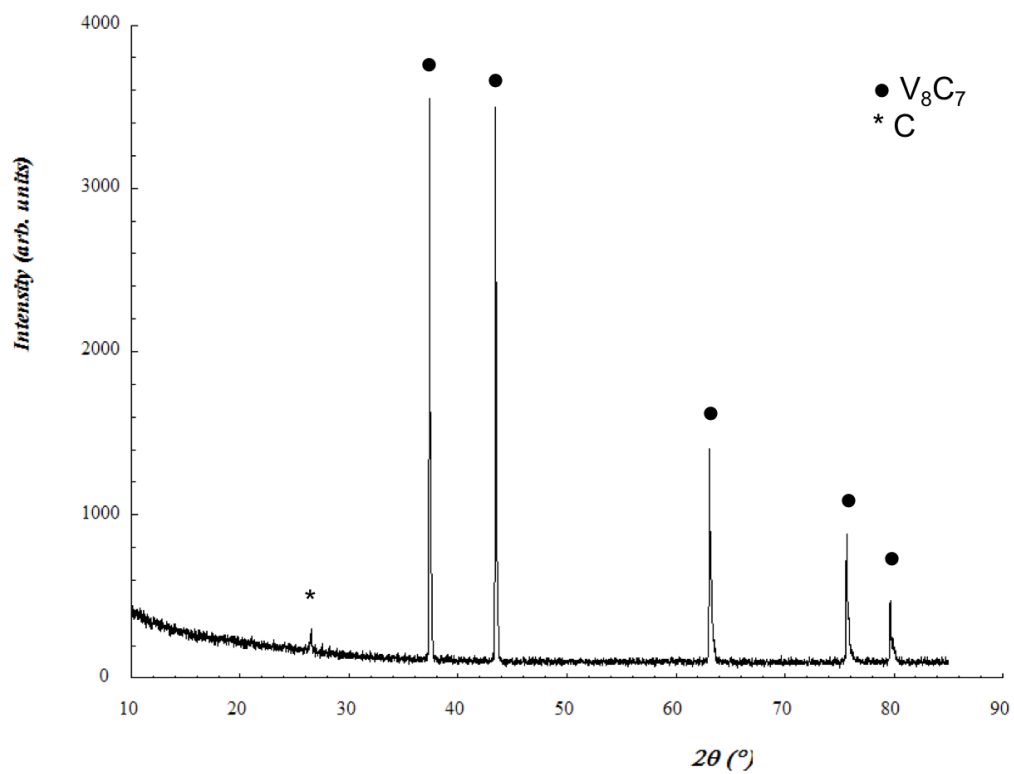


**Figure 7-5** PXRd pattern taken ex-situ from vanadium metal plus graphite (8:7) heated in a MMC reactor for 30 seconds at a power of 800 W.

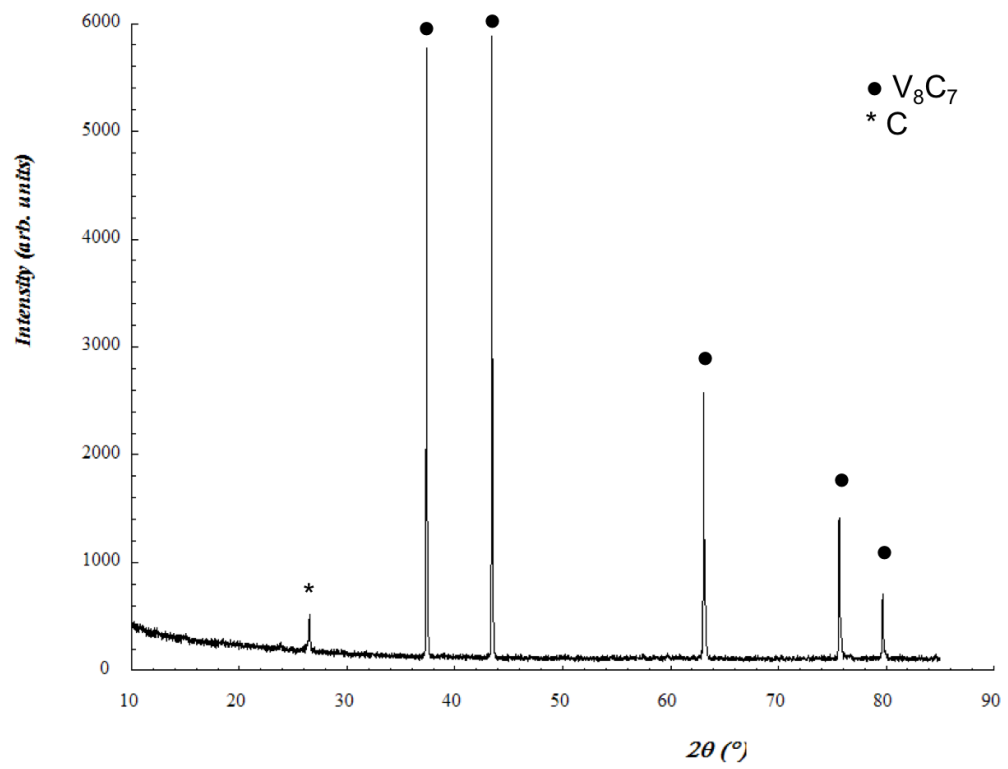


**Figure 7-6** PXRd pattern taken ex-situ from vanadium metal plus graphite (8:7) heated in a MMC reactor for 2 min at a power of 800 W.

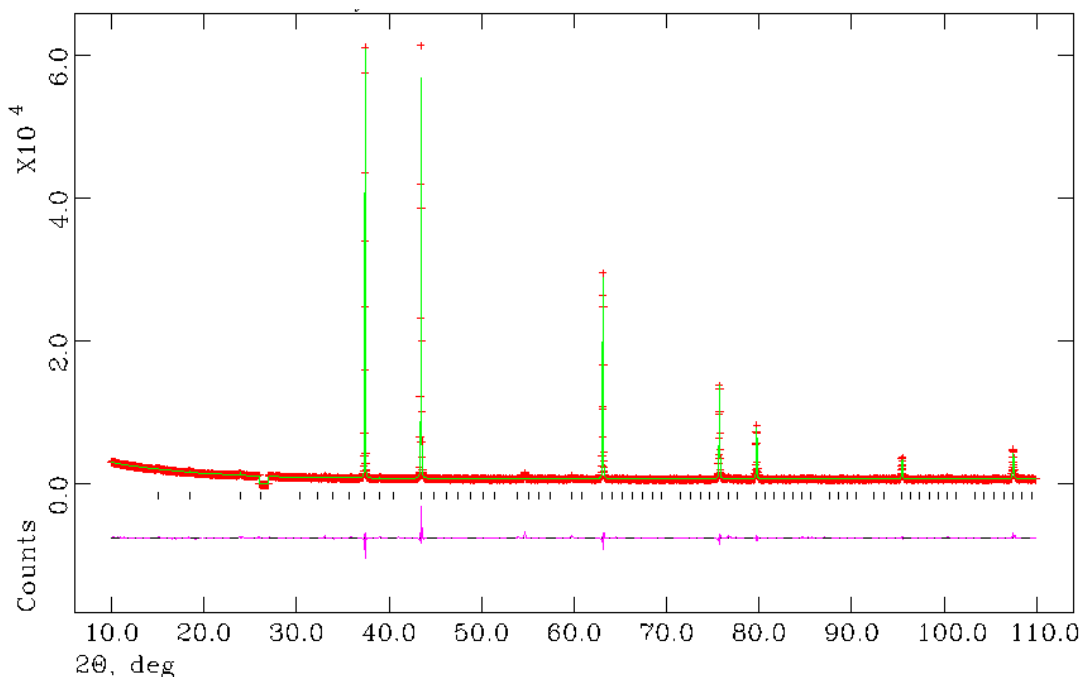


**Figure 7-7** Observed (*plusses*), calculated (*solid green line*), and difference (*solid purple line*) profile plot for the Rietveld refinement against PXRD data for the vanadium carbide superstructure  $V_8C_7$ , synthesized from vanadium metal and carbon in 6 minutes in a MMC reactor at power of 800 W. Tick marks denote  $V_8C_7$  diffraction peaks. The (002) graphite reflection at  $2\theta = 26.5^\circ$  was excluded from the refinement.

**Table 7-2** Crystallographic data from Rietveld refinement against PXRD data for  $V_8C_7$  prepared from vanadium metal and carbon in 6 minutes in an MMC reactor at a power of 800 W.

<b>Phase data</b>	
Chemical Formula	$V_8C_7$
Crystal system	Cubic
Space group	$P4_332$
$a$ (Å)	8.33073(4)
Volume (Å <sup>3</sup> )	578.16(1)
$Z$	4
Formula weight (g mol <sup>-1</sup> )	491.61
Calculated density (g cm <sup>-3</sup> )	5.64748
$R_{wp}$	0.0592
$R_p$	0.0404
$\chi^2$	3.916

**Table 7-3** Atomic parameters from Rietveld refinement against PND data for  $V_8C_7$  synthesized from vanadium metal and graphite heated in a MMC for 6 minutes at a power of 800 W.

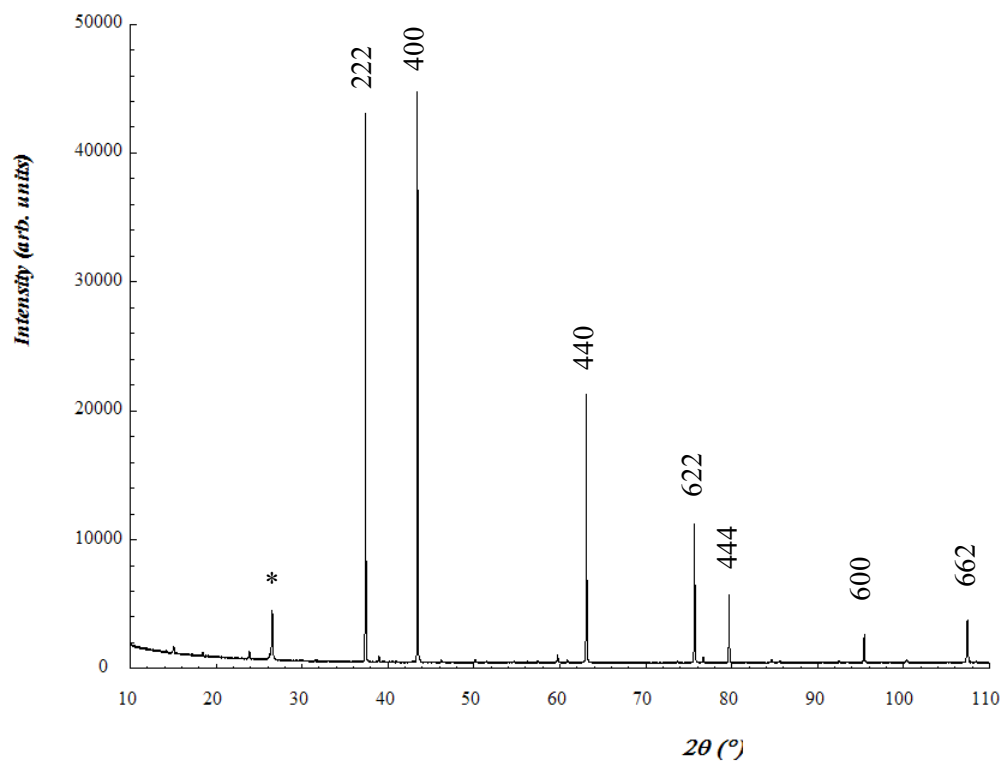
<b>Atomic parameters</b>						
Atom Type	Wyckoff Site	Fractional Coordinates			$U_{\text{iso}} (\text{\AA}^2)$	Site Occupancy
		$x/a$	$y/b$	$z/c$		
V(1)	$8c$	0.3750	0.3750	0.3750	0.01230(4)	1.0
V(2)	$24e$	0.1250	0.3750	0.1250	0.01230(4)	1.0
C(1)	$4a$	0.1250	0.1250	0.1250	0.00212(8)	1.0
C(2)	$12d$	0.1250	0.617951(4)	0.632049(2)	0.00212(8)	1.0
C(3)	$12d$	0.1250	0.382966(2)	0.867034(5)	0.00212(8)	1.0

**Table 7-4** Selected atomic lengths (Å) and angles (°) from Rietveld refinement against PND data for V<sub>8</sub>C<sub>7</sub> synthesized from vanadium metal and graphite heated in a MMC for 6 minutes at a power of 800 W.

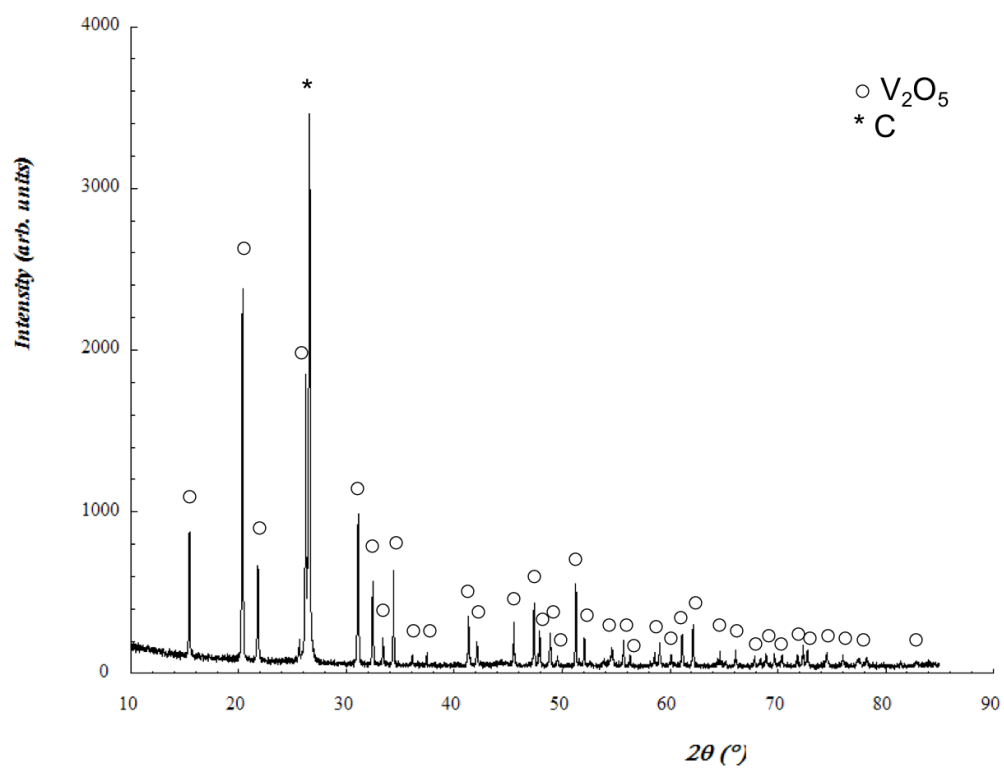
<b>Bond Distances (Å)</b>			
V(1)–V(1)	2.94536(1)	V(2)–C(3)	2.0833(6)
V(1)–V(2)	2.94536(1)	C(1)–V(2)	2.08268(1)
V(1)–C(2)	2.175(12)	C(2)–V(1)	2.175(12)
V(1)–C(3)	2.118(19)	C(2)–V(2)	2.0866(10)
V(2)–V(2)	2.94536(1)	C(2)–V(2)	1.994(11)
V(2)–C(1)	2.08268(1)	C(3)–V(1)	2.118(19)
V(2)–C(2)	1.994(11)	C(3)–V(2)	2.048(18)
V(2)–C(2)	2.0866(10)	C(3)–V(2)	2.0833(6)
V(2)–C(3)	2.048(18)		

<b>Bond Angles (°)</b>			
C(2)–V(1)–C(2)	87.62(28)	V(2)–C(1)–V(2)	180.0(0)
C(2)–V(1)–C(3)	93.3(6)	V(1)–C(2)–V(1)	85.2(6)
C(2)–V(1)–C(3)	177.4(4)	V(1)–C(2)–V(2)	87.41(33)
C(2)–V(1)–C(3)	90.040(22)	V(1)–C(2)–V(2)	175.0(6)
C(3)–V(1)–C(3)	89.0(5)	V(1)–C(2)–V(2)	89.78(5)
C(1)–V(2)–C(2)	90.0(0)	V(2)–C(2)–V(2)	92.37(27)
C(1)–V(2)–C(2)	87.52(30)	V(2)–C(2)–V(2)	173.0(9)
C(1)–V(2)–C(3)	89.0(5)	V(2)–C(2)–V(2)	95.2(7)
C(1)–V(2)–C(3)	178.6(7)	V(1)–C(3)–V(1)	88.1(10)
C(2)–V(2)–C(2)	95.1(6)	V(1)–C(3)–V(2)	178.1(10)
C(2)–V(2)–C(3)	177.2(4)	V(1)–C(3)–V(2)	89.0(5)
C(2)–V(2)–C(3)	89.0(5)	V(1)–C(3)–V(2)	89.967(34)
C(2)–V(2)–C(3)	87.47(31)	V(2)–C(3)–V(2)	91.0(5)
C(2)–V(2)–C(3)	93.5(7)	V(2)–C(3)–V(2)	92.0(11)
C(3)–V(2)–C(3)	92.0(1)	V(2)–C(3)–V(2)	177.3(14)
V(2)–C(1)–V(2)	90.0(0)		



**Figure 7-8** PXRD pattern taken ex-situ from vanadium(V) oxide plus graphite (4:27) heated for 6 minutes in a SMC microwave reactor for 2 minutes at a power of 1 kW. All reflections can be attributed to  $V_8C_7$  except the one marked with \*, which belongs to the (002) reflection from graphite.



**Figure 7-9** PXRd pattern taken ex-situ from vanadium(V) oxide plus graphite (4:27) heated for 0 seconds in an MMC microwave reactor at a power of 800 W.

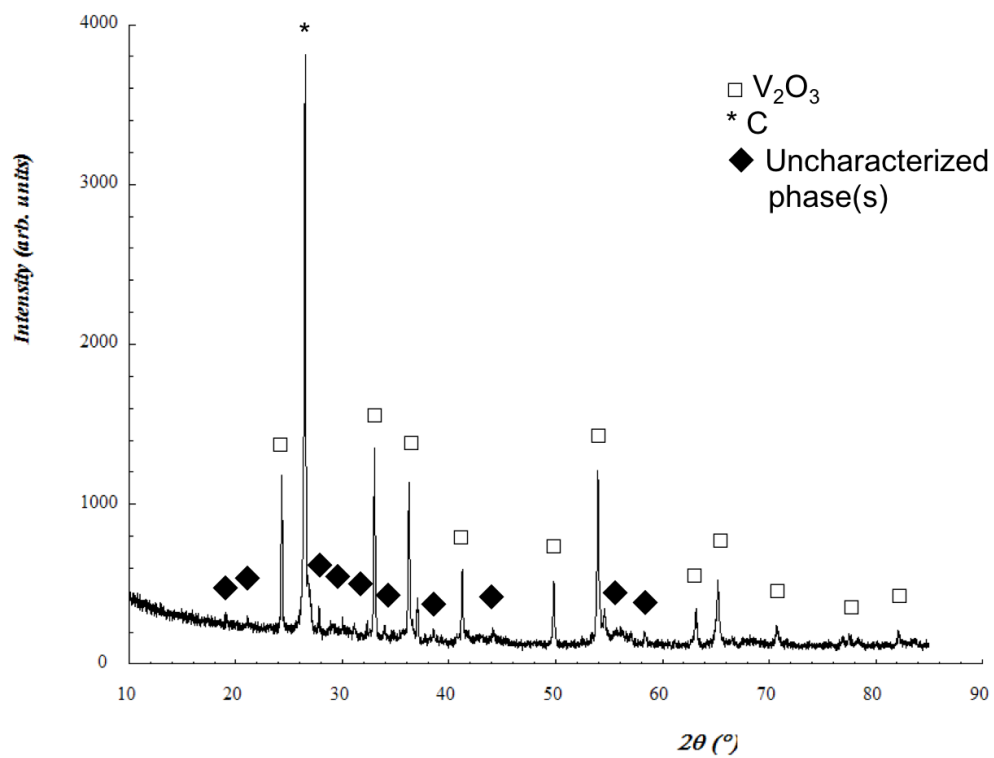


**Figure 7-10** PXRd pattern taken ex-situ from vanadium(V) oxide plus graphite (4:27) heated for 30 seconds in an MMC microwave reactor at a power of 800 W.

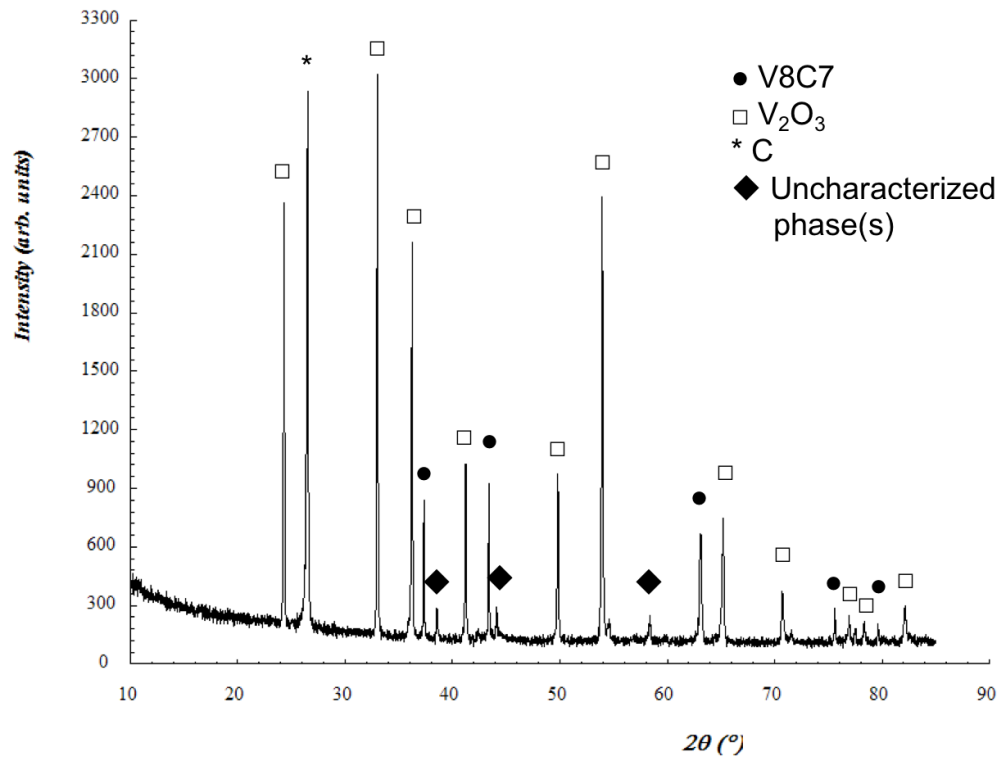


**Figure 7-11** PXR D pattern taken ex-situ from vanadium(V) oxide plus graphite (4:27) heated for 1 minute in an MMC microwave reactor at a power of 800 W.

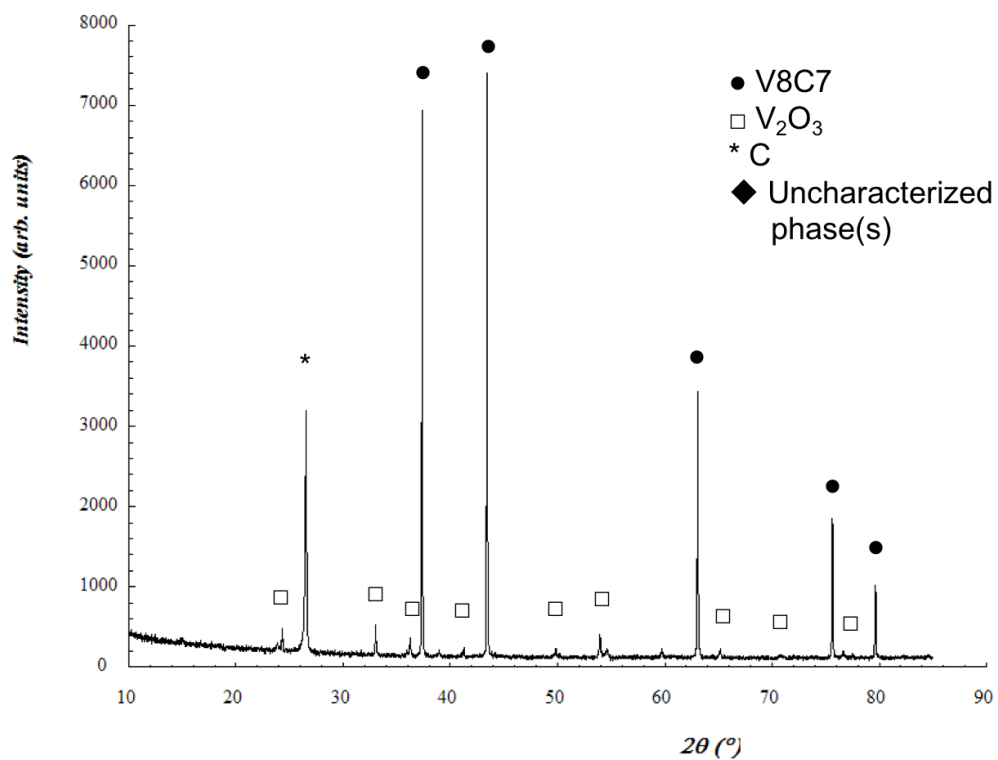


**Figure 7-12** PXR D pattern taken ex-situ from vanadium(V) oxide plus graphite (4:27) heated for 2 minutes in an MMC microwave reactor at a power of 800 W.

## Tables and Figures for Chapter 4:

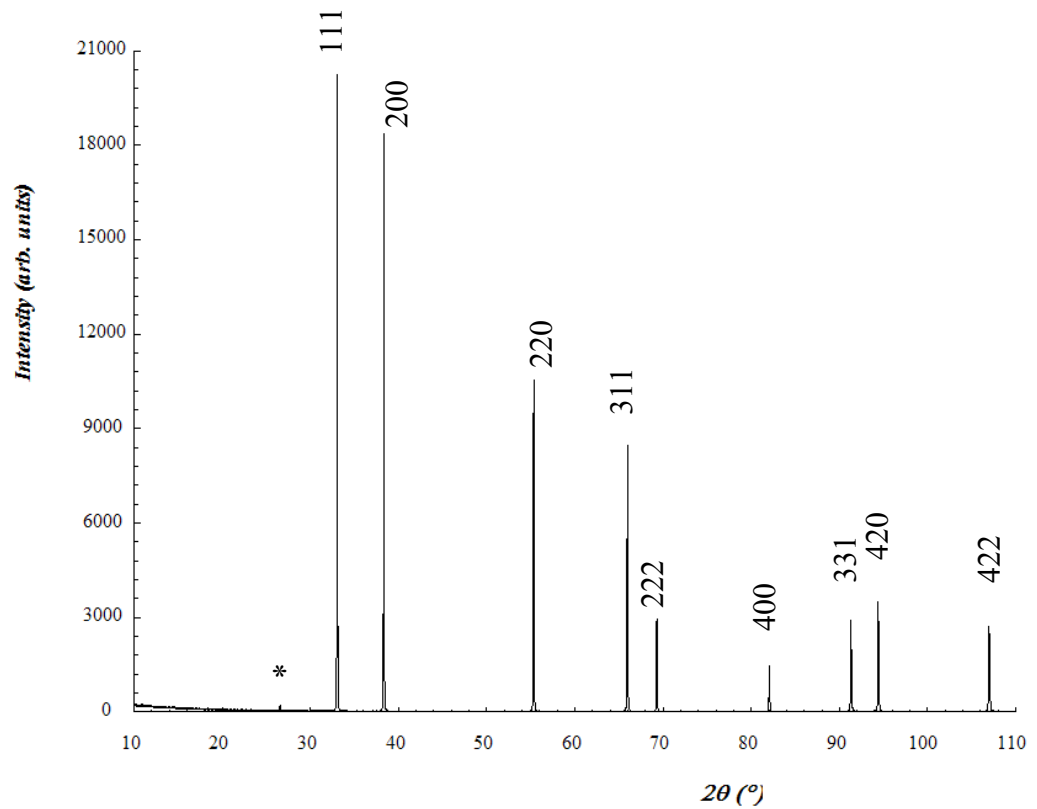


**Figure 7-13** PXRd pattern taken *ex-situ* from zirconium metal plus graphite (1:1) heated in a SMC reactor for 6 minutes at a power of 1 kW under Ar. All reflections can be attributed to ZrC except the one marked with \*, which belongs to the (002) reflection from graphite.

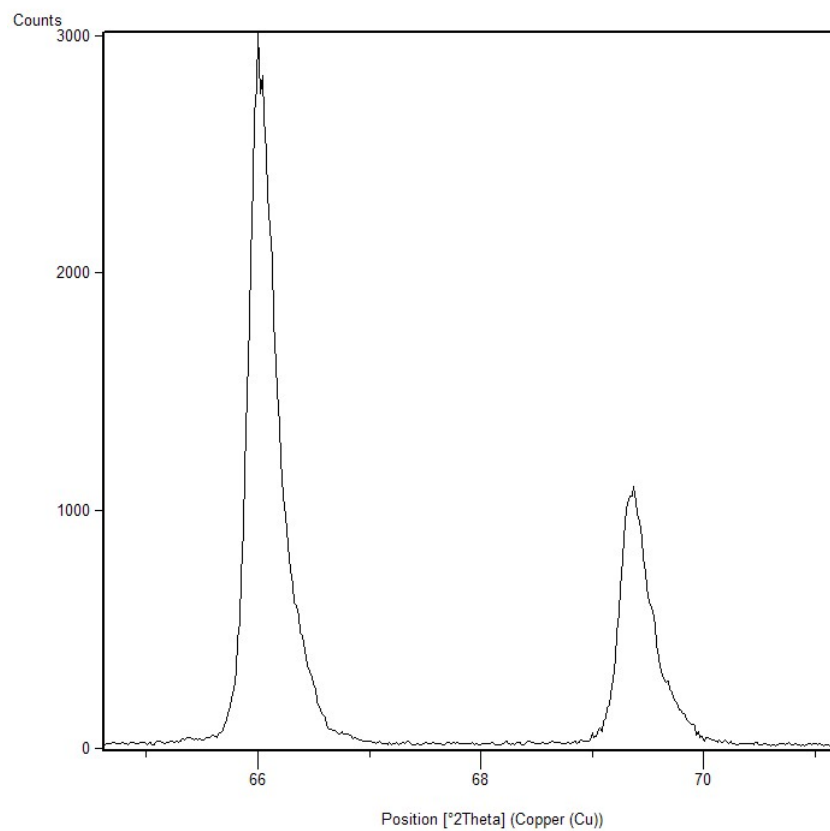


**Figure 7-14** Magnified image of the ZrC PXR pattern after a 10-minute reaction illustrating the unsymmetrical nature of the reflections at 66° and 69.5° 2 $\theta$  angles.

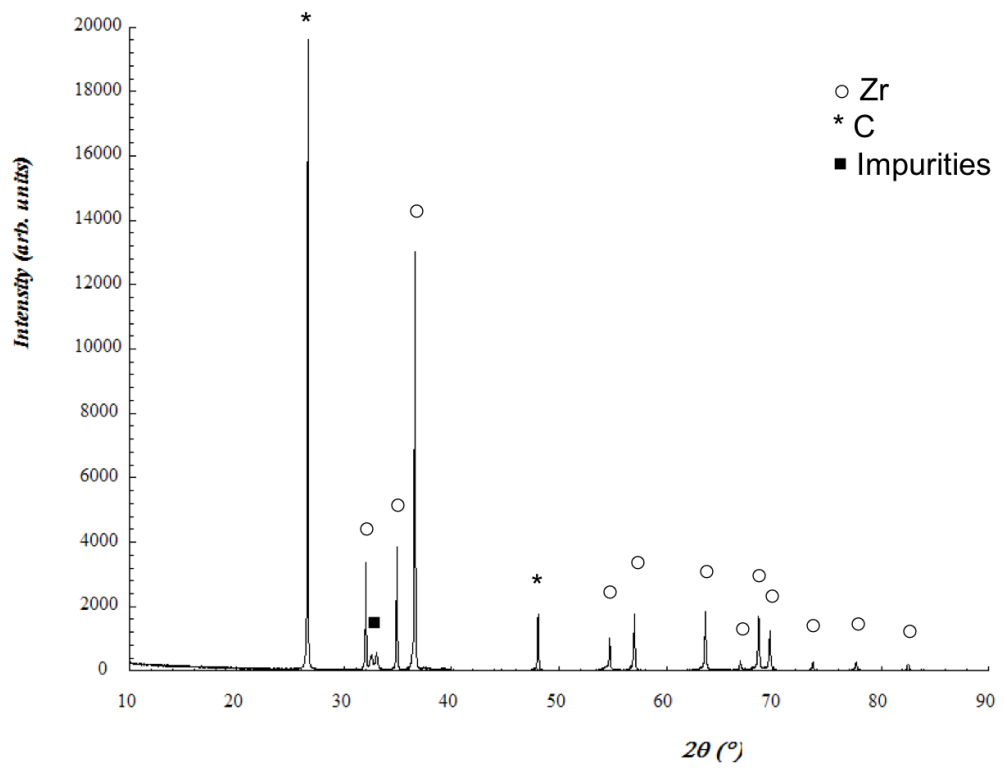


**Figure 7-15** PXR D pattern taken ex-situ from zirconium metal plus graphite (1:1) heated in a MMC reactor for 0 seconds at a power of 800 W. Impurities were present in the Zr starting material bought from Alfa Aesar.

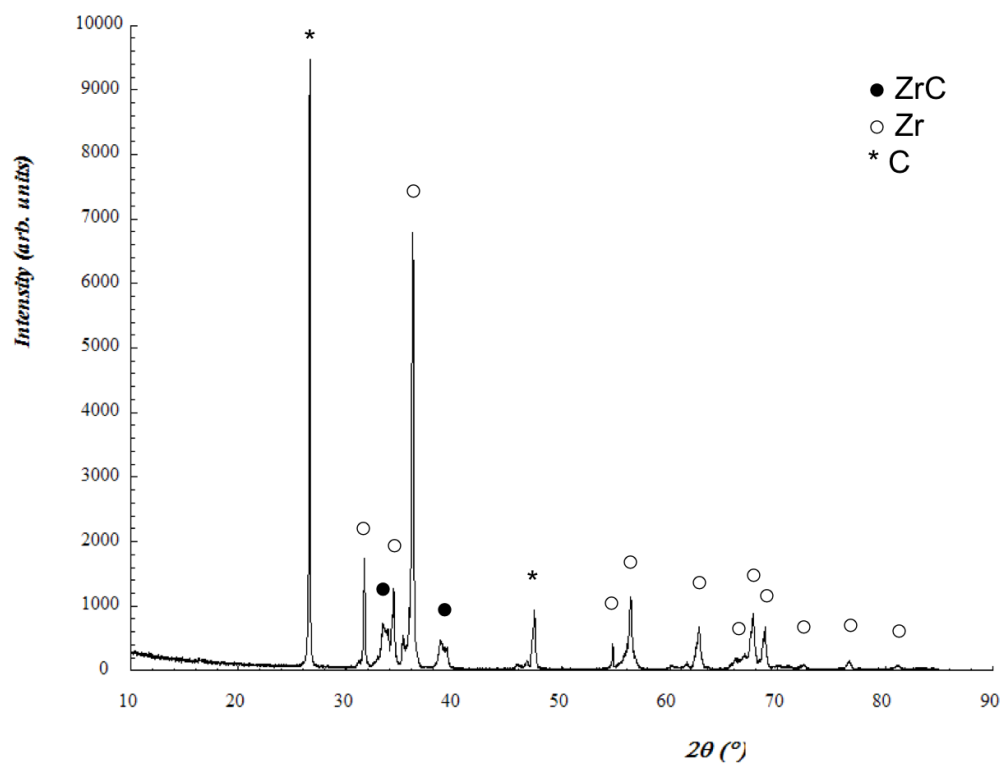


**Figure 7-16** PXR D pattern taken ex-situ from zirconium metal plus graphite (1:1) heated in a MMC reactor for 5 minutes at a power of 800 W.

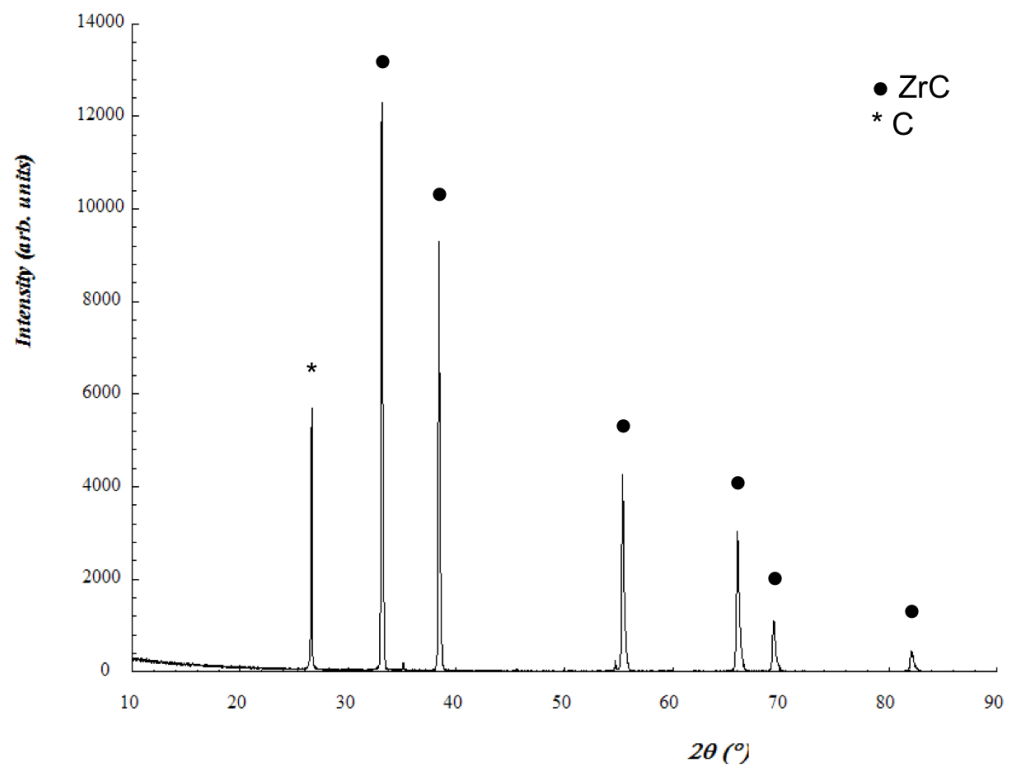


**Figure 7-17** PXRD pattern taken ex-situ from zirconium metal plus graphite (1:1) heated in a MMC reactor for 10 minutes at a power of 800 W.

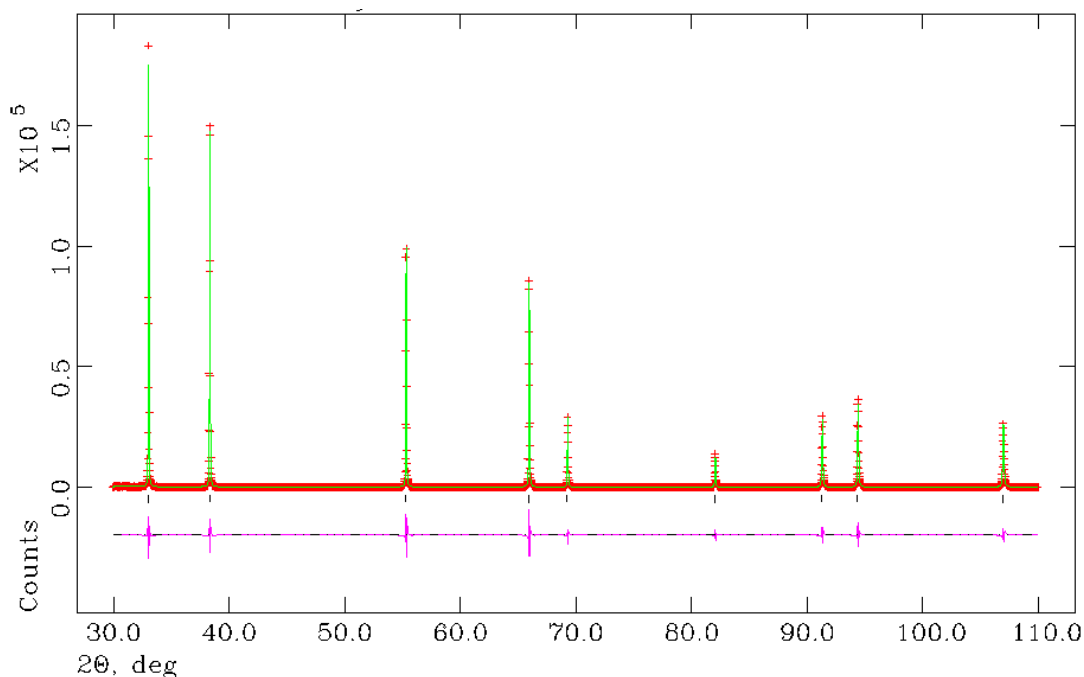


**Figure 7-18** Observed (plusses), calculated (solid green line), and difference (solid purple line) profile plot for the Rietveld refinement against PXRD data for the MW-synthesized ZrC from zirconium metal and graphite. Tick marks denote ZrC diffraction peaks

**Table 7-5** Crystallographic data from Rietveld refinement against PXRD data for ZrC prepared from zirconium metal and carbon in 20 minutes in an MMC reactor at a power of 800 W.

<b>Phase data</b>	
Chemical Formula	ZrC
Crystal system	Cubic
Space group	<i>Fm</i> -3 <i>m</i>
<i>a</i> (Å)	4.69559(5)
Volume (Å <sup>3</sup> )	103.53(2)
<i>Z</i>	4
Formula weight (g mol <sup>-1</sup> )	103.23
Calculated density (g cm <sup>-3</sup> )	6.5297
<i>R</i> <sub>wp</sub>	0.1451
<i>R</i> <sub>p</sub>	0.1057
$\chi^2$	18.46

**Table 7-6** Atomic parameters from Rietveld refinement against PND data for ZrC synthesized from zirconium metal and graphite heated in a MMC for 20 minutes at a power of 800 W.

<b>Atomic parameters</b>					
Name	Fractional coordinates			U <sub>iso</sub>	Occup.
	<i>x/a</i>	<i>y/b</i>	<i>z/c</i>		
Zr1	0.0000	0.0000	0.0000	0.00130(2)	1.0
C1	0.5000	0.5000	0.5000	0.00795(5)	1.0